Valley dynamics and excitonic properties in monolayer transition metal dichalcogenides

Louis Bouet

Université Fédérale

Toulouse Midi-Pyrénées

THÈSE

En vue de l'obtention du

DOCTORAT DE L'UNIVERSITÉ DE TOULOUSE

Délivré par *L'INSTITUT NATIONAL DES SCIENCES APPLIQUEES*
Discipline ou spécialité : *Nanophysique*

Présentée et soutenue par *Louis BOUET*
Le *9 Octobre 2015*

Valley dynamics and excitonic properties in monolayer transition metal dichalcogenides

---

JURY

Jean-Yves CHANE-CHING	Directeur de recherche au CNRS	Examinateur
Bernard GIL	Directeur de recherche au CNRS	Rapporteur
Tobias KORN	Privatdozent (HDR)	Examinateur
Xavier MARIE	Professeur des Universités	Directeur de thèse
Henri MARIETTE	Directeur de recherche au CNRS	Rapporteur
Bernard PLAÇAIS	Directeur de recherche au CNRS	Examinateur
Bernhard URBASZEK	Directeur de recherche au CNRS	Directeur de thèse

---

Ecole doctorale : *SDM : Nano-physique, nano-composants, nano-mesures - COP 00*
Unité de recherche : *Laboratoire de Physique et Chimie des Nano-Objets (UMR 5215)*
Directeur(s) de Thèse : *Bernhard URBASZEK* et *Xavier MARIE*
Rapporteurs : *Bernard GIL* et *Henri MARIETTE*

N° ordre ?

THESE

présentée à

L'INSTITUT NATIONAL DES SCIENCES APPLIQUEES DE TOULOUSE

vue de l'obtention du

DOCTORAT DE L'UNIVERSITE DE TOULOUSE

Spécialité : Nanophysique

par

Louis BOUET

Valley dynamics and excitonic properties in monolayer transition metal dichalcogenides

Soutenue le 9 Octobre 2015, à Toulouse

devant la commission d'examen :

Rapporteur	B. GIL	Directeur de Recherche au CNRS, Laboratoire Charles COULOMB
Rapporteur	H. MARIETTE	Directeur de Recherche au CNRS, Institut NEEL
Examinateur	B. PLAÇAIS	Directeur de Recherche au CNRS, Laboratoire Pierre AIGRAIN
Examinateur	T. KORN	Privatdozent (HDR), Uni. Regensburg
Examinateur	J.-Y. CHANE-CHING	Directeur de Recherche au CNRS, (CIRIMAT-LCMIE)
Directeur de thèse	B. URBASZEK	Directeur de Recherche, LPCNO-CNRS
Directeur de thèse	X. MARIE	Professeur des Universités, INSA Toulouse

Cette thèse a été préparée au sein du Laboratoire de Physique et Chimie des Nano-Objets, UMR 5215 INSA-CNRS-UPS.

The possibility of isolating transition metal dichalcogenide monolayers by simple experimental means has been demonstrated in 2005, by the same technique used for graphene. This has sparked extremely diverse and active research by material scientists, physicists and chemists on these perfectly two-dimensional (2D) materials.

Their physical properties in monolayer form are appealing both from the point of view of fundamental science and for potential applications. Transition metal dichalcogenide monolayers such as MoS_2 have a direct optical bandgap in the visible and show strong absorption of the order of 10% per monolayer. For transistors based on single atomic layers, the presence of a gap allows to obtain high on/off ratios.

In addition to potential applications in electronics and opto-electronics these 2D materials allow manipulating a new degree of freedom of electrons, in addition to the spin and the charge : Inversion symmetry breaking in addition to the strong spin-orbit coupling result in very original optical selection rules. The direct bandgap is situated at two non-equivalent valleys in k-space, K^+ and K^-. Using a specific laser polarization, carriers can be initialized either in the K^+ or K^- valley, allowing manipulating the valley index of the electronic states. This opens up an emerging research field termed "valleytronics".

The present manuscript contains a set of experiments allowing understanding and characterizing the optoelectronic properties of these new materials. The first chapter is dedicated to the presentation of the scientific context. The original optical and electronic properties of monolayer transition metal dichalcogenides are demonstrated using a simple theoretical model. The second chapter presents details of the samples and the experimental setup. Chapters 3 to 6 present details of the experiments carried out and the results obtained. We verify experimentally the optical selection rules. We identify the different emission peaks in the monolayer materials MoS_2, WSe_2 and $MoSe_2$. In time resolved photoluminescence measurements we study the dynamics of photo-generated carriers and their polarization. An important part of this study is dedicated to experimental investigations of the properties of excitons, Coulomb bound electron-hole pairs. In the final experimental chapter, magneto-Photoluminescence allows us to probe the electronic band structure and to lift the valley degeneracy.

Résumé

La possibilité de créer des monocouches de dichalcogenures à métaux de transition (MoS2, WSe2,MoSe2 pour ceux étudiés dans ce manuscrit) a été démontrée récemment (2005) et a ouvert la voie à l'étude de ces matériaux sous leur forme 2D. Il apparaît depuis que les propriétés de ces semi-conducteurs sous leur forme monocouche offrent des perspectives intéressantes à la fois du point de vue de la physique fondamentale et des potentielles applications qui peuvent en découler ; en plus de bénéficier d'un fort couplage avec la lumière, l'existence d'un gap important (situé dans le visible, 1.7-1.8 eV) permet entre autres de réaliser des transistors d'épaisseur mono-atomique. Par ailleurs, la physique de ces matériaux est prometteuse pour les applications dans le domaine de l'optoélectronique. En effet, lorsque le matériau est affiné jusqu'à la monocouche atomique, son gap optique devient direct et la brisure de symétrie d'inversion associée au fort couplage spin-orbite provoque l'apparition de règles de sélection optique originales qui relient directement la polarisation de la lumière émise ou absorbée à une des deux vallées non-équivalentes de l'espace réciproque. Cela ouvre la possibilité d'explorer une nouvelle physique, basée sur l'indice de vallée et intitulée en conséquence vallée-tronique, avec

comme perspectives futures la manipulation de l'indice de vallée et l'exploitation d'effets liés à cette relation originale entre propriétés optiques et électroniques (effet vallée-Hall par exemple). Ce manuscrit de thèse regroupe une série d'expériences réalisées dans le but de comprendre et caractériser les propriétés optoélectroniques de ces matériaux. Un premier chapitre introductif présente le contexte scientifique de ces travaux de recherche et démontre l'origine des propriétés électroniques et optiques de ces matériaux via un modèle théorique simple. Le second chapitre présente en détails les échantillons étudiés ainsi que le dispositif expérimental utilisé lors des mesures. Enfin les chapitres 3 à 6 détaillent les expériences menées et les résultats obtenus ; le lecteur y trouvera des mesures de photoluminescence apportant la démonstration expérimentale des règles de sélection optique, l'identification des différents raies spectrales d'émission pour les différents types d'échantillons mentionnés plus haut ainsi que des mesures de photoluminescence résolues en temps permettant d'extraire la dynamique des propriétés des porteurs photo-générés. Une part importante de ce manuscrit est consacrée à l'étude expérimentale des propriétés excitoniques de ces matériaux dont la structure de bande électronique est finalement sondée via des études de magnéto-spectroscopie.

Acknowledgment

Beyond the horizon of the place we lived when we were young
In a world of magnets and miracles...
(High hopes, Pink Floyd)

To my teachers and all the people who feed my thirst for knowledge and arouse my curiosity.

To my family who supported me, raised me in the best way I could have wished and let me do my own choices.

To Marine, with all my love.

I spend in total three years and a half in the Optoelectronics Group in the laboratory of physics and chemistry of nano-objects, including a 6 months internship and my PhD. Those years have been very rich from the scientific point of view, and not only. I had the chance to cross the way of many interesting people without whom this work would have never existed.

First of all, I would like to thank Jean-Yves Chane Ching, Bernard Gil, Tobias Korn, Henri Mariette and Bernard Plaçais for accepting to be part of my thesis defense commission, for their questions and more generally for the interest they express for this work. A special thanks to Henri Mariette and Bernard Gilles who review the manuscript and provide me a very positive feedback.

I would like to thank Bruno Chaudret for welcoming me in the Laboratoire de Physique et Chimie des Nano-Objets. I am also very grateful to Bertrand Raquet, now director of INSA, previously head of the physics department, who in addition to be a great teacher, gave me the very good advice to ask for PhD opportunity in the quantum optoelectronic group.

I am grateful to many people I met, worked with; who helped me in very different ways, and without who those 3 years as a PhD student would have been much poorer. I tried to list them all but I probably forget some, please forgive me and receive my thanks for the time we spend together!

- Thierry Amand: Thank you a lot Thierry, for all our conversations and all your explanations about quantum mechanics as well as solid state physics, group theory and so on. Without all your inputs, this manuscript would look completely different and my knowledge and understanding of physics would be much poorer. I am extremely grateful to you for all that!

- Andrea Balocchi: Thank you for your private lessons of physical optics dear professor! I am also glad that you teaches me "'Ondes et propagation"' and "'Diffraction optics"' in 2nd and 3rd year at INSA, despite appearances I learned really a lot. Finally I have to write that you are the Mozart of laser alignment and at least a 6th dan physicist, thanks a lot for all your help!

- Michel Bonnet: Thank you Michel for hiring me as a "'doctorant chargé d'enseignement"'. I learned a lot from you, as a teacher and then as a colleague. Thank you for that!

- Helène Carrère: Helene, your lecture "'electrostatique"' was clearly a trigger that convinced me to choose the physics department. It was really nice to be the colleague of someone so gentle, of constant good humor and with a deep sense of humor! Also, I was glad to have a such good teacher as pedagogy referent! I hope that we will meet again and maybe share another drink or two, at the Dubliners or somewhere else!

- Mikhail Durnev: Thank you Misha for our collaboration and the time we spend together in France. It was a pleasure to discuss science with you in the lab or skiing at Ax-les-Thermes. I will also keep a very good memory of that evening dedicated to cheese, wine and guitar! He hope we will meet again, in Toulouse or in St Petersbourg!

- Mikhail Glazov: Dear Misha thank you so much for all your inputs and for our collaboration! I learned a lot at your contact both concerning physics and Russian culture. It was a pleasure to see you in Toulouse and I hope we will meet again in France or in Russia!

- Ian Gerber: All your inputs of theoretical calculations added a great value to our work on TMDCs and to this manuscript. Thank you for teaching me quantum mechanics and for our collaborations!

- Sergej Kunz: Thank you Sergej for our discussions and for the time we spend together in the experiment room! I wish you all the best for the futur.

- Takashi Kuroda: Working with Dr. Takashi Kuroda was a great chance for me. In addition to be an excellent physicist and experimentalist, he is a remarkable man for his deep sense of humanity. I am also really grateful to him for his invitation to work to the National Institut for Material Science. This month and a half I spend in Japan was clearly the most exciting adventure of my thesis. It was a unique chance to work in a completely different cultural environment. Arigatou gozaimasu Kurodasan!

- Delphine Lagarde: Delphine taught me experimental physics with Gregory and I am very grateful to her for that. She is a very kind colleague and I'll always remember the time we spend together in the experiment room performing time resolved spectroscopy on MoS_2 monolayers. I wish you all the best, as well as to your family and I hope that we will be able to run a 10km or the INSA raid together next time!

- Takaaki Mano: I was very lucky to collaborate with Dr. Takaaki Mano who provide us high quality samples, allowing us to perform measurements on state of the art quantum dots grown by droplet epitaxy. Thank you very much!

- Xavier Marie: Xavier, thank you for your trust. It was a great chance for me to have you as a thesis director. Thank you for all the opportunities you provides me and all the physics I learned at your contact during those 3 years, as well as for your communicative enthusiasm and energy!

- Jonas Nilsson: Dear Jonas, thank you for those three weeks we spend together in the dark performing experiments on nuclear spin physics. This was an intense but fruitful start for my thesis that putted me on the right track.

- Pierre Renucci: I had the chance to appreciate Pierre both as a teacher and as a colleague. In addition to our discussions about physics that bring me a lot, it was also great to discuss music with you and to share a similar sense of humor. Thank you for all this Pierre, once again, sorry for that night during the NEXT conference and I'll keep you up to date of the last news of La Depeche and co.

- Gregory Sallen: Thank you very much for everything you taught me concerning experimental physics and especially the single dot spectroscopy setup! Thanks to you I was able to start quickly and efficiently my thesis work and to contribute to experimental measurements during my internship! I am very grateful to you for that!

- Bernhard Urbaszek: Dear Bernhard thank you for everything! Thank you for trusting me and hiring me as an internship and then as a PhD student. I consider myself very lucky for having you as PhD director, both for the scientific guidance and for all the opportunities you provided to me. Your directions were a key element that allows me to achieve a successful thesis, with many scientific results and a lot of new experiences (in the lab as an experimental physicist, but also in conferences and for collaborative work in Italy, Germany, England, Japan). In addition to the scientific content, I really appreciate our exchanges and discussions ; among others you make me discover Bear's Den, Bon Iver, Sixto Rodrigez as well as Jeannette Walls... In short, you contribute greatly to the richness of those 3 years experience and I am really grateful to you for that. Ein letzes mal, vielen dank Bernhard!

- Mael Vidal: Dear Mael thank you for all the time we spend together in the experiment room and for our innumerable discussions. I wish you all the best for your thesis and for the futur!

- Liu Xiangming: Thank you for welcoming me in your lab at the NIMS, and for allowing me to participate to your measurements. I was glad to work and discuss with you. I wish you good luck for the futur and tell me if one day you come to Toulouse!

- Gang Wang: Dear Gang thank you for our collaboration. It was a pleasure to be your colleague and to work with you. I wish you all the best and good luck for your next adventure in the US and in China!

- And also : Sawsen, Philippe, Tian-Tian, Cong-Tu, Cédric, Simone, Cathy, Francis, Sébastien, Angélique, Pascal Gérard, Reasmey Tan, Thomas Blon, Julian Carrey, Benjamin Lassagne, Etienne Palleau, Pierre Moutet, Damien, Michel Fortune, Elisabeth, Brice, Khalled Karrai, Pierre François Braun and all others... Thank you so much!

Contents

Introduction

The quantum optoelectronic group of the laboratory for physics and chemistry of nano-objects (LPCNO, UMR 5215) dedicates its research activities to the field of semiconductors. The research work of the group is focused on semiconductor optics and carriers spin dynamics in semiconductor nano-structures. [1–4].

Spintronics is a research field that aims to use carriers spin states as an information vector and to realize electronic functions using the spin as support [5]. It is a very dynamic research field in which the quantum optoelectronics group is involved. The group has worked on a variety of systems, for example quantum dots (QDs), quantum wells and electrical spin injection.

I joined the group in this context in the beginning of 2012, as a master student. I was first involved in the research field of spintronics, studying dynamic nuclear polarization in strain free GaAs quantum dots under applied magnetic field, but very quickly another new exciting subject emerged in parallel. Due to our strong collaboration with the Chinese academy of science, we were able to verify in monolayer MoS_2, only a few weeks after the prediction of the chiral interband selection rules, that the valley index can be initialized optically.

This marks the starting point of our involvement in this international, collaborative and highly competitive research field of coupled spin- and valley-physics in 2D semiconductors. This new research field is very promising in terms of potential applications[6]. It has already been demonstrated that it is possible to use TMDC monolayers to fabricate atomically thin transistors[7], as well as optoelectronics components, such as LEDs[8; 9] or ultra sensitive photodetectors[10]. Current international research is aimed at potential solar-cell applications, non-linear optical crystals for frequency doubling (second harmonic generation) or more prospective applications such as valleytronics devices.

From a fundamental physics point of view, the valley equivalent of the spin-hall effect, termed valley-hall effect has been predicted [11] and a lot of experimental effort is currently under way to experimentally demonstrate it [12].

The valley index is manipulated optically in TMDC monolayers. Therefore the fundamental experiments on optical selection rules, exciton binding energies and radiative lifetimes presented in this thesis are helpful in the context of both valleytronics and optoelectronics device development.

It is important to underline that this work benefited greatly from local, national and international collaborations. Theoretical modeling and interpretation were conducted in close collaboration with I. Gerber, from the LPCNO (DFT calculation) and with our collaborators from the Ioffe institut, M.M. Glazov, E.L. Ivchenko and M. V. Durnev (k.p theory, group theory and many fruitful discussions). Sample preparation benefited from our collaboration with E. Palleau from the LPCNO as well as with our collaborators from the Chinese Academy of Science, C.R. Zhu and B.L. Liu. This work was partially funded by ERC Grant No. 306719, ANR MoS2ValleyControl and Programme Investissements d'Avenir ANR-11-IDEX-0002-02, reference ANR- 10-LABX-0037-NEXT.

Scope of this thesis

This thesis aims to present the major part of our contribution to this field of Valleytronics. In the first chapter, an introduction to Transition Metal Dichalcogenides (TMDCs) will be presented, including a short history of the field as well as a detailed introduction to these materials and Valley index related physics.

The second chapter presents an overview of the investigated samples, as well as a detailed presentation of our experimental setup.

In the third chapter, using mainly photoluminescence spectroscopy, we investigate the robustness of the optically created polarization under different experimental conditions, such as strong transverse magnetic fields, broad temperature range (from 4K to 300K) and varying excitation laser power.

The fourth chapter is dedicated to time resolved PL investigations on both MoS_2 and WSe_2 monolayers. For both materials, we find fast exciton emission decay times, showing that cw detected measurements results are only influenced by what happens in the first ps after the carrier initialization. Spectrally well defined exciton resonances in ML WSe_2 allow to uncover differences between neutral and charged exciton dynamics. Theoretical analysis, developed in collaboration with M. M. Glazov, demonstrates that the neutral excitons in different K-valleys are coupled by the Coulomb exchange interaction, which can lead to an admixture between states from different k-valleys. We finally discuss the use of the trion as a candidate for optically initialized valley Hall experiments.

In the fifth chapter we investigate the exciton properties in WSe_2 monolayers. Exciton binding energies of hundreds of meV are measured due to the strong vertical confinement, reduced dielectric screening and high effective masses demonstrating clearly that excitons govern the direct optical transitions for all TMDCs monolayers. We show that the light-matter interaction in monolayer WSe_2 is strongly enhanced when the incoming electro-magnetic wave is in resonance with the energy of the exciton states, below the electronic bandgap. We also perform second harmonic generation (SHG) spectroscopy as a function of laser energy and polarization at T=4K. At the exciton resonance energies we record an enhancement by up to 3 orders of magnitude of the SHG efficiency. The energy and parity of the exciton states showing the strong resonance effects are identified in 1 and 2-photon photoluminescence excitation experiments. Exciton excited states identification, corroborated by first principle calculations allows us to determine an exciton binding energy of the order of 600 meV in ML WSe_2.

Finally, in the sixth chapter we present the result of magneto-optics experiments at T=4K performed on two different transition metal diselenides monolayers, namely $MoSe_2$ and WSe_2. The aim of this comparative study is to perform photoluminescence (PL) experiments on $MoSe_2$ and WSe_2 monolayers in magnetic fields up to ± 9 Tesla in the same set-up, and to measure the neutral exciton and trion emission energy and polarization. We vary the laser excitation energy and helicity, which allow to distinguish between laser induced and magnetic field induced valley polarization, which show very different dependencies on the applied magnetic field when comparing ML $MoSe_2$ with ML WSe_2. We uncover that in ML $MoSe_2$ the valley polarization of the neutral and the charged exciton (trion) can be tuned with the magnetic field, independent of the excitation laser polariza-

tion. In the investigated ML WSe_2 sample the evolution of the valley polarization depends for the trion both on the applied magnetic field and the excitation laser helicity, for the neutral exciton valley polarization only on the latter. For both systems we observe a clear Zeeman splitting (valley splitting) for the neutral exciton and the trion of about ± 2 meV at $B_z \mp 9$ T. The extracted g-factors for both exciton complexes in both materials are of the order of $g \approx -4$.

Chapter 1

Introduction to transition metal dichalcogenides monolayers

1.1 A new family of 2D semiconductors

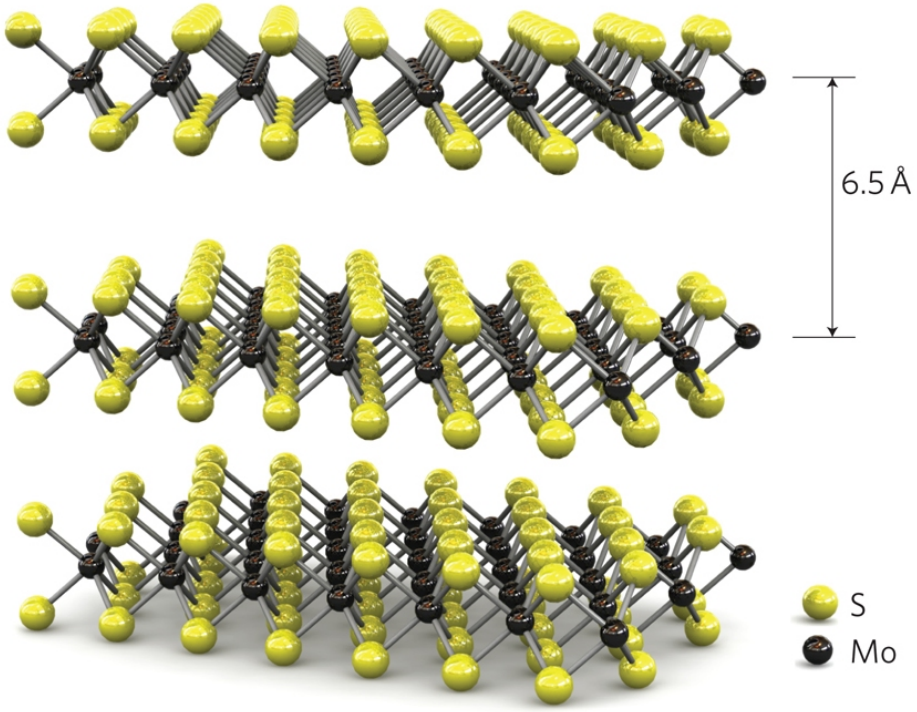

Figure 1: Three-dimensional representation of the structure of MoS_2, which is the same for all TMDCs. Single layers, ≈3 Å thick, are hold together by Van-der-Walls interactions. The distance between two layer is about 6.5 Å. Figure extracted from ref [7]

Bulk MoS_2, used for its catalytic properties and for dry lubrication, is known to be an indirect gap semiconductor (gap = 1.29eV)[13]. In their article published in April 2005[14], K. S. Novoselov and colleagues demonstrate the possibility to fabricate, by simple mechanical cleavage, a 2D crystal from layered crystals. The materials investigated in this article include, among other, the well known graphite and transition-metal dichalcogenides (TMDC) such as MoS_2. In this same article, those 2D crystals are demonstrated to be stable, at room temperature and in air, opening up possibility to study a wide range of new 2D materials. The 3D representation of the TMDC crystal is displayed in figure1.

Among the investigated single layered materials, a 2D TMDC, namely MoS_2, is described as "'a heavily doped semiconductor with an activation gap $\geq 0.6eV$"'. In September 2010, K. F. Mak and co. reported their study of photonic properties of single layered and few layered MoS_2 [15], simultaneously with Splendiani and co. [8]. They demonstrate that with decreasing thickness, the band structure of the material changes to finally become a direct gap semiconductor when thinned to a monolayer (ML). The MoS_2 ML shows an increase of 10^4 in luminescence quantum efficiency compared to the bulk material, motivating further investigations. It appears that the same trend applies to the other TMDC ML studied here, WSe_2 [16], $MoSe_2$ [17].

In May 2012, D. Xiao and co. [11], simultaneously with T. Cao et al. [18] published a theoretical study revealing that inversion symmetry breaking together with spin-orbit coupling leads to coupled spin and valley physics in 2D TMDCs. This allow to control spin and valley index in these materials, paving the way for a new research field named "'Valleytronics"'. In addition to their optical properties, TMDCs attract also attention because of their electronic properties[6] as semiconductors, they can be used to fabricate new devices, such as atomically flat transistors[7], Schottky junctions[19] and optoelectronic devices such as ultrasensitive photodetectors [10], LEDs [8; 9], ...

The prediction of the chiral optical selection rules has motivated the quantum optoelectronic group to investigate TMDC MLs through optical spectroscopy. This thesis aims to present a summary of our contribution to this international, collaborative and highly competitive research field (see figure 2).

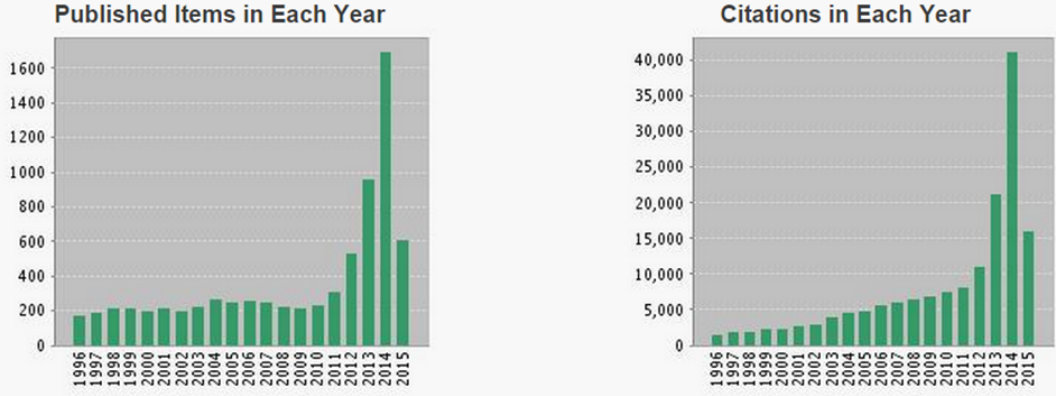

Figure 2: Statistics from web of knowledge website (May 2015). More than 9000 articles on TMDCs are published since 20 years, among them, about 4000 are published since 2012.

After this short historical background, we are now going to present TMDCs main electronic and optical properties. For this, we developed a simple 2 band k.p approach which, combined with state of the art data, will give an overview of those new materials properties.

1.2 Electronic band structure of TMDCs

Different approaches have been used up to now in order to predict the band structure of TMDCs, among which different variants of density functional approaches (DFT) [20; 21] or tight binding approaches (LCAO) [22–24]. These techniques, requiring moderate to strong computational efforts, have the merit to predict the energy bands in the whole crystal Brillouin zone, shown in figure 3.

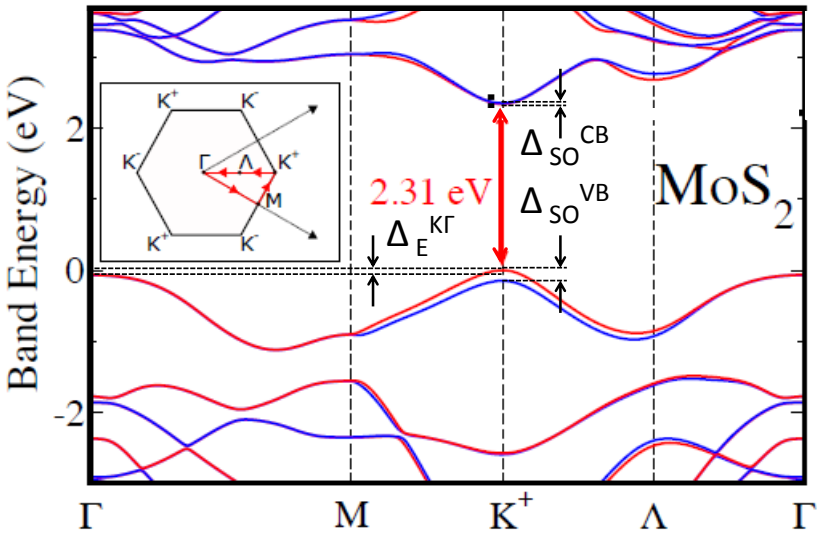

Figure 3: Overview of the band structure of monolayer MoS_2 as obtained from DFT calculations (collaboration with I. Gerber). Spin-Orbit coupling is taken into account. Various band-edge energy differences and spin-splittings are indicated: $\Delta_E^{K\Gamma}$ is the energy splitting between the K and Γ points of the valence band. Δ_{SO} are the spittings due to spin orbit coupling.

However, modeling the bands close to high symmetry points can be also derived from the k.p approach [25], with much lighter computational efforts, which is enough to retain the main electronic and optical properties close to these points[26].

We will now present the most simple 2 band k.p approach and will show how it allows to uncover the peculiar physical properties of TMDCs monolayers, it will give a first estimation of effective electron mass and demonstrate the optical selection rules that will be presented in the next section. State of the art values for band splittings and effective masses are presented at the end of this section.

The following description applies to all ML TMDCs crystals MX_2 where the transition metal is taken as M = Mo, W and the chalcogenide is X = S, Se, Te.

1.2.1 TMDC direct and reciprocal lattice

The basis vectors of the Bravais lattice presented in figure 4, taking $(O, \vec{e}_X, \vec{e}_Y, \vec{e}_Z)$ as the $\mathbb{R}^2$ frame, are chosen as:

$$\vec{a_1} = a_0\left(\frac{1}{2}, -\frac{\sqrt{3}}{2}\right), \vec{a_2} = a_0\,(1,0)$$

The positions of the metal atoms (Mo, W) are given, within an arbitrary crystal translation $\vec{T}_{n_1,n_2} = n_1\vec{a_1} + n_2\vec{a_2}$ $(n_1, n_2 \in \mathbb{Z}^2)$, by their Cartesian coordinates:

$$\vec{R_1} = \frac{a_0}{\sqrt{3}}(0,-1), \vec{R_2} = \frac{a_0}{\sqrt{3}}\left(\frac{\sqrt{3}}{2}, \frac{1}{2}\right), \vec{R_3} = \frac{a_0}{\sqrt{3}}\left(-\frac{\sqrt{3}}{2}, \frac{1}{2}\right)$$

Defining the space rotation by: $C_3^{\mp 1} = \Re_{\vec{e}_Z}\left(\pm\frac{2\pi}{3}\right)$, it follows that : $\vec{R_2} = C_3^{-1}\vec{R_1}$ and $\vec{R_3} = C_3\vec{R_1}$

The basis vectors of the reciprocal network are given as usual by:

$$\vec{b_1} = \frac{2\pi}{\Omega_0}\left(\vec{a_2} \times \vec{k}\right), \vec{b_2} = \frac{2\pi}{\Omega_0}\left(\vec{k} \times \vec{a_1}\right)$$

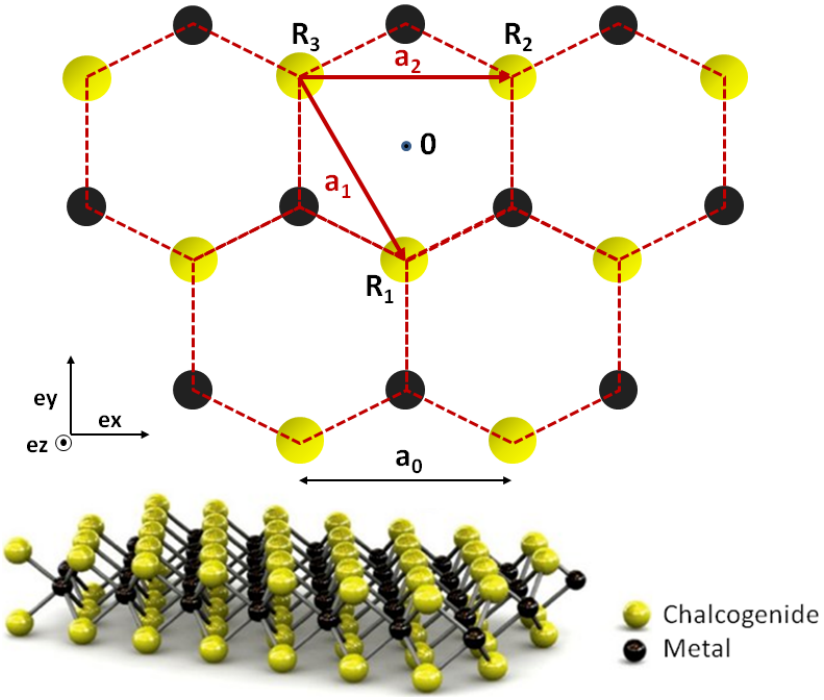

Figure 4: Elementary cell Ω of TMDC compounds. The full lattice is generated by paving the space with cells obtained from Ω by translations $\vec{T}_{n_1,n_2} = n_1\vec{a_1} + n_2\vec{a_2}$ ($n_1, n_2 \in \mathbb{Z}^2$). The yellow spheres represent the metallic elements (W, Mo, ...) and the blue spheres represents chalcogen element (S, Se, Te, ...). The plane of the figure is the one of metallic elements. The position of the chalcogen elements of the upper and lower planes are projected onto the figure plane (see inset).

where $\Omega_0 = (\vec{a_1} \times \vec{a_2}).\vec{k}$ is the surface of the lattice elementary cell. This yields, in the Cartesian (O, $\vec{e}_X$, $\vec{e}_Y$) frame :

$$\vec{b_1} = \frac{4\pi}{a_0\sqrt{3}}(0,-1), \vec{b_2} = \frac{4\pi}{a_0\sqrt{3}}\left(\frac{\sqrt{3}}{2}, -\frac{1}{2}\right)$$

The Brillouin zone can then be constructed as the Wigner cell of the reciprocal lattice. The zone edge K^+ and K^- points are deduced, as well as their equivalents $K^+_{\pm 3}$ and $K^-_{\pm 3}$.

$$\vec{K}^+ = \frac{4\pi}{3a_0}(1,0), \vec{K}^+_3 = C_3^{-1}\vec{K}^+ = \frac{4\pi}{3a_0}\left(-\frac{1}{2}, \frac{\sqrt{3}}{2}\right), \vec{K}^+_{-3} = C_3\vec{K}^+ = \frac{4\pi}{3a_0}\left(-\frac{1}{2}, -\frac{\sqrt{3}}{2}\right)$$

1.2.2 TMDC crystal symmetry

We examine now in detail the TMDC crystal symmetry from geometrical arguments. Defining the translation operator $\hat{T}_{n_1,n_2}$ associated to the crystal translation of $\vec{T}_{n_1,n_2}$ by:

$$\hat{T}_{n_1,n_2}\psi(\vec{r}) = \psi(\vec{r} - \vec{T}_{n_1,n_2}) \tag{1.1}$$

thus:

$$\hat{T}_{n_1,n_2} = e^{i\frac{\hat{p}}{\hbar}\vec{T}_{n_1,n_2}}$$

By definition, the crystal is invariant when performing any space translation. From Bloch's theorem, a complete set of Eigen-functions can be obtained for an infinite crystal as:

$$\psi_{v,\vec{q}}(r) = \frac{1}{\sqrt{S}}e^{i\vec{q}.\vec{r}}\vec{u}_{n,q}(r) \tag{1.2}$$

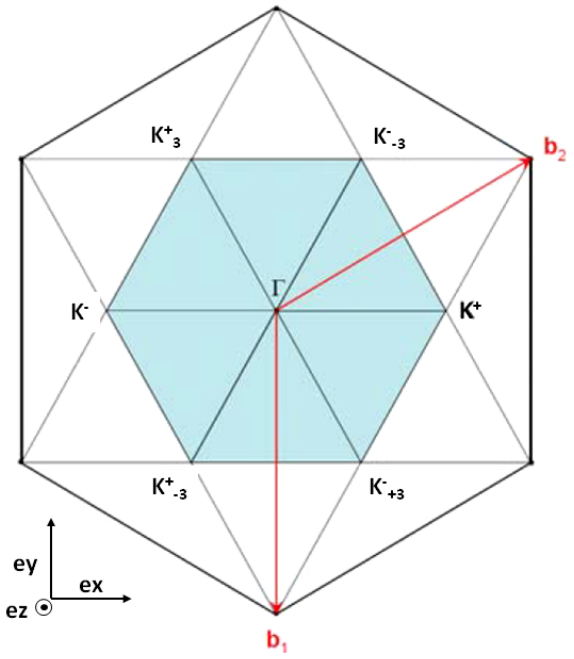

Figure 5: Reciprocal lattice of TMDC compounds, and first Brillouin zone Ω^* (blue shaded area). The full reciprocal lattice is generated by paving the space with cells obtained from Ω^* by translations $\vec{G}_{n_1,n_2} = p_1\vec{b_1} + p_2\vec{b_2}(p_1, p_2 \in \mathbb{Z}^2)$.

where $u_{n,q}(\vec{r})$ has the lattice periodicity. The whole crystal surface is $S = N\Omega_0$ and we apply Born von Karman cyclic boundary conditions. This means that we consider as equivalent two translations which differ by a macro-cell translation, i.e. $\psi_{\nu,\vec{q}}(\vec{r} - \vec{T}_{m_1N_1,m_2N_2}) = \psi_{\nu,\vec{q}}(\vec{r})$ with $(m_1, m_2) \in \mathbb{Z}^2$ and $N = N_1N_2$ cells in the crystal. $\vec{T}_{m_1N_1,m_2N_2} = m_1(N_1\vec{a}_1) + m_2(N_2\vec{a}_2)$.

$$\left\{\hat{T}_{n_1,n_2} \equiv \hat{T}_{n_1',n_2'}\right\} \Leftrightarrow \left\{\exists \hat{T}_{m_1N_1,m_2N_2} : \hat{T}_{n_1,n_2} - \hat{T}_{n_1',n_2'} = \hat{T}_{m_1N_1,m_2N_2}, (m_1, m_2) \in \mathbb{Z}^2\right\}.$$

Note here that the translation symmetry is restricted to the plane of the 2D crystal, and $\vec{q}$ is in the wavevector plane : $\vec{q} = q_x\vec{e}_X + q_y\vec{e}_Y$.

On the other hand, in a simple tight binding approach, the orbital Eigen-functions can be obtained as Bloch waves:

$$\psi_{m,q}(r) = \frac{1}{\sqrt{N}}\sum_{\vec{R}_I} e^{i\vec{q}.\vec{R}_I}\phi_m(\vec{r} - \vec{R}_I); m = c, v; \vec{R}_I \in \text{crystal}. \tag{1.3}$$

where the summation runs over the $N = N_1N_2$ cells of the crystal. The Born-von Karman (B.V.K.) boundary conditions allow us to restore the translation symmetry.

We check first that Bloch-waves are Eigen-functions of the translation operators:

$$\hat{T}_{n_1,n_2}\psi_{m,q}(\vec{r}) = \frac{1}{\sqrt{N}}\sum_{\vec{R}_I} e^{i\vec{q}.\vec{R}_I}\phi_m(\vec{r} - \vec{R}_I - \vec{T}_{n_1,n_2})$$

$$\hat{T}_{n_1,n_2}\psi_{m,q}(\vec{r}) = \frac{1}{\sqrt{N}}\sum_{\vec{R}_I'} e^{i\vec{q}.(\vec{R}_I' - \vec{T}_{n_1,n_2})}\phi_m(\vec{r} - \vec{R}_I')$$

where: $\overrightarrow{\mathrm{R}'_{\mathrm{I}}} \equiv \overrightarrow{\mathrm{R}_{\mathrm{I}}} + \overrightarrow{\mathrm{T}}_{n_1,n_2}$

$$\hat{\mathrm{T}}_{n_1,n_2}\psi_{m,q}(\overrightarrow{r}) = \frac{1}{\sqrt{\mathrm{N}}} e^{-i\overrightarrow{q}.\overrightarrow{\mathrm{T}}_{n_1,n_2}} \sum_{\overrightarrow{\mathrm{R}_{\mathrm{I}}}} e^{i\overrightarrow{q}.\overrightarrow{\mathrm{R}'_{\mathrm{I}}}} \phi_m(\overrightarrow{r} - \overrightarrow{\mathrm{R}_{\mathrm{I}}} - \overrightarrow{\mathrm{T}}_{n_1,n_2})$$

where the sums runs over the N cells of the crystal. Since we use the B.V.K. periodic boundary conditions, $\overrightarrow{q} = \frac{p_1}{\mathrm{N}_1}\overrightarrow{b_1} + \frac{p_2}{\mathrm{N}_2}\overrightarrow{b_2}$ with $(p_1, p_2) \in \mathbb{Z}^2$ the following identity holds:

$$e^{-i\overrightarrow{q}.\overrightarrow{\mathrm{T}}_{m_1\mathrm{N}_1,m_2\mathrm{N}_2}} = 1, (m_1, m_2) \in \mathbb{Z}^2.$$

$$\sum_{\overrightarrow{\mathrm{R}'_{\mathrm{I}}}} e^{i\overrightarrow{q}.\overrightarrow{\mathrm{R}'_{\mathrm{I}}}} \phi_m(\overrightarrow{r} - \overrightarrow{\mathrm{R}'_{\mathrm{I}}}) = \sum_{\overrightarrow{\mathrm{R}_{\mathrm{I}}}} e^{i\overrightarrow{q}.(\overrightarrow{\mathrm{R}_{\mathrm{I}}} + \overrightarrow{\mathrm{T}}_{n_1,n_2})} \phi_m(\overrightarrow{r} - \overrightarrow{\mathrm{R}_{\mathrm{I}}} - \overrightarrow{\mathrm{T}}_{n_1,n_2})$$

$$\sum_{\overrightarrow{\mathrm{R}'_{\mathrm{I}}}} e^{i\overrightarrow{q}.\overrightarrow{\mathrm{R}'_{\mathrm{I}}}} \phi_m(\overrightarrow{r} - \overrightarrow{\mathrm{R}'_{\mathrm{I}}}) = \sum_{\overrightarrow{\mathrm{R}_{\mathrm{I}}}} e^{i\overrightarrow{q}.(\overrightarrow{\mathrm{R}_{\mathrm{I}}} + \overrightarrow{\mathrm{T}}_{n_1,n_2} - \overrightarrow{\mathrm{T}}_{m_1\mathrm{N}_1,m_2\mathrm{N}_2})} \phi_m(\overrightarrow{r} - \overrightarrow{\mathrm{R}_{\mathrm{I}}} - \overrightarrow{\mathrm{T}}_{n_1,n_2} + \overrightarrow{\mathrm{T}}_{m_1\mathrm{N}_1,m_2\mathrm{N}_2})$$

where $(m_1, m_2) \in \mathbb{Z}^2$ are chosen for each $\overrightarrow{\mathrm{R}_{\mathrm{I}}}$ so that $\overrightarrow{\mathrm{R}_{\mathrm{I}}} + \overrightarrow{\mathrm{T}}_{n_1,n_2} - \overrightarrow{\mathrm{T}}_{m_1 n_1,m_2\mathrm{N}_2}$ belongs to the initial summation range: $-\frac{\mathrm{N}_j}{2} < \left(n_j - r_j \mathrm{N}_j\right) \leq \frac{\mathrm{N}_j}{2}$ with (j=1,2). Hence:

$$\sum_{\overrightarrow{\mathrm{R}'_{\mathrm{I}}}} e^{i\overrightarrow{q}.\overrightarrow{\mathrm{R}'_{\mathrm{I}}}} \phi_m(\overrightarrow{r} - \overrightarrow{\mathrm{R}'_{\mathrm{I}}}) = \sum_{\overrightarrow{\mathrm{R}_{\mathrm{I}}}} e^{i\overrightarrow{q}.\overrightarrow{\mathrm{R}_{\mathrm{I}}}} \phi_m(\overrightarrow{r} - \overrightarrow{\mathrm{R}_{\mathrm{I}}})$$

Finally, we obtain:

$$\hat{\mathrm{T}}_{n_1,n_2}\psi_{m,q}(\overrightarrow{r}) = e^{-i\overrightarrow{q}.\overrightarrow{\mathrm{T}}_{n_1,n_2}} \psi_{m,q}(\overrightarrow{r}) \tag{1.4}$$

which demonstrate that Bloch-waves are Eigen-functions of the translation operators of the translation group $(\hat{\mathscr{T}}, +)$.

The point group of the TMDC crystal is D_{3h}. The simple group of the crystal contains the following symmetry operation $\mathscr{O}$ in the notations and conventions of Koster, Dimmock and Wheeler [27] (see figure 6):

$$\mathscr{O} \in \mathfrak{G}_p = \left(\left\{e, \sigma_h, \mathrm{C}_3, \mathrm{C}_{-3} = \mathrm{C}_3^2, s_3 = \sigma_h \mathrm{C}_3, s_3^2 = \sigma_h \mathrm{C}_3^2, \mathrm{C}_2, \mathrm{C}_2^{'}, \mathrm{C}_2^{''}, \sigma_v, \sigma_v^{'}, \sigma_v^{''}\right\}, \circ\right) \tag{1.5}$$

where $\circ$ denotes the composition of symmetry operations.

The corresponding operation $\hat{\mathrm{O}}$ in the Hilbert space of electron states are generally defined in coordinate representation as:

$$\psi^{'}(\overrightarrow{r}) = \hat{\mathrm{O}}\psi(\overrightarrow{r}) = \psi\left[\mathscr{O}^{-1}(\overrightarrow{r})\right]$$

The D_{3h} group representation and the corresponding basis functions are reproduced in annexe A.

1.2.3 Symmetry analysis of electronic states at K^+ and K^- points of the Brillouin zone

The direct bandgap of ML TMDCs is located at the K^+ and K^- points of the Brillouin zone (see figure 7), in contrast to semiconductors like GaAs, where the direct gap is at the center of the Brillouin zone, at the Γ point. Therefore, symmetry analysis of electronic states at these point is of primary importance to predict optical properties of ML TMDC materials.

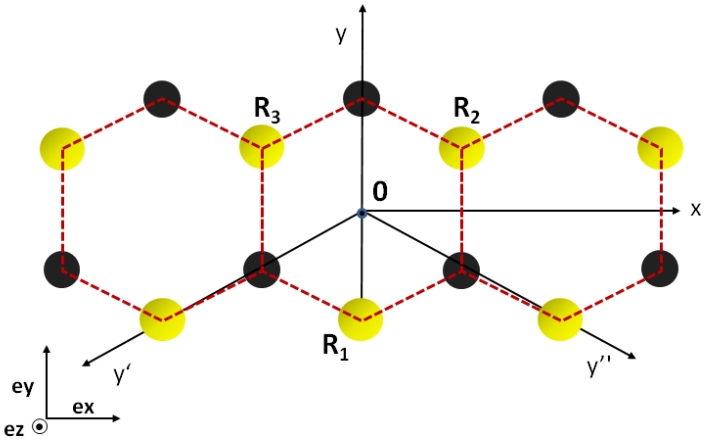

Figure 6: The principal symmetry axis for the rotation of order 3 is (O_z). The axis of order 2 rotations are $(O_y, O_{y'}, O_{y''})$. The plane of the figure is the symmetry plane of the mirror σ_h. There are three mirror operations $\sigma_v, \sigma_v^{'}, \sigma_v^{''}$ defined respectively from the planes $(yOz), (y^{'}Oz), (y^{''}Oz)$.

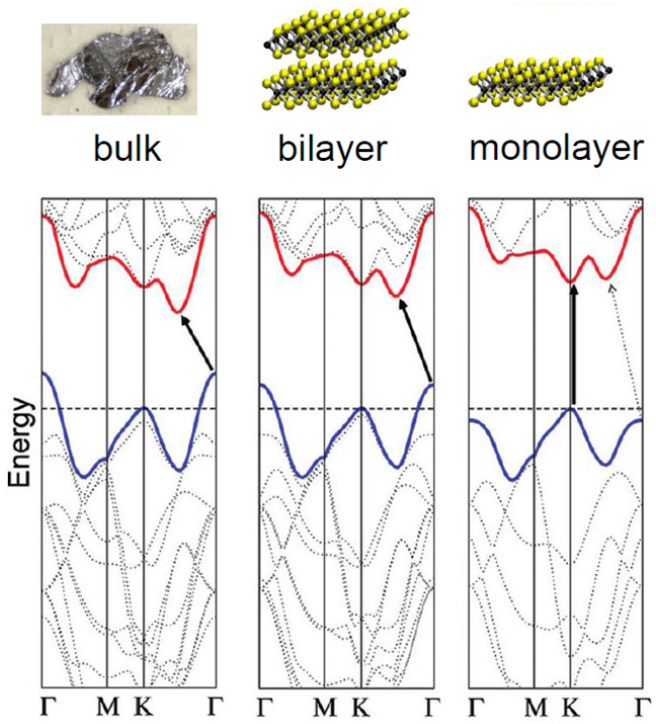

Figure 7: **MoS_2 band diagram for different layer number.** The conduction band (in red) and the valence band (in blue) evolves with the number of layer to finally lead to a direct gap at the K^+ point when thinned to a monolayer. Figure extracted from ref. [8].

The zone edge point corresponding to these points correspond to a lower symmetry group, called the wave-vector group of $\overrightarrow{K}^+(\overrightarrow{K}^-)$. The remaining symmetry operations of the crystal, vector $\overrightarrow{K}^+(\overrightarrow{K}^-)$ system are:

$$\mathcal{O} \in \mathfrak{G}_p(\overrightarrow{K}^+) = \left(\{e, \sigma_h, C_3, C_{-3} = C_3^2, s_3 = \sigma_h C_3, s_3^2 = \sigma_h C_3^2\}, \circ\right) \tag{1.6}$$

The same obtained for $G_p(\overrightarrow{K}^-)$. The D_{3h} group representation and the corresponding basis functions are reproduced in annexe A.

For spinor representation, one must also add $\bar{e}$ and all the transformations $\bar{\mathcal{O}} = \bar{e}\mathcal{O}$ to $G_p(\overrightarrow{K}^+)$, where $\bar{e}$ is the space transformation defined as:

$$\bar{e} = \Re_{\overrightarrow{e}_Z}(\pm 2\pi)$$

One sees that the three order 2 axis as well as the three reflexions on planes containing the order 3 rotation axis (O_z) and one of the axes $O_y, O_{y'}, O_{y''}$ have disappeared, since they put in relation non-equivalent points (e.g. K^+ and K^-) of the reciprocal lattice. However, the proper $C_{\pm 3}$ and improper $S_{\pm 3}$ rotations of order 3 remain, since they establish a correspondence between equivalent point of the reciprocal lattice (e.g. K^+ and $K^+_{\pm 3}$), which means that they let $K^+(K^-)$ invariant within a translation $\overrightarrow{G}_{p_1,p_2}$ of the reciprocal lattice T^*. The set $\mathfrak{G}_p\ (\overrightarrow{K}^+)$ is called the wave vector group. The ensemble of images of $K^+(K^-)$ by $\mathfrak{G}_p$is called by definition the star of $K^+(K^-)$:

$${}^*\overrightarrow{K}^+ = \left\{\overrightarrow{K_i} = \mathcal{O}(\overrightarrow{K}^+), \forall \mathcal{O} \in \mathfrak{G}_p\right\}, {}^*\overrightarrow{K}^- = \left\{\overrightarrow{K}_i^- = \mathcal{O}(\overrightarrow{K}^-), \forall \mathcal{O} \in \mathfrak{G}_p\right\}$$

Thus here ($G_p = D_{3h}$) :${}^*\overrightarrow{K}^+ = \overrightarrow{K}^+, \overrightarrow{K}^-$ since $\overrightarrow{K}^- = C_2\overrightarrow{K}^+ = \sigma_v\overrightarrow{K}^+$. Similarly: ${}^*\overrightarrow{K}^- = \overrightarrow{K}^-, \overrightarrow{K}^+$. We see that the only symmetry compatible with $(D_{3h} \cup \overrightarrow{K}^+)$ is $G_p(\overrightarrow{K}^+) = C_{3h}$. It can be easily checked that the C_{3h} group is commutative, so that all its representations are one-dimensional. Under the operations of the wave-vector group, i.e. those leaving $\overrightarrow{K}^+$ invariant within an arbitrary translation $\overrightarrow{G}_{p_1,p_2}$, the linearly independent functions possessing the same energy and the same wave-vector $\overrightarrow{K_i}$ are transformed into one another and form the basis of some wave vector group representation, also called the small representation [28].

The wave vector groups $G_p(\overrightarrow{K}^+)$ and $G_p(\overrightarrow{K}^-)$ correspond both to C_{3h}: they are isomorph; they transform into one another by time reversal symmetry $\hat{K}$.

We give finally the compatibility table between D_{3h} and $\left\{C_{3h} : \overrightarrow{K}^+(\overrightarrow{K}^-)\right\}$[27]:

D_{3h}	Γ_1	Γ_2	Γ_3	Γ_4	Γ_5	Γ_6	Γ_7	Γ_8	Γ_9
$C_{3h} : \overrightarrow{K}^+(\overrightarrow{K}^-)$	Γ_1	Γ_2	Γ_3	Γ_4	$\Gamma_5 + \Gamma_6$	$\Gamma_2 + \Gamma_3$	$\Gamma_7 + \Gamma_8$	$\Gamma_9 + \Gamma_{10}$	$\Gamma_{11} + \Gamma_{12}$

Table 1.1: Full compatibility table of D_{3h} and C_{3h} in the double group representations showing that all the two dimensional representations of D_{3h} break into the sum of one dimensional representation of C_{3h}.

Symmetry of conduction band in $K^+(K^-)$:

Let us start with the description of Wannier conduction states. The lowest Wannier conduction states in K^+ transforms like: $\phi_c(\overrightarrow{r}) \approx d_{2z^2-x^2-y^2}$ [11; 21] along the operations of C_{3h} so that:

$$\Rightarrow \phi_c(\overrightarrow{r}) \in \Gamma_1$$

Note here that, according to equation 1.3, we cannot yet deduce the Bloch state symmetry. Indeed $\psi_{c,K^+}(r) = \frac{1}{\sqrt{N}} \sum_{\vec{R_I}} e^{i\vec{K^\pm}.\vec{R_I}} \phi_c(\vec{r} - \vec{R_I})$; we are at the $K^\pm$ point and not at the Γ point. Therefore $k \neq 0$ in contrast to GaAs.

We shall now identify the symmetry of the Bloch state close to K^+ and K^- points by examining how they transform under the symmetry operations of the group of wave-vector point group.

By calculating the effect of $\hat{C}_3$ and $\hat{C}_3^{-1}$ rotations in electron state space, it can be shown (see annexe B) that:

$$\hat{C}_3^{\pm 1} \psi_{c,\vec{K}^+}(\vec{r}) = e^{\pm i \frac{2\pi}{3}} \psi_{c,\vec{K}^+}(\vec{r}) \tag{1.7}$$

To obtain a representation to which $\psi_{c,\vec{K}^+}(\vec{r})$ belongs without any ambiguity, we check now how the Bloch waves transform with the transformation $\hat{\sigma}_h$. Obviously $\hat{\sigma}_h \psi_{c,\vec{K}^+}(\vec{r}) = \psi_{c,\vec{K}^+}(\vec{r})$.

Using the character table of the group [27] (presented in annexe A) and the fact that all representations are one-dimensional here (so the character is equal to the eigenvalue of the operator), we see that the only representation which character is $e^{\pm i \frac{2\pi}{3}}$ for $\hat{C}_3^{\pm 1}$ and +1 for $\hat{\sigma}_h$ is Γ_2.

In conclusion the conduction states at K^+ point transform according to the Γ_2 representation.

Using the same method it can be checked that the conduction states at K^- point transform according to the Γ_3 representation. Also this is consistent with the fact that K^+ and K^- correspond to each other by time reversal symmetry.

Symmetry of valence bands states in $K^\pm$:

If we assume that at the K^+ point the orbital functions in the Wannier-wave transform like[11; 21]:

$$\phi_v(\vec{r}) \approx d_{x^2-y^2-2ixy} \Rightarrow \phi_v(\vec{r}) \in \Gamma_2$$

we can show (see annexe B), similarly as in the previous section, that:

$$\hat{C}_3^{\pm 1} \psi_{v,\vec{K}^+}(\vec{r}) = \psi_{v,\vec{K}^+}(\vec{r}) \tag{1.8}$$

Since we have also $\hat{\sigma}_h \psi_{v,\vec{K}^+}(\vec{r}) = \psi_{v,\vec{K}^+}(\vec{r})$, we can conclude from the character table [27] (see annexe A) that the valence orbital functions transform unambiguously according to the the Γ_1 representation.

We can show that the valence orbital states in K^- will also transform according to the Γ_1 representation which is consistent with time reversal symmetry that relates K^+ and K^- points.

1.2.4 K.P theory at Brillouin zone corners $K^\pm$

Following the Kane's method [25], we perform now a perturbation calculation in order to get the dispersion curves $E_m(\vec{k})$ close to the $K^\pm$ points. According to this theory , the one electron hamiltonian is:

$$\hat{H} = \frac{\hat{p}^2}{2m_0} + V(\vec{r}) \tag{1.9}$$

where $V(\vec{r})$ is the effective electrostatic potential of the crystal, and has its symmetry properties ($V(\mathcal{O}^{-1}\vec{r}) = V(\vec{r})$) and m_0 is the vacuum electron mass.

The resulting displaced Schrödinger equation which should be satisfied by $u_{n,\vec{k}}(\vec{r})$ is in general:

$$\hat{h}_k u_{n,\vec{k}}(\vec{r}) = E_{n,\vec{k}} u_{n,\vec{k}}(\vec{r})$$

where $\hat{h}_k = \frac{1}{2m_0}(\hat{p} + \hbar\vec{k})^2 + V(\vec{r})$. The discrete energy states are determined by the periodicity of the function $u_{n,\vec{k}}(\vec{r})$: $u_{n,\vec{k}}(\vec{r}) = u_{n,\vec{k}}(\vec{r} + \vec{T}_{n_1,n_2})$ and $\nabla_{\vec{r}} u_{n,\vec{k}}(\vec{r}) = \nabla_{\vec{r}} u_{n,\vec{k}}(\vec{r} + \vec{T}_{n_1,n_2})$ which yield specific boundary conditions at the edge of the first Wigner zone. We assume as usual that if the solution is known at a given $\vec{k}_0$ point, then the solution at any point $\vec{k}$ in the neighborhood of $\vec{k}_0$ can be obtained from the solutions in $\vec{k}_0$ since they constitute a complete basis of periodical functions. We will use the stationary perturbation theory, the perturbation operator to $\hat{h}_{k_0} = \frac{1}{2m_0}(\hat{p} + \hbar\vec{k}_0)^2 + V(\vec{r})$, $V(\vec{r})$ being given by:

$$\hat{w}(\vec{k}) \equiv \hat{h}_{\vec{k}} - \hat{h}_{\vec{k}_0}$$

We obtain : $\hat{w}(\vec{k}) = \frac{1}{2m_0}(\hat{p} + \hbar\vec{k})^2 - \frac{1}{2m_0}(\hat{p} + \hbar\vec{k}_0)^2$, i.e.:

$$\hat{w}(\vec{k}) = \frac{\hbar(\vec{k} - \vec{k}_0)}{m_0}\hat{p} + \frac{\hbar^2}{2m_0}(k^2 - k_0^2) \tag{1.10}$$

Note that this perturbation can only couple electron states with the same spin.

As $\hat{w}(\vec{k}_0) = 0$, the family of solutions $u_{\vec{k}_0} = \left\{u_{n,\vec{k}_0}(x)\right\}(n \in \mathbb{N}^*)$ is an Eigen-basis for $\hat{h}_{\vec{k}_0}$. Since $\hat{h}_{\vec{k}} = \hat{h}_{\vec{k}_0} + \hat{w}(\vec{k})$, the matrix elements of $\hat{w}(\vec{k})$ in the basis $u_{\vec{k}_0}$ can be written:

$$\left\langle u_{n,\vec{k}_0} \middle| \hat{w}(\vec{k}) \middle| u_{n',\vec{k}_0} \right\rangle_\Omega = \frac{\hbar(\vec{k} - \vec{k}_0)}{m_0}\left\langle u_{n,\vec{k}_0} \middle| \hat{p} \middle| u_{n',\vec{k}_0} \right\rangle_\Omega + \frac{\hbar^2}{2m_0}(k^2 - k_0^2)\left\langle u_{n,\vec{k}_0} | u_{n',\vec{k}_0} \right\rangle_\Omega$$

i.e.:

$$\left\langle u_{n,\vec{k}_0} \middle| \hat{w}(\vec{k}) \middle| u_{n',\vec{k}_0} \right\rangle_\Omega = \frac{\hbar(\vec{k} - \vec{k}_0)}{m_0}\left\langle u_{n,\vec{k}_0} \middle| \hat{p} \middle| u_{n',\vec{k}_0} \right\rangle_\Omega + \frac{\hbar^2}{2m_0}(k^2 - k_0^2)\delta_{n,n'} \tag{1.11}$$

It is known that the basis $u_{\vec{k}_0}$ can be taken as a basis for the sub-space $\mathcal{E}_{\vec{k}_0}$, generated by the Eigen solutions of the equation $\hat{h}_k u_{n,\vec{k}}(\vec{r}) = E_{n,\vec{k}} u_{n,\vec{k}}(\vec{r})$. Thus we will use the matrix representation of $\hat{h}_k$ and $\hat{w}(\vec{k})$ in this basis, which elements are the Eigenfunctions $u_{n,\vec{k}_0}(x)$ associated to the Eigen-energies $E_{n,\vec{k}_0}$, assumed to be known.

From the stationary perturbation theory, the first order correction $E^{(1)}_{n_0,\vec{k}_0}(\vec{k})$ to the energy $E_{n_0,\vec{k}_0}$ of the state $\left|u_{n_0,\vec{k}_0}\right\rangle$, n_0 being an arbitrary band ($n_0 \in \mathbb{N}^*$), can be written as:

$$E^{(1)}_{n_0,\vec{k}_0}(\vec{k}) = \left\langle u_{n_0,\vec{k}_0} \middle| \hat{w}(\vec{k}) \middle| u_{n_0,\vec{k}_0} \right\rangle_\Omega$$

$$E^{(1)}_{n_0,\vec{k}_0}(\vec{k}) = \frac{\hbar(\vec{k} - \vec{k}_0)}{m_0}\left\langle u_{n_0,\vec{k}_0} \middle| \hat{p} \middle| u_{n_0,\vec{k}_0} \right\rangle_\Omega + \frac{\hbar^2}{2m_0}(k^2 - k_0^2)\delta_{n_0,n_0}$$

i.e.

$$\mathrm{E}^{(1)}_{n_0,\vec{k}_0}(\vec{k}) = \frac{\hbar(\vec{k}-\vec{k}_0)}{m_0}.\tilde{\vec{p}}^{\vec{k}_0}_{n_0,n_0} + \frac{\hbar^2}{2m_0}(k^2-k_0^2) \tag{1.12}$$

We evaluate now the second order correction to the energy for the non-degenerated orbital state $\mathrm{E}_{n_0,\vec{k}_0}$, $\mathrm{E}^{(2)}_{n_0,\vec{k}_0}(\vec{k})$ (Indeed, due to the spin orbit interaction, the orbital degeneracy is lifted, so that only states with the same spin state are coupled by the perturbation $\hat{w}$). We get:

$$\mathrm{E}^{(2)}_{n_0,\vec{k}_0}(\vec{k}) = \left(\frac{\hbar}{m_0}\right)^2(\vec{k}-\vec{k}_0)^2\sum_{n\neq n_0}\frac{\left|\left\langle u_{n_0,\vec{k}_0}\left|\hat{w}(\vec{k})\right|u_{\vec{k}_0,n}\right\rangle_\Omega\right|^2}{\mathrm{E}_{n_0,\vec{k}_0}-\mathrm{E}_{n,\vec{k}_0}} \tag{1.13}$$

One can show from symmetry considerations (see annexe C) that defining:

$$\vec{p}_{m,m'}(\vec{k_0}) \equiv \left\langle \psi_{m,\vec{k}_0}\left|\hat{p}\right|\psi_{m',\vec{k}_0}\right\rangle$$

and

$$\tilde{\vec{p}}_{m,m'}(\vec{k_0}) \equiv \left\langle u_{m,\vec{k}_0}\left|\hat{p}\right|u_{m',\vec{k}_0}\right\rangle_\Omega$$

that the identity holds

$$\vec{p}_{m,m'}(\vec{k_0}) = \tilde{\vec{p}}_{m,m'}(\vec{k_0}) + \hbar\vec{k_0}\delta_{m,m'} \tag{1.14}$$

So that, for $\vec{k_0} = \vec{\mathrm{K}}^+$:

$$\vec{p}_{m,m'}(\vec{\mathrm{K}}^+) = \tilde{\vec{p}}_{m,m'}(\vec{\mathrm{K}}^+) + \hbar\vec{\mathrm{K}}^+\delta_{m,m'}$$

The similar identity holds for $\vec{\mathrm{K}}^-$.

From the identity established above, we have for $n \neq n_0$:

$$\begin{aligned}\left\langle u_{n_0,\vec{k}_0}\left|\hat{w}(\vec{k})\right|u_{n,\vec{k}_0}\right\rangle_\Omega &= \frac{\hbar(\vec{k}-\vec{k}_0)}{m_0}\left\langle u_{n_0,\vec{k}_0}\left|\hat{p}\right|u_{n,\vec{k}_0}\right\rangle_\Omega \\ &= \frac{\hbar(\vec{k}-\vec{k}_0)}{m_0}.\tilde{\vec{p}}_{n_0,n}(\vec{k}_0) \\ &= \frac{\hbar(\vec{k}-\vec{k}_0)}{m_0}.\vec{p}_{n_0,n}(\vec{k}_0)\end{aligned}$$

One get thus:

$$\mathrm{E}^{(2)}_{n_0,\vec{k}_0}(\vec{k}) = \left(\frac{\hbar}{m_0}\right)^2(\vec{k}-\vec{k}_0)^2\sum_{n\neq n_0}\frac{\left|\left\langle u_{n_0,\vec{k}_0}\left|\hat{p}\right|u_{\vec{k}_0,n}\right\rangle_\Omega\right|^2}{\mathrm{E}_{n_0,\vec{k}_0}-\mathrm{E}_{n,\vec{k}_0}}$$

We finally get the development:

$$\begin{aligned}\mathrm{E}_{n_0,\vec{k}_0}(\vec{k}) = \mathrm{E}_{n_0,\vec{k}_0} &+ \frac{\hbar(\vec{k}-\vec{k}_0)}{m_0}.\tilde{p}_{n_0,n}(\vec{k}_0) + \frac{\hbar^2}{2m_0}(k^2-k_0^2) \\ &+ \frac{\hbar^2}{m_0}(\vec{k}-\vec{k}_0)^2\sum_{n\neq n_0}\frac{\left|\tilde{p}_{n_0,n}(\vec{k}_0)\right|^2}{\mathrm{E}_{n_0,\vec{k}_0}-\mathrm{E}_{n,\vec{k}_0}} + \mathrm{O}\left[(\vec{k}-\vec{k}_0)^3\right]\end{aligned}$$

Defining the Kane's energy as $\epsilon^{\vec{k}_0}_{n_0,n} \equiv \frac{2\left|\tilde{p}_{n_0,n}(\vec{k}_0)\right|^2}{m_0}$, we get thus in general, in the neighbourhood of $\vec{k_0}$:

$$\forall k \in]\vec{k_0} - \kappa, \vec{k_0} + \kappa[,$$

$$\mathrm{E}_{n_0,\vec{k}_0}(\vec{k}) = \mathrm{E}_{n_0,\vec{k}_0} + \frac{\hbar(\vec{k}-\vec{k}_0)}{m_0}.\tilde{p}_{n_0,n}(\vec{k}_0) + \frac{\hbar^2}{2m_0}(k^2-k_0^2) + \frac{\hbar^2}{2m_0}(\vec{k}-\vec{k}_0)^2 \sum_{n\neq n_0} \frac{\epsilon^{\vec{k}_0}_{n_0,n}}{\mathrm{E}_{n_0,\vec{k}_0} - \mathrm{E}_{n,\vec{k}_0}} + \mathrm{O}\left[(\vec{k}-\vec{k}_0)^3\right]$$

Taking now the specific case of $\vec{k_0} = \vec{\mathrm{K}}^+$ and using the previously established identity, we get:

$$(p_\pm)_{m,m'}(\vec{\mathrm{K}}^+) = (\tilde{p}_\pm)_{m,m'}(\vec{\mathrm{K}}^+) + \hbar\vec{\mathrm{K}}^+\delta_{m,m'}, (m,m') \in \{c,v\} \tag{1.15}$$

It follows that, for m'=m and as we demonstrated above $\psi_{v,\vec{\mathrm{K}}^+} \in \Gamma_1$ and $\psi_{c,\vec{\mathrm{K}}^+} \in \Gamma_2$:

$$\vec{p}_{m,m} = \left\langle \psi_{\vec{\mathrm{K}}^+,c} \middle| \hat{p} \middle| \psi_{\vec{\mathrm{K}}^+,c} \right\rangle = \left\langle \psi_{\vec{\mathrm{K}}^+,v} \middle| \hat{p} \middle| \psi_{\vec{\mathrm{K}}^+,v} \right\rangle = 0$$

indeed, $\hat{p} \notin \Gamma_1$, $\hat{p}_+ \in \Gamma_2, \hat{p}_- \in \Gamma_3, \hat{p}_Z \in \Gamma_4$ (c.f. Basis function of group C_{3h} in annexeA), therefore we have at the K^+ point:

$$\begin{aligned}
\left\langle \psi_{\vec{\mathrm{K}}^+,v} \middle| \hat{p} \middle| \psi_{\vec{\mathrm{K}}^+,v} \right\rangle &\in \Gamma_1^* \times \Gamma_2 \times \Gamma_1 = \Gamma_2 \neq \Gamma_1 \\
&\in \Gamma_1^* \times \Gamma_3 \times \Gamma_1 = \Gamma_3 \neq \Gamma_1 \\
&\in \Gamma_1^* \times \Gamma_4 \times \Gamma_1 = \Gamma_4 \neq \Gamma_1 \\
\left\langle \psi_{\vec{\mathrm{K}}^+,c} \middle| \hat{p} \middle| \psi_{\vec{\mathrm{K}}^+,c} \right\rangle &\in \Gamma_2^* \times \Gamma_2 \times \Gamma_2 = \Gamma_2 \neq \Gamma_1 \\
&\in \Gamma_2^* \times \Gamma_3 \times \Gamma_2 = \Gamma_3 \neq \Gamma_1 \\
&\in \Gamma_2^* \times \Gamma_4 \times \Gamma_2 = \Gamma_4 \neq \Gamma_1
\end{aligned}$$

the same calculation at the K^- point leads to the same conclusion, therefore:

$$\vec{p}_{m,m} = 0 \tag{1.16}$$

and thus:

$$\mathrm{E}_{m,\vec{\mathrm{K}}^+}(\vec{k}) = \mathrm{E}_{m,\vec{\mathrm{K}}^+} + \frac{\hbar(\vec{k}-\vec{\mathrm{K}}^+)}{m_0}.(-\hbar\vec{\mathrm{K}}^+) + \frac{\hbar^2}{2m_0}(k^2-\mathrm{K}^{+2}) + \frac{\hbar^2}{2m_0}(\vec{k}-\vec{\mathrm{K}}^+)^2 \sum_{n\neq m} \frac{\epsilon^{\vec{\mathrm{K}}^+}_{m,n}}{\mathrm{E}_{m,\vec{\mathrm{K}}^+} - \mathrm{E}_{n,\vec{\mathrm{K}}^+}} + \mathrm{O}\left[(\vec{k}-\vec{\mathrm{K}}^+)^3\right]$$

By developing the two first terms of the above expression, we have:

$$\frac{\hbar(\vec{k}-\vec{\mathrm{K}}^+)}{m_0}.(-\hbar\vec{\mathrm{K}}^+) + \frac{\hbar^2}{2m_0}(k^2-\mathrm{K}^{+2}) = \frac{\hbar^2}{2m_0}(\vec{k}-\vec{\mathrm{K}}^+)^2$$

we get finally

$$\mathrm{E}_{m,\vec{\mathrm{K}}^+}(\vec{k}) = \mathrm{E}_{m,\vec{\mathrm{K}}^+} + \frac{\hbar^2}{2m_0}(\vec{k}-\vec{\mathrm{K}}^+)^2 + \frac{\hbar^2}{2m_0}(\vec{k}-\vec{\mathrm{K}}^+)^2 \sum_{n\neq m} \frac{\epsilon^{\vec{\mathrm{K}}^+}_{m,n}}{\mathrm{E}_{m,\vec{\mathrm{K}}^+} - \mathrm{E}_{n,\vec{\mathrm{K}}^+}} + \mathrm{O}\left[(\vec{k}-\vec{\mathrm{K}}^+)^3\right]$$

$$\mathrm{E}_{m,\vec{\mathrm{K}}^+}(\vec{k}) = \mathrm{E}_{m,\vec{\mathrm{K}}^+} + \frac{\hbar^2}{2m_0}.(\vec{k}-\vec{\mathrm{K}}^+)^2\left\{1+\sum_{n\neq m}\frac{\epsilon^{\vec{\mathrm{K}}^+}_{m,n}}{\mathrm{E}_{m,\vec{\mathrm{K}}^+}-\mathrm{E}_{n,\vec{\mathrm{K}}^+}}\right\}+\mathrm{O}\left[(\vec{k}-\vec{\mathrm{K}}^+)^3\right] \quad (1.17)$$

A similar expression is obtained in K^-. We conclude that due to the symmetry of the Bloch states in K^+ and K^-, the conduction and valence bands present a local extremum. The effective mass is defined from the curvature of the bands:

$$\frac{m_0}{m^*_m} = 1+\sum_{n\neq m}\frac{\epsilon^{\vec{\mathrm{K}}^\pm}_{m,n}}{\mathrm{E}_{m,\vec{\mathrm{K}}^+}-\mathrm{E}_{n,\vec{\mathrm{K}}^\pm}}$$

$$\mathrm{E}_{m,\vec{\mathrm{K}}^\pm}(\vec{k}) = \mathrm{E}_{m,\vec{\mathrm{K}}^+} + \frac{\hbar^2}{2m^*_m}.(\vec{k}-\vec{\mathrm{K}}^\pm)^2+\mathrm{O}\left[(\vec{k}-\vec{\mathrm{K}}^\pm)^3\right]$$

In a two band theory, $m\in\{c,v\}$ and we get simply:

$$\frac{m_0}{m^*_c} = 1+\sum_{n\neq m}\frac{\epsilon^{\vec{\mathrm{K}}^\pm}_{c,v}}{\mathrm{E}_{c,\vec{\mathrm{K}}^+}-\mathrm{E}_{v,\vec{\mathrm{K}}^\pm}} = 1+\frac{\epsilon^{\vec{\mathrm{K}}^\pm}_{c,v}}{\mathrm{E}_{cv}} = 1+\frac{2\left|\tilde{p}_{c,v}(\vec{\mathrm{K}}^+)\right|^2}{m_0\mathrm{E}_{cv}} \quad (1.18)$$

$$\frac{m_0}{m^*_v} = 1+\sum_{n\neq m}\frac{\epsilon^{\vec{\mathrm{K}}^\pm}_{v,c}}{\mathrm{E}_{v,\vec{\mathrm{K}}^+}-\mathrm{E}_{c,\vec{\mathrm{K}}^\pm}} = 1-\frac{\epsilon^{\vec{\mathrm{K}}^\pm}_{v,c}}{\mathrm{E}_{cv}} = 1-\frac{2\left|\tilde{p}_{c,v}(\vec{\mathrm{K}}^+)\right|^2}{m_0\mathrm{E}_{cv}} \quad (1.19)$$

The hole mass is thus:

$$\frac{m_0}{m^*_{hv}} = -1+\frac{\epsilon^{\vec{\mathrm{K}}^\pm}_{v,c}}{\mathrm{E}_{cv}} = -1+\frac{2\left|\tilde{p}_{c,v}(\vec{\mathrm{K}}^+)\right|^2}{m_0\mathrm{E}_{cv}}$$

Clearly, in the k.p approach, the conduction and top valence band hole effective masses differ.

Defining the average mass from the average curvature of the conduction and hole dispersion curves at the gap:

$$\frac{m_0}{m^*_{cv}} = \frac{m_0}{2}\left(\frac{1}{m^*_c}+\frac{1}{m^*_h}\right)$$

we get $\frac{m_0}{m^*_{ch}} = \frac{2\left|\tilde{p}_{c,v}(\vec{\mathrm{K}}^+)\right|^2}{m_0\mathrm{E}_{cv}}$, which implies $\mathrm{E}_{cv} = 2m^*_{ch}\left|\frac{\tilde{p}_{c,v}(\vec{\mathrm{K}}^+)}{m_0}\right|^2$ or $\mathrm{E}_{cv} = 2m^*_{ch}\tilde{v}^2_{c,v}$.

In the last expression, we have induced the Kane's speed:

$$\tilde{v}_{c,v} = \left|\frac{\tilde{p}_{c,v}(\vec{\mathrm{K}}^+)}{m_0}\right| = \left|\frac{\tilde{p}_{c,v}(\vec{\mathrm{K}}^-)}{m_0}\right|$$

If now we derive the perturbation matrix representation in the basis of Bloch amplitudes $\mathrm{U}_{\mathrm{K}^+}$, letting $\vec{q} = \vec{k}-\vec{\mathrm{K}}^+$, we take:

$$\left[\hat{h}_{\vec{k}}\right]_{\mathrm{U}_{\mathrm{K}^+}} = \left[\hat{h}_{\vec{\mathrm{K}}^+}\right]_{\mathrm{U}_{\mathrm{K}^+}} + \left[\hat{w}(\vec{k})\right]_{\mathrm{U}_{\mathrm{K}^+}}$$

$\vec{q}.\tilde{\vec{p}}_{c,v}(\vec{\mathrm{K}}^+)$ can be further simplified due to symmetry properties at K^+ point using the expression $\left(\vec{p}_{\pm}\right)_{m,m'}(\vec{\mathrm{K}}^+) = \left(\tilde{\vec{p}}_{\pm}\right)_{m,m'}(\vec{\mathrm{K}}^+)$ (m≠m').

$$\vec{q}.\vec{p}_{c,v}(\vec{\mathrm{K}}^+) \equiv \frac{1}{2}\left(q_+.p_{c,v;-}+q_-.p_{c,v;+}\right) = \frac{1}{2}\left(q_+\left\langle\Psi_{\vec{\mathrm{K}}^+,c}\middle|\hat{p}_-\middle|\Psi_{\vec{\mathrm{K}}^+,v}\right\rangle + q_-\left\langle\Psi_{\vec{\mathrm{K}}^+,c}\middle|\hat{p}_+\middle|\Psi_{\vec{\mathrm{K}}^+,v}\right\rangle\right)$$

Since $\hat{p}_+ \in \Gamma_2, \hat{p}_- \in \Gamma_3$ and as we demonstrated above $\psi_{v,\vec{K}^+} \in \Gamma_1$ and $\psi_{c,\vec{K}^+} \in \Gamma_2$, we have thus [27]

$$\left\langle \psi_{\vec{K}^+,c} \middle| \hat{p}_- \middle| \psi_{\vec{K}^+,v} \right\rangle \in \Gamma_2^* \times \Gamma_3 \times \Gamma_1 = \Gamma_2 \neq \Gamma_1 \Rightarrow \left\langle \psi_{\vec{K}^+,c} \middle| \hat{p}_- \middle| \psi_{\vec{K}^+,v} \right\rangle = 0$$

$$\left\langle \psi_{\vec{K}^+,c} \middle| \hat{p}_+ \middle| \psi_{\vec{K}^+,v} \right\rangle \in \Gamma_2^* \times \Gamma_2 \times \Gamma_1 = \Gamma_1$$

$$\vec{q}\,.\,\vec{p}_{\,c,v}(\vec{K}^+) \equiv \frac{1}{2}\left(q_+.p_{c,v;-} + q_-.p_{c,v;+}\right) = \frac{1}{2}\left(q_- \left\langle \psi_{\vec{K}^+,c} \middle| \hat{p}_+ \middle| \psi_{\vec{K}^+,v} \right\rangle\right)$$

Since : $\left\langle \psi_{\vec{K}^+,c} \middle| \hat{p}_+ \middle| \psi_{\vec{K}^+,v} \right\rangle^* = \left\langle \psi_{\vec{K}^+,v} \middle| (\hat{p}_+)^\dagger \middle| \psi_{\vec{K}^+,c} \right\rangle = \left\langle \psi_{\vec{K}^+,v} \middle| \hat{p}_- \middle| \psi_{\vec{K}^+,c} \right\rangle$ we get, in the case of two-band approximation, the simpler form:

$$\left[\hat{h}_{\vec{q}}\right]_{U_{K^+}} = \frac{\hbar^2}{2m_0} q^2 [1] + \begin{pmatrix} E_{\vec{K}^+,c} & \frac{\hbar^2}{2m_0} q_- p_{c,v;+} \\ \frac{\hbar^2}{2m_0} q_+ p_{c,v-} & E_{\vec{K}^+,v} \end{pmatrix}$$

By a proper phase choice of the relative phase between $\psi_{\vec{K}^+,v}$ and $\psi_{\vec{K}^+,c}$, it is possible to choose $\left\langle \psi_{\vec{K}^+,c} \middle| \hat{p}_+ \middle| \psi_{\vec{K}^+,v} \right\rangle \in \mathbb{R}_+$ so that we can let:

$$v_K \equiv \frac{p_{c,v;+}(\vec{K}^+)}{2m_0} = \frac{p^*_{c,v;+}(\vec{K}^+)}{2m_0}$$

which correspond to Kane speed parameter.

Finally, we get:

$$\left[\hat{h}_{\vec{q}}\right]_{U_{K^+}} = \left(\frac{E_{\vec{K}^+,c} + E_{\vec{K}^+,v}}{2} + \frac{\hbar^2}{2m_0} q^2\right)[1] + \begin{pmatrix} \frac{E_{\vec{K}^+,g}}{2} & \hbar v_K q_- \\ \hbar v_K q_+ & -\frac{E_{\vec{K}^+,g}}{2} \end{pmatrix}$$

where $E_{g,\vec{K}^+} \equiv E_{cv,\vec{K}^+}$ is the TMDC material gap at the K^+ point. The dispersion curves are:

$$E_{\vec{K}^+,c}(\vec{q}) = \left(\frac{E_{\vec{K}^+,c} + E_{\vec{K}^+,v}}{2} + \frac{\hbar^2}{2m_0} q^2\right) + \sqrt{\left(\frac{E_{\vec{K}^+,g}}{2}\right)^2 + \hbar^2 v_K^2 q^2}$$

$$E_{\vec{K}^+,v}(\vec{q}) = \left(\frac{E_{\vec{K}^+,c} + E_{\vec{K}^+,v}}{2} + \frac{\hbar^2}{2m_0} q^2\right) - \sqrt{\left(\frac{E_{\vec{K}^+,g}}{2}\right)^2 + \hbar^2 v_K^2 q^2}$$

We obtain (with the Kane energy $\epsilon^K_{c,v} = 2m_0 v_K^2$ here)

$$\frac{m_0}{m_c^*} = 1 + \frac{\epsilon^K_{c,v}}{E_g}$$

$$\frac{m_0}{m_{hv}^*} = -1 + \frac{\epsilon^K_{c,v}}{E_g}$$

The two band Hamiltonian at the K^- point is directly obtained by operating the time reversal on $\left[\hat{h}_{\vec{q}}\right]_{U_{K^+}}$. Thus: $\left[\hat{h}_{\vec{q}}\right]_{U_{K^-}} = \left[\hat{h}_{-\vec{q}}\right]^*_{U_{K^+}}$ [28] and finally:

$$\left[\hat{h}_{\vec{q}}\right]_{U_{K^-}} = \left(\frac{E_{\vec{K}^-,c} + E_{\vec{K}^-,v}}{2} + \frac{\hbar^2}{2m_0} q^2\right)[1] + \begin{pmatrix} \frac{E_{\vec{K}^-,g}}{2} & -\hbar v_K q_+ \\ -\hbar v_K q_- & -\frac{E_{\vec{K}^-,g}}{2} \end{pmatrix}$$

The dispersion curves are the same in the neighborhood of K^+ and K^- as expected at zero magnetic field.

The "'relativistic"' picture:
The expression obtained for the dispersion curves is analogous to the relativistic expression of the electron energy in the frame of Paul Dirac's approach:

$$E_{-}^{\text{Dirac}} = \pm\sqrt{m_0^2c^4 + p^2c^2}$$

Taking the average for the two bands, one obtains $E_g \approx 2m^*_{c(hv)}v_K^2$ and the dispersion equation can be written as:

$$E_{\vec{K}^{\pm},c}(\vec{q}) \approx +\sqrt{(m_c^*)^2 v_K^4 + \hbar v_K^2 q^2}$$

$$E_{\vec{K}^{\pm},v}(\vec{q}) \approx -\sqrt{(m_v^*)^2 v_K^4 + \hbar v_K^2 q^2}$$

in full analogy with the Dirac result: we see that Kane speed plays the role of the light speed c and the effective conduction/hole mass plays the role of the electron rest mass m_0 in vacuum. This is why the electrons close to the Brillouin zone edge corner are often called "'massive Dirac Fermions"' in the literature, despite the fact that that Kane's speed is much slower than the light speed ($v_K \approx 10^{-3}c$).

1.2.5 Spin orbit interaction

Since spin orbit shifts the bands without mixing them in C_3h point group, we have only to replace the gaps by:

$$E_{c,v}^{\uparrow(\downarrow)} = E_{c,v} \pm \frac{1}{2}(\Delta_{S0}^{CB} - \Delta_{S0}^{VB})$$

where we have introduced the spin orbit splitting in the conduction Δ_{S0}^{CB} and valence bands Δ_{S0}^{VB}. It follows that the effective masses differ from the band separating $E_{c,v}^{\uparrow}$ and $E_{c,v}^{\downarrow}$ since these gaps are different now. The Kane speed parameter does not change in the two cases, since it depends only on the orbital part of the Bloch states.

Finally, introducing the Pauli matrices $(\hat{\sigma_X}, \hat{\sigma_Y}, \hat{\sigma_Z})$, $\frac{\hat{S}_Z}{2}$ the spin operator, taking the convention $q\pm = \mp\frac{q_X \mp q_Y}{\sqrt{2}}$ and labeling the $K^{\pm}$ valley by the index $\tau = \pm 1$, we obtain:

$$\left[\hat{h}_{\tau,\vec{q}}\right] = \left(\frac{E_{\vec{K}^{\pm},c} + E_{\vec{K}^{\pm},v}}{2} + \frac{\hbar^2}{2m_0}q^2\right)[1] + \frac{E_{g,\vec{K}^{\pm}}}{2}\hat{\sigma_Z} + \hbar v_K \frac{i}{\sqrt{2}}(q_X\hat{\sigma_Y} + \tau q_Y\hat{\sigma_X}) + \tau\frac{\Delta_{S0}^{CB}}{2}(\hat{\sigma_Z} + \hat{1})\hat{S}_Z - \tau\frac{\Delta_{S0}^{VB}}{2}(\hat{\sigma_Z} - \hat{1})\hat{S}_Z \quad (1.20)$$

Figure 8 illustrates the system's band structure at K^+ and K^- points.

Finally, we display here state of the art values (from DFT calculations, extracted from ref [26]) for the effective masses as well as for band splittings. Note that contrary to what we expected from our simple 2 band k.p approach, the effective masses for valence and conduction bands are very close (see tables in figures 9 and 10). This is due to the influence of other bands, neglected in our simple calculation. This can be taken into account by increasing the number of bands in the k.p model, as in ref. [26] where a 4 bands

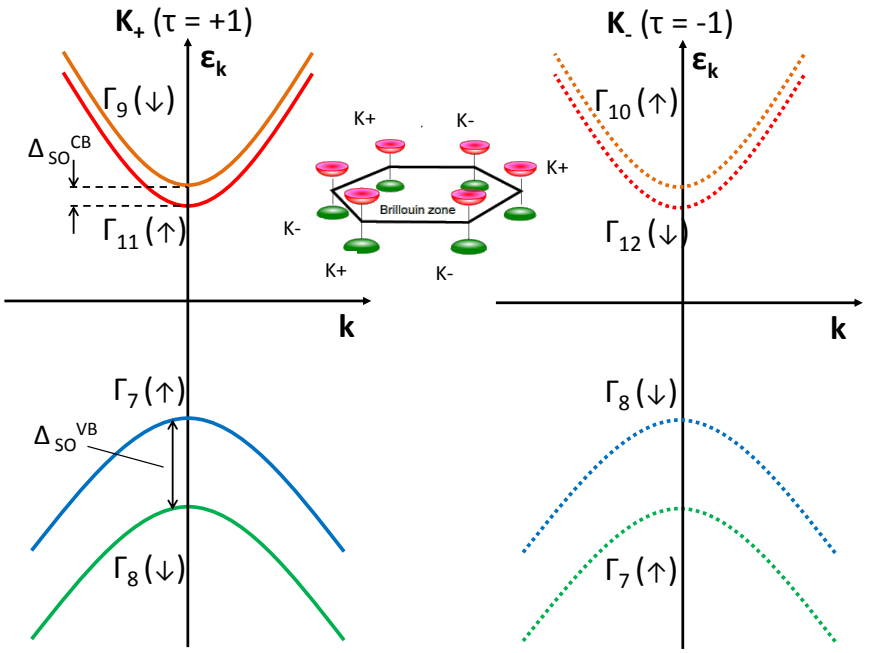

Figure 8: **Schematic illustration of monolayer MoS_2 band structure.** The bands are labeled by the corresponding irreducible representations with arrows in parentheses showing electron spin orientation. Spin-orbit splittings are displayed. An inset sketches the Brillouin zone. The order of conduction band states is shown in accordance with Ref. [22]

model was developed. The empirical input parameters for this improved model are then mapped on DFT calculation.

The calculated results are, when possible, compared to experimental values. The main characterization techniques of TMDC electron states are Scanning Tunneling Spectroscopy (STS) [20; 29] which allows to determine the single particle bandgap of TMDCs and the Angle Resolved Photo-Emission Spectroscopy (ARPES) [17], which allows to determine the upper valence band dispersion curves and in the best cases the valence spin-orbit splitting. However the conduction electron dispersion curves are not yet accessible with this technique. The particular case of the spin-orbit splitting can also be estimated by simple photoluminescence absorption techniques, as presented in section 2.1. Note also that interestingly, according to calculations [22] the sign of the spin-orbit splitting in the conduction band changes depending on the considered material.

	MoS_2	$MoSe_2$	WS_2	WSe_2	$MoTe_2$	WTe_2
$m_{cb}^{(1)}/m_e$ (HSE,LDA)	0.46	0.56	0.26	0.28	0.62	0.26
$m_{cb}^{(1)}/m_e$ (PBE,PBE)	0.47	0.58	0.27	0.29	0.61	0.25
$m_{cb}^{(2)}/m_e$ (HSE,LDA)	0.43	0.49	0.35	0.39	0.53	0.39
$m_{cb}^{(2)}/m_e$ (PBE,PBE)	0.44	0.50	0.36	0.40	0.51	0.38
$C_{3w}^{(1)}$ (eVÅ^3) (HSE,LDA)	−3.36	−3.11	−2.8	−3.02	−3.85	−5.86
$C_{3w}^{(1)}$ (eVÅ^3) (PBE,PBE)	−3.57	−2.94	−1.8	−2.44	−3.95	−17.54
$C_{3w}^{(2)}$ (eVÅ^3) (HSE,LDA)	−3.34	−3.12	−3.14	−3.23	−3.86	−4.90
$C_{3w}^{(2)}$ (eVÅ^3) (PBE,PBE)	−3.49	−2.86	−2.54	−2.97	−4.04	−9.67
$2\Delta_{cb}$ (meV) (HSE,LDA)	3	22	−32	−37	36	−52
$2\Delta_{cb}$ (meV) (PBE,PBE)	3	20	−31	−37	32	−54
n_{cb} (10^{12} cm^{-2}) (HSE,LDA)	0.54	4.5	4.68	6.03	7.97	8.48

Figure 9: Table extracted from ref [26]. Band dispersion parameters and spin-splittings at the K^+ and K^- points in the CB from DFT calculations. $m_{cb}^{(1)}$ ($m_{cb}^{(2)}$) is the effective mass of the $K_{cb}^{(1)}$ ($K_{cb}^{(2)}$) band, and similarly for trigonal warping parameters $C_{3w}^{(1)}$($C_{3w}^{(2)}$). m_e is the free electron mass. n_{cb} is the electron density above which the upper spin-split CB starts to fill.

	MoS_2	$MoSe_2$	WS_2	WSe_2	$MoTe_2$	WTe_2
$m_{vb}^{(1)}/m_e$ (HSE,LDA)	−0.54	−0.59 (−0.64)	−0.35	−0.36	−0.66	−0.34
$m_{vb}^{(1)}/m_e$ (PBE,PBE)	−0.54	−0.60 (−0.60)	−0.36	−0.36	−0.62	−0.32
Exp	−0.6±0.08[a]	−0.67±0.4[b]				
$m_{vb}^{(2)}/m_e$ (HSE,LDA)	−0.61	−0.7 (−0.72)	−0.49	−0.54	−0.82	−0.58
$m_{vb}^{(2)}/m_e$ (PBE,PBE)	−0.61	−0.7 (−0.69)	−0.50	−0.54	−0.77	−0.54
Exp	−0.6±0.08[a]	−0.75±0.3[b]				
$C_{3w}^{(1)}$ (eVÅ^3) (HSE,LDA)	6.16	5.67	4.59	6.47	5.44	6.77
$C_{3w}^{(1)}$ (eVÅ^3) (PBE,PBE)	6.08	5.21	6.07	5.79	5.46	17.61
$C_{3w}^{(2)}$ (eVÅ^3) (HSE,LDA)	5.78	5.42	5.50	5.18	5.14	4.83
$C_{3w}^{(2)}$ (eVÅ^3) (PBE,PBE)	5.71	5.064	5.04	4.78	5.09	9.08
$2\Delta_{vb}$ (meV) (HSE,LDA)	148	186	429	466	219	484
$2\Delta_{vb}$ (meV) (PBE,PBE)	148	184	425	462	213	480
Exp (meV)	≈140[c]	≈180[e]	≈400[g],	≈400[g]		
	≈150[d]	≈180[f]	380[h]	≳460[k]		
	160[m]	≈200[m]	410[i]	400[l]		
	140[n]		400[j]	510[m]		
	140[p]		400[l]	~500[q]		
	138[r]	202[r]	379[r]	404[r]		
			391[t]	412[t]		
				430[x]		

Figure 10: Table extracted from ref [26]. Effective masses and spin-splittings at the Kpoint in the VB from DFT calculations.$m_{cb}^{(1)}$ ($m_{cb}^{(2)}$) is the effective mass of the $K_{cb}^{(1)}$ ($K_{cb}^{(2)}$) band, and similarly $C_{3w}^{(1)}$($C_{3w}^{(2)}$). m_e is the free electron mass. Experimental values are shown in rows denoted by 'Exp'.

1.3 Optical properties and selection rules close to the TMDC monolayer gap

The hamiltonian of the crystal under incident electromagnetic (e.m.) plane wave can be written as:

$$\hat{\mathrm{H}} = \frac{(\hat{p} - q\vec{\mathrm{A}})^2}{2m_0} + \mathrm{V}(\vec{r})$$

where $\vec{\mathrm{A}}(\vec{r}, t) = \vec{e}\,\mathrm{A}$ is the vector potential of the e.m. field, taking the Coulomb gauge $\hat{p}.\vec{\mathrm{A}} = \vec{\mathrm{A}}.\hat{p}$ so that:

$$\hat{\mathrm{H}} = \frac{\hat{p}^2}{2m_0} + \mathrm{V}(\vec{r}) + \frac{|q|\vec{\mathrm{A}}.\hat{p}}{m_0} + \frac{q^2\mathrm{A}^2}{2m_0} = \hat{\mathrm{H}}_0 + \hat{\mathrm{W}}_{opt}$$

with

$$\hat{\mathrm{H}}_0 = \frac{\hat{p}^2}{2m_0} + \mathrm{V}(\vec{r})$$

and

$$\hat{\mathrm{W}}_{opt} = \frac{|q|\vec{\mathrm{A}}.\hat{p}}{m_0} + \frac{q^2\mathrm{A}^2}{2m_0} \approx \frac{|q|\vec{\mathrm{A}}.\hat{p}}{m_0}$$

Using the first order perturbation optical hamiltonian:

$$\hat{\mathrm{W}}_{opt}(\vec{r}) = e^{-i\omega t}\hat{\mathrm{F}} + e^{i\omega t}\hat{\mathrm{F}}^{+}$$

where $\hat{\mathrm{F}}$ stands for absorption and $\hat{\mathrm{F}}^{+}$ stems for emission process; with:

$$\hat{\mathrm{F}} = \frac{|q|\mathrm{A}_0}{2m_0} e^{i\vec{k}.\vec{r}}\,\vec{e}.\hat{p}$$

and $\hat{\mathrm{F}}^{+}$ being the complex conjugate of $\hat{\mathrm{F}}$.

In addition, as in our experimental configuration the light propagates along $\mathrm{O_Z}$ axis, this reduces to:

$$\hat{\mathrm{F}} = \frac{|q|\mathrm{A}_0}{2m_0} e^{i\vec{k}_{\mathrm{Z}}.\vec{z}}\,\vec{e}_{\perp}.\hat{p}_{\perp}$$

with $\vec{e}_{\perp} = (e_{\mathrm{X}}, e_{\mathrm{Y}})$ and $\hat{p}_{\perp} = \left(\hat{p}_{\mathrm{X}}, \hat{p}_{\mathrm{Y}}\right)$ in the $\left(\mathrm{O}, \vec{e}_{\mathrm{X}}, \vec{e}_{\mathrm{Y}}\right)$ frame.

Since $\lambda \gg d$, we can take $e^{i\vec{k}_{\mathrm{Z}}.\vec{z}} \approx 1$ (dipolar approximation) and finally:

$$\hat{\mathrm{F}} \approx \frac{|q|\mathrm{A}_0}{2m_0}\vec{e}_{\perp}.\hat{p}_{\perp}$$

Fermi's golden rule gives us [30]:

$$\left|\frac{\partial \mathrm{P}}{\partial t}\right|_{v\to c} = \frac{2\pi}{\hbar}\left|< f|\hat{\mathrm{F}}|i >\right|^2 \delta(\mathrm{E}_f - \mathrm{E}_i - \hbar\omega)$$

Because of the micro-reversibility principle, absorption and emission optical selection rules are the same, so we will only consider here the absorption process. Therefore, the term $\hat{\mathrm{F}}^{+}$ is neglected because energetically out of resonance (it would have worked for emission process). As $\hat{\mathrm{F}}^{+}$ is the complex conjugate of $\hat{\mathrm{F}}$, all this is consistent with the time

reversal symmetry of the process.

Therefore, the application of Fermi's golden rule gives us:

$$\left|\frac{\partial \mathrm{P}}{\partial t}\right|_{v\to c} = \frac{q^2 \mathrm{A}_0^2 \pi}{2\hbar m_0^2} \left| < \psi_c | \overrightarrow{e}_\perp . \hat{p}_\perp | \psi_v > \right|^2 \delta(\mathrm{E}_f - \mathrm{E}_i - \hbar\omega)$$

The interband matrix element is defined as:

$$\Gamma_{c,v}(\overrightarrow{k}) = \left\langle \psi_{c,\overrightarrow{k'}} \left| \overrightarrow{e}_\perp . \hat{p}_\perp \right| \psi_{v,\overrightarrow{k}} \right\rangle$$

using the Bloch function basis, we have then:

$$\Gamma_{c,v}(\overrightarrow{k}) \approx \delta_{\overrightarrow{k},\overrightarrow{k'}} \overrightarrow{e}_\perp . \left\langle u_{c,\overrightarrow{k}} \left| \hat{p}_\perp \right| u_{v,\overrightarrow{k}} \right\rangle_\Omega$$

which yields to the optical selection rules. Note that we assume that:

$$\overrightarrow{e}_\perp . \left\langle u_{c,\overrightarrow{k}} \left| \hat{p}_\perp \right| u_{v,\overrightarrow{k}} \right\rangle_\Omega \approx \overrightarrow{e}_\perp . \left\langle u_{c,\overrightarrow{\mathrm{K}}^\pm} \left| \hat{p}_\perp \right| u_{v,\overrightarrow{\mathrm{K}}^\pm} \right\rangle_\Omega = \overrightarrow{e}_\perp^* \left\langle u_{c,\overrightarrow{\mathrm{K}}^\pm} \left| \hat{p}_\perp \right| u_{v,\overrightarrow{\mathrm{K}}^\pm} \right\rangle_\Omega$$

where $|u_c>$ (resp. $|u_v>$) correspond to conduction state (valence state).

Let us now see the special case of the circular polarization basis, which leads to chiral selection rules: under σ_+ excitation, we have:

$$\overrightarrow{e}_{\sigma+} = \begin{cases} e_\mathrm{X} = 1/\sqrt{2} \\ e_\mathrm{Y} = i/\sqrt{2} \\ e_\mathrm{Z} = 0 \end{cases}$$

in the circular basis, we have $e_\pm = \mp \frac{e_\mathrm{X} \mp i e_\mathrm{Y}}{\sqrt{2}}$, therefore:

$$\overrightarrow{e}^*_{\sigma+} = \begin{cases} e_+ = -\frac{1-i(-i)}{2} = 0 \\ e_- = +\frac{1+i(-i)}{2} = +1 \\ e_\mathrm{Z} = 0 \end{cases}$$

under σ_- excitation:

$$\overrightarrow{e}^*_{\sigma-} = \begin{cases} e_+ = -\frac{1-i(i)}{2} = -1 \\ e_- = +\frac{1+i(i)}{2} = 0 \\ e_\mathrm{Z} = 0 \end{cases}$$

similarly, we define:

$$\hat{p} = \begin{cases} \hat{p}_+ = -\frac{\hat{p}_x - i\hat{p}_y}{\sqrt{2}} \\ \hat{p}_- = +\frac{\hat{p}_x + i\hat{p}_y}{\sqrt{2}} \\ \hat{p}_0 = \hat{p}_z \end{cases}$$

finally we get in this basis adapted to circular polarization:

$$\Gamma^{\pm\sigma}_{c,v}(\overrightarrow{k}) \approx \frac{1}{\sqrt{2}} \left\langle u_{c,\overrightarrow{k}} \left| \left(\hat{p}_x \pm i\hat{p}_y\right) \right| u_{v,\overrightarrow{k}} \right\rangle_\Omega \tag{1.21}$$

According to Basis Functions corresponding to C_{3h} symmetry [27], which is the one we are interested in because corresponding to K^+ and K^- points of the Brillouin zone, $\hat{p}_x + i\hat{p}_y$ transform according to Γ_2 representation and $\hat{p}_x - i\hat{p}_y$ transform according to Γ_3 representation. Note here that, according to ab-initio calculations, K^+ and K^- correspond to the conduction band minima (respectively to valence band maxima) for monolayers and therefore define the symmetry of the states involved into optical transitions.

We demonstrated in the previous section that at the K^+ point of the Brillouin zone, the conduction states transforms according to the Γ_2 representation and the valence states transform according to the Γ_1 representation. We need now to take into account the $\pm 1/2$ spin of the carriers and therefore the spin-orbit coupling and its resulting effect on the optical states representation.

For C_{3h} symmetry, spin up transform according to Γ_7 representation [27], while spin down transform according to Γ_8 representation. At the K^+ point, this gives us for conduction states:

$$\Gamma_2 \times \Gamma_7 = \Gamma_{11}, \Gamma_2 \times \Gamma_8 = \Gamma_9$$

and for valence states:

$$\Gamma_1 \times \Gamma_7 = \Gamma_7, \Gamma_1 \times \Gamma_8 = \Gamma_8$$

Note that the spin orbit coupling interaction simply shifts the bands and doesn't mix spin states, so the conduction (resp. valence) orbital states remain pure in spin.

At the K^- point, the same procedure gives us for the conduction states:

$$\Gamma_3 \times \Gamma_7 = \Gamma_{10}, \Gamma_3 \times \Gamma_8 = \Gamma_{12}$$

and for valence states:

$$\Gamma_1 \times \Gamma_7 = \Gamma_7, \Gamma_1 \times \Gamma_8 = \Gamma_8$$

We can now uncover the optically coupled states and deduce the optical selection rules for TMDCs ML materials, at the K^+ point:

- For σ+ excitation $< u_c|\hat{p}_x + i\hat{p}_y|u_v >$

$$(\Gamma_{11})^* \times \Gamma_2 \times \Gamma_7 = \Gamma_{12} \times \Gamma_2 \times \Gamma_7 = \Gamma_8 \times \Gamma_7 = \Gamma_1$$

$$(\Gamma_9)^* \times \Gamma_2 \times \Gamma_7 = \Gamma_{10} \times \Gamma_2 \times \Gamma_7 = \Gamma_7 \times \Gamma_7 = \Gamma_5 \neq \Gamma_1$$

$$(\Gamma_{11})^* \times \Gamma_2 \times \Gamma_8 = \Gamma_{12} \times \Gamma_2 \times \Gamma_8 = \Gamma_8 \times \Gamma_8 = \Gamma_6 \neq \Gamma_1$$

$$(\Gamma_9)^* \times \Gamma_2 \times \Gamma_8 = \Gamma_{10} \times \Gamma_2 \times \Gamma_8 = \Gamma_7 \times \Gamma_8 = \Gamma_1$$

  Only the transitions $\Gamma_7 \rightarrow \Gamma_{11}$ and $\Gamma_8 \rightarrow \Gamma_9$ are possible at the K^+ point and under σ+ excitation as indicated in figure 3.

- For σ− excitation $< u_c|\hat{p}_x - i\hat{p}_y|u_v >$

$$(\Gamma_{11})^* \times \Gamma_3 \times \Gamma_7 = \Gamma_{12} \times \Gamma_3 \times \Gamma_7 = \Gamma_9 \times \Gamma_7 = \Gamma_2 \neq \Gamma_1$$

$$(\Gamma_9)^* \times \Gamma_3 \times \Gamma_7 = \Gamma_{10} \times \Gamma_3 \times \Gamma_7 = \Gamma_{11} \times \Gamma_7 = \Gamma_6 \neq \Gamma_1$$

$$(\Gamma_{11})^* \times \Gamma_3 \times \Gamma_8 = \Gamma_{12} \times \Gamma_3 \times \Gamma_8 = \Gamma_9 \times \Gamma_8 = \Gamma_4 \neq \Gamma_1$$

$$(\Gamma_9)^* \times \Gamma_3 \times \Gamma_8 = \Gamma_{10} \times \Gamma_3 \times \Gamma_8 = \Gamma_{11} \times \Gamma_8 = \Gamma_2 \neq \Gamma_1$$

  No optical transitions are possible at the K^+ point and under σ- excitation.

at the K^- point:

- For σ+ excitation $< u_c|\hat{p}_x + i\hat{p}_y|u_v >$

$$(\Gamma_{12})^* \times \Gamma_2 \times \Gamma_7 = \Gamma_{11} \times \Gamma_2 \times \Gamma_7 = \Gamma_{10} \times \Gamma_7 = \Gamma_4 \neq \Gamma_1$$

$$(\Gamma_{10})^* \times \Gamma_2 \times \Gamma_7 = \Gamma_9 \times \Gamma_2 \times \Gamma_7 = \Gamma_{12} \times \Gamma_7 = \Gamma_3 \neq \Gamma_1$$

$$(\Gamma_{12})^* \times \Gamma_2 \times \Gamma_8 = \Gamma_{11} \times \Gamma_2 \times \Gamma_8 = \Gamma_{10} \times \Gamma_8 = \Gamma_3 \neq \Gamma_1$$

$$(\Gamma_{10})^* \times \Gamma_2 \times \Gamma_8 = \Gamma_9 \times \Gamma_2 \times \Gamma_8 = \Gamma_{12} \times \Gamma_8 = \Gamma_5 \neq \Gamma_1$$

  There is no possible transitions at the K^- point and under σ+ excitation.

- For σ− excitation $< u_c|\hat{p}_x - i\hat{p}_y|u_v >$

$$(\Gamma_{12})^* \times \Gamma_3 \times \Gamma_7 = \Gamma_{11} \times \Gamma_3 \times \Gamma_7 = \Gamma_7 \times \Gamma_7 = \Gamma_5 \neq \Gamma_1$$

$$(\Gamma_{10})^* \times \Gamma_3 \times \Gamma_7 = \Gamma_9 \times \Gamma_3 \times \Gamma_7 = \Gamma_8 \times \Gamma_7 = \Gamma_1$$

$$(\Gamma_{12})^* \times \Gamma_3 \times \Gamma_8 = \Gamma_{11} \times \Gamma_3 \times \Gamma_8 = \Gamma_7 \times \Gamma_8 = \Gamma_1$$

$$(\Gamma_{10})^* \times \Gamma_3 \times \Gamma_8 = \Gamma_9 \times \Gamma_3 \times \Gamma_8 = \Gamma_8 \times \Gamma_8 = \Gamma_6 \neq \Gamma_1$$

  The transitions $\Gamma_8 \rightarrow \Gamma_{12}$ and $\Gamma_7 \rightarrow \Gamma_{10}$ are possible at the K^- point and under σ- excitation.

We finally obtain the selection rules displayed in figure 3. In contrast to GaAs, we see that in a given K valley, the helicity of the light does not allow to discriminate between the spin-orbit split band pairs. In monolayer TMDCs, the helicity allows in fact to discriminate between the two non-equivalent valley K^+ and K^-.

The chiral selection rules obtained are at the heart of the new optical properties of TMDC materials and will be of central interest in this work.

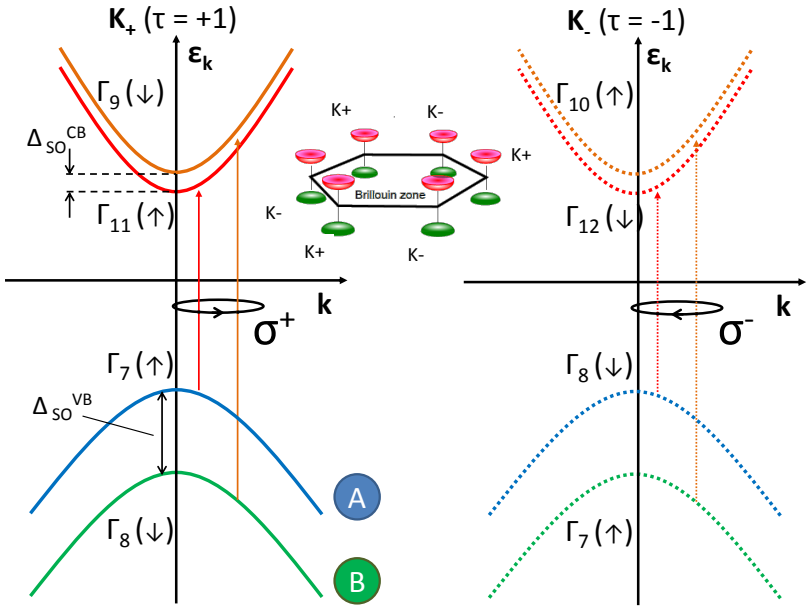

Figure 11: **Schematic illustration of monolayer MoS_2 band structure.** The bands are labeled by the corresponding irreducible representations with arrows in parentheses showing electron spin orientation. Solid and dashed arrows show the active optical transitions at the normal incidence in σ^+ and σ^- polarization, respectively. An inset sketches the Brillouin zone. The order of conduction band states is shown in accordance with Ref. [22]. Spin orbit coupling splits the valence band, leading to A and B exciton series, therefore in the $K^{\pm}$ valley both the A and B exciton transitions are indicated. SO coupling splits also the valence band, but this splitting is not spectrally resolved (see section 2.1).

1.4 Conclusion

In this chapter we first presented a brief historical summary of the field. We then present a simple theoretical model, demonstrating the symmetry of the conduction and valence states at their minima situated at the K^+ and K^- point of the Brillouin zone in reciprocal space. Using a 2-band k.p model, we obtain a rough estimation of the effective masses and we summarize state of the art values for the key parameters, such as the spin-orbit splitting amplitude and effective masses, extracted from the literature. Finally, using symmetry arguments, we demonstrated the original interband chiral selection rules of those materials.

We are now going to present our experimental setups used to investigate the excitonic properties and K^+ Valley dynamics in ML TMDCs. We describe into details their characteristics such as spatial, spectral, polarization and temporal resolution, pointing out their capabilities as well as their limits.

Chapter 2

Samples presentation and Experimental setups for micro-photoluminescence measurements

2.1 Samples: presentation and preparation

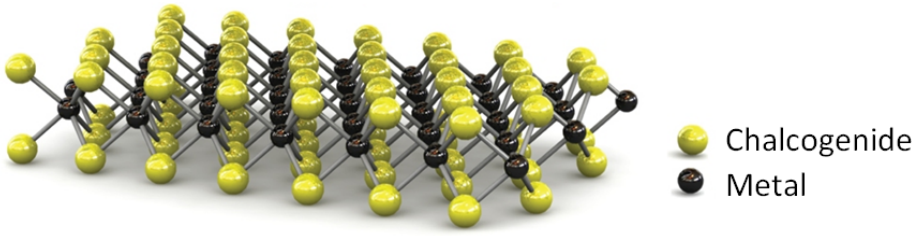

Figure 1: Three-dimensional representation of the structure of MoS_2. Single layers, ≈3 Å thick, can be extracted using adhesive tape-based micromechanical cleavage (cf. section 1.1). Figure extracted from ref [7]

As detailed by Novoselov et al. [14], TMDCs are layered crystals, with strong in-plane bonds and weaker Van-der-Walls bonds that hold the different layers together. Those Van-der-Walls bonds can be easily broken and simply using an adhesive tape ("'scotch tape"'), it is possible to separate them and to fabricate a monolayer.

Due to the randomness of the process, flakes of different size and thickness are obtained and a real experimental challenge is to find the monolayer area (often very small, few µm size, somewhere in a 1 cm^2 area). For this, an efficient procedure is to use first an optical contrast identification (see figures 2d, 3d and 4d) and to confirm such identification by optical spectroscopy (reflectivity, photoluminescence (PL), second harmonic generation (SHG) spectroscopy, Raman, ...).

2.1.1 MoS_2 monolayers

Our MoS_2 sample was obtained by the so called "'scotch tape-technique"', by mechanical exfoliation. The monolayer area was at first identified by optical contrast and then confirmed by PL measurements.

Figure 2 summarizes the main characterizations we perform on the sample. Using a doubled Nd:YAG laser source, we were able to excite highly non-resonantly and to observe

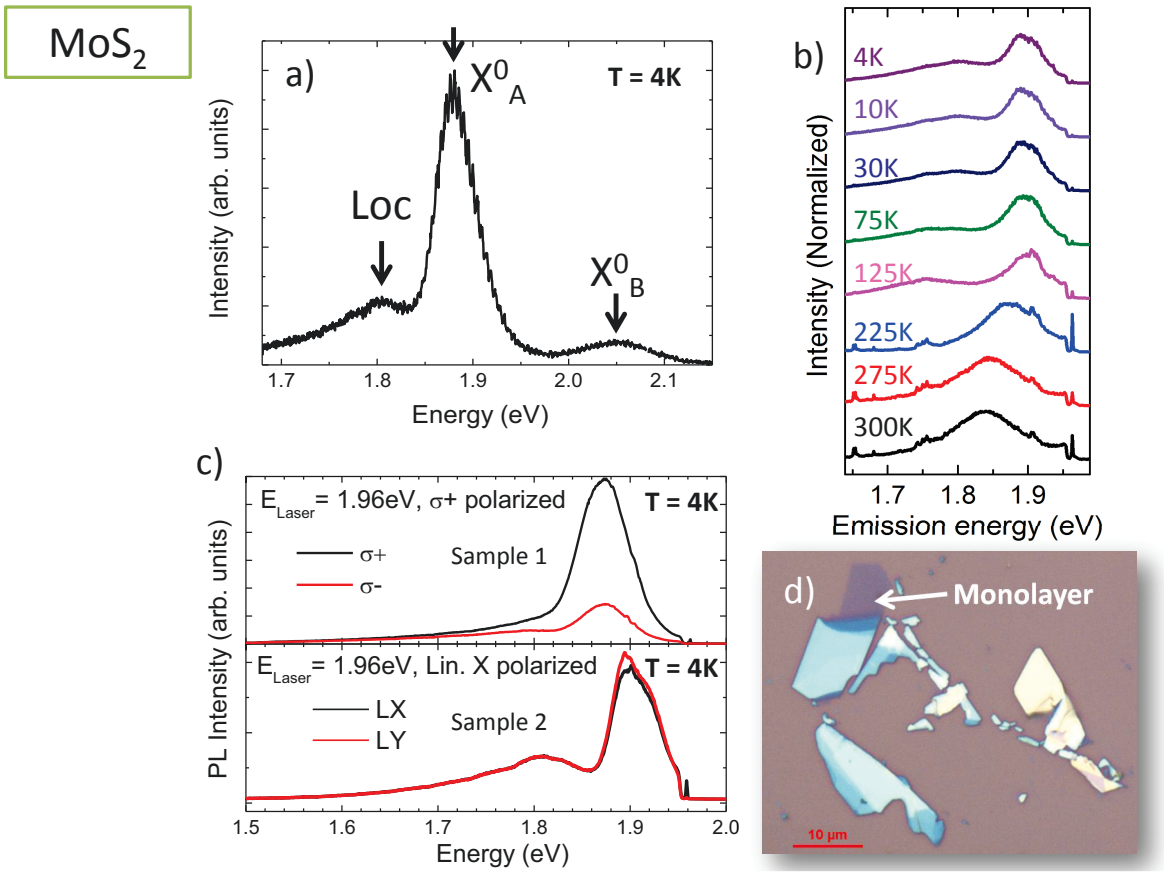

Figure 2: **Overview of MoS_2 monolayer sample.** (a) PL spectra under highly non-resonant excitation. One can see both X^0_A and X^0_B exciton lines allowing to estimate an energy splitting of ≈ 170 meV, in good agreement with both experimental and theoretical values of the literature [26]. Indeed $E_{X^0_B} - E_{X^0_A} = \Delta^{VB}_{SO} - \Delta^{CB}_{SO} - \left(E^{X^0_A}_B - E^{X^0_B}_B\right) \approx \Delta^{VB}_{SO}$ if we consider that $\Delta^{VB}_{SO} \gg \Delta^{CB}_{SO}$ and $E^{X^0_A}_B \approx E^{X^0_B}_B$. (b) Temperature dependance of the PL emission. (c) Circular and linear polarization of the PL under respectively circular and linear excitation (two different sample were used, which explain the differences between the spectra) (d) Picture of the monolayer area of the sample under an optical microscope.

both emission of neutral A-exciton X^0_A and neutral B-exciton X^0_B and to extract (despite the underestimation due to potential Stokes-shift) the valence band splitting (see fig. 2a).

In figure 2b we display the PL temperature dependence. We can see that the main peak, corresponding to the A optical transition, persist even at room temperature, whereas the other peak disappear when the temperature increase. This behavior can correspond to localized states, which is consistent with the lower polarization degree of this PL peak. A more detailed study is discussed in chapter 3.

Finally, the curves presented in figure 2c shows that the main peak of the emitted PL is highly circularly polarized under circular excitation. The linear polarization degree obtained under linear excitation is much lower and concentrated on a small range of the PL energy. We can imagine that this main peak is actually composed by the spectral contributions of many excitonic states (for instance the trion and X^0, that can be linearly polarized). Unfortunately the emission peak is too broad to allow to discriminate between different excitonic complexes contributions.

MoS_2 was historically the first 2D material to see its original physical properties un-

covered (see section 1.1), although it is an interesting material, we will see in the following that the higher optical quality of ML $MoSe_2$ and WSe_2 allows us to uncover more details of exciton and valley physics.

2.1.2 WSe_2 monolayers

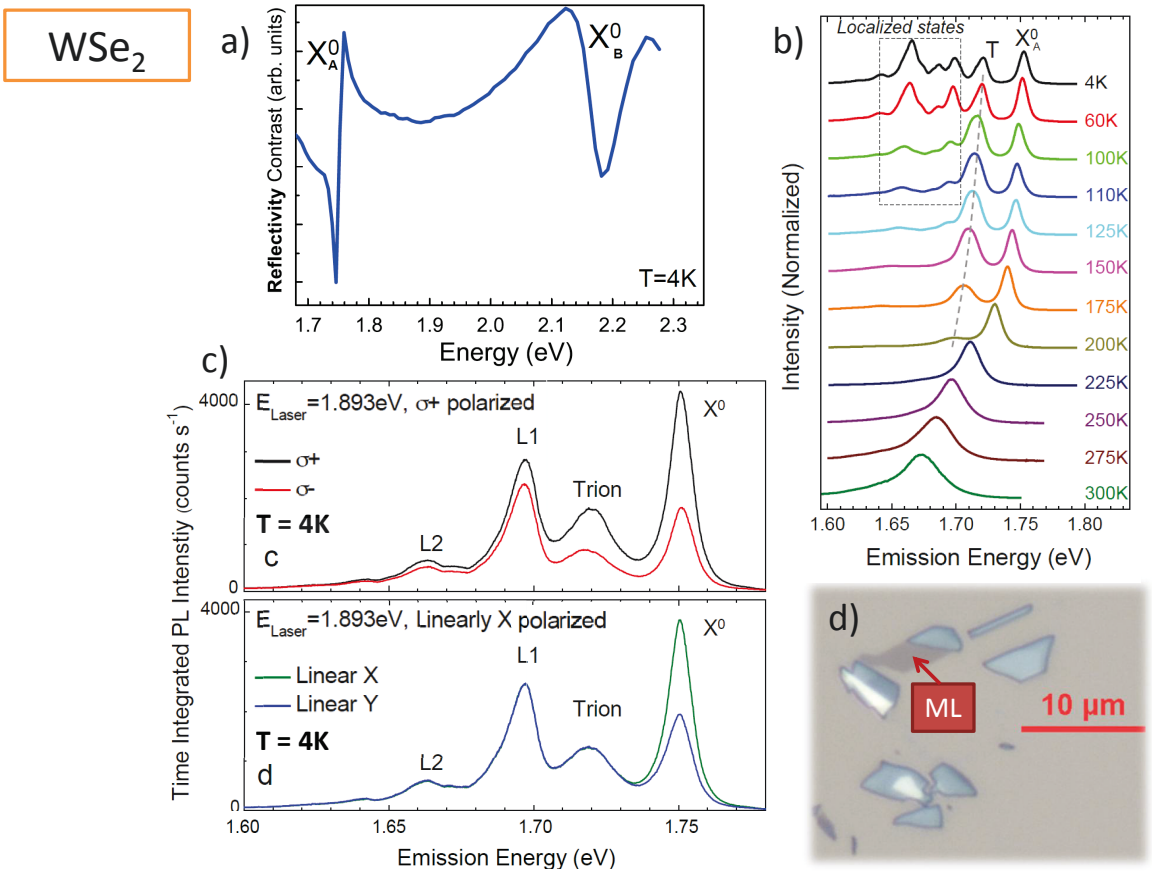

Figure 3: **Overview of WSe_2 monolayer sample.** (a) Reflectivity measurement allowing to extract an energy splitting between X^0_A and X^0_B lines of $\approx$ 450 meV, in good agreement with both experimental and theoretical values of the literature [26] (b) Temperature dependance of the PL emission. (c) Circular and linear polarization of the PL under respectively circular and linear excitation (T = 4 K). (d) Picture of the monolayer area of the sample under an optical microscope.

The sample used to investigate WSe_2 ML physical properties was provided by a company, "'2D semiconductors"', dedicated to monolayer and heterostructures production. According to the supplier[31], our sample of monolayer tungsten diselenide flakes have been exfoliated from bulk tungsten diselenide onto 90nm silicon oxide and measures from 5µm up to 40µm in lateral size. A full set of characterizations is performed on each monolayer flake, which involve mainly Raman spectroscopy (extracted form supplier website):

"'Raman spectroscopy data is taken on every single-layer flakes. Typically, flakes show two prominent Raman peaks at 139.5cm-1 (E^2_g - in plane phonon mode-) and 249.5cm^{-1} (A^1_g out-of-plane mode) and the FWHM (full-width-at-half-maximum) is less than 5cm^{-1}"'.

Our sample shows indeed a very high optical quality, as can be seen in figure 3 which summarize the characterizations we perform on the sample. More than the FWHM of the

localized peak mentioned by the supplier, the clear separation by 30 meV of the trion (PL FWHM 15 meV) and neutral exciton (PL FWHM 10 meV) demonstrate the sample quality. This constitutes also an advantage compared to MoS_2 ML samples where the PL linewidth is much broader (70 meV).

In addition, we measure the valence band splitting by reflectivity measurements (fig. 3a), and conduct several experiments in order to check the different peaks identification.

The PL temperature dependence (fig. 3b) demonstrates that low energy peaks are very likely localized states; they disappear as we raise the temperature above 150K, whereas the intensity of the two main peaks (neutral X_A^0 and charged exciton T) remains strong over a broader temperature range (T≤200 K). At room temperature, only the X_A^0 exciton can be clearly identified in the emission.

The identification of the transitions is also based on the polarization analysis shown in figures 3c. Under linearly polarized laser excitation, only the highest energy peak shows linear polarization in emission and is therefore ascribed to the X^0, as a coherent superposition of valley states is created [32]. This observation of exciton alignment is independent of the direction of the incident laser polarization, which confirms that the observed linear polarization is not due to macroscopic birefringence in the sample. The strong remaining coherence in figure 3c following non-resonant excitation is linked to the direct optical generation of the neutral exciton excited state X^0 2s for the laser energy used [33], energetically below the free carrier absorption and well below the B-exciton. Also double resonant Raman scattering might play a role [34]. Under circularly polarized excitation in figure 3c, the two highest energy transitions are strongly polarized, as expected for the X^0 and the trion. Please note that such characterization has been done for a large number of WSe_2 ML samples, exfoliated by 2D semiconductors and in our group.

2.1.3 $MoSe_2$ monolayers

For the fabrication of $MoSe_2$ ML sample we developed a more advanced technique, inspired from the literature [35]. A polydimethylsiloxane (PDMS, a silicon based organic polymer) stamp has been used in addition to the tape to proceed to the exfoliation and precise releasing of monolayers flakes. This technique was also successfully applied to fabricate hetero-structures, which was the original purpose of the mentioned reference [35], but the study of those samples is out of the scope of this thesis.

Our sample shows a high optical quality, with only two narrow (about 10meV), well separated peaks in PL, corresponding respectively to the neutral exciton X^0 and to the trion (see fig. 4c). We extract an energy splitting of ≈ 220 meV between X_A^0 and X_B^0 (fig. 4a). We also show here the temperature dependence of the PL, the evolution of the $MoSe_2$ properties with temperature variations are discussed by Tongay and co. in the following reference [36].

It turns out that none of the peaks of the emitted PL is polarized, neither under circularly polarized excitation, nor under linearly polarized excitation [37]. This might be due to the very small energy difference (about 46meV) between the Γ and Λ point of the conduction band [37], that, associated to very strong binding energy of excitons in this materials (see also chapter 5) might change the selection rules and thus, do not follow the chiral selection rules presented in section 1.3.

Note also that the size of our monolayer area is bigger than for the other 2D TMDCs. This seems to be due to the change of exfoliation technique as the same trend has since then been observed for other TMDC materials.

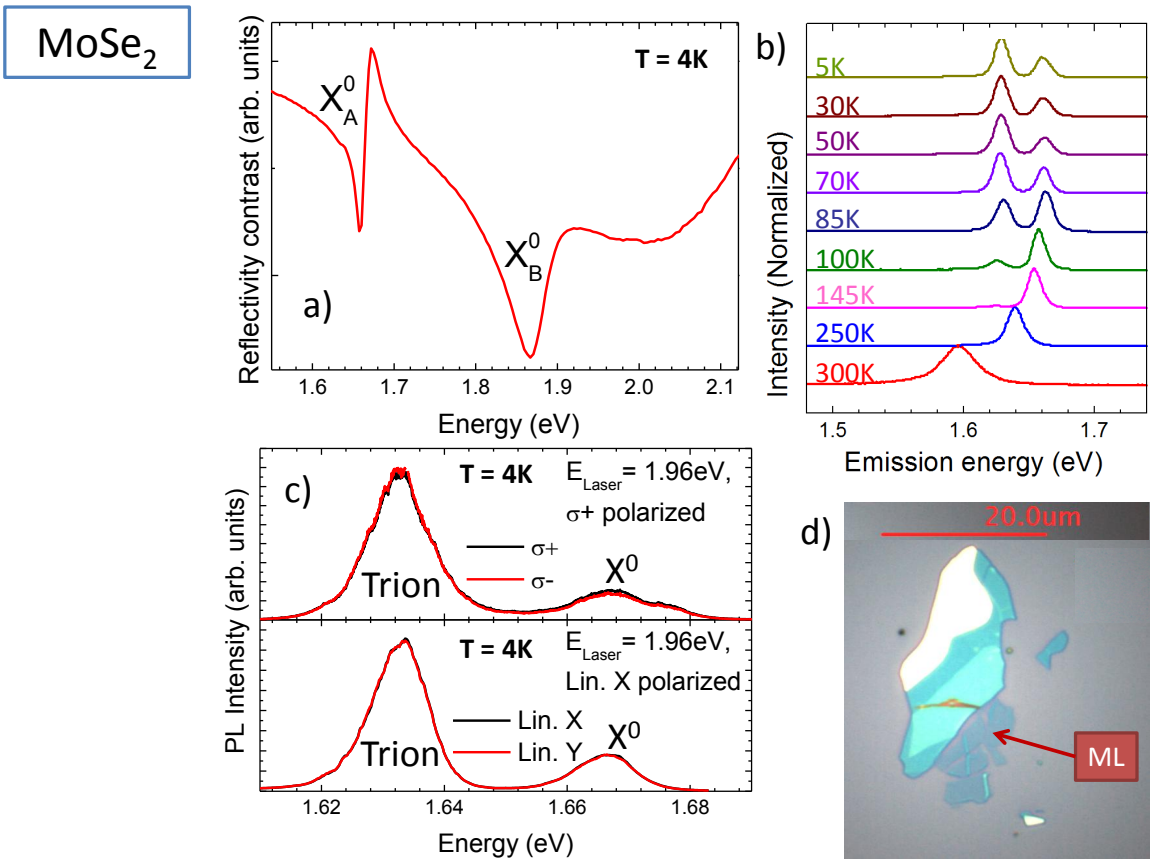

Figure 4: **Overview of $MoSe_2$ monolayer sample.** (a) Reflectivity measurement allowing to extract an energy splitting between X^0_A and X^0_B of ≈ 220 meV, slightly above experimental and theoretical values of the literature [26] (b) Temperature dependance of the PL emission. (c) Circular and linear polarization of the PL under respectively circular and linear excitation. (d) Picture of the monolayer area of the sample under an optical microscope

2.2 Introduction to the setup

Our original setup has been developed to fulfill the requirements of single nano-objects studies. Indeed, another important part of my research work (out of the scope of this thesis) has been dedicated to the studies of quantum dot properties, especially optical manipulation of electron and nuclear spins [38–41]. Although the setup has been somehow adapted for TMDCs study, the experimental challenges are very similar and a lot of experimental know-how can be directly transferred from one research field to the other. For both, main requirements involve:

(i) a high spatial resolution. The typical size of the studied quantum dots is few tens of nm radius (20-30nm) and nm hight (3-5nm). Addressing a single quantum dot is therefore a challenge and requires an excitation laser spot smaller than 1 µm in addition to a reduced spatial density of dots on the sample. Even so, we need to be able to move the position of our sample with a nanometric resolution in the 3 direction in space to be able to optimize our optical alignment and reach the required spatial precision. Concerning TMDCs, the exfoliated monolayer flakes were originally only few µm large (typically 5 µm). Benefiting from such high spatial resolution, it was possible to focus on a single flake and even to uncover some spatial dependance of the PL properties of the same flake. We used two microscope objectives during our experiments, the very large emission spec-

tra (hundreds of meV) of some TMDCs imposed us to use an achromatic objective. The reader will find all the useful technical precision concerning this part in the dedicated section 2.3.2. Note also that the spatial resolution is useless if the vibration level of the cryostat is too high, or if it moves too much when a magnetic field is applied. The performances of our cryostats are summarized in the section 2.4.

(ii) a high polarization resolution. Using both the optical selection rules and excitation polarization in order to control injected carrier spins/valley indices or using both selection rules and the emitted PL polarization to analyze the carrier spin orientation/valley index when they recombine is the starting point of our experiments for both quantum dots and TMDC monolayers. For experiments reported here, we mainly use quarter wave plate and half wave plate associated with Glan-Taylor analyzer and polarizer. Occasionally, liquid crystal retarder were used. The overall polarization purity has been kept about 99% when tested on the laser reflection. Additional details are given in section 2.3.3.

Some requirements are more specific to TMDCs. For QDs, the imaging system of the initial setup was very rough, being used only to figure out letters or numbers used to identified mesa positions on our sample. For TMDCs, an additional challenge was to identify the monolayer flake among hundreds of flakes of random size and shapes (challenge inherent to the exfoliation technique, see figure 5). For that, a more accurate imaging system was needed (even if we managed to target the monolayer flake using silver paint marks during the first experiments). The use of a setup mounted on an optical table (AttoDry700 setup), as well as the use of an multi-element microscope objective instead of a single lens (traditionally used in quantum dots measurements) allows us to add an imaging system adapted to the experiments.

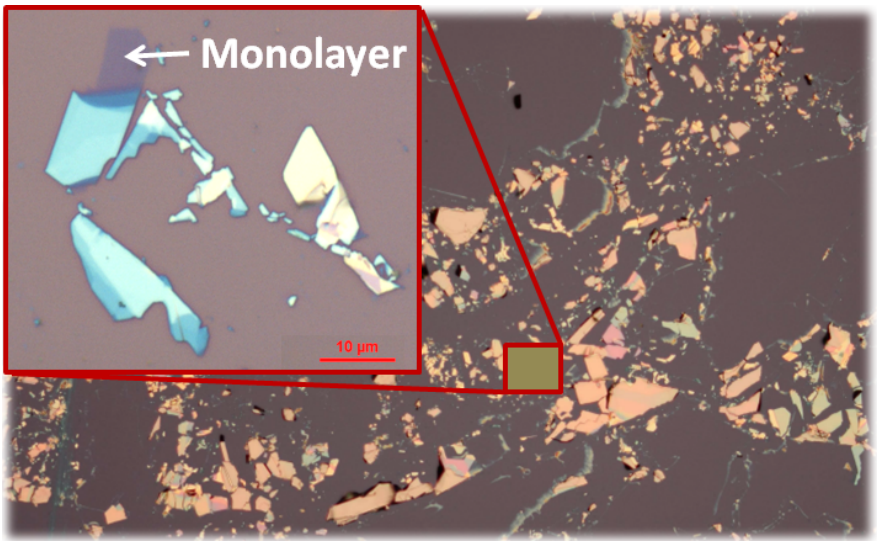

Figure 5: Typical example of a TMDC monolayer flake among other exfoliated flakes. Here one can see the difficulty of finding the monolayer area. The insert shows a zoom on the area of interest where lay several flakes of MoS_2 including the monolayer area (in grey). Its size is only few µm large, which underline the importance of the use of a micro-photoluminescence setup for the study of this material.

Another requirement specific to TMDC is the use of the streak camera setup. The emitted PL signal of quantum dots is usually too weak for TRPL measurements, when those measurements are of essential interest for TMDCs. We therefore add to the new setup the possibility to switch between two detection equipments: a high resolution spectrometer coupled to highly sensitive Si-CCD camera or a S20 Hamamatsu Streak camera coupled

to its spectrometer, allowing us to perform time resolved photoluminescence measurements (see dedicated section 2.5).

Finally, the spectral resolution of our setup is very high (see section 2.3.4 for more details), been dimensioned to uncover μeV changes in the extremely narrow (< 40μeV, resolution limited) quantum dot emission peaks. Such high spectral resolution is not necessary for TMDC experiments; since the emission spectra are much larger (from ten to hundreds of meV), we can only resolve much bigger effects (hundreds of μeV shifts).

The two different setups used for the experiments presented in this thesis are presented here. The most widely used, referred to as Atto700 due to the corresponding cryostat Attodry700, is presented first. For the second one, referred to as Atto1000 (Attodry1000 cryostat) and used in magneto-PL experiments, only the parts that differs from Atto700 are presented into detail.

The reader will also find some details concerning experimental difficulties inherent to experiments on TMDC.

2.3 Microscope setup

2.3.1 Confocal microscope principle

The idea of a confocal microscopy was invented by Marvin Minsky 1953 and patented 1957 [42]. Brakenhoff and co. [43] and Wilson with Shepphard [44] developed the principle further adapted to applications. Confocal microscopy is an optical imaging technique used to increase optical resolution and contrast of a micrograph by using point illumination and a spatial pinhole to reject light coming from an out-of-focus plane in specimens, the name "confocal" stems from this configuration. In micro-photoluminescence spectroscopy the aim of confocal microscope is to only collect in-focus luminescence to increase the spatial selectivity of the setup.

For the Atto700 setup, we didn't use a pinhole to reject the out-of-plane PL; it was not necessary for the required spatial selectivity of our experiments and as the detection path is long, light emitted out of the focal plane (which is not perfectly collimated) is lost before entering our detection setup.

For the Atto1000 setup, we need to use optical fibers to connect the setup to its excitation source and to its detection setup (because of the system configuration, we cannot use an optical table so the whole microscope is built using Thorlabs cage system). Therefore, the fiber core in which we focalize the output PL (about 5μm) acts as a pinhole and we have exactly the configuration described in figure 6 with a single point source (excitation fiber core) and a pinhole (detection fiber core).

The Atto700 setup is presented in figure 7(an overview of the setup including the cryostat and the spectrometer is presented in figure 16). All the optical paths (excitation, detection and imaging) go through the same optical objective (not represented here, see also fig. 16): our system is confocal, excitation and detection address the same focal plane.

- the imaging path starts from the imaging light source, a bright red LED (635nm). The light is collimated, then reflected by a first 50/50 beamsplitter and sent to another beamsplitter on the top of the microscope to overlap the other light paths. This second beamsplitter in mounted on a flip mount adapter in order to be easily removed during experiments (no influence on the signal level or on the polarization analysis). The incoming light is then focussed onto the sample; we managed

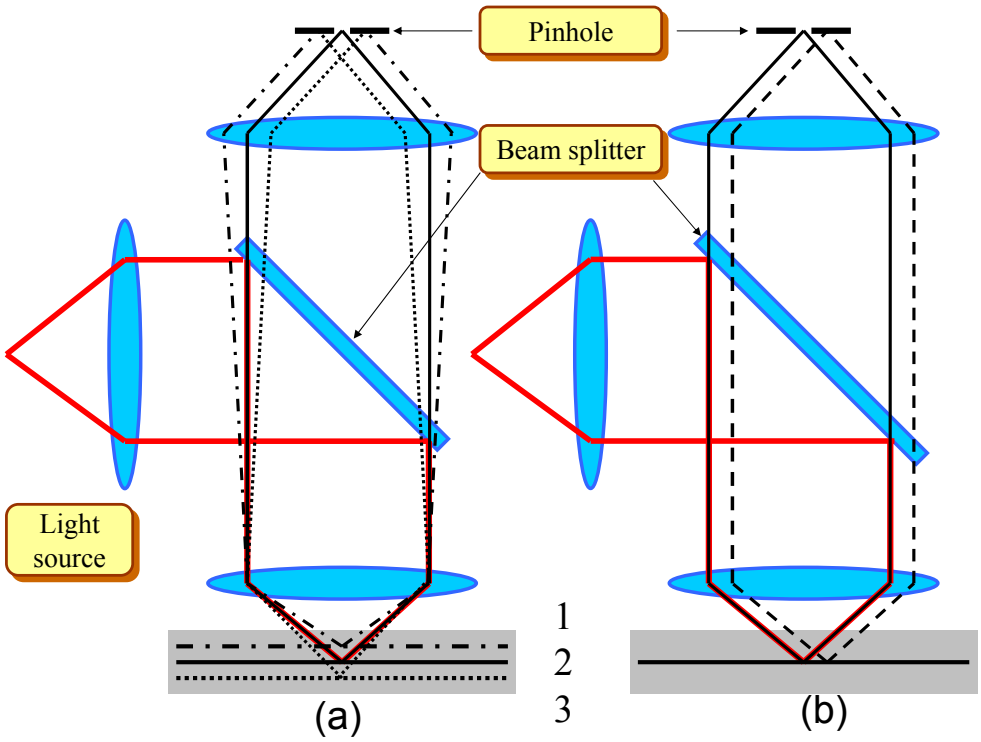

Figure 6: Principle of the confocal microscopy adapted to micro-photoluminescence spectroscopy. (a) Because of the pinhole filtering, only the PL emitted in the focal plane can be transmitted, which increases considerably the vertical spatial selectivity of our measurement. The luminescences from plane 1 and 3 are not focused onto the pinhole plane and are not detected. (b) the overlap between detection and excitation path needs to be as perfect as possible; on one hand the PL will be emitted only from the illuminated area, on the other hand only the PL emitted from the position corresponding to the image of the pinhole through the system will be collected.

to slightly degrade the collimation in order to have a rather homogeneous illumination. Then the same setup guides the reflected light from the sample to the first beamsplitter, which is that time crossed, and finally to the imaging camera, allowing us to observe the sample.

- the excitation path starts from the laser source. The linearly polarized light crosses first the half wave plate and the Glan-Taylor linear polarizer. The use of the half wave plate is to align the polarization of the incoming light with respect to the polarizer axis (depending on this alignment, the transmitted power will change, as the polarizer will only allow the component of light polarized along its polarization axis to go through). The Glan-Taylor polarization axis is aligned with respect to the s axis of the glass plate used as a beamsplitter. This allows us both to maximize the excitation power and to avoid the polarization degradation (this point will be developed in section 2.3.3). The reflected beam cross a quater waveplate oriented at $\pi/4$ from the glass plate s and p axis. The circularly polarized light is send to the sample, crossing the cryostat windows and then focalized on the sample by the objective.

- the generated PL is then collected by the same objective and collimated. The beam crosses the quater wave-plate and the two glass plates, both oriented $\pi/4$ from the

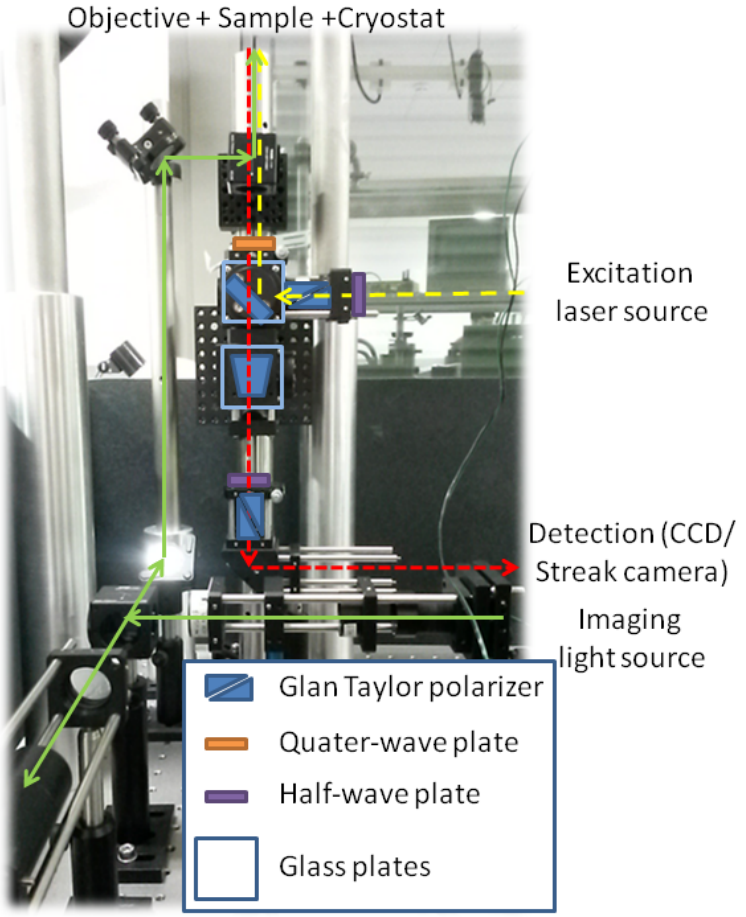

Figure 7: Atto700 experimental setup (see also fig. 16). One can identify all the optical elements used, as well as the different light paths. The yellow large-dotted arrows represent the excitation path, the red thin-dotted arrows represent the detection path that is sent into one of our detection setup. Finally, the green path represents the imaging path, coming from the lighting diode, going to the sample and then coming back to the imaging camera.

incidence axis and rotated of $\pi/2$ one respectively to the other. That way, axis s and p are inverted from one plate to the other and their effects on the polarization compensate each other (see section 2.3.3). The PL cross then a half wave-plate and a Glan-Taylor linear polarizer, allowing to analyze its polarisation; indeed the transmitted intensity is proportional to the orientation of the incident light polarization with respect to the polarizer axis that can be rotated using the half wave-plate. Therefore the combination of the quater wave-plate, the half wave-plate and the linear polarizer allows a complete analysis of the PL polarization based on the variation of the transmitted intensity with the wave-plates respective orientation. Finally the transmitted PL is send in a detection setup; either a high resolution spectrometer coupled to a highly sensitive Si-CCD camera or spectrometer coupled to a S20 streak camera allowing time resolved measurement in addition to the intensity and spectral resolution 2.5.

As can be seen in figure 8, the Atto1000 setup is very similar in terms of elements used except for the imaging system which is only composed by a camera. The only difference is that the detection and excitation light path are connected to optical fibers instead of free beams. The optomechanic elements are adapted to the cage system, as the cryostat configuration gives us no possible access to optical table (see section 2.4.2).

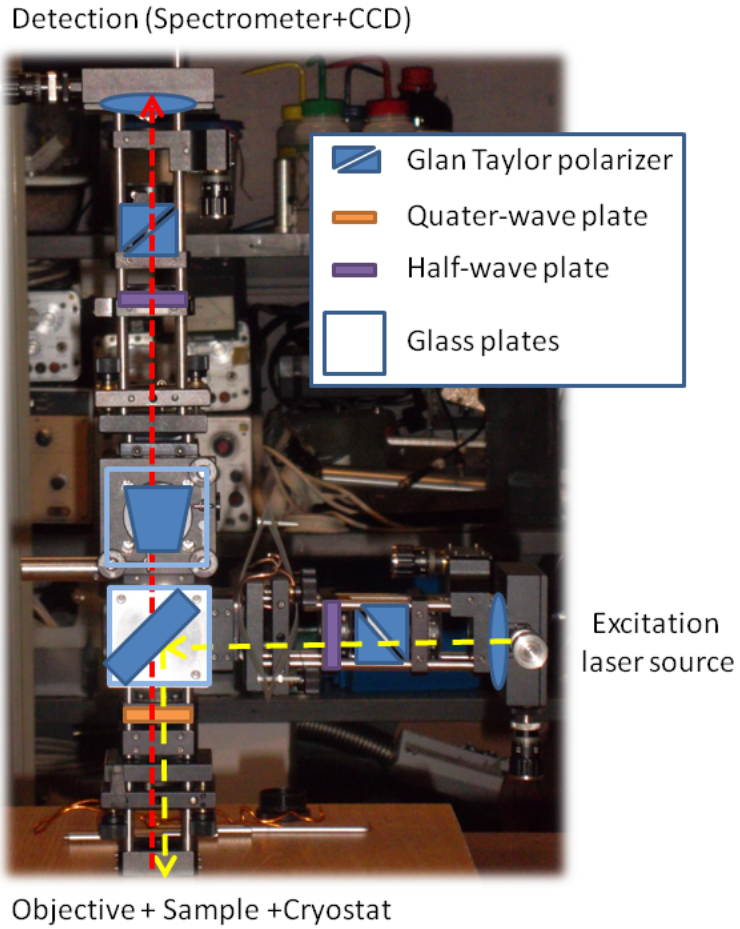

Figure 8: Atto1000 experimental setup. One can identify all the optical elements used, as well as the different light paths. The yellow large-dotted arrows represent the excitation path, the red thin-dotted arrows represent the detection path that is sent into one of our detection setup. The imaging camera, not visible here, is fixed to the above cube, capturing the light reflected on the sample.

2.3.2 Spatial resolution

Spatial resolution is crucial for micro-photoluminescence measurements. As can be seen in figure 5, the monolayers flakes studied are only a few µm large, which motivates the use of such setup. In addition, such high spatial selectivity allows us to probe the spatial homogeneity of our samples (see chapter 3). The spatial resolution was especially challenging for quantum dot experiments performed with these set-ups. This part of my activity is out of the scope of this manuscript [38–41].

Our overall spatial resolution is given by the size of our detection spot and by our positioning precision in the 3 spatial directions. This is achieved using piezo-positionners provided by Attocube that allow to move with a 10nm precision with a coarse range of 5mm, even at 4K and in strong magnetic fields. So our positioning is so precise compare to the size of our spot (at least some hundreds of nm) that we can consider only the spot size for our spatial resolution limit.

The spatial resolution depends basically on the objective numerical aperture. The first objective we used was a single aspheric lens, provided by attocube with the cryostats. Such objective with a high NA and a comfortable working distance ($\approx$1.5 mm) is extremely convenient for quantum dot experiments. Because TMDCs spectral widths are very large

(several tens of meV, compared to μeV for quantum dots), we soon realized that the chromatic aberration affects our measurements (see figure 10) and we bought an achromatic, multi-element objective suitable for low temperature measurements. This objective is the most widely used for the work presented in this thesis and will be referred as Partec objective based on the supplier's name. The single lens was only used for magneto-spectroscopy measurements because of the high magnetic field compatibility.

Based on previous research work done using confocal microscopes [45] we will use the well known Rayleigh criteria as a convenient way to estimate theoretically our lateral resolution Δ_x.

$$\Delta_x = \frac{0.61 \times \lambda}{\mathrm{NA}_{Objective}}$$

Using a He-Ne laser with λ = 633nm, we obtain for Δ_x the values summarized in table 2.1.

Objective	Attocube	Partec
NA	0.65	0.82
Calculated lateral resolution Δ_x	590	470
Measured spatial selectivity (beam FWHM, in nm)	820±80	715±70

Table 2.1: Lateral resolution estimation, based on the Rayleigh criteria, for each objective

The Rayleigh criterion gives us the spatial resolution as closer points cannot be distinguished because of the recovery of a diffraction patern. In our specific system, the spatial resolution is also related to the smallest spot we will be able to excite and detect during PL experiments. We measured this specification of our system experimentally and refer to it as the spatial selectivity of our microscope; placing a grating made of aluminum reflective stripes with a 5μm period in the setup instead of the sample, we moved the attocube piezo positionners step by step and recorded the intensity. Knowing the grating spatial period and steps being almost constant, it is easy to deduce the distance and to obtain the figure 9a.

By calculating the first derivative of the intensity as a function of the distance and by fitting the obtained curve using a Gaussian (see figure 9b), we obtain the FWHM of the beam, that give us another a lateral spatial selectivity of 715±70nm with the Partec objective (the measurements have been performed using a He-Ne laser source at 633nm).

For the Attocube objective measurement, one can notice a less sharp slope and less square shape showing that the spatial selectivity is slightly lower than for the Partec. Unfortunately, the curve of the first derivative for this objective is more noisy and smoothing the curve affects a lot the results, making it difficult to extract a precise value. For that reason, we model the convolution of a step function (which stem for the grating) with a Gaussian (which stem from the light beam) and fit our data using this model. We find a lateral spatial resolution of 820±80nm. The same technique for the Partec gave similar results as previously estimated.

Note that the beam FWHM is related to the $\frac{1}{e^2}$ width (equal to the distance between the two points on the marginal distribution that are $1/e^2$ times the maximum value) by a factor ≈1.699, which implies that 95% of the incident power is focused on a 1.2μm diameter spot.

As mentioned above, the chromatic aberration is important in the case of the single lens, Attocube objective (see. figure 10a. Despite its impressive effects on the spectral

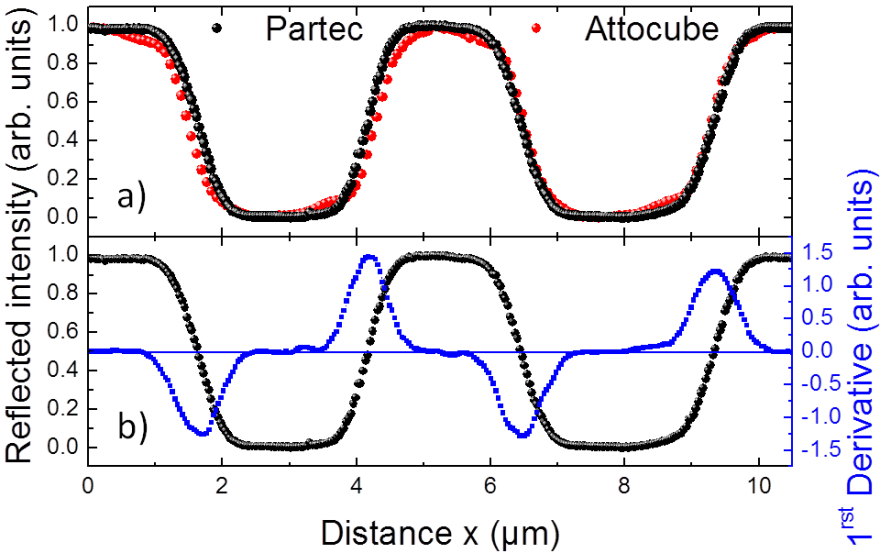

Figure 9: **Spatial selectivity measurements** performed using an HeNe laser source (633nm) (a) Evolution of the intensity reflected by the grating vs the distance traveled. The black curve is the one obtained for the Partec objective and the red correspond to Attocube objective. (b) The black curve is the same as a., Intensity(Distance) for Partec objective, the blue curve is the first derivative of the black curve that gives access to the FWHM of the incident beam

shape, it doesn't really affect measurements like polarization or relative energy shift because they implies to calculate a difference between a σ+ and a σ- measurement. If the photon collection vs wavelength changes with the z position, for the same z position this collection efficiency remain the same for σ+ or σ- and thus, the measured value is correct and will be the same for different z positions. The problem is to find a reference for the overall shape to compare the relative intensity for the different peaks, which is a necessary requirement to monitor the temperature dependance. Achromaticity is even more importantly for PLE measurement, because the focal plane has to remain the same for different excitation wavelength. Using a non-achromatic objective is impossible here because the emitted PL intensity would be modulated by focalization accuracy that will change from one wavelength to the other.

The use of the Partec objective for those experiments solves the problem. As one can see on the figure 10b, we do not notice any chromatic aberration. If the z position changes the intensity of the collected signal, its shape remains the same. Suppressing chromatic aberration allows us to compare different samples, their shape evolution and to perform accurate PLE experiments (see section 5).

On the other hand, polarization and relative energy shift measurements can be safely performed using the Attocube objective, which was done for magneto-PL measurements. In addition, for the different measurements performed, we used the same signal optimization procedure which allowed us to keep practically the same shape (corresponding to the blue curve in figure 10a).

Finally we have a submicronic spatial resolution, measured at 715±70nm for our commonly used setup (all measurement except magneto-PL measurements). Thanks to our achromatic objective, we eliminate chromatic aberrations which allows us to compare the PL shape from sample to sample, their evolution with temperature and to perform accurate PLE experiments.

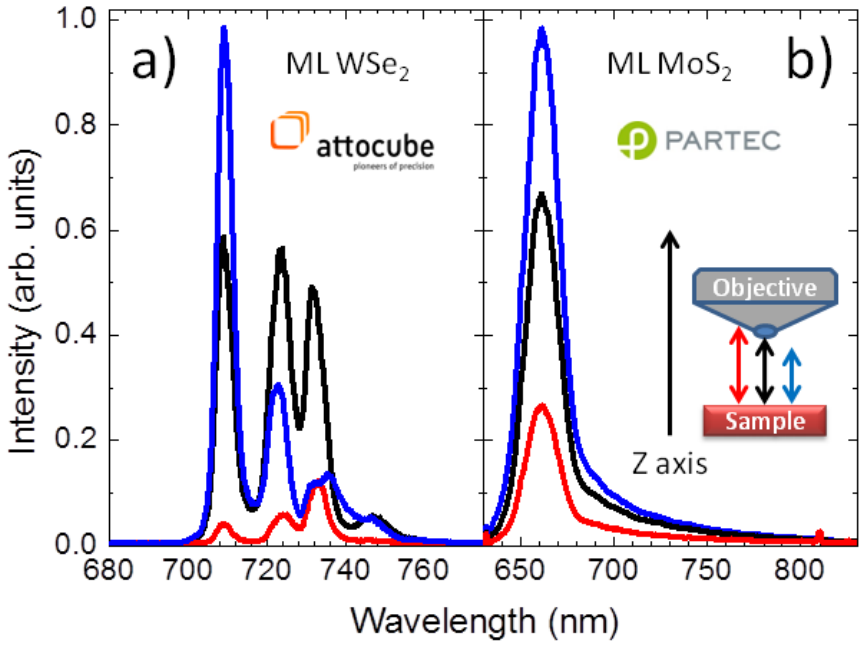

Figure 10: (a)Chromatic aberration effect on WSe_2 ML spectra with single lens objective. Depending on the optimized wavelength the PL shape changes. Note that it is relatively easy to always optimize the same peak and keep the same shape during experiments. (b)Chromatic aberration effect on MoS_2 ML spectra with achromatic objective. Here only the signal intensity changes. The material observed here is MoS2, highly subject to chromatic aberration because of its large spectral width (as for the WSe_2 ML, the relative intensity between high and low energy changes a lot with z when using the single lens objective) .

2.3.3 Polarization resolution

Polarization control and measurement is of key interest for the study of TMDCs ML materials. Indeed, the optical selection rules (detailed in section 1.3) implies that by controlling the polarization and the energy of an incident photon, it is possible to decide in which valley of the k space its absorption will create a conduction band electron. This is similar to the control of spin orientation in GaAs quantum dots [46] but here, in addition to the spin orientation, we have access to the carrier k-valley index. Symmetrically, when a photon is emitted, the analysis of its polarization and energy gives access to the spin orientation and k-valley index of the recombined conduction electron. The circular polarization degree is defined as follow:

$$P_{circular} = \frac{I_{\sigma^+} - I_{\sigma^-}}{I_{\sigma^+} + I_{\sigma^-}}$$

With I_{σ^+} (resp. I_{σ^-} the intensity of the positive (resp. negative) circularly polarized component.

Similarly we define the linear polarization degree as follow:

$$P_{linear} = \frac{I_X - I_Y}{I_X + I_Y}$$

With I_X (resp. I_Y) the intensity of the linearly polarized component along the X axis (resp. Y).

For that reason, we need to reach a high degree of control of the polarization in our setup. The first difficulty we met is the confocality: because out detection and excitation

path need to overlap each other, we need a beamsplitter somewhere. This beamsplitter will reflect or transmit differently the incoming light polarization component oriented perpendicularly or parallel to the reflexion plane (respectively s or p component). This will, for instance, make elliptical a circularly polarized incoming light or rotate a linearly polarized light, degrading both our excitation and detection polarization.

An elegant solution to that problem consists in compensating this effect by using another beamsplitter, rotated by $\pi/2$ around the light propagation axis so the s and p incidences are inverted between the two beamsplitters (see also figure 11a to d). Indeed, if the two beamsplitters are perfectly identical, tilted with exactly the same angle with respect to the incoming light ($\pi/4$ in our case) their s and p reflexion coefficients are the same. If we orient them in order to reflect the incoming light into perpendicular directions, as the incoming light polarization remain the same, the axis perpendicular to the reflexion plane (s) for the first beamsplitter will be the axis parallel to reflexion plane for the other (p). So the transmitted light will be attenuated by a factor $R_s * R_p$ but its polarization will be unchanged. This works well, as can be seen in figure 11e and f: we obtain almost perfect polarization compensation.

For the excitation, in order to maximize the power, we decided to use only one reflexion (no possible compensation then), but we align the Glan-Taylor axis with respect to the s axis of the glass plate. This way, the incoming linear polarization is not affected by the p axis and the light is simply attenuated, its polarization doesn't change (otherwise it would have rotated). We simply align our quarter wave-plate $\pi/4$ from this direction to create a circular polarization.

Note that we oriented coherently the detection basis. The axis of the detection Glan-Taylor polarizer is parallel or perpendicular (we change from one to the other by rotating the detection half wave-plate of $\pi/4$) to this same direction given by the s axis of the glass plate.

The values presented in figure 11 represent the limit of our polarisation resolution. Taking into account the repeatability of the wave plate positioning, the small retardance changes vs the emission wavelength (TMDC spectra are broad and the wave plate retardance varies slightly with the wavelength), the error due to the fit used for data treatment and the fact that we repeat the error twice because each operation is done for σ+ and σ- (respectively X and Y) to calculate the polarization, we can in the worst cases estimate an overall error for our polarization measurements of ± 2% , which is already enough for the measurements presented in this thesis.

Note that to maximize the collected signal, we decided to use thick glass plates as a beamsplitter. In addition to avoid interferences issue, it also has the advantage to be highly similar from one piece to the other and when they are coated together, when can obtain two identical components, which is important for polarization compensation.

For the measurement using the Atto1000 setup, we use liquid crystal retarders (LCR) to measure the polarization. An LCR acts as a tunable waveplate with retardation $\Delta\lambda = 0 - 3/4\lambda$ (or even $0 - 5/4\lambda$ depending on the LCR). A standard LCR consists of a cavity filled with liquid crystals. The electric field generated by the applied bias align the LC molecules and acts on the wave propagation through the LCR medium as a wave retarder. The molecules modify the retardation light propagation with polarization along the principal axis of component.

The main advantage is that using a National Instrument standard DAQ PCI card, it was

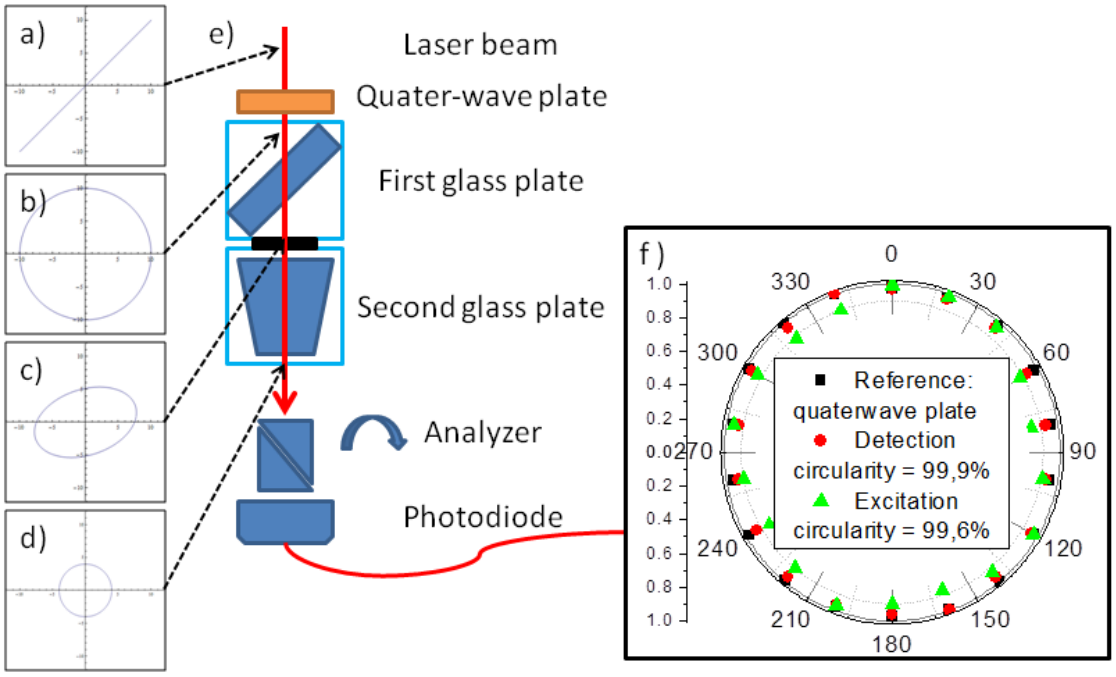

Figure 11: (a-d) Theoretical contour plots showing the light polarization at different locations in our microscope. The influence of s and p transmission have been exaggerated in order to produce a more visible effect. (e) Scheme of our calibration setup. The quarter waveplate is oriented at $\pi/4$ with respect to in linear polarization of the incoming light. The two glass plate are rotated by $\pi/2$ with respect to each other so the s and p axis are inverted. (f) Experimental contour plot of the circularly polarized light after crossing our setup. The black curve corresponds to the polarization before crossing the cubes, the red curve corresponds to the polarization of the transmitted light after crossing the two cubes, i.e. the configuration corresponding to the scheme (e), the green curve corresponds the polarization obtained after reflection on the first glass plate (with an incoming light linearly polarized along the plate s axis) and crossing of the quarter wave plate.

possible to change the retardance in order to measure the polarization simply by changing the applied bias to the LCR. This allows to completely computer control the measurements and to increase the overall setup stability by suppressing any mechanical action from the user, such as manually rotating a $\lambda/4$ or $\lambda/2$ waveplate.

Figure 12 summarizes the calibration procedure. Linearly polarized light propagates through the LCR, its polarization axis oriented at $\pi/4$ from the LCR neutral axis. Depending on the applied bias, one component of the light is delayed with respect to the other and the light polarization can become elliptical, circular, then elliptical along the perpendicular, linear perpendicular the initial polarization... Any retardation is possible. Then the light propagates through another linear polarizer which transmits only the polarization component parallel to its axis. The same procedure is repeated after a $\pi/2$ rotation of the analyzer. The recorded transmitted intensity allows to deduce the polarization corresponding to each bias: when the curves crosses, the intensity is the same along two perpendicular and the light polarization is circular (the applied bias correspond to $\lambda/4$ or $3\lambda/4$ dephasing). When one curve reach a minima and the other a maxima, the polarization is linear and oriented along one analyzer axis (the applied bias correspond to $\lambda/2$ or λ dephasing), ect...

Those LCR have been demonstrated to have similar polarization resolution as standard commercial achromatic waveplate [47]. However they show a more important wavelength dependance (they are achromatic only on few tens of meV range), which lead us to

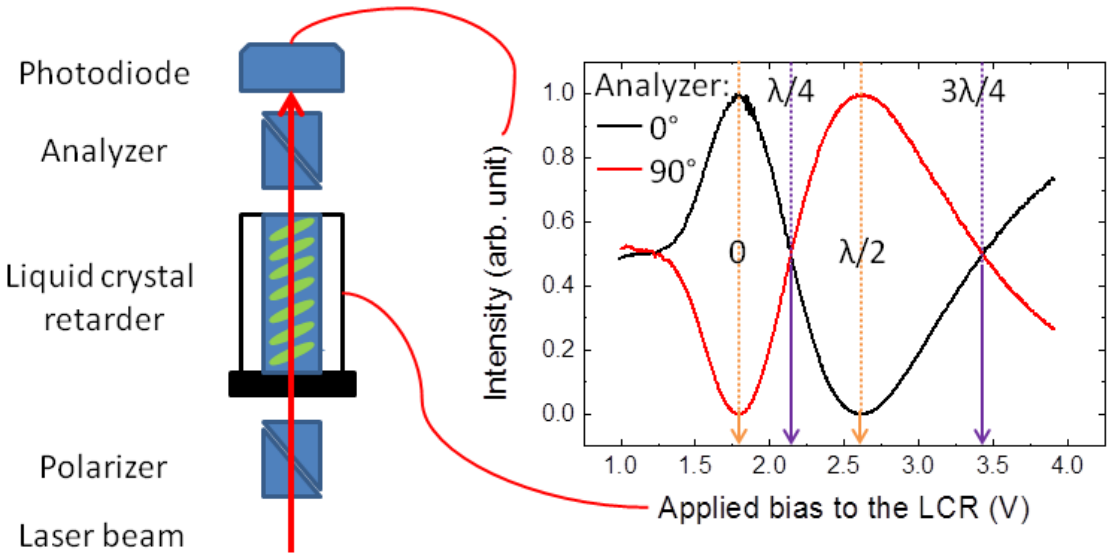

Figure 12: LCR calibration. The scheme represent the calibration setup: the linearly polarized light cross the LCR and is delayed, the polarized light then crossed a Glan-Taylor polarizer and the intensity transmitted in recorded. Then the analyser is rotated of $\pi/2$ and the measurement is repeated. The recorded calibration of transmitted light vs applied bias gives access to the bias corresponding to the desired delay.

calibrate it for the central wavelength of each peak we studied (see section 6). Using the same pessimistic estimate as for achromatic waveplates, we evaluate the overall error of our polarization measurements to be about ± 2%.

2.3.4 Spectral resolution

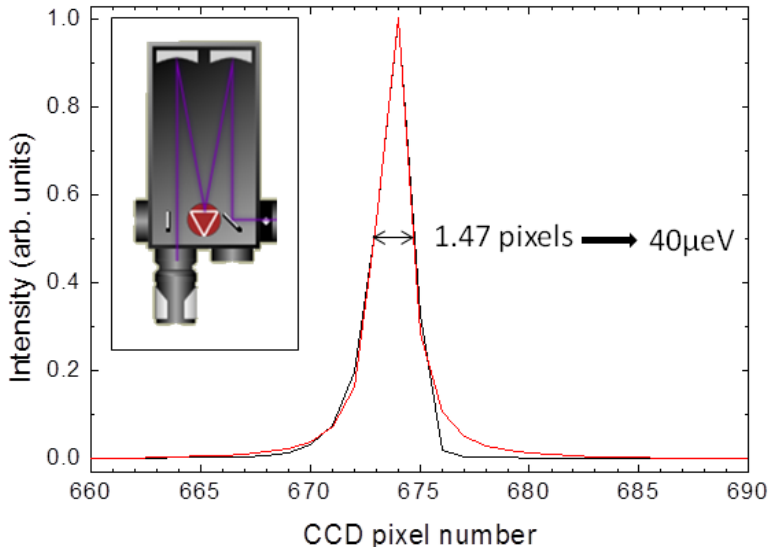

Figure 13: Image of the system response when illuminated with the grating positioned at order 0. This allows us to check that our CCD camera is correctly positioned and that we indeed reach the highest resolution. The value displayed here is calculated using the dispersion of our 1200 lines grating at the second order. (Inset): spectrometer configuration. The resolution limit is directly the image on the CCD of the entrance slit illuminated by a monochromatic light source.

As mentioned above, our setup being originally developed for quantum dots mea-

Grating (lines/mm)	Spectral range (nm)	Dispersion nm/mm	Pixel resolution (@700nm) (μeV)
300	174	6.5	290
600	85	3.2	72
1200	41	1.52	38

Table 2.2: The characteristics of the monochromator Acton SpectraPro 2500i for different gratings.

Grating (lines/mm)	Spectral range (nm)	Dispersion nm/mm	Resolution (nm)
100	170	28.2	0.7
600	28	4.7	0.12
1200	14	2.35	0.06

Table 2.3: The characteristics of the monochromator Horiba iHR320 for its different gratings.

surements (μeV range), the spectral resolution we can achieve is largely sufficient for ML TMDCs, for which the PL is in the tens of meV range. If this originates from intrinsic reasons or is simply due to sample optical quality, even for state of the art samples is still an open question[48].

The spectrometer used consists of a 0.5 m focal length monochromator Acton SpectraPro 2500i with a turret of 3 gratings with respectively 300, 600, 1200 lines/mm and a liquid nitrogen cooled Charge-Coupled Device (CCD) camera (RoperScientific)[49]. The characteristics of the monochromator are given in the Table 2.2. The monochromator includes a direct digital grating scan mechanism with full wavelength scanning capabilities. The gratings are blazed at $\lambda = 0.5$ μm.

Figure 13 shows the spectrometer configuration we used (see inset). The spectra is the calibration spectra, our final resolution being given by the width of the image of the entrance slit by the spectrometer projected on the CCD chip. Here, using the second order of the most resolving grating (1200 lines/mm) this width corresponds to 40 μeV, which is then the smallest energy splitting we can resolve directly, without using a fitting procedure.

We also display here (see table 2.3) the characteristics of the monochromator Horiba iHR320. This spectrometer is used for TRPL measurements coupled to a streak camera (see section 2.5). The table 2.3 presents the spectral resolution of the detection setup when performing TRPL measurements (section 4).

The CCD-camera used, specifically designed for spectroscopy applications, consists of a rectangular photo-active region (an epitaxial layer of silicon) with 100 x 1340 pixels with size: 20 x 20 μm. The capacitors are based on the photoelectric effect where an incident photon is converted to an electron-hole pair. The generated electrons are transferred to a neighbor capacitor causing each capacitor to accumulate an electric charge. The whole accumulated electron packet is then transferred to the read-out zone where it is converted into a digital value.

In order to improve the signal-to-noise ratio the CCD-camera is cooled with liquid nitrogen, lowering the dark noise current. Furthermore the camera operates in back illuminated geometry, i.e. in contrary to the common front illuminated systems the light arrives at the back surface of the capacitor so it can strike the photocathode layer without

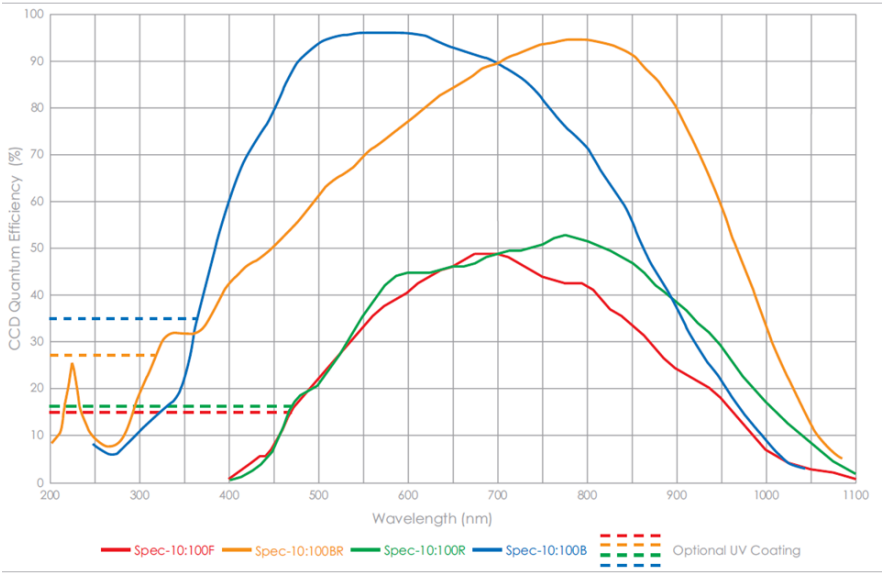

Figure 14: Extracted from Princeton Instrument spec. sheet. The CCD camera we use is the one corresponding to the yellow curve.

passing through the wiring layer, increasing substantially the amount of light captured. This geometry, as well as the deep depletion treatment allow to reach a quantum efficiency as high as 90 % at 700nm (see figure 14). Moreover, it presents the advantage to almost avoid etaloning effects as the thicker photosensitive region offers a greater absorption path, which minimizes the chance for multiple reflections occurring inside the etalon like photosensitive region structure.

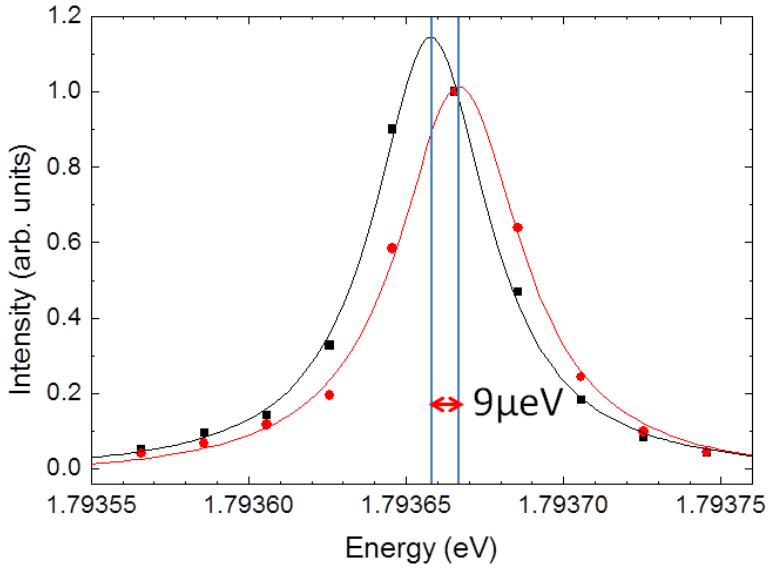

Figure 15: Example of spectra of quantum dots transitions fitted using a Lorenzian curve. Despite the fact the row data do not allows to see a clear splitting, the fit shows it clearly. We proceed TMDCs spectra the same way, even if their much larger width bring us to much less extrem resolution requirement.

Figure 15 shows that for really narrow transitions (few tens of µeV), fitted by Lorentzian curves, the central energy of the transition can be determined extremely precisely. Therefore the smallest energy splitting we can measure is in the µeV range. In the case of TMDCs, the emission peaks are so broad that the fitting procedure tend to lower the spec-

tral resolution; indeed as the shape is not a perfect Gaussian or Lorentzian, it is difficult to find the exact the central position of such broad peak. Nonetheless, we can safely claim an overall spectral precision of ±100μeV, which is clearly enough with respect to the measurements presented in this thesis.

2.4 Helium free cryostat

Despite the fact that some optical properties of TMDCs are studied at room temperature, low temperature measurements are of strong interest to uncover fine details: it allows us to reduce the thermal energy, keeping the carrier energy closer to the minimum of conduction and valence bands, reducing the number of phonons and their interactions with carriers and inhibiting interband transfer between spin up and spin down states in the conduction band (even at room temperature the spin orbit splitting is much larger than thermal energy in the valence band, see section 1.3 in chapter 1). Among other interests: optical transition are narrower, selection rules purer and the reduced number of interactions allows a better understanding of the investigated material intrinsic physical properties.

For those reasons, we use cryostats to carry out measurements at low temperature (typically 4K). Those equipments have to fulfill strict requirements in term of vibration level and stability, including when a strong magnetic field is applied in the case of the AttoDry1000. Since liquid helium supply became highly expensive, we use helium free cryostats, in which the helium is used as a gas and then liquified following standard thermodynamical cycle of compression, cooling and expansion, requiring only cooling water and electricity. The peculiar geometry of each cryostat require an adaptation of the setup, the AttoDry700 being the one used for most experiments presented in this thesis, except for the magneto-PL measurements (chapters 3).

2.4.1 Attodry700

As mentioned above, the Attodry700 setup is the one we used for all our experiments except magneto-PL measurements. Indeed, in addition to fulfill our measurement specifications (see a summary in figure 17), for most types of measurements performed on TMDCs, it has several practical advantages compared to Attodry1000 setup, its use is easier for:

(i) imaging and finding monolayers: as presented to the reader in section 2.1, TMDCs monolayers are identified by optical contrast among thousands of flakes of random size and shape. An inherent difficulty is to be able to find it again once the sample is placed in the closed cryostat and cooled down to 4K. A correct imaging system helps a lot (including mainly a microscope objective and an external light source). The implementation of such system was rather easy for the Attodry700, as all optical elements can be placed on a large and stable optical table. This makes this setup more suitable for TMDCs experiments than the Attodry1000 for which weight and size has to be limited to maximize the setup stability.

(ii) temperature dependent measurements: in the Attodry700, the thermal contact between the heater and the sample is ensured by a copper plate which allows a rapid thermal equilibrium to establish, while the same process through an exchange gas (used in Attodry1000) is much slower.

(iii) time-resolved photoluminescence measurements: measurement setup dedicated to the Attodry1000 requires the use of optical fibers; indeed it plays the role of the pinhole

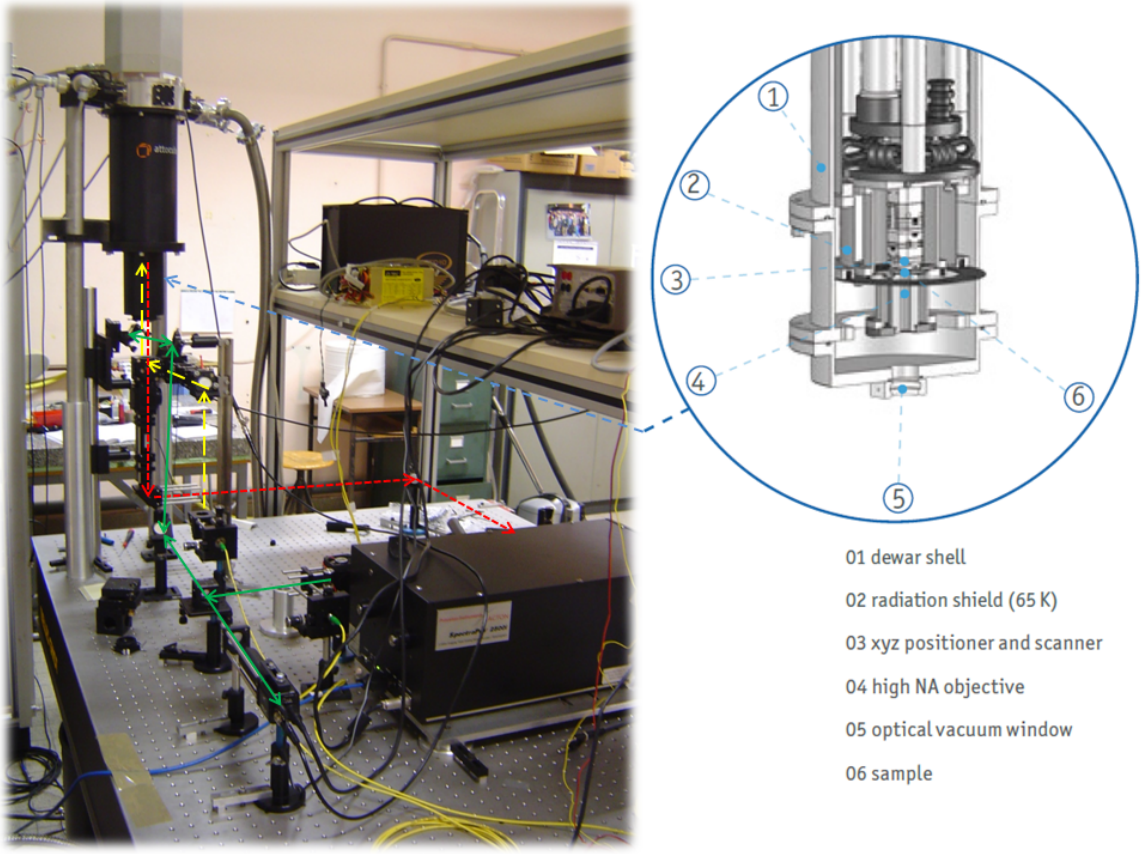

Figure 16: Attodry700 experimental setup. The blue circle provide informations about the inner structure of the cryostat. One can also see the confocal microscope on the optical table. The yellow large-dotted arrows represent the excitation path, the red thin-dotted arrows represent the detection path that can be send either into the high resolution spectrometer (visible on the picture) or in the streak camera (not visible here). Finally, the green path represents the imaging path, coming from the lighting diode, going to the sample and then coming back to the imaging camera.

Gerneral Specifications		
sample environment	cryogenic vacuum, sample cooled via braids	
temperature isolation	vacuum isolation, radiation shielded	
bottom loading system	quick and easy sample exchange (optional: side door incl. window)	
damping	internal anti-vibration damping system	
mounting hole seperation sample space	300 mm x 300 mm (adapters for imperial available) 50 mm (diameter) x 110 mm (height) or 90 mm (diameter) x 170 mm (height)	
Performance Data		
temperature range	2.8 .. 300 K	
cool-down time	< 2 h typically to 4 K (without load) < 4 h (incl. positioners and objective)	
temp. stability (4 .. 70 K)	< ±0.010 K	
nominal cooling power of pulse tube cooler	7 W at 65 K, 250 mW at 4.2 K	
temperature @ sample	4 K	< 7 K
Sample Positioning		
positioners and scanners	coarse positioners ANPxyz101 with piezo scanner ANSxy100 (optional)	
step size	0.05 .. 3 µm @ 300 K, 10 .. 500 nm @ 4 K	
coarse range	5 x 5 x 5 mm³	
scan range	up to 50 x 50 µm² @ 300 K, 30 x 30 µm² @ 4 K	

Figure 17: Summary of Attodry700 performances

in the confocal microscope and it allows to maintain the beam position stable, which is not possible if a free laser beam comes from a distant table due to the cryostat vibrations. The use of optical fibers leads unavoidably to a temporal dispersion of the laser excitation pulse and of the emitted PL. A simple estimation based on suppliers specsheet gives:

$$\mathrm{D}.\Delta\lambda_{Exc}.\mathrm{L} = 300.1.10^{-2} = 3ps$$

for the excitation pulse and

$$\mathrm{D}.\Delta\lambda_{Exc}.\mathrm{L} = 300.25.10^{-2} = 75ps$$

for the emitted PL.

Such reduction of our temporal resolution is not acceptable due to the fast emission time of TMDC MLs (see chapter 4). On the other hand, the use of the Attodry700 allows to send excitation laser as a free beam and send the emitted PL in our streak camera the same way. Therefore Attodry700 setup is the most convenient for time resolved photoluminescence measurements.

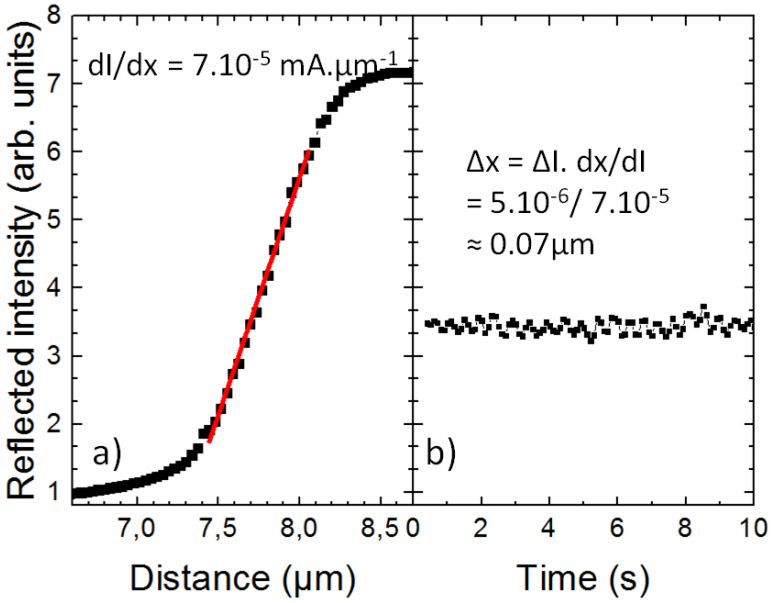

Figure 18: Characterization of Attodry700 mechanical stability. The step slope gives us the relation between amplitude and lateral displacement (same measurement as for fig. 9). We then recorded the amplitude evolution with time, as the full system was running, and the extreme values combined with the slope give us the amplitude of the spatial displacement, about 70nm for our system.

A very high mechanical stability is required for our experiments. The mechanical movements of each cryostat we used is specified below 150nm, which was confirmed experimentally as presented in figure 18. The actual mechanical displacement remains even below 100nm, well below our spot size, and therefore doesn't affect our spatial resolution. The table in figure 17 shows an overview of the other cryostat capabilities.

2.4.2 Attodry1000

The Attodry1000 (see picture 19) provides us the valuable possibility to apply a magnetic field to our sample[50; 51]; among other interests, performing magneto-optics allows to lift spin or angular momentum degeneracies and extract the Landé g-factors, a technique

Figure 19: Picture of Attodry1000 cryostat. The optical head presented above is placed on the top of the insert visible in black here on the picture. The tube being mechanically decoupled of the rest of the setup to reduce vibrations, the cage system fit perfectly our needs to build an optical system that could stick together with the tube without touching anything else, which is not possible using an optical table.

General Specifications	
technology	ultra-low vibration, pulse-tube based closed-cycle cryostat designed for scanning probe microscopy applications
sample environment	helium exchange gas
sample space	49.7 mm diameter probe bore fitting all attocube inserts
sample exchange	top loading system for quick access
Performance Data	
temperature range	4.. 300 K (optional temp. controller required)
cool down time of measurement insert	approx. 2 h (depending on insert)
cool down time of system (system without magnet)	~ 5-10 h
cool down time of system (system incl. 9 T magnet)	~ 10-15 h
temperature stability	< ±10 mK expected (4.. 50 K) < ±25 mK guaranteed (4.. 50 K)
cooling power at sample location	> 5 mW @ 5 K
Pulse Tube Based Pre-Cooler	
nominal cooling power (4.2 K)	> 900 mW
power consumption	max. 9.0 kW, 7.2 kW steady state
cooling	water cooling (requires local infrastructure)
Dimensions	
cryostat (width x depth x height)	1120 x 640 x 1050 mm³
Options	
superconducting magnet	9 T (others & vector magnets available)
Temperature controller	2 channel (magnet + sample temperature)

Figure 20: Summary of Attodry1000 performances

successfully used formerly to study the bandstructure and excitonic effects of semiconductors [28]. Using a Voigt module developed in collaboration with Attocube, we were also able to apply this magnetic field in the sample plane, in the geometry used for Hanle measurements (see section 3.4).

As mentioned above, the geometry we use for the microscope dedicated to the Attodry1000 cryostat makes it difficult to find a monolayer: the image quality is lower and

the visible area is reduced. Also, as the thermal contact with the sample is ensured by an exchange gas, to reach equilibrium can take a long time and as the sample temperature cannot be completely decoupled from the superconducting coils, it is tricky to heat the sample and keep the coil temperature below the critical temperature as it has been done for experiment reported in chapter 3. Finally, we cannot use our achromatic objective, which is not magnetic-compliant, as detailed in the corresponding section 2.3.2. Even if this doesn't affect the measurements we carried out with this system, it makes some other types of experiences difficult (like PLE experiments under magnetic field).

Beside this, the system is extremely convenient and reliable (see figure 20). Being extremely stable, we were able to automatize the measurements, controlling the applied field and the measured polarization. This allows us to extract Landé g-factors with a very high precision, as well as to monitor precisely emitted PL polarization dependances in applied magnetic field (see chapter 6).

2.5 Time resolved photoluminescence setup

To access the time evolution of the photoluminescence is of key interest when studying the optoelectronic properties of a new material. Especially, one can uncover the dynamics of photogenerated carriers, based on optical selection rules associated to each material. This allows to investigate the band structure, to estimate the created exciton binding energy, developing a more precise understanding of physical properties than using simply time integrated measurements.

As the reader will see in the corresponding chapter 4, ps resolution is required to investigate TMDC PL dynamics. We aim to present here our setup, its performance and its intrinsic limitations as well as the working principle of the equipment we use, excitation sources and detectors.

2.5.1 Streak camera

According A. Balocchi et al. authors of ref. [52], a very clear and detailed book on time resolved optical spectroscopy: "'The streak camera is a multichannel device allowing for the simultaneous measurement of the dynamics of light events with picosecond or subpicosecond resolution, as a function of either their wavelength components (if coupled to a spectrometer) or their spatial position (if coupled to an imaging optical system). The fundamental principle is the conversion of a light phenomenon temporal profile into a spatial one. This is achieved in several steps. The light signal is first converted by photoemission into electrons whose emission time is temporally resolved by spatial dispersion, and finally back-converted into photons for optical detection."'

The basic principle of a streak camera can be summarized as follows (Fig. 21): the incoming light (in our case the PL signal) is imaged onto a photocathode where the light is converted into electrons by photoelectric effect. The resulting flux of electrons, an electronic replica of the light pulse, is then focused, accelerated, and sent into a deflection region constituted by two deflection plates. Simultaneously, a very fast sweeping voltage is applied in this region, vertically deflecting the traversing electrons proportionally to their arrival time. A temporal sequence is thus linearly converted into a spatial one, the vertical axis. The electronic flux is then amplified by a micro-channel plate and reaches a phosphorous screen that will emit fluorescence when an electron hit its surface. A CCD capture the intensity vs spatial position to finally provide a three dimension image (see figure 23) allowing to get at the same time:

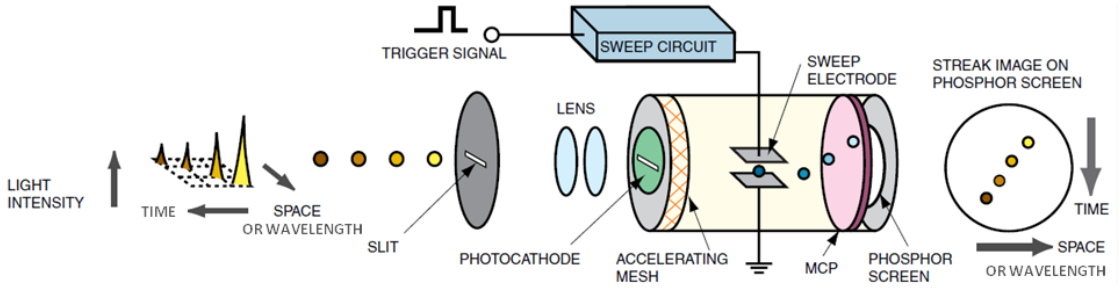

Figure 21: Working principle of streak tube system (Extracted from "'guide to streak cameras"' edited by Hamamatsu).

(i) the intensity of the signal. The intensity of the photo-generated electron flux is proportional to the incoming signal intensity which is therefore directly linked to the intensity of the phosphorous screen.

(ii) a temporal repartition of this intensity. Indeed, the vertical direction is directly related to the arrival time of the incoming photon.

(iii) a spatial or spectral information. Indeed the repartition along the horizontal axis is not affected by the tube. Setting a spectrometer in between the microscope and the streak entrance (as we did), allows to separate the different spectral contributions and therefore the time dependance of the different component of the PL emission.

Reference [52] offers an accurate and detailed overview of the capabilities and intrinsic limitations of this instrument and the reader can refer to it for further developments. We will now focus only on the instrument we used for the measurements.

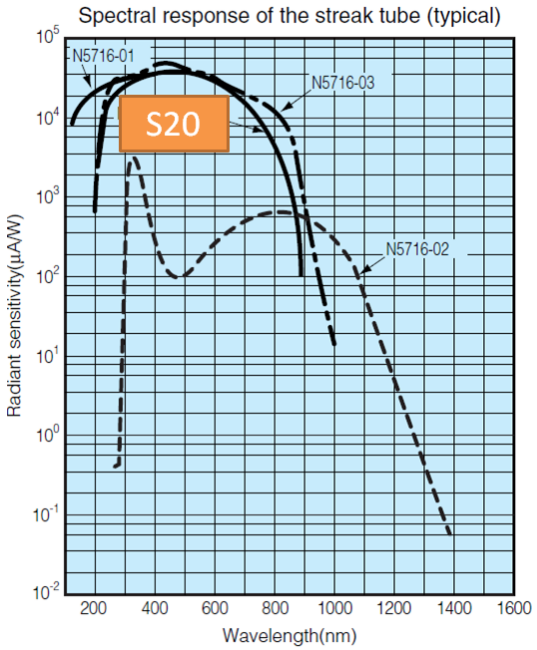

Figure 22: Typical spectral response of the streak tube we use, referred as S20 (spectral range corresponding to the visible range). Hamamatsu (Japan)

As one can see in figure 22, the radiant sensitivity of our S20 streak camera is above 10^4 μA/W for the whole spectral range of TMDCs ML PL.

As we will see in the dedicated section 4, PL emission time of TMDCs are in the ps range. The supplier Hamamatsu specifies a temporal resolution better than 2ps at 800nm for our streak camera. The resolution is defined as the FWHM of an ultrashort incident

Time range number	Temporal range (ps)	Resolution (ps)
1	157	5
2	809	8
3	1542	12
4	2263	17

Table 2.4: Temporal performances of the S20 streak tube[53].

light pulse (similarly to the FWHM of a monochromatic wave gives the spectral resolution of a spectrometer).

The values we measure using a 100 lines/mm grating are presented in table 2.4. However one must keep in mind that this doesn't mean that we cannot measure a pulse shorter than the resolution. Similarly as for spectral resolution, data processing allows to go beyond; for instance in time range 1, a 5ps incident pulse will have a FWHM larger than 5ps due to streak camera response broadening (due to time jitter among others). Using a deconvolution procedure to separate the streak response from the incoming signal allows to extract its emission time (even if the precision is lower). The true limitation is that the measured signal FWHM (so convolution of the pulse duration with the streak's response) must be larger than the resolution.

Another limitation of our TRPL measurements was the precision with which it is possible to synchronize two successive spectra (for instance, one using X linear and one using Y linear detection). This makes our error larger in polarization resolved TRPL. To reduce it, we add a delay line to our setup and we separate a part of the excitation beam that we delayed, attenuated and finally send into the streak camera synchronously with the measured PL signal. That way we add a fixed reference to our successive spectra allowing to increase the temporal resolution of our polarization resolved TRPL measurements. Note that using a double monochromator in substractive mode in order to compensate the temporal dispersion would increase our temporal resolution.

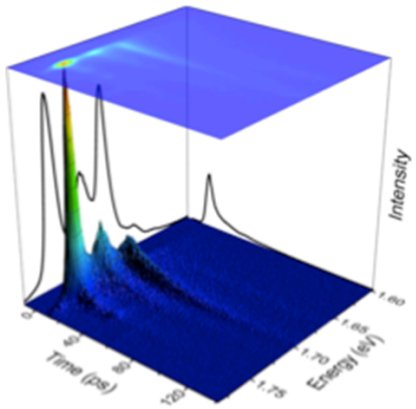

Figure 23: Example of 3D image issued from TRPL measurements. The color scale stems for the intensity, the in-plane dimensions contain both the temporal and spectral information.

2.5.2 Pulsed laser sources

To perform the measurement presented in this thesis, we use several types of laser sources. Continuous (cw) laser sources, like HeNe (632.8nm) or doubled Nd-YAG (512nm) were

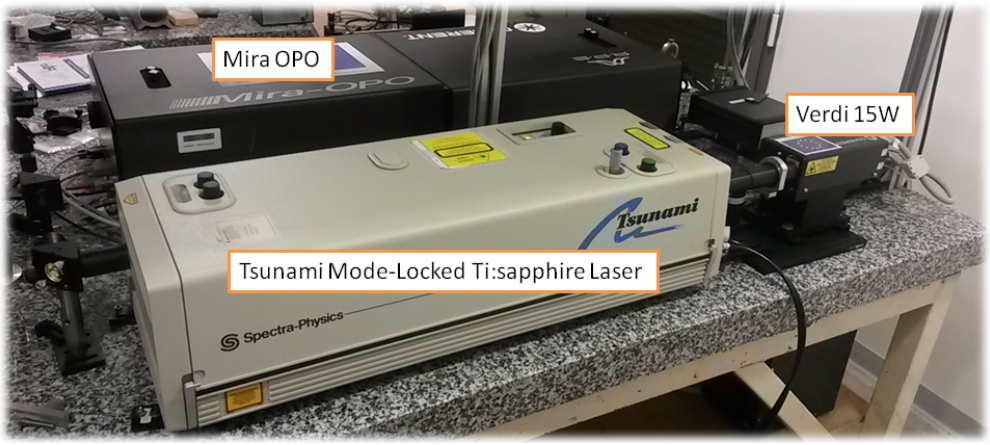

Figure 24: Picture of our picosecond pulsed laser chain.

used for magneto-PL, temperature-dependent PL and some polarization characterization measurements. Things are more complex for TRPL and PLE measurements; because varying the excitation wavelength was a necessity, we used a laser chain composed of a tunable frequency doubled optical parametric oscillator (OPO) synchronously pumped by a mode-locked Ti:Sa laser (see picture figure 24). The first stage of our laser chain is a continuous, high power, doubled Nd-YAG (512nm, 15W) from Spectra Physics. This laser is used to pump a picosecond Tsunami Mode-Locked Ti:sapphire Laser (also from Spectra Physics). Which is set around 800 nm with an output power about 1.5-2 Watts and the output beam is then send into a Mira Fan-PP type OPO (supplied by APE-Coherent). Through optical parametric amplification and intracavity second order harmonic generation, this allows to generate picosecond pulses with typical pulse and spectral width are 1.6 ps and 3 meV respectively; the repetition rate is 80 MHz. This equipment allows us to tune the laser wavelength between 500 and 740 nm (1 to 1.5 µm when not doubled) which allowed us to perform detailed optical spectroscopy on TMDC MLs.

The working principle of those laser sources, pulsed laser sources and OPO will not be discussed here, because it would requires the introduction of numerous concepts. The reader can refer to reference [30] by Rosencher and Vinter. Knowing the output beam characteristics is enough to understand and discuss our experimental results. We will simply provide here the specifications of the picosecond Tsunami Ti:sapphire laser and of the Mira OPO to confirm our setup capabilities (see figures 25, 26, 27 and 28).

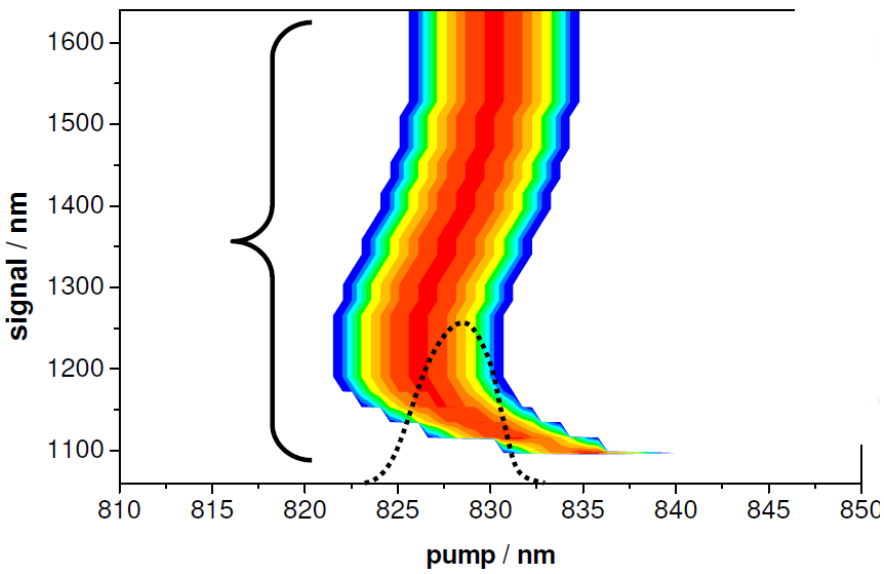

Figure 25: Phase matching of the periodically poled OPO crystal used for optical parametric amplification

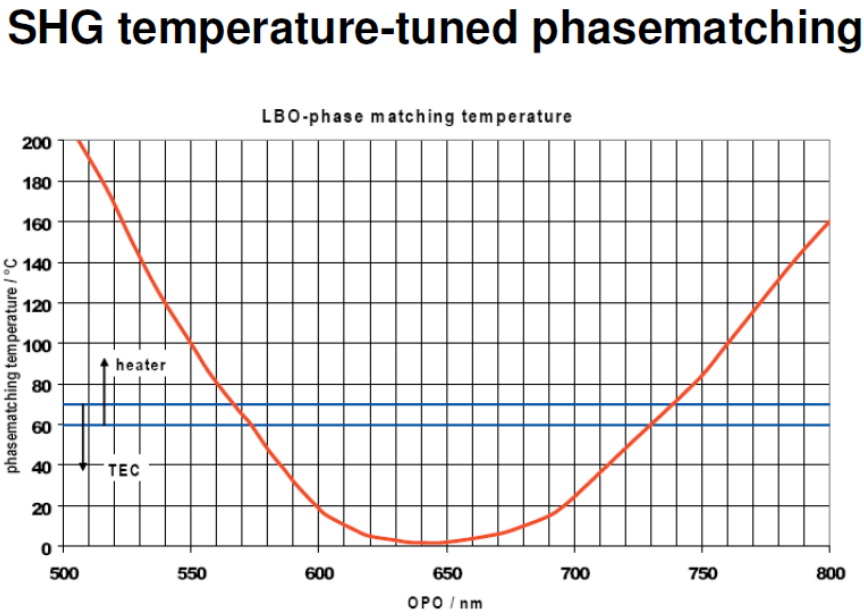

Figure 26: Temperature tuned phase matching of the LBO crystal used for frequency doubling

	710 nm Blue (B)	790 nm Standard (S)	850 nm Mid (M)	900 nm Long (L)
Average Power[2]				
with <10 W TEM_{00} pump	500 mW	1.3 W	1.3 W	700 mW
pulse width[3]	<2 ps	<2 ps	<2 ps	<2 ps
with 5 W TEM_{00} pump	400 mW	1 W	800 mW	500 mW
pulse width[3]	<2 ps	<2 ps	<2 ps	<2 ps
Long Pulse Average Power[2]				
with <10 W TEM_{00} pump	500 mW	1.3 W	1.3 mW	700 mW
pulse width[3,4]	30/60 ps	30/60 ps	30/60 ps	30/60 ps
with 5 W TEM_{00} pump	400 mW	1 W	800 mW	500 mW
pulse width[3,4]	30/60 ps	30/60 ps	30/60 ps	30/60 ps
Tuning Range (nm)				
with <10 W TEM_{00} pump	690–800	720–850	780–900	840–1000
with 5 W TEM_{00} pump	690–800	720–850	780–900	840–1000
Repetition Rate (nominal)[5]	80 MHz			
Noise[6]	<0.5%			
Stability	<5%			
Spatial Mode	TEM_{00}			
Beam Diameter at 1/e2 points	<2 mm			
Beam Divergence, full angle	<.06 mrad			
Polarization	>500:1 vertical			

Figure 27: Specification of our picosecond Tsunami Ti:sapphire

Bulk Crystal Mira-OPO	**KTP**		**CTA**
Model	VIS-1[1]	IR-1	IR-3
Cavity Configuration	Ring cavity with intracavity SHG	Linear cavity	Linear cavity
Tuning Range[2] (high power)(nm)			
Signal SHG	525 to 660	-	-
Signal	1050 to 1320	1050 to 1320	1350 to 1600 (1400 to 1700 option available)
Idler (option)	2200 to 3000	2200 to 3000	1600 to 1900 (1700 to 2100 option available)[7]
Tuning Range[3] (low power)(nm)			
Signal SHG	530 to 605	-	-
Signal	1060 to 1210	1060 to 1210	1350 to 1600 (1400 to 1700 option available)
Idler (option)	2300 to 2850	2300 to 2850	1600 to 1830 (1700 to 1830 option available)[7]
Average Power (mW)			
Verdi V18 pumped Mira HP-F	>750 at 580 nm	>750 at 1160 nm	>750 at 1550 nm
Verdi V10 pumped Mira-900F	>200 at 580 nm	>240 at 1160 nm	>200 at 1550 nm
Verdi V5 pumped Mira-900F	>60 at 580 nm	>80 at 1160 nm	>60 at 1550 nm
Pulse Width[4]			
fs version (typical)	250 fs for 130 fs pump pulse		200 fs for 130 fs pump pulse
ps version (typical)	1.6 ps for 1.4 ps pump pulse		1.6 ps for 1.4 ps pump pulse
Time-Bandwidth Product all versions (typical)	0.6		
Repetition-Rate (nominal)(MHz)	76 (other rep. rates up to 90MHz available on request)		
Pump Threshold (mW)	<500		
Noise[5,6] (%)	<0.5		
Spatial Mode	TEM_{00}		
Typical Beam Diameter (1/e²)(mm)	1.25		
Typical Beam Divergence (full-angle)(mrad)	1.3		
Polarization	Horizontal for IR signal (>100:1) Vertical for Idler (>100:1) Vertical for VIS (>100:1)		

Figure 28: Specification of our picosecond Mira OPO

2.6 Conclusion

In the first part of this chapter, we presented the samples we used in the experiments reported in this thesis. A set of characterization experiments is given for each of them and the reader will find here all the necessary information required for the detailed optical spectroscopy results presented throughout this thesis.

We then presented our experimental setups : the Atto700 used for most of our experiments and the Atto1000 used for magneto-PL experiments. Both present excellent stability in terms of temperature and of mechanical displacements. In addition, both systems demonstrate high performances in terms of spatial selectivity, polarization resolution and spectral resolution. The system Atto700 is somehow more suitable for certain types of experiments like temperature dependance or PLE and is therefore used for experiment at zero magnetic field.

Finally we presented our TRPL measurement setup, including the S20 Hamamatsu Streak camera and pulsed laser chain composed of a 15W VERDI pump laser, a pulsed Tsunami Ti:Sa that is also used to pump a frequency doubled OPO, the whole chain allowing us to generate pico-second pulses with a frequency rate of 82MHz for a large wavelength range (500 to 1500 nm).

In the next chapter, we will describe our optical spectroscopy results on ML TMDCs, starting with time integrated measurements on MoS_2 MLs.

Chapter 3

Optical spectroscopy of MoS_2 monolayers: selective valley excitation

In MoS_2 monolayers the circular polarization (σ^+ or σ^-) of the absorbed or emitted photon can be directly associated with selective interband carrier excitation in one of the two non-equivalent K valleys (K_+ or K_-, respectively), as demonstrated in chapter 1 (see details in section 1.3).

This chiral optical valley selectivity has been theoretically predicted [11; 18; 54] with encouraging experimental results, obtained simultaneously in Columbia university, Hong-Kong, Beijing and in our group in Toulouse, reporting indeed strong polarization of the photoluminescence (PL) emission in ML MoS_2 [18; 50; 55; 56].

Several original experimental schemes were proposed to use a stable valley index in analogy to the electron charge or spin as an information carrier in AlAs [57] and graphene samples with deliberately broken inversion symmetry [50; 58–60]. The simple valley initialization via polarized laser excitation makes ML MoS_2 an extremely promising system for valleytronics.

In this chapter, using mainly photoluminescence spectroscopy, we investigate the robustness of the optically created valley polarization under different experimental conditions, such as strong transverse magnetic fields, broad temperature range (from 4K to 300K) and varying excitation laser power.

This characterization is of key importance for a potential applications of this new material.

3.1 Effect of the temperature on carriers valley index in MoS_2 monolayers

Experiments reported in this section were carried out on mechanically exfoliated sample provided by SPI supply (see part 2.1.1 for more details). We used the experimental setup described in section 2.4.1 for the PL measurements. The design of the microscope has been specifically adapted for those experiments, as presented in section 2.3, to be able to tune the laser excitation power over several orders of magnitude.

Please note also that all discussions are devoted to the high energy peak ***A*** observed from 4 K (centered at ≈ 1.9 eV) to room temperature which is attributed to the exciton emission, expected to obey the selection rules presented in section 1.3 and represented in figure 2. Please refer to section 2.1 for more information concerning the PL emission spectra and peaks identification.

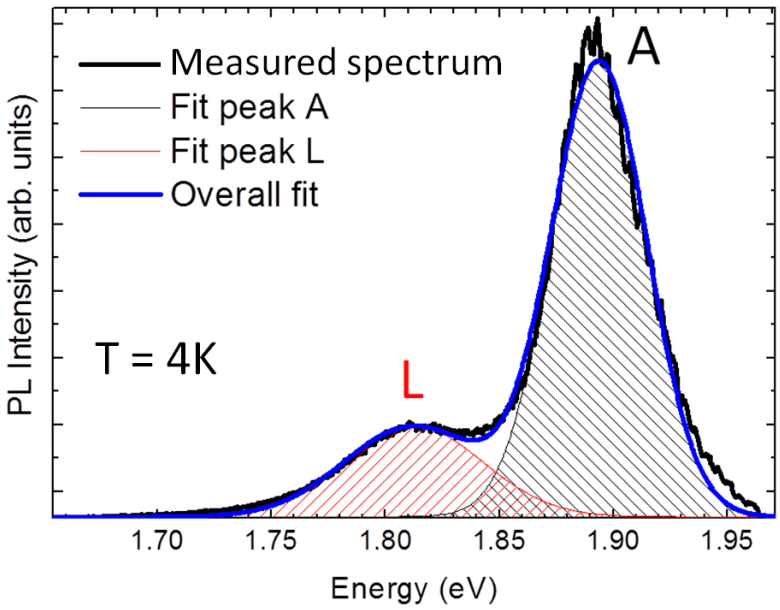

Figure 1: Typical PL emission spectra of an MoS_2 monolayer. Respective intensities of peaks A (exciton) and L (localized states) are extracted by fitting two Gaussians (red and black curves respectively).

Indeed, the low energy peak ***L*** centered at 4K close to 1.8 eV, which is only detectable for T < 175 K is most likely linked to localized exciton states [61]. The emission intensity of peak ***L*** has been found to depend, among other factors, on the substrate material used, SiO_2 or BN [55], and can be strongly reduced through oxide coverage [62].
We access separately the polarization properties of the two dominant peaks ***A*** and ***L*** of the PL emission by fitting two Gaussians as shown in Fig.1.

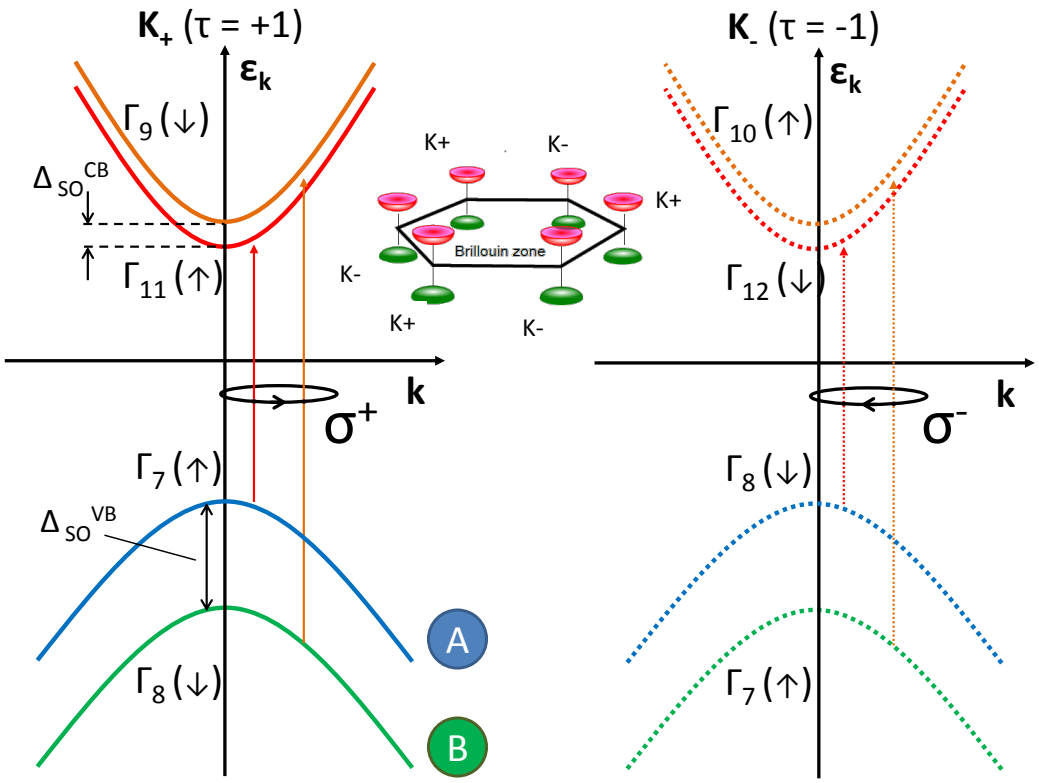

Figure 2: **Schematic illustration of MoS_2 band structure.** The bands are labeled by the corresponding irreducible representations with arrows in parentheses demonstrating electron spin orientation. Solid and dashed arrows show the transitions active at the normal incidence in σ^+ and σ^- polarization, respectively. An inset sketches the Brillouin zone. The order of conduction band states is shown in accordance with Ref. [22]. The spin-orbit splitting of the order of $\Delta_{SO}^{VB} = 150$meV is indicated.

Because of the original selection rules of this material (figure 2), by investigating the PL circular polarization degree, we are able to monitor if the optically created carriers change valley in k-space. Our approach is to trace the change of valley index experimentally via the photon emission, that would have the opposite polarization compared to the excitation laser.
Our first target was to see what occurs when the temperature increases, if optically generated carriers can change valley through scattering with phonons of suitable wavevector for example. Changing valley requires in addition a change in spin state and orbital angular momentum. Therefore a change in valence carrier spin state and hence valley in k-space will be far less likely in a MoS_2 ML than the common spin flip mechanisms evoked in well studied semiconductors like GaAs [63] for instance.

Following excitation with a circularly σ^+ polarized HeNe laser we observe at T = 4 K strongly circularly σ^+ PL polarized emission. Here the polarization of the exciton peak ***A*** is 87%, see Fig.3d, close to the theoretically predicted 100% for the direct transition.

When raising the temperature no measurable change occurs for the ***A*** line polarization up to about T = 50 K, beyond this temperature a steady decrease of the emitted polarization is observed. At room temperature, a substantial polarization of 40% remains, as demonstrated in Fig.3a, indicating that selective optical k-valley excitation with a polarized laser is still possible.
Those values have to be considered with caution; although the trend remains the same,

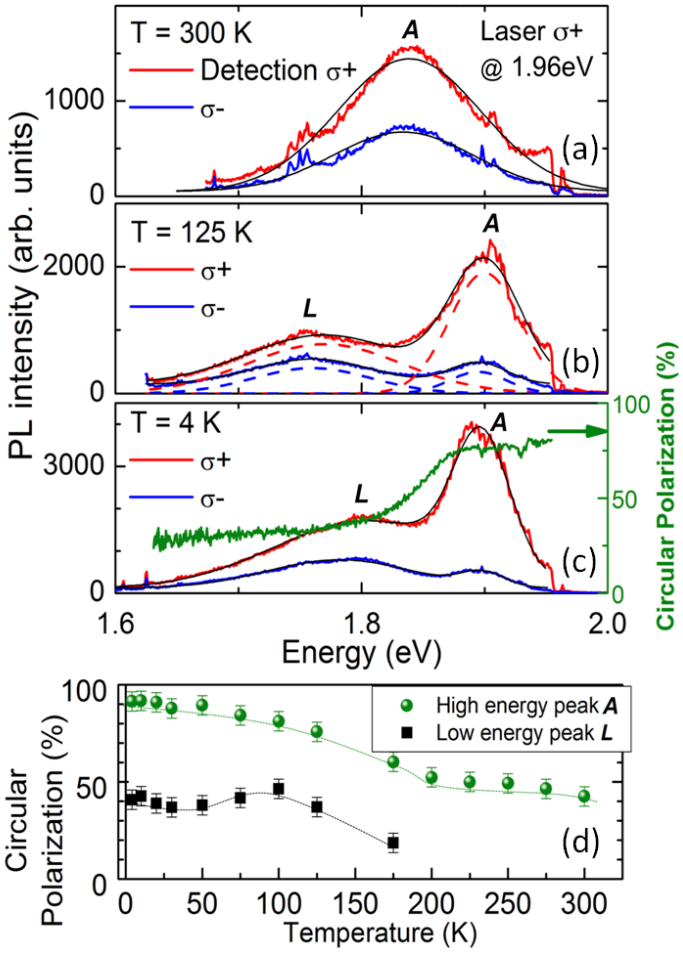

Figure 3: (a) PL spectra co-polarized (red) and cross-polarized (blue) with respect to the σ^+ polarized excitation laser (HeNe at 1.96eV). At 300 K only the high energy exciton peak ***A*** is detectable. Black curves indicate fit to the data with Gaussians. (b) same as (a) but at T = 125 K. Both ***L*** and ***A*** peaks are detectable and the polarization degree is extracted by fitting them separately (dashed lines). (c) same as (b) but at T = 4 K, the (green) right axis shows the circular polarization. PL intensity drops as a function of temperature, counts in (a)-(c) are normalized for better visibility.(d) Measured PL circular polarization degree of a 1ML MoS_2 as a function of temperature. Low energy peak (***L***) not detectable for T > 175 K. Dotted lines are a guide to the eye

the achieved degree of circular polarization varies strongly with experimental conditions. Thanks to the high spatial resolution of our microscope, we are able to investigate *different* regions of the *same* MoS_2 monolayer as the sample is mounted on piezo-positioners with a step-size in the nm-range. In another study realized on another sample and presented in figure 4, we find measurable variations of the polarization for different positions in the monolayer. The first type of spectra have a more pronounced A-exciton emission and only a very small contribution of the localized exciton. Analysing the A-exciton emission, we find P_c on the order of 70% at 4K and 10% at 300K. The second type of spectra is about 15 meV red-shifted with a more pronounced contribution of localized excitons. Here the A-exciton emission is more polarized, with P_c on the order of 85% at 4K and 25% at 300K, close to the values reported above. Strong power and excitation energy dependance are also detailed further in this section.

Fig.5 presents the σ^+ and σ^- circularly polarized PL intensity and the corresponding circular polarization following highly non-resonant excitation at 2.33 eV. In this case both ***A*** and ***B*** VB to CB transitions are possible (see bandstructure in figure 2) and we observe

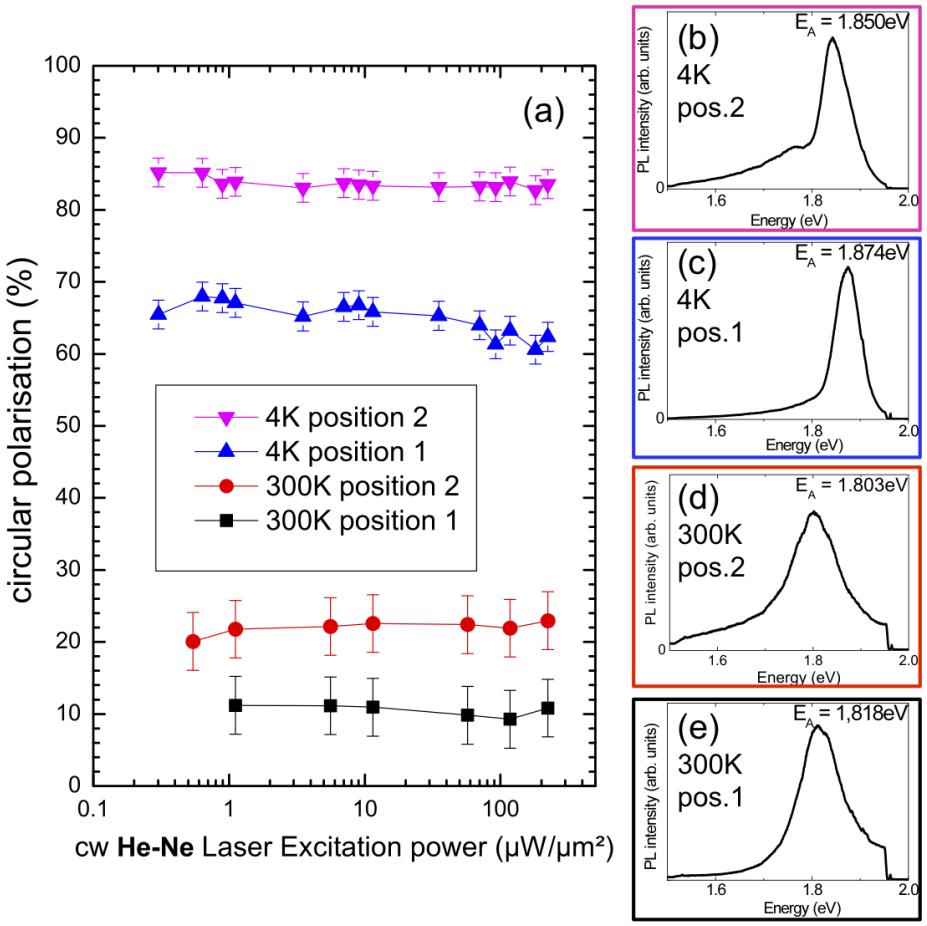

Figure 4: **Photoluminescence of monolayer MoS_2 using cw HeNe Laser** (a) Polarization of the PL emission at 300K: black squares from *position 1* on the sample, red circles from *position 2*; at 4K:blue upwards triangles *position 1*, pink downwards triangles *position 2*. (b) spectrum of PL at 4K at *position 2*, the energy of the maximum A-exciton emission is E_A (c) PL at 4K at *position 1* (d) PL at 300K at *position 2* (e) PL at 300K at *position 1*

indeed hot luminescence from the CB to ***B*** band transition, which is polarized up to about 30%. At this high laser energy the valley selectivity is not very high as the ground state transition *A* is only about 10% polarized. The distance in energy between ***A*** and ***B*** bands is ≈ 170 meV, in good agreement with the predicted 150 meV [54]. Based on the predicted strict valley selectivity, hot luminescence from the B-exciton is polarized dominantly σ^+, because the radiative recombination rate is fast compared to the combined rates of the processes necessary to emit σ^- polarized light (i.e. change in K-valley, spin and orbital angular momentum) The polarization observed for peak ***B*** is not 100% probably due to the fact that the 2.33 eV laser excitation photogenerates carriers far from the minimum of the K_+ and K_- valleys, where optical selection rules might be very different as compared to states close to the $K_\pm$ points [64].

Note that we do not have a clear spectral signature that would allow identifying the exciton charge state as suggested in Ref.[55]. In contrast to WSe_2 and $MoSe_2$ MLs (see chapter 1), the MoS_2 emission linewidth is very large (about 70meV). We therefore assume, in accordance with the intriguing polarization properties, the existence of neutral X^0 and/or negatively charged excitons X^- (the residual doping of MoS_2 ML is n-type [65]). The negatively charged exciton X^- consists of two electrons in a singlet state and an unpaired

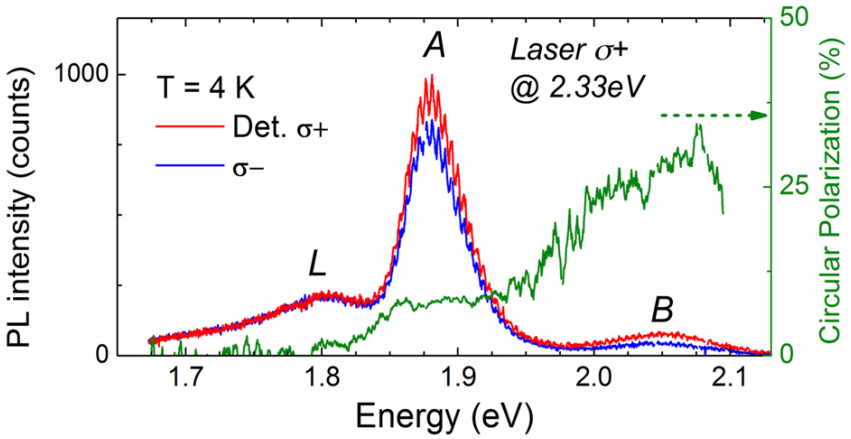

Figure 5: PL spectra at T = 4 K co-polarized (red/light gray) and cross-polarized (blue/dark gray) with respect to the σ^+ polarized highly non-resonant excitation laser at 2.33eV. Transitions ***L*** and ***A*** are visible in addition to the ***B*** exciton. The small periodic signal variations are due to optical interference in the set-up. The (green) right axis shows the PL circular polarization.

hole. Measuring the PL polarization allows monitoring directly the orientation of the hole spin as electron-hole Coulomb exchange effects essentially cancel out. For the X^0, following $\sigma^\pm$ photon absorption, bright excitons with a total (pseudo-)spin of +1 or -1 are created. Dipole allowed optical transitions conserve the spin. So if only one of the carriers (electron or hole) flips, the X^0 becomes dark and non-radiative recombination might be favoured. To observe PL polarization change from the recombination of an exciton both carriers have to be flipped (the exciton spin flips as a whole) [63]. We will detail this process, based on Coulomb exchange effects, later in the manuscript, see section 4.2. In a simple particle picture, to observe σ^- emission following optical excitation with σ^+ light, involves for both X^0 and the X^- a hole spin flip by going from valley K_+ to K_-. In this context, changing the temperature has several consequences:

(i) Phonon assisted intervalley scattering ($K_+ \rightarrow K_-$) can be activated, since the average occupation number of acoustic and optical phonons increases for modes with wavevector $q \simeq |K_+ - K_-|$, thus increasing the probability of intervalley transfer for both electrons and holes.

(ii) Due to the increase of the electron average kinetic energy, the average k-linear terms responsible for the electron spin splitting increase, while the elastic collision time decreases within a given valley. This may lead to an overall decrease of the conduction electron-spin relaxation time [63]. However, we re-emphasize that an inter valley transfer both for electrons *and* holes is necessary to observe PL polarization decay.

(iii) As the temperature is increased, the emission energy decreases [61] but the laser energy is kept constant at 1.96 eV, which is very close to resonance with the top VB ***A*** to bottom of the CB direct transition at T < 50 K, see figure 8.

In an oversimplified, independent particle picture (neglecting excitons effects) when raising the temperature, carriers further and further away from the K_+ point are optically injected [1] and the consistently high PL polarization observed in Fig.3d indicates that the chiral valley selectivity is as predicted very high throughout the valley [18]. At room temperature the laser is close to resonance with VB ***B*** with the opposite spin in the same valley. Note that this does not change the emission polarization (still σ^+) if the K_+ val-

[1] Due to the presence of strong excitonic effects the A and B resonances are composed of an ensemble of electronic states occupying a certain portion of the Brillouin zone.

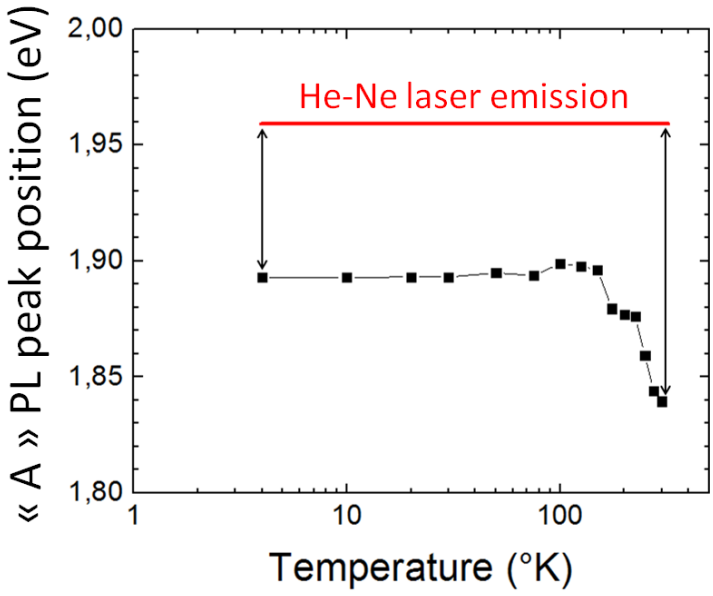

Figure 6: Evolution of energy position of the A exciton peak with temperature. The red line represent the energy position of the HeNe laser source used for excitation.

ley is populated which could explain why we still measure 40% polarization at 300 K. To fully understand the origin of the remaining PL polarization, not observed to this degree in previous reports [55; 56], time resolved measurements should be employed to extract the exact ratio of the radiative lifetime as compared to the valley/spin lifetime that determines the steady state PL polarization. In such highly confined systems, strong excitonic effects are expected [66] and a strong binding energy (oscillator strength) could also lead to ultrashort emission time and thus strongly limit the conclusions that can be draw from our cw measurements. Results of time resolved spectroscopy will be discussed in chapter 4 and excitonic effects in chapter 5.

3.2 Dependence of optical valley index initialization on laser excitation energy

Taking into account the shift of exciton A when the temperature increases (see fig 8), we expect that the fidelity of valley initialization at 300 K could be strongly improved using a laser energy closer to the ***A*** to CB resonance. In order to further test this hypothesis, we perform measurements using a tunable laser source: a frequency doubled optical parametric oscillator synchronously pumped by a mode locked Ti:Sa laser (OPO, see also section 2.5.2).

As presented in figure 7a, we first measure the circular polarization (P_c) dependance of the PL as a function of laser excitation energy at 4K. The time-integrated PL is detected at its peak energy (1.867 eV and 1.828 eV at T=4 K and 300 K respectively). As already observed by different groups [50; 55; 56; 67] the PL circular polarization degree and thus the valley initialization decrease at T=4 K (figure 8a) when the laser excitation energy increases : it varies for the sample investigated here from $P_c \simeq 50\%$ for E_{Laser} = 1.958 eV down to a value close to zero for E_{Laser} = 2.06 eV, similar to the findings by Kioseoglou et al[67]. We observe that P_c slightly increases again up to $P_c \simeq 10\%$ for E_{Laser} = 2.2 eV. Though the polarization minimum is observed roughly in the region where the B-exciton is photogenerated (see the vertical dotted line), its origin needs further clarification since

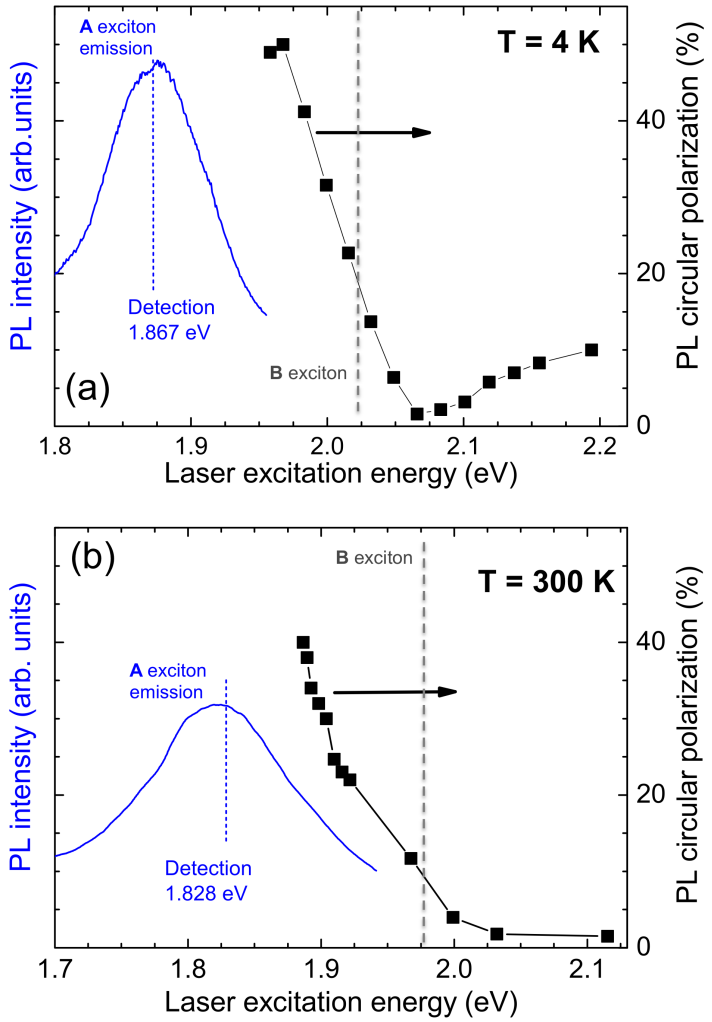

Figure 7: **PL polarization as a function of laser excitation energy** (a) T = 4K, $P_{Laser} \simeq 550\ \mu W/\mu m^2$ detected on the A-exciton PL maximum E_{Det} = 1.867 eV. The A-exciton emission (blue) is shown. (b) same as (a) but for T = 300 K, $P_{Laser} \simeq 950\ \mu W/\mu m^2$, E_{Det} = 1.828 eV

the B-exciton absorbs and emits the same light helicity as the A-exciton in a given K valley [11; 18]. The energetically close lying indirect transition from the Γ valley valence band to the conduction band (see figure 8)could play a role [64; 68].

A key result is presented in figure 7b. We perform the same PLE experiments as in figure 7a, but at room temperature. When the laser is far from resonance, we observe close to zero polarization. Remarkably, as we lower the laser energy and become more and more resonant, the polarization drastically increases, in the same manner as at 4K. For the closest energy to resonance that was achievable in practice with our set-up (filter cut-off for stray laser light), we measure an emission polarization of P_c(300K) = 40%, close to the maximum observed at 4K of P_c(4K) = 50% [69]. This is very encouraging as optical initialization of valley polarization with a suitable excitation source can therefore be very efficient even at room temperature. Here it would be extremely useful to investigate how the strong Coulomb interaction [70–73] influences the polarization at 300K. Indeed strong excitonic effects in this system close to the ideal two-dimensional confinement limit have been predicted [66] with exciton binding energies of $E^{2D}_{Ryd} \approx 800$ meV (Bohr radius $a_B \approx 1$nm), which raises questions concerning the most reliable determination of direct bandgap of MoS_2 (discussed in chapter 5).

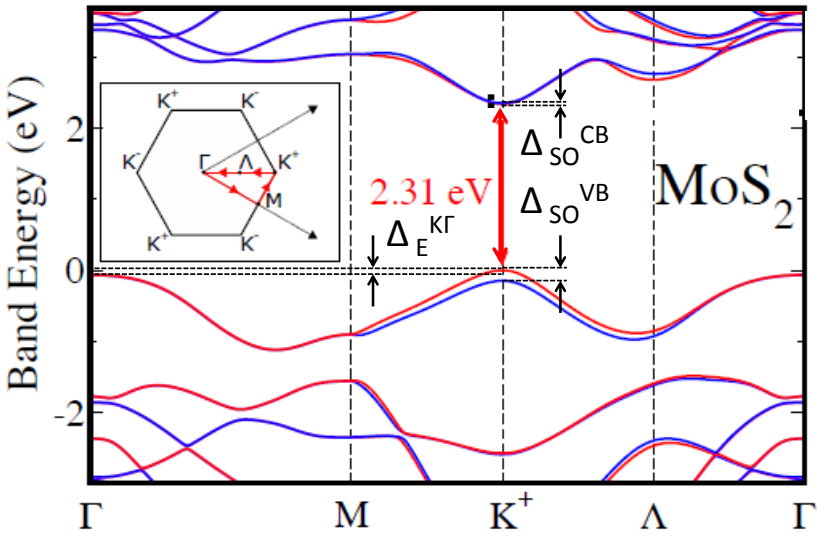

Figure 8: G_0W_0 band structure for freestanding MoS_2 ML. The energy difference between the topmost valence bands at Γ and K point is only 68meV ($\Delta_E^{K\Gamma}$ in the figure, on the left side). Zero energy represents the Valence Band Maximum. The red arrow marks the free carrier bandgap at 2.31eV, the optical bandgap is several hundreds of meV lower due to the exciton binding energy. Work performed in collaboration with I. Gerber [37].

3.3 Influence of laser excitation power on optically created polarization

As can be seen in the previous section, changing excitation sources lead to differences in the measured polarization values. This is linked to the particular properties of the laser sources:

First, the cw HeNe laser emission is spectrally narrower than the pulsed OPO. The short emission time of the pulsed light source (about 1ps) leads unavoidably to a broadening of the spectral emission (about 3 meV). As the PL polarization changes abruptly for different laser energies (see figure 7) it is difficult to directly compare the PL polarization measured using OPO excitation with the results obtained using HeNe excitation. Moreover, laser filtering is more challenging with OPO, our filter being specially dedicated to HeNe wavelength, its transmission change abruptly for wavelength longer than 633nm. For this reason, it is not possible to excite as close to the transition using the OPO as when using a HeNe laser source.

Second, although the average laser power monitored with a photodiode, which is used to measure the laser power plotted in figure 9 and 10, might be comparable in the experiments, the power is several orders of magnitude lower than the peak power in pulsed operation. Over the investigated power range using HeNe laser source, the polarization does not change drastically, in contrast to the measurements with the OPO excitation. This could be easily explained by the fact that the photogenerated carrier density is much larger with the OPO pulsed excitation compared to the cw He-Ne excitation.

In the experiments above we investigate the dependance of the PL polarization with excitation power. We find as a general trend that the PL polarization decreases as the laser power increases, a shown in figure 9(c). The laser excitation power range used for the results presented in this thesis is still within the linear absorption regime (below saturation,

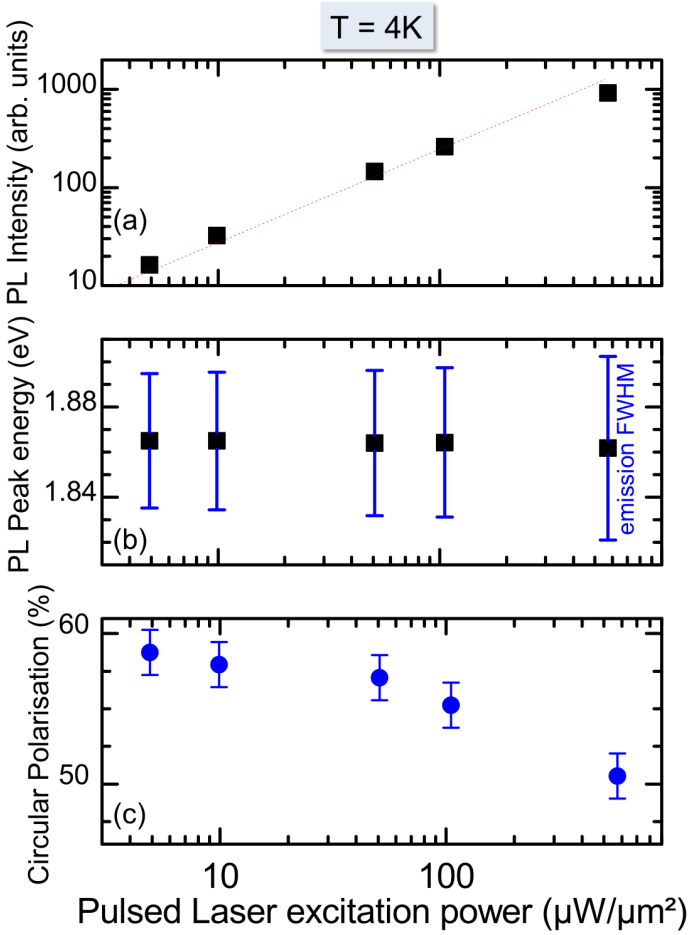

Figure 9: **Power dependence of photoluminescence under pulsed laser excitation at 4K** using detection at E_{Det} = 1.867 eV and E_{Laser} = 1.965 eV (a) PL intensity as a function of laser power (b) peak position of A-exciton PL emission (black squares). The FWHM of the transitions is indicated (blue lines). (c) PL circular polarization degree detected at central point of PL kinetics as a function of laser power (blue circles).

see figure 9a) and does not induce any measurable sample degradation. The laser power used in the experiments is dictated by practical considerations: at low power the signal level has to be sufficient to achieve a high signal-to-noise ratio, at high excitation power structural damage of the MoS_2 monolayer has to be avoided. In figure 9(a) we show the PL intensity as a function of laser power over 2 orders of magnitude. Note also that over the investigated power range using HeNe laser source, the polarization does not change drastically and correspond to the low power regime of the OPO.

The transition energy is constant for the laser power range investigated, see figure 9(b). We therefore conclude that sample lattice heating is an unlikely cause of this polarization decrease.

In figure 10(a) we confirm that also at 300K we are still working in the linear absorption regime. Figure 10(b) shows a decrease of the PL circular polarization degree as the laser power increases, similar to the trend shown at low temperature. Further work has to be performed to clarify the origin of this power dependance.

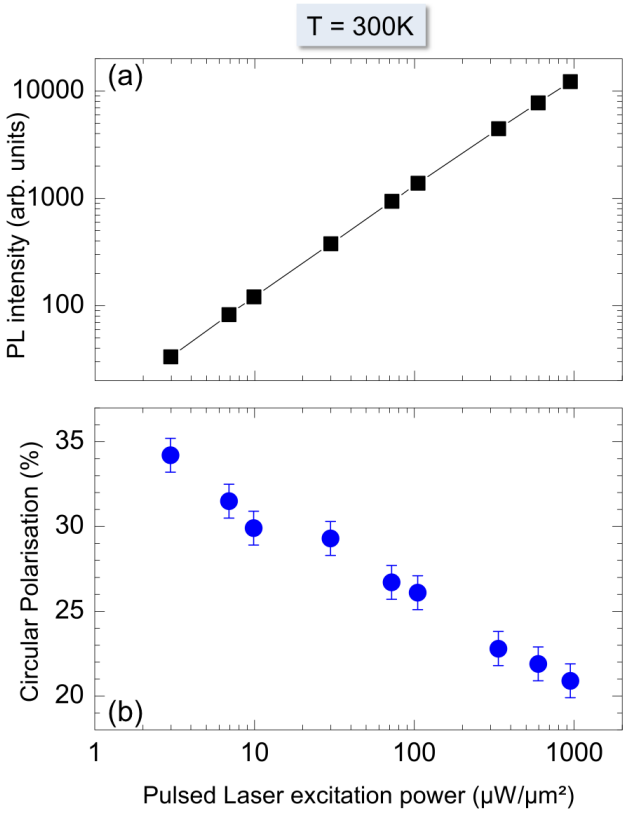

Figure 10: **Power dependence of Photoluminescence under pulsed Laser excitation at 300K** E_{Laser} = 1.913 eV (a) PL intensity as a function of laser power (black squares) (b) PL circular polarization degree detected at E_{Det} = 1.828 eV as a function of laser power (blue circles).

3.4 Valley polarization in transverse magnetic field

Another crucial experimental test for the stability of the optically created valley polarization is the application of a transverse magnetic field. The spin quantization axis is chosen along the light propagation direction, i.e. perpendicular to the MoS_2 layer as indicated in the inset of Fig.8a, where the magnetic field B_T is applied in the MoS_2 plane. In a classical picture for free carrier spins, the application of a magnetic field perpendicular to the spin quantization axis results in a precession of the spin around the applied field. As a result the spin component along the quantization axis measured via the PL polarization degree in the circular basis would strongly decrease and eventually average out to zero in standard Hanle experiments [63]. With this simple picture in mind the constant polarization observed at T = 4 K in transverse magnetic fields up to 9T and at T = 100 K in a field of B_T = 6 T shown in Fig.8b seems very surprising.

The emission is based on the dipole allowed recombination of a conduction electron with a valence hole, that we have detailed in Fig.2. The main contribution to the strong optical absorption of ≈ 10% [8; 15; 55; 74] comes from the Mo *d* orbitals. The local trigonal symmetry of electron states in monolayer MoS_2 at $K_\pm$ points is C_{3h} in Koster notation [27]. This leads us to predict that:

(i) the only symmetry allowed coupling introduced by a transverse magnetic field B_T is in principle between VB ***A*** and VB ***B***, and between VB ***A*** and CB, all of the same valley. This coupling would *not* change the emitted light polarization. In addition, the large energy difference between these bands makes this coupling vanishingly small.

(ii) B_T does not couple states of inequivalent K_+ and K_- valleys. If the states have in-

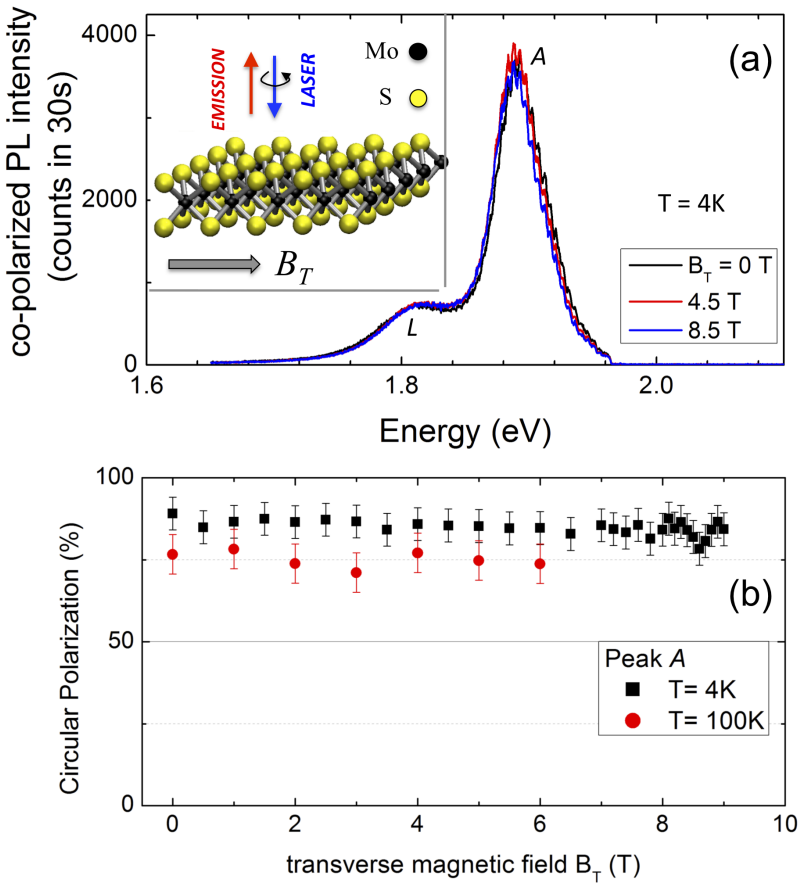

Figure 11: (a) Comparison of PL spectra of a single MoS_2 ML recorded for a transverse magnetic field B_T = 0, 4.5 and 8.5 T under otherwise identical experimental conditions using HeNe laser at 1.96eV. Inset: experimental geometry. (b) Measured PL circular polarization degree of the PL as a function of the applied transverse magnetic field B_T for ***A*** exciton at T = 4 K (squares) and at T = 100 K (circles).

deed the predicted symmetry, even a strong transverse field B_T would result in a constant emission polarization when increasing B_T. Our results seem to validate this prediction, even at elevated temperatures of 100 K in a field of B_T = 6 T as shown in Fig.8b, in addition to the initial reports in [56] for small fields.

The experimental results presented in the next chapter showing a very fast PL emission time could also explain the absence of Hanle depolarization (no spin precession can occur before such ultrafast photon emission).

Moreover, the work performed on excitonic effects in TMDCs (see chapter 5) on the key role played by exciton physics should be considered to re-interpret these early magneto-PL measurements in Voigt geometry.

3.5 Conclusion

In this chapter we investigate the robustness of the circular polarization of the PL emitted by an MoS_2 ML under various experimental conditions. The degree of circular polarization of the PL decreases when the temperature increases, which might be due to activation of phonon assisted intervalley scattering, but also to the increase of the energy distance between PL emission energy, which decreases with the temperature, and the laser energy,

which remain constant. This last argument is supported by the PLE experiments we performed. We show a drastic decay of the PL circular polarization degree as the excitation energy becomes less and less resonant. We demonstrate a strong recovery of the polarization at room temperature when we excite closer to the A-exciton resonance.

The polarization of the PL varies also with the excitation power, identifying the origin of this behavior requires further work and is not clarified here.

Finally, applying a magnetic field up to 9T perpendicularly to the spin quantization axis shows no measurable effects. This might simply be due to the elevated symmetry of our crystal which does not allow to couple states of inequivalent K+ and K- valleys through the application of a transverse magnetic field. It is also very likely that the strong excitonic effects that will be discussed in chapter 5 play a role and that the emission time is too short to allow to see any significant depolarization effects for the applied magnetic field range.

The next chapter is dedicated to time-resolved PL experiments that we use to further understand the carrier and valley index dynamics in TMDCs materials. We will understand the limits for interpreting the time-integrated PL results presented here and in the literature in general, as PL emission times are in the ps range.

Chapter 4

Valley dynamics in MoS_2 and WSe_2 monolayers

For both MoS_2 and WSe_2 monolayers, optical transitions across the direct bandgap in the visible region are governed by chiral selection rules, allowing optical valley initialization. As detailed in chapter 1, the valley polarization is protected by the strong spin-orbit splitting in the valence and (especially for WSe_2) conduction band [11], leading in principle to a high stability for the valley degree of freedom. The high circular photoluminescence (PL) polarization degree reported in time integrated measurements in ML MoS_2 (cf. chapter 3) and ML WSe_2 [32] seems to confirm this prediction.

The stability of the created valley polarization is crucial for manipulating the electron valley degree of freedom in transport measurements [12] or with successive laser pulses in optical control schemes. Thus, we need to uncover the dynamics of the PL polarization, to extract the exact ratio of the radiative lifetime as compared to the valley/spin lifetime that determines the steady state PL polarization.

In this chapter, we perform time resolved PL experiments on both MoS_2 and WSe_2 monolayers. For both materials, we find fast exciton emission decay times, showing that time integrated measurements results are only influenced by what happens in the first ps after the carrier initialization. Spectrally well defined exciton resonances in ML WSe_2 allow to uncover differences between neutral and charged exciton dynamics. Theoretical analysis, developed in collaboration with M. M. Glazov at the Ioffe Institute, demonstrates that the neutral excitons in different K-valleys are coupled by the Coulomb exchange interaction [75], which can lead to an admixture between states from different k-valleys [76]. We finally discuss the use of the trion as a candidate for optically initialized valley Hall experiments [77].

Despite certain differences between TMDC systems, one can see general trends appearing. Their common features are strong carrier confinement, direct band gap in the visible / near infrared and chiral interband selection rules. By studying both MoS_2 and WSe_2 in this chapter, we aim to uncover general physical properties of TMDCs.

Experiments reported in this section were carried out on mechanically exfoliated sample provided by SPI supply (for MoS_2) and by 2D Semiconductors (for WSe_2), see also parts 2.1.1 and 2.1.2 for more details. We used the experimental setup described in section 2.5 for the time resolved measurements and the Attodry700 cryostat (see section 2.4.1).

4.1 Time and polarization resolved PL measurements in MoS_2 and WSe_2 monolayers

Here again it is important to underline that for both MoS_2 and WSe_2 monolayers, the circular polarization (σ^+ or σ^-) of the absorbed or emitted photon can be directly associated with selective carrier excitation in one of the two non-equivalent K valleys (K_+ or K_-, respectively). Selection rules are recalled on figures 1.a and 4.a of the present chapter. One can find more details in section 1.3.

Therefore, we are able to monitor directly the valley index dynamics by using our time and polarization resolved microscope setup.

4.1.1 Experiments on MoS_2 MLs

In chapter 3, optical valley initialization in ML MoS_2 has been based on the analysis of the large circular polarization degree P_c of the emitted light from the direct bandgap observed in continuous wave (cw) measurements following circularly polarized laser excitation. An important drawback is the drastic decrease of P_c as the temperature is raised to 300K. In a simple approach, the stationary (time integrated) polarization is determined by the initially created polarization P_0, the lifetime of the electron-hole pair τ and the polarization decay time τ_s through $P_c = P_0/(1+\tau/\tau_s)$ [46]. We emphasize that the polarization decay time in ML TMDCs does not correspond directly to the carrier spin flip time as in most semiconductors like GaAs [46], but it includes the scattering time between the two non-equivalent K valleys (K_+ or K_-) [11].

Here we first discuss time resolved PL measurements on MoS_2 monolayers. Figure 1a displays the total photoluminescence intensity dynamics at T=4 K following a σ^+ polarized picosecond excitation laser pulse with an energy E_{laser} = 1.965 eV, which is within the broad A-exciton absorption line [55; 72]. The detection energy corresponds to the PL peak energy E_{Det} = 1.867 eV. The average laser power used for all experiments is below 1 $mW/\mu m^2$, well below absorption saturation and in the absence of sample heating effects, as discussed in detail in section 3.3 (see previous chapter). We do not observe any variation of the dynamics when the detection energy is varied within the A-exciton spectrum. Indeed the A exciton emission is most likely dominated by the negatively charged X^- emission, with a weaker contribution from the neutral exciton emission X^0. The emission of both complexes is strongly polarized due to the chiral optical selection rules in monolayer MoS_2 [72].

Though the MoS_2 PL dynamics is very fast we see in figure 1 that it occurs on a slightly longer time scale compared to the one defined by the temporal resolution of the set-up (compare the MoS_2 PL and laser pulse detection in figure 1a). Using a deconvolution

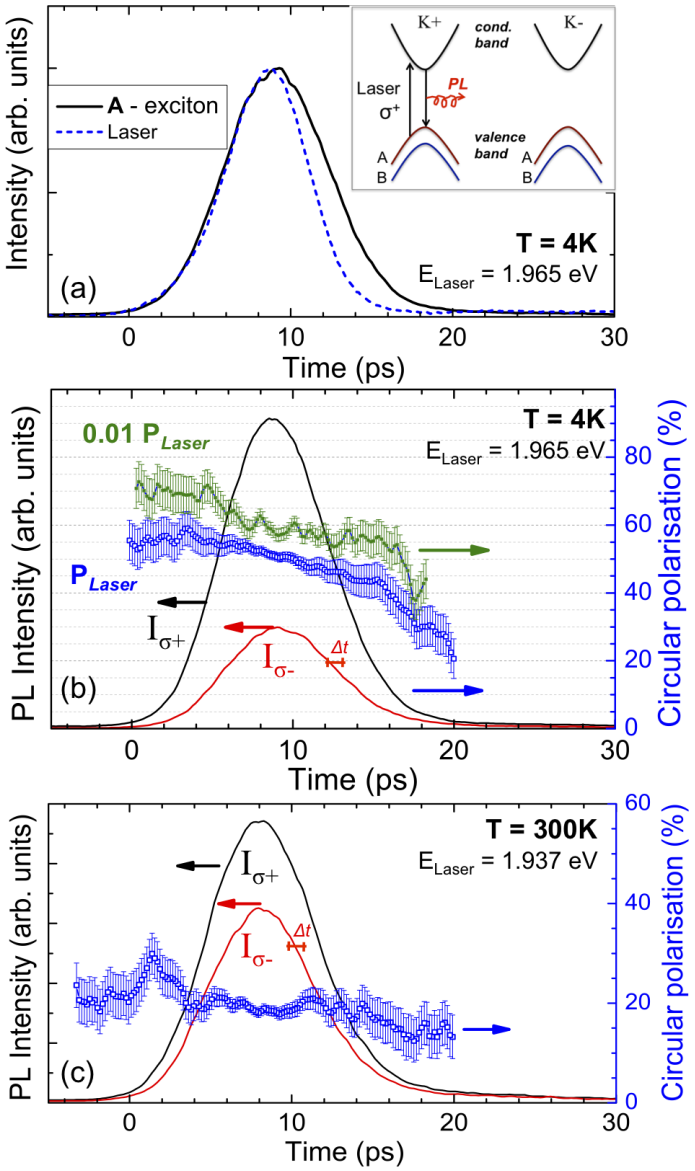

Figure 1: **Time resolved photoluminescence of A-exciton.** (a) Laser pulse (blue line) and PL emission (black line) intensity at T = 4 K detected at maximum of A-exciton PL E_{Det} = 1.867 eV as a function of time. Inset: Chiral optical selection rules in 1ML MoS_2 (b) T=4K, E_{laser} = 1.965 eV, E_{Det} = 1.867 eV. Laser polarization σ^+. Left axis: σ^+ (σ^-) polarized PL emission intensity presented in black (red) as a function of time. Right axis: Circular polarization degree during exciton emission (blue hollow squares: excitation power $P_{laser} \simeq 550\ \mu W/\mu m^2$, green full squares:0.01 P_{laser}), errors bars take into account uncertainty in time origin $\Delta t \sim 0.7 ps$. (c) same as (b), but for T=300K, E_{laser} = 1.937 eV, E_{Det} = 1.828 eV.

based on Gaussian functions we can infer that the MoS_2 emission time is about 4 ps. We emphasize that this fast PL dynamics is obtained in excitation conditions where exclusively the A-exciton (not B) in the K_+ valley is excited (see inset of Fig.1a). Here the energy difference between excitation and detection is relatively small, with $E_{laser} - E_{Det}$ about 100 meV.

Detailed deconvolution procedure:

For our measurement of the emission time, we consider for simplicity both curves of figure1a as Gaussian, as well as the laser peak and the streak camera response. It is well

known that the convolution of two Gaussians is another Gaussian with square standard deviation σ being the sum of the square of the two others [78]. Therefore, as soon as we know the standard deviation for the streak camera response, we can extract the effective PL time decay from our experimental value: $\sigma^2_{exp} = \sigma^2_{\mathrm{PL}} + \sigma^2_{streak}$

As we measured the laser emission decay time (cf. figure1a) and we know the theoretical temporal width of our laser pulse, we can extract the streak response from our data and deduce the effective PL time decay:

$$\sigma^2_{laser_{exp}} = \sigma^2_{laser_{\mathrm{PL}}} + \sigma^2_{\mathrm{streak}}$$
$$\sigma^2_{signal_{exp}} = \sigma^2_{signal_{\mathrm{PL}}} + \sigma^2_{\mathrm{streak}}$$
$$\sigma^2_{signal_{exp}} = \sigma^2_{signal_{\mathrm{PL}}} + \sigma^2_{laser_{exp}} - \sigma^2_{laser_{\mathrm{PL}}}$$

Indeed, for Gaussian, standard deviation and full width at half maximum (FWHM) are related as follow: $\mathrm{FWHM} = 2\sqrt{2\ln(2)} \times \sigma$ [79]. Therefore:

$$\mathrm{FWHM}_{signal_{\mathrm{PL}}} = 2\sqrt{2\ln(2)} \times \sqrt{\sigma^2_{signal_{\mathrm{exp}}} - \sigma^2_{laser_{\mathrm{exp}}} + \sigma^2_{laser_{\mathrm{PL}}}}$$
$$\mathrm{FWHM}_{signal_{\mathrm{PL}}} = \sqrt{\left(\mathrm{FWHM}_{signal_{\mathrm{exp}}}\right)^2 - \left(\mathrm{FWHM}_{laser_{\mathrm{exp}}}\right)^2 + \left(\mathrm{FWHM}_{laser_{\mathrm{PL}}}\right)^2}$$

Numerical application: $\mathrm{FWHM}_{signal_{\mathrm{PL}}} = \sqrt{(6.4)^2 - (5.3)^2 + (1.6)^2} \simeq 4\mathrm{ps}$

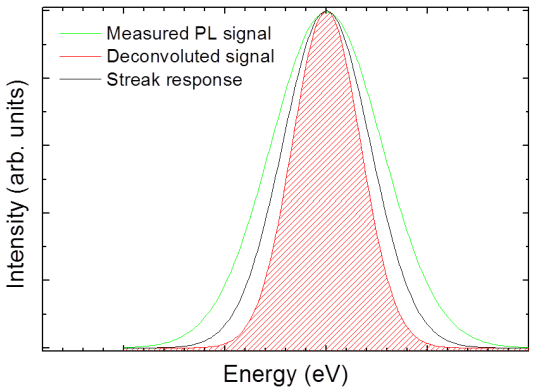

Figure 2: **Convolution of the two Gaussians governing the time-resolution.** Green curve corresponds to the signal we measured, the black curve represents the behavior of the streak camera and the red curve is the processed data which gives us a PL emission decay of about 4ps for MoS_2. The ratio between each curve is the correct one, which underline how close to the resolution limits we are.

In figure 1b, the right ($I_{\sigma+}$) and left ($I_{\sigma-}$) circularly polarized luminescence components have been detected using a σ^+ polarized laser (measured $P_c^{laser} > 99\%$). Remarkably the PL circular polarization degree is large and remains almost constant during the short exciton emission, around 50% for a laser excitation power $P_{laser} \simeq 550\ \mu W/\mu m^2$ (blue curve in figure 1b). Lowering the excitation power by two orders of magnitude has a strong impact: the polarization still remains nearly constant, but at a higher value of 60% (green curve in figure 1b). As $P_0 < P_c^{laser}$ either the polarization generation at this laser energy is not 100% efficient (due to the optical selection rules) or there exist an ultrafast, initial polarization decay due to intervalley relaxation much shorter than 1ps that we do not resolve. This hypothesis is supported by the fact that the valence states at the Γ point

are very close in energy to the states at the K point (a few meV [64]) in MoS_2.

Due to the sequential recording of σ^+ and σ^- polarized kinetics there is an experimental uncertainty of $\Delta t \sim 0.7ps$ when fixing the time origin of the σ^+ emission with respect to σ^-. This results in an experimental uncertainty when determining the circular PL polarization, as indicated by the error bars in figure 1b. As a result of this time jitter and the short exciton emission time, our experiments on MoS_2 do not allow an accurate determination of the spin/valley relaxation time τ_s. This uncertainty has been reduced later for measurements conducted on WSe_2 monolayers by adding a delay line that gives us an additional temporal reference.

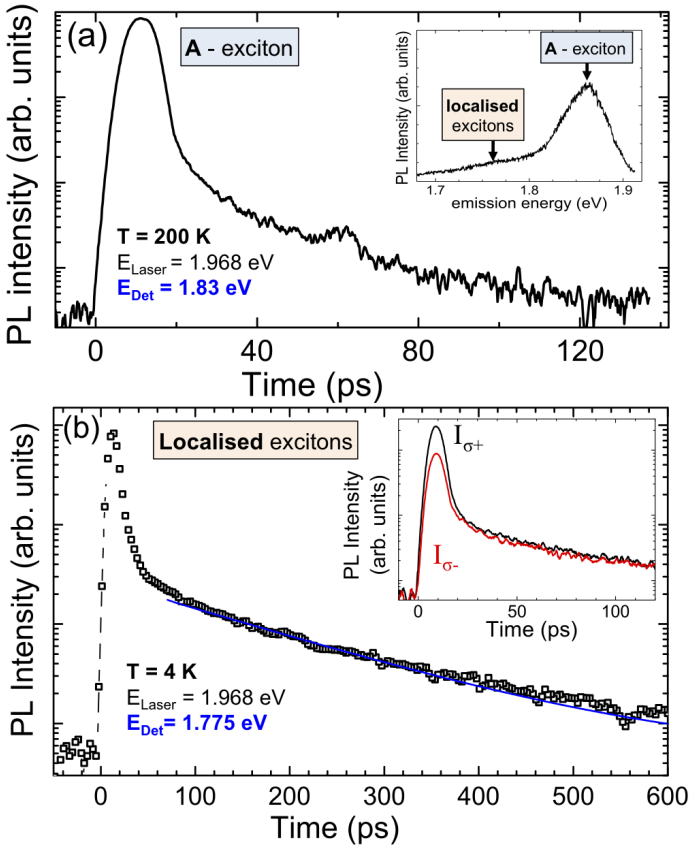

Figure 3: **Time resolved photoluminescence** (a) T=200K, E_{laser} = 1.968 eV, E_{Det} = 1.83 eV. **A-exciton** PL intensity as function of time, plotted in log-scale to emphasize weak, slow component that appears when raising T. The small peak at about 50ps is due to a laser reflection in the set-up. Inset: cw-PL spectrum at T=4K showing energy of intrinsic A-exciton emission and localised exciton emission. (b) T=4K, E_{laser} = 1.968 eV, E_{Det} = 1.775 eV. **Localised exciton** PL intensity as a function of time (black). Blue line: fit with a single exponential decay ($\tau_{loc} \simeq 125ps$). Inset: The polarization resolved emission of A-exciton and localized exciton which spectrally slightly overlap.

The emission time at room temperature is very similar to the one at 4K with $\tau \sim 4.5ps$. Figure 1c shows $P_c \simeq 20\%$ constant in time for a laser excitation energy E_{laser} = 1.937 eV. The dependence of P_c as a function of the excitation laser energy has been discussed in section 3.2. Remarkably the PL circular polarization degree which probes the valley initialization measured in time-resolved experiment is similar to the one obtained in time-integrated experiments as a result of the very short exciton lifetime and the absence of measurable polarization decay within this short emission time. Please note here that

for both TRPL and time-integrated measurements, excitation conditions are similar, with same laser energy and power.

In figure 3a we show that when raising the temperature, in addition to the ps exciton decay a longer lived component is observed. This is similar to the findings of [61] under highly non-resonant excitation. This measured long lived PL component is essentially unpolarized in figure 3a and the intensity is very weak (about one order of magnitude) compared to the short, main PL emission and for that reason, is presented in logarithmic scale. Therefore even at room temperature the short component, see figure 1c, determines P_c. In addition to the main A-exciton also localized excitons emitting at lower energy (E_{Det} = 1.775 eV) are observed [50; 55; 61], see inset of figure 3a. The localized exciton emission decays within about 125ps at T=4K (see figure 3b) and is not detectable at higher temperature. The polarization dynamics is shown in the inset of figure 3b: as the A-exciton and the broad, localized exciton emission spectrally slightly overlap, we detect the remaining A-exciton polarization at short times, before detecting the essentially unpolarized emission of the localized excitons. It is important to note that the localized exciton polarization dynamics is expected to be more sensitive to the sample parameters (substrate material, interface defects, etc...) than the A-exciton emission.

4.1.2 Experiments on WSe_2 MLs

If for ML MoS_2 the neutral exciton (X^0) and the charged exciton (trion) emission cannot be clearly spectrally separated due to the broad transitions, for ML WSe_2 the situation is different, as one can see on figure 12 (see also chapter 1). The well separated transitions allow us to monitor independently the valley dynamics for the different excitonic complexes and thus uncover some notable differences.

For ML WSe_2 experiments the laser excitation energy is E_{laser} = 1.893 eV, which is 140 meV above the neutral A-exciton emission energy and clearly below the B-exciton absorption (confirmed in reflectivity measurements, see figure 6 as the energy difference between A and B valence states is on the order of 450meV). The time integrated PL emission at T=4K stems from the recombination of X^0, trions and localised excitons. The emission attributed to localized states is not detectable any more for temperatures above 125K (cf. section 2.1.2), confirming the intrinsic nature of only the X^0 and trion (T) transitions. Note that the temperature dependent PL was performed at a sample position slightly different from the measurements presented in this chapter, which only changes the relative intensity of the localized states. The PL recorded in figure 12 is very similar to the emission reported for this system in [32], where a bias was applied to the ML WSe_2. Considering the commonly observed residual n-type doping, the trion charge is most likely to be negative, as assumed for the discussion below. Note that this assumption is not critical for ML WSe_2. The trion valley polarization is protected by the large spin-splitting Δ_{SO} in the valence band ($\Delta_{SO}^{VB} \approx 430$ meV [54] at $k = K_{\pm}$) and the conduction band ($\Delta_{SO}^{CB} \approx 30$ meV [22; 80]). Charge tunable structures [32] would be ideal to investigate alternatively the positively or negatively charged trion.

In TRPL experiments we observe striking differences between the main transitions, as on can see from figure 12a and figure 12b. We first discuss the emission times, that can be compared in figure 12b and that are summarized in table 4.1. The main X^0 emission time

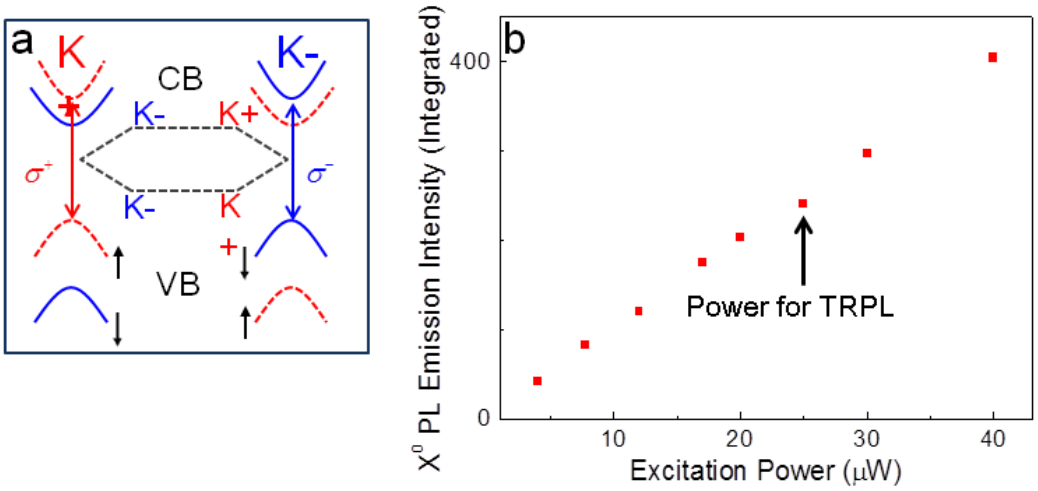

Figure 4: (a) optical interband selection rules for monolayer WSe_2 according to [22]. Note that the order of CB spinstates is reversed with respect to MoS_2 (b) power dependence of PL intensity under pulsed laser excitation. Linear behavior shows the absence of saturation for the power used for measurements.

cannot be clearly resolved by our experiment, it decays within 4ps, in a very similar way to ML MoS_2 (cf. figure 1).

In ref [32] a strong linear polarization degree of the X^0 PL in WSe_2 was observed. This has been interpreted as evidence for the generation of valley coherence i.e. the coherent superposition of K+ et K- valley polarization. As a result of the short PL emission time, the coherence time could be as short as a few ps and still result in a strong linear polarization degree of the time-integrated PL. If the short X^0 emission time is limited by radiative recombination (in this system with predicted [71; 81] and measured [33] exciton binding energies of several hundred meV) or by non-radiative processes, is still an open question. The 2 to 3 orders of magnitude weaker PL emission at later times can be fitted by a simple exponential decay with a characteristic time of 33±5 ps. We have checked carefully using the full dynamic range of our detector that this long-lived decay is not simply due to spectral overlap with other longer-lived transitions. The origin of this longer time might be linked to a long-lived emission from neutral excitons localized at fluctuations of the crystal potential [82; 83] or to initially dark excitons. Note that this type of weak localization is qualitatively different from forming bound states such as the D^0X in GaAs, that might have parallels dynamics to the complexes L1 and L2.

Peak	main decay time τ (ps)
L1	80
L2	30
Trion	≈ 20
X^0	≤ 4

Table 4.1: Summary of decay times measured for WSe_2 monolayers.

After discussing the neutral exciton, we now investigate the trion. The trion PL emission can be fitted by a bi-exponential decay. We observe no measurable risetime of the trion PL signal within our resolution. The initial trion decay is clearly longer than for the X^0 as can be seen already in figure 12c and we extract a decay time of about 18±2 ps. Similar decay times in differential reflectivity for ML WSe_2 have been found at room tem-

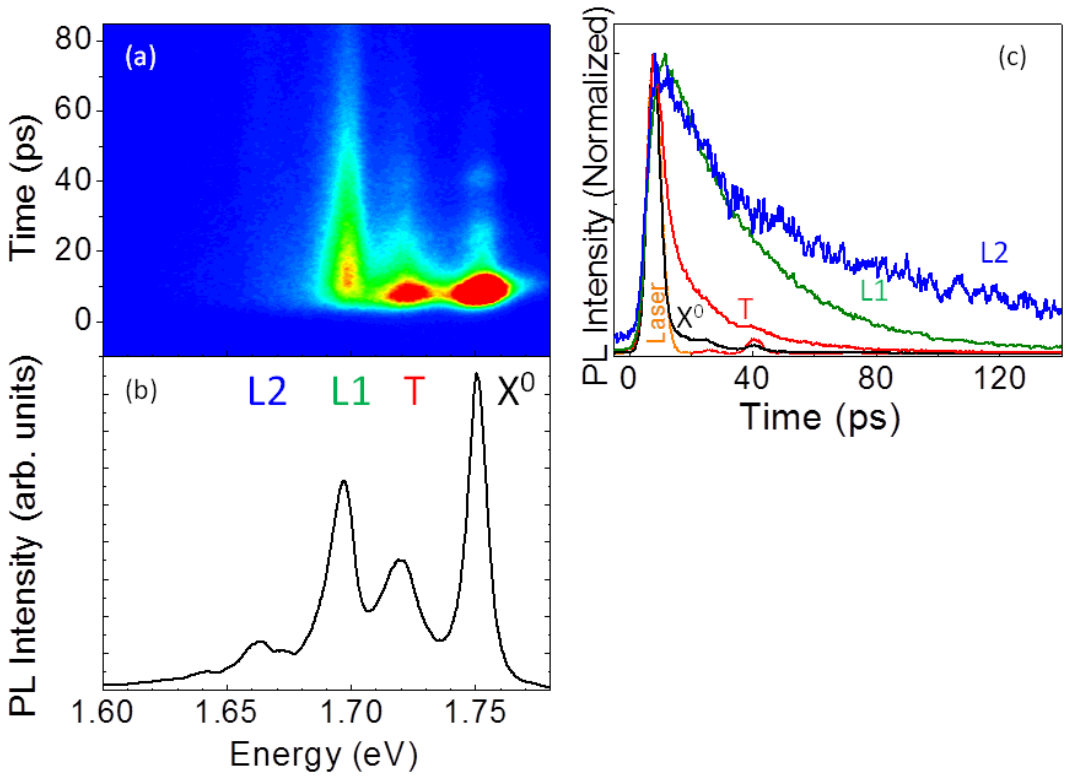

Figure 5: (a) Streak camera image of TRPL total intensity showing different emission times for X^0, trion and localized states. Blue (red) corresponds to zero (5000) counts.(b) Time integrated PL spectrum, typical for WSe_2 monolayer. The peaks corresponding to X^0, trion and localized states are labeled (c) Normalized PL dynamics (total peak intensity) for each peak at T=4K. Time decays are extracted and presented in table 4.1

perature in ref. [84], where trion and X^0 spectrally overlap and cannot be resolved. At longer times we extract an emission with a decay of 30±3 ps, similar to the case of the X^0. In general the longer emission times allow for a more detailed polarization analysis in the case of the trion compared to the ultra-short X^0 emission. The trion emission time being longer than the X^0 emission time is a trend also observed in III-V [85] and II-VI [86] semiconductor quantum wells, where the longer trion emission time was ascribed to a lowering of the oscillator strength due to a stronger localization. In the ML WSe_2 sample investigated here, the strong optical signature of trion PL at high temperature (T > 150K) hints at the existence of trions independent of spatial localization, see reflectivity measurements on figure 6 and, for comparison, recent reflectivity measurements on ML WS_2 [87; 88].

For the localized peak labeled L1 we record a clear, mono-exponential decay of the PL intensity. The majority of photons resulting from L1 recombination are emitted after the main X^0 and trion recombination, see figure 12. The decay time extracted here is 32±2 ps. The considerably less intense transition L2 also decays mono-exponentially, albeit with a considerably longer characteristic time of 80±6 ps. In temperature dependent measurements, we find for T > 125 K that the emission from the L1 and L2 peaks is negligible compared to the X^0 and the trion lines (see section 2.1 dedicated to sample presentation for more details). The emission times measured here for X^0, trion, L1 and L2 transitions remain essentially constant for the the laser excitation energies used (1.851, 1.893 and 1.968 eV). The exact energy position and intensity ratio of L1 and L2 can

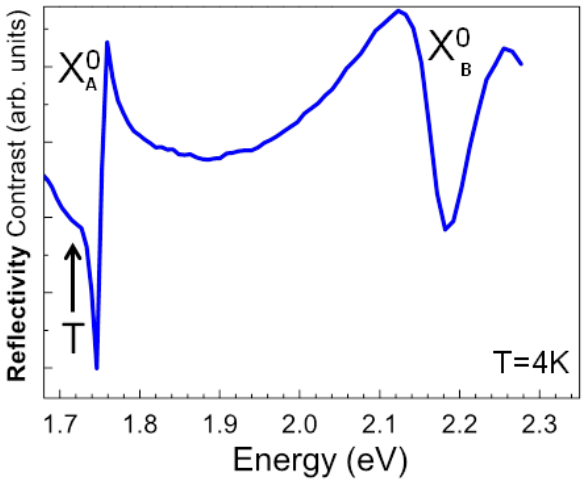

Figure 6: Reflectivity measurements on WSe_2 ML at T= 4 K (using a white light source). We labeled the position of the trion (T) using a black arrow.

vary from sample to sample as they are most likely related to crystal imperfections. The behavior of the intrinsic X^0 and trion transitions, which are the focus of the discussion below, is reproducible from sample to sample.

4.1.3 Discussion MoS_2 MLs

The few time resolved measurements reported in the literature for 1ML MoS_2 use highly non-resonant excitation and did not analyse the polarization of the emission [61; 89; 90]. In [55] and [89] the authors suggest that non-radiative recombination of the excitons could explain the first, short decay observed from 4K to 300K. We can infer from our time and polarization resolved measurements that the detected polarization in time-integrated experiments is due to the emission during this short time window. If this initial decay is indeed limited by non-radiative processes or an intrinsic exciton lifetime still needs to be clarified. The exciton binding energy is estimated to be in the hundreds of meV range [70; 71; 73] confirmed in recent experiments [91]. Systems with large exciton binding energies such as organic films and carbon nanotubes have intrinsic exciton radiative lifetimes on the order of a few ps [92–94]. In our measurements the PL decay time τ does not change with temperature within our time resolution, we do not observe any activation or any other typical signature of non-radiative processes. For comparison, for high quality GaAs quantum well structures the free Wannier-exciton radiative recombination time increases with temperature [95].

An argument in favor of a radiative exciton decay within a few ps comes from the observation of the B-exciton emission, 150meV higher in energy than the A-exciton (cf. chapter 3), as radiative recombination of the B-exciton is in competition with non-radiative decay and relaxation to the A-exciton. Indeed very recent calculations performed in Cornell university predicted a radiative lifetime of excitons in MoS_2 of about 1ps [88]

Another interesting perspective could also be to investigate the influence of the substrate on the polarization dynamics. Here we used MoS_2 MLs on SiO_2/Si, the most practical substrate for (opto-)electronic devices. Although time resolved experiments on suspended MoS_2 MLs gave similar time-resolved absorption results to experiments using substrates [89], a comparison with MoS_2 on BN where the localised exciton emission was suppressed [55; 72] would be important to clarify the nature of the observed PL emission.

The very fast exciton decay time measured here in MoS_2 MLs could help explaining, among other reasons, that the application of a transverse magnetic fields does not influence the polarization of the ML PL: this would be the case only if the precession time is shorter than 4ps.

4.1.4 Discussion WSe_2 MLs

Concerning WSe_2 MLs, fast exciton decay time for the X_0 could explain the high degree of coherence between valley excitons probed through the observation of stationary, linearly polarized luminescence in WSe_2 devices (following linearly polarized excitation, see chapter 5). Concerning ML WSe_2 valley dynamics: due to the fast decay time of the main X^0 emission, we cannot extract a meaningful polarization decay time. However, in a simple picture the stationary (time integrated) polarization is determined by the initially created polarization P_0, the lifetime of the electron-hole pair τ and the polarization decay time τ_s through $P_c = P_0/(1+\tau/\tau_s)$ [55; 96]. As a direct consequence of the very short emission time τ measured here, even for valley polarization decay times in the ps range steady-state measurements can still yield a substantial P_c and could explain the strong polarization measured for this material (cf. section 2.1.2). Due to the short X^0 PL emission time, no meaningful dynamics can be measured for the linear polarization, which corresponds to the valley coherence dynamics. Note here that valley coherence in WSe_2 is also investigated via magneto-spectroscopy measurements (see section 6.2). The strong valley coherence observed in cw-PL in previous section 2.1.2 stems mainly from photons emitted within 4ps.

The initial trion emission time is much longer than the one of the X^0 in figure 12b, it decays within a few tens of ps, well above the temporal resolution of our experiment. The longer trion emission time allows us to access the time evolution of the valley polarization. This point will be discussed in section 4.3.

4.2 Exciton spin polarization decay due to long range exciton Coulomb exchange in transition metal dichalcogenides monolayers

According to recent theoretical work that we carried out in collaboration with M.M. Glazov [76] neutral excitons from non-equivalent K valleys in TMDCs are coupled by the long range electron hole Coulomb exchange interaction (see also [77; 97]). As a result, exciton spin states are an admixture of states active in $\sigma+$ and $\sigma-$ polarization. Thus, any interaction leading to a phase shift could lead to a rapid decay of the optically initialized circular polarization, in close analogy to neutral exciton spin depolarization in GaAs quantum wells [75]. This will contribute to the fast polarization decay observed in 1ML MoS_2 in pump-probe experiments [98; 99] and in 1ML WSe_2 in Kerr rotation experiments [100] .

This relaxation mechanism does not provide intervalley transfert of electrons; it can be viewed as a simultaneous flip of both electrons and hole spin. The neutral exciton polarization is much more fragile than expected from an oversimplified single particle picture where strong spin-orbit coupling and selective valley excitation prevents valley depolarization.

According to our theoretical estimation [76], we assume that the exciton spin decays due to a Dyakonov-Perel' type mechanism.[101] Hence, the spin decay law is exponential

and spin relaxation rates are given by[75; 102]

$$\frac{1}{\tau_{zz}} = \frac{2}{\tau_{xx}} = \frac{2}{\tau_{yy}} = \langle \Omega_K^2 \tau_2 \rangle, \tag{4.1}$$

where Ω_K is the effective in-plane magnetic field corresponding to the exciton exchange interaction and the angular brackets denote averaging over the energy distribution and $\tau_2 = \tau_2(\varepsilon_K)$ is the relaxation time of second angular harmonics of the distribution function.

A theoretical estimate of τ_{zz} can be obtained taking into account that, in realistic experimental conditions, owing to the fast energy relaxation in the system, the spread of excitons in the energy space is limited by the collisional broadening, $\sim \hbar/\tau_2$, rather than by the kinetic energy distribution. Under this assumption, the trend for the spin decoherence rate can be obtained from Eqs. (4.1) taking into account that [cf. Ref. [75]]

$$\langle \Omega_K^2 \tau_2 \rangle \simeq \Omega_{K_\Gamma}^2 \tau_2, \tag{4.2}$$

where $K_\Gamma = \sqrt{2M\Gamma_h/\hbar^2}$ and $\Gamma_h = 1/(2\tau_2)$ describes the k-space extension of an excitonic wave "packet". It follows then that the scattering time cancels in the right hand side of Eq. (4.2) and

$$\tau_{zz} = \frac{4\hbar\left(q\tau_{rad}\right)^2}{M} \tag{4.3}$$

For an order of magnitude estimate, we set the exciton mass $M = m_e + m_h = m_0(0.46+0.54)$ equal to the free electron mass[26; 70]. We also set $\tau \approx \tau_{rad} = 4.5$ ps. Assuming the PL decay time measured in section 4.1.1 is governed by radiative processes, realistically τ should be regarded as a lower bound of τ_{rad}. We estimate the radiation wavevector $q = \sqrt{\varkappa_b}\omega_0/c$ assuming $\hbar\omega_0 = 1.867$ eV and $\varkappa_b = 5$ (being half of the substrate high-frequency dielectric constant), and obtain $\tau_{zz} \approx 4$ ps. This value is in reasonable agreement with the value of $\tau_s \simeq 7$ ps estimated from PL experiments and with recent pump-probe measurements.[98; 99]. It is important to highlight that even with a value of τ_{zz} in the ps range a high polarization can be obtained in time-integrated measurements as the PL decay time τ is also ultra-short (see section 4.1.1).

Similarly to the circular polarization degree whose decay is governed by τ_{zz}, the linear polarization decay for the neutral A-exciton is governed by the in-plane pseudospin relaxation times τ_{xx} and τ_{yy}. As follows from Eq. (4.1) they are of the same order of magnitude as τ_{zz}.

4.3 Stable valley index for trions in WSe_2 MLs

The discussion below is devoted to the observed trion dynamics in WSe_2 monolayers, that we cannot distinguish from exciton in ML MoS_2.

Establish precise requirements for valley index manipulation is out of the scope of this thesis. However it seems obvious that if a given excitonic complex exhibits a stable valley index and a reasonable radiative lifetime, its chances to fulfill such requirements are higher than in the X^0 case. Indeed, because of the long range Coulomb exchange interaction, a fast polarization decay time of about 400fs has been measured for X^0 [100] in WSe_2 ML. We also saw in this chapter that its emission time is only a few ps.

The initial trion emission time is much longer than the X^0 one as observed in figures 12 and 13a. It decays within few tens of ps (see table 4.1), comfortably above the temporal resolution of our experiment. The longer trion emission time allows us to access the time

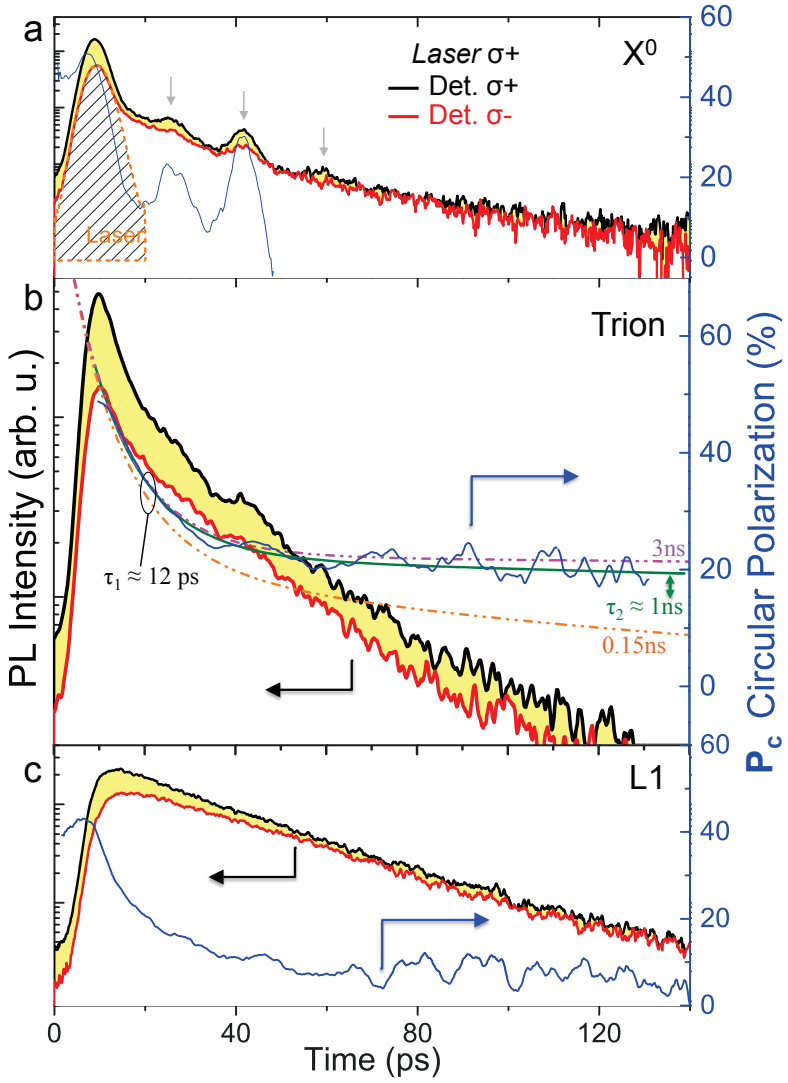

Figure 7: **Time resolved photoluminescence.** T=4K. Laser polarization σ^+. (a) Left axis: X^0 PL emission (in log-scale) co-polarized (black) and cross-polarized (red) with respect to the excitation laser as a function of time. Right axis: circular polarization degree of the PL emission. As the PL intensity decays very quickly, we clearly observe a periodic signal of laser reflections, marked by arrows. (b) same as (a), but for trion emission. The polarization well reproduced by a bi-exponential decay using an initial, fast decay time of τ_1 =12 ps and a long decay time τ_2 =1 ns (solid green line). Lower bounds (dotted orange line for τ_2 =150 ps) and upper bounds (dotted purple line for τ_2 =3 ns) of the slow decay are shown. (c) same as (a), but for localized exciton emission L1.

evolution of the valley polarization. In figure 13b it can be seen that the trion polarization decays with 12 ps from 50% down to 20%, followed by a second decay with a characteristic time of the order of 1ns. The first decay can be linked to the co-existence of trions and excitons during the first few picoseconds and could be due to exchange interaction effects. Once the vast majority of neutral excitons has recombined, the trion polarization evolves differently. This second polarization decay is slower, probably because, in a first approximation, single particle spin flips are needed in addition to valley scattering to change the PL polarization. Given the large spin splittings, these events are scarce and the polarization decays very slowly.

Concerning the origin of the initial 12 ps decay: The trion could be either generated

directly following photon absorption (phonon assisted process), or by a localized electron capturing a free exciton. This second scenario is unlikely, as within the initial decay of 12ps the neutral exciton polarization would have already decayed to zero before capture, which is in contradiction with the strong, remaining trion valley polarization. Due to strong Coulomb exchange in this system [77] a trion fine structure is estimated to be in the few meV range, for instance between trion configurations with the excess electron in the same or different valley with respect to the generated electron-hole pair. Although the linewidth of the PL emission of the trion is considerably smaller in ML WSe_2 (about 10 meV) than in MoS_2 (about 70meV), we cannot extract any trion fine structure splitting for the investigated samples and there are currently no reports in the literature. Clear theoretical predictions for the trion polarization dynamics including Coulomb exchange are currently not available, but it can be expected that the trion fine structure influences the trion polarization dynamics observed here. Also the recently reported electronic exciton-trion coupling could play a role [103].

For times $t \geq 40\ ps$ we can infer a typical decay time of the order of 1ns: compare in figure 13b the data and the plotted exponential decay (solid green line). Please note that a typical decay time of 150 ps gives an estimation that is clearly below the observed experimental polarization (orange dash-dotted line in figure 13b). Measurements carried out at different laser excitation energies show similarly encouraging results.

The emission of localized states we labeled L1 shows a fast initial polarization decay with a characteristic time of about 13 ps before reaching a polarization plateau as in the trion case, albeit at a smaller value around 8%. It is difficult to interpret this dynamics as the origin of those "'localized"' states is still unknown.

In conclusion, the trion PL polarization dynamics shows clear, experimental proof of the robustness of the optically initialized valley polarization. Its emission time and its long polarization decay time makes it an ideal candidate for future valley index manipulation experiments.

4.4 Conclusion

In this chapter we investigate the PL emission dynamics of two different TMDCs MLs; MoS_2 and WSe_2.

For MoS_2 it was not possible to distinguish the emission component which originates from the neutral exciton from the one which originates from the trion. The overall emission time is very short, a few ps. Such a short emission time prevent us to investigate the polarization decay, which is also expected to be in the ps range due to coupling of K^+ and K^- states by the long range exciton Coulomb exchange.

For WSe_2, the excellent optical quality of the sample allows to clearly distinguish between the neutral exciton, the trion and the localized states. Although the X^0 PL emission decays very quickly (4ps, same configuration as MoS_2), the trion emission is much longer (tens of ps) and allows to monitor the polarization decay time. The decay is at first fast (τ_1 = 12ps) but after 40ps, the polarization remains almost constant (τ_2 = 1ns $\gg$ emission time).

This demonstrates the robustness of the optically initialized valley polarization and makes the trion a possible candidate for future valley index manipulation experiments.

The very fast emission time reported in the present chapter indicates that the excitonic effects play a central role in the physics of those new materials. In the next chapter, we will

use several spectroscopy techniques to directly demonstrate the important role played by excitons in TMDCs materials.

Chapter 5

Excitonic effects in monolayer WSe_2

In this chapter, we investigate the exciton properties in WSe_2 monolayers.

Exciton binding energies of hundreds of meV are measured due to the strong vertical confinement, reduced dielectric screening and high effective masses. It is clear now that excitons govern the direct optical transitions for all TMDCs monolayers [20; 33; 70; 71; 81; 87; 91; 104; 105].

Here we show that the light-matter interaction in monolayer WSe_2 is strongly enhanced when the incoming electro-magnetic wave is in resonance with the energy of the exciton states, below the electronic bandgap. We perform second harmonic generation (SHG) spectroscopy as a function of laser energy and polarization at T=4K. At the exciton resonance energies we record an enhancement by up to 3 orders of magnitude of the SHG efficiency. The energy and parity of the exciton states showing the strong resonance effects are identified in 1 and 2-photon photoluminescence excitation experiments. Exciton excited states identification, corroborated by first principle calculations allows us to determine an exciton binding energy of the order of 600 meV in ML WSe_2.

Initially, TMDCs ML intrinsic unique spin and k-valley phenomena have been described in a single particle picture, which was used for simplicity in chapter 3. That was called into question in chapter 4, in which we already explained the fast polarization decay of the X^0 exciton as due to the intervalley coupling via the Coulomb exchange interaction. Indeed, in reality electrons and holes are bound by the strong Coulomb interaction and form excitons which in a standard 2D system like GaAs quantum wells can be described by a Rydberg series, analogous to the hydrogenic system, with even ns and odd np states (n=1, 2, 3, ...). In TMDCs MLs, large exciton binding energies of few hundreds of meV are expected due to the strong 2D confinement, the rather large effective electron mass and small effective dielectric constant [70; 71; 81; 105]. The strong impact of exciton states on the new physics related to valley index manipulation and non-linear optical effects are revealed in this chapter [33].

In the experiments reported below (figures 14 and 2), we combine the energy and the high polarization selectivity of non-linear and linear optical spectroscopy to first uncover the excited exciton spectrum of excited exciton states and second, excite the exciton resonances for controlled valley state preparation. We clearly distinguish between absorption maxima associated with effects of exciton-phonon coupling and excited exciton states (2s, 2p, ...) [106–108]. The positions of the exciton states and the free carrier bandgap are affirmed by one-photon and two-photon optical spectroscopy measurements together with ab initio GW-Bethe Salpeter Equation calculations [109] developed in collaboration with I. Gerber at the LPCNO. These measurements coupled to calculations yield a good estimation of the exciton binding energy. We observe additional excitonic resonances by performing second harmonic generation (SHG) excitation spectroscopy, which allows us to tune the frequency doubling efficiency over three orders of magnitude. Following resonant excitation of the excited exciton states we demonstrate strong exciton valley polarization. Our measurements show that significant exciton valley coherence [32], corresponding to the generation of a coherent superposition of two exciton spin states from the K+ and K- valleys, can be created with a two-photon process. This demonstrates that the exciton alignment can be controlled with an excitation energy much lower than the band gap. None of these effects were demonstrated before in 2D or quasi-2D systems.

5.1 Experimental results

Measurements presented in this chapter were performed using the Attodry700 cryostat, the cw detection system is composed of an acton500i spectrometer and a Si-CCD camera. For the 2Photon-PLE (Excitation of Photoluminescence) experiments, the flake is excited by picosecond pulses generated by a tunable optical parametric oscillator (OPO) synchronously pumped by a mode-locked Ti:Sa laser. The wavelength can be tuned between 1 and 1.6 μm. The typical pulse and spectral width are 1.6 ps and 3 meV respectively; the repetition rate is 80 MHz. For the 1Photon-PLE the excitation is provided by the frequency doubled OPO pulses. In that case the laser power has been kept in the µW range, i.e. in the linear absorption regime.

We investigate individual WSe_2 ML flakes obtained by micro-mechanical cleavage of bulk WSe_2 crystal (from 2D Semiconductors, USA) on 90 nm SiO_2 on a Si substrate. The 1ML region is identified by optical contrast (figure 1a) and by photoluminescence (PL) spectroscopy. More details on sample and measurement setup can be found in chapters 1 and 2.

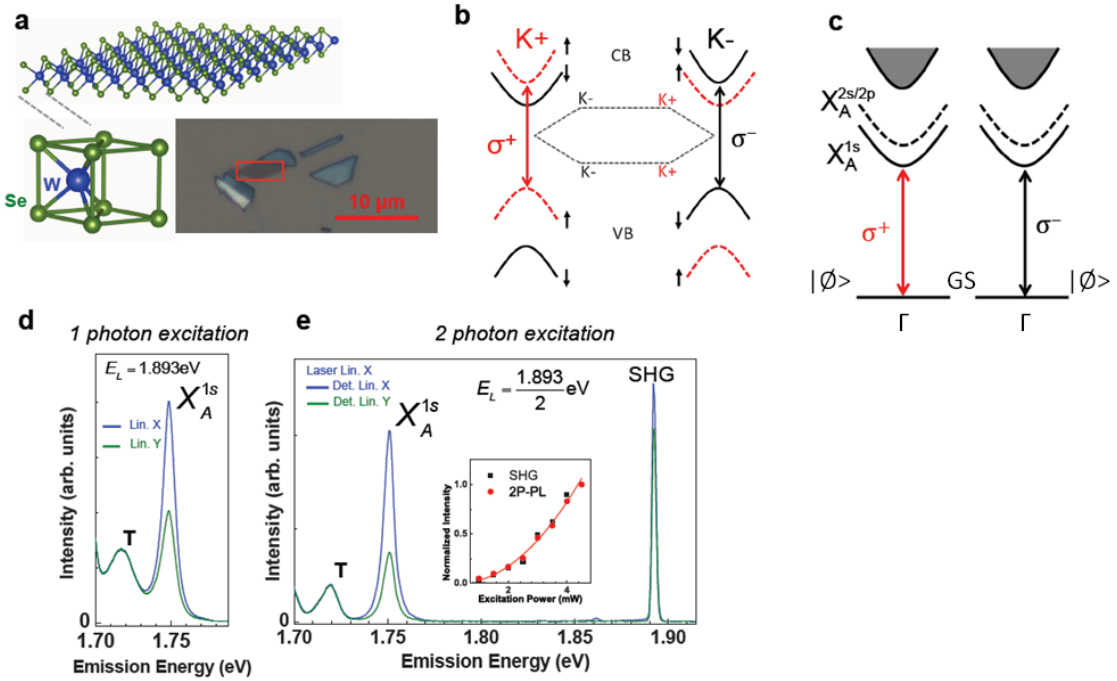

Figure 1: (a) Monolayer (ML) WSe_2 structure with broken inversion symmetry. The ML is identified by optical contrast measurements as is marked by the dashed rectangle. (b) Optical valley selection rules for circularly polarized laser excitation in the single particle picture for ML WSe2. (c) Optical valley selection rules in the exciton representation. For simplicity, only the A-exciton series is shown. (d) Optical valley coherence generation following absorption of one, linearly polarized photon. The neutral exciton X_A^{1s} and the trion (T) transitions are marked. PL spectra co-polarized (cross) with the laser are shown in blue (green). The onset of the localized state emission can be seen at low energy. (e) Optical valley coherence generation via two-photon absorption at T=4K. The neutral exciton $X_A^{1s}$and the trion (T) transitions are marked. PL spectra co-polarized (cross) with the laser are shown in blue (green).

In the experiments presented here the light is propagating perpendicular to the 2D layer plane. Thus the selection rules for interband transitions impose that the one-photon absorption occurs on the ns (n is an integer) exciton states whereas np states will be allowed for two photon transitions [106; 107].

Figure 14e displays the results of two-photon optical spectroscopy experiments performed on the WSe_2 ML for a linearly polarized excitation laser with energy $E_{laser} = 0.946$ eV, much lower than the optical gap of around 1.7eV. The narrow line at $E = 1.893eV = 2 \times E_{laser}$ corresponds to the laser Second Harmonic Generation (SHG) in the WSe_2 ML. The PL components at lower energy at E= 1.75 eV and E= 1.72 eV are the neutral and charged exciton (trion) spectra respectively. Under linearly polarized laser excitation, only the highest energy peak shows linear polarization in emission and is therefore ascribed to the neutral exciton ground state X_A^{1s} (simple bound electron-hole pair), as a coherent superposition of valley exciton spin states is created [32; 110]. As expected both the X_A^{1s} luminescence intensity following two-photon absorption and the SHG intensity increase quadratically with the laser excitation power (see inset in figure 14e) [111–113].

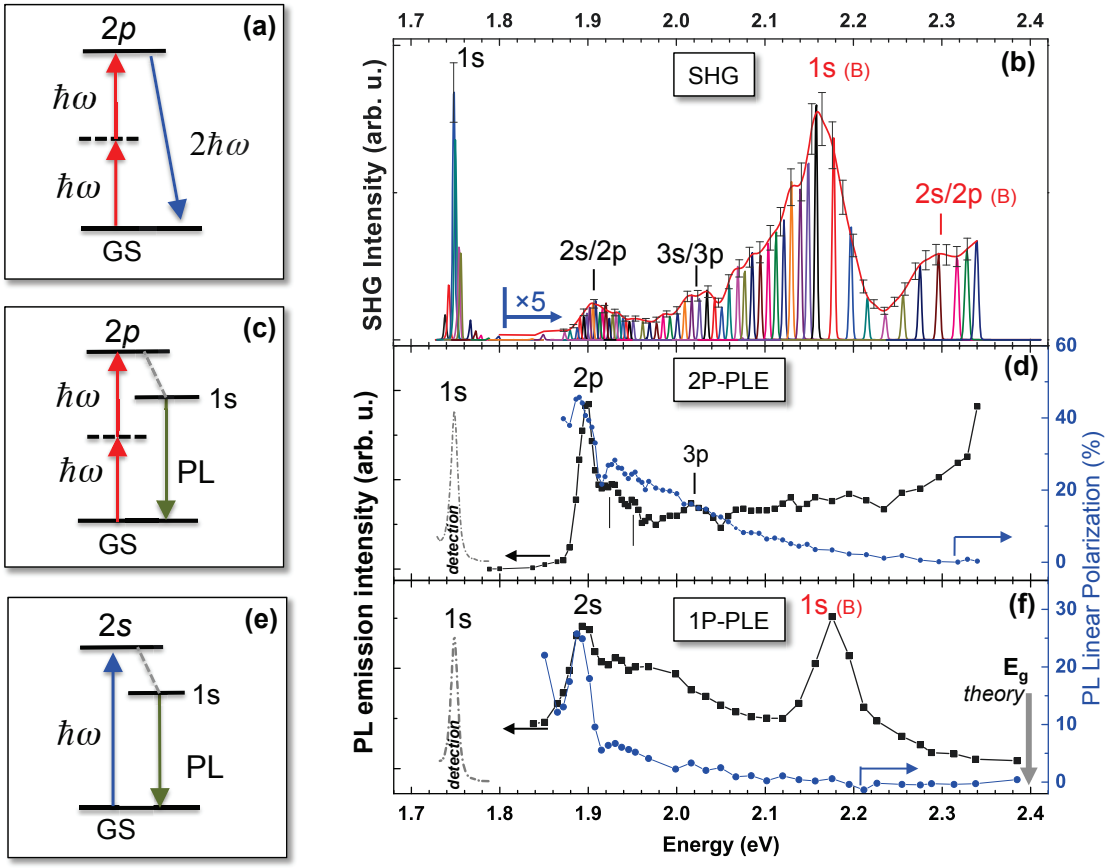

Figure 2: (a) schematic for SHG when 2 incident photons energy is resonant with the 2p state of the A-exciton (b) results of SHG spectroscopy at T=4K as a function of $2\hbar\omega$. (c) schematic for 2 photon PLE (d) 2 photon PLE intensity (left axis, black squares) and linear polarization (right axis, blue circles) as a function of $2\hbar\omega = 2E_{Laser}$). (e) schematic for 1 photon PLE (f) 1 photon PLE intensity (left axis, black squares) and linear polarization (right axis, blue circles)as a function of $\hbar\omega$. The dashed green line in (c) and (e) represent the energy relaxation path, e.g. by phonon emission.

5.2 Complementary spectroscopy techniques allow excitonic state identification

Here we focus on the optical spectroscopy of the neutral X_A exciton in ML WSe_2 which is characterized by a luminescence spectrum with FWHM≈ 10 meV at T=4 K. This is much narrower than the spectra measured so far for MoS_2 MLs (see section 2.1 and 3) [15; 50]. This allows a precise determination of the exciton excited state spectra both for one or two photon optical spectroscopy experiments. An additional advantage of choosing this material is that the maximum of the valence band at the Γ point lies more than 500 meV below the K point [54] whereas for ML MoS_2 this energy difference is just a few tens of meV according to recent calculations [64; 70]. When performing the excitation spectroscopy in ML WSe_2, the excitation of indirect transitions should thus not energetically overlap with key features associated to the direct transition of excited exciton states.

5.2.1 Second Harmonic Generation spectroscopy.

To uncover exciton resonances we employ, among others, a non-linear optical technique with distinctly different polarization selection rules due to the intricate interplay between the electric and magnetic dipole interaction. Broken inversion symmetry and strong light

matter interaction make ML WSe_2 an ideal material for non-linear optics. SHG generation at a *fixed* wavelength is commonly used for few layer TMDCs to probe crystal inversion symmetry [111–113].

In the experiment in figure 2b, the intensity of the SHG signal is plotted as a function of twice the excitation laser photon energy. Over the scanned range between 1.7 and 2.4eV, we observe for all energies a measurable SHG signal. Strikingly we observe a variation in SHG intensity over 3 orders of magnitude in fig.2b, although the excitation power is kept constant in the experiments.

A particularly surprising feature of these experiments is the strong SHG signal when the two-photon laser energy is in resonance with 1s A-exciton (1.75eV) and 1s B-exciton (2.17eV), whose energies were determined in the same sample through PL and reflectivity [110] (see figure 6 in section 4.1.2). The clear SHG resonances observed indicate therefore that contributions beyond the usual electric-dipole coupling of the light-matter interaction are involved. Below we outline the key concepts [33]:
The signal plotted in figure 2b is directly related to the non-linear dielectric susceptibility tensor $\chi^{(2)}$ that can be evaluated with third order time dependent perturbation theory. As only very recently demonstrated for bulk ZnO, where the exciton binding energy is strong ($E_B^{1s} \approx 60$ meV), the efficiency of SHG depends not only on the symmetry of the crystal, but also on that of the exciton states [114; 115]. Close to resonance of an excitonic state $|\Psi_{exc}\rangle$ one can write:

$$\chi^{(2)}_{ijk}(-2\omega;\omega,\omega) \propto \langle\varnothing|\hat{V}_i^{2\omega}\frac{|\Psi_{exc}\rangle\langle\Psi_{exc}|}{E_{exc}-2\omega\hbar-i\Gamma_{exc}}\hat{V}_j^{\omega}\sum_{\nu}\frac{|\Psi_{\nu}\rangle\langle\Psi_{\nu}|}{E_{\nu}-\omega\hbar-i\Gamma_{\nu}}\hat{V}_k^{\omega}|\varnothing\rangle$$

The term with $E_{exc}-2\omega\hbar-i\Gamma_{exc}$ is dominant over similar terms obtained in the summation over all possible virtual exciton states (ν), as for a real, excitonic state the damping $\Gamma_{exc} \ll \Gamma_{\nu}$ since it lives longer than a virtual state. The tensor components (i,j,k) may belong to the $+,-,0$ standard set, where +(-) correspond to right (left) circularly polarized components and 0 to z-polarized ones, z is perpendicular to the ML. To go beyond the electric dipole approximation, the exciton-photon is expanded as:

$$\hat{V}_i^{\omega} = \hat{V}_i^{DE}(\omega) + \hat{V}_i^{QE}(\omega) + \hat{V}_i^{DM}(\omega) + h.c. \tag{5.1}$$

where $\hat{V}_i^{DE}(\omega)$, $\hat{V}_i^{QE}(\omega)$, $\hat{V}_i^{DM}(\omega)$ are respectively the matrix elements corresponding to electric dipole, electric quadrupole and magnetic dipole [116]. The matrix element corresponding to the electric quadrupole (QE) interaction vanishes in ML WSe_2 for symmetry reasons, in contrast to bulk ZnO. We can write the remaining 2 interactions, namely the electric (DE) and magnetic dipole (DM) interactions for pure $\sigma^{\pm}$ circularly polarized light as:

$$\hat{V}_{\pm}^{DE} = -ie\frac{\mathscr{E}_0}{4m_0\omega}e^{i\omega t}(\hat{p}_x \pm i\hat{p}_y) \tag{5.2}$$

$$\hat{V}_{\pm}^{DM} = iek_Z q_Z \frac{\mathscr{B}_0}{2m_0}\vec{e}.e^{i\omega t}\hat{L}_{\pm} \tag{5.3}$$

where e corresponds to electron charge, m_0 is the electron vacuum mass, $q_Z = q = c/\omega$ and $\mathscr{B}_0 = \mathscr{E}_0/c$ [116]. It can be seen that the DM and the DE interactions are never in competition for a given transition, but are complementary to each other. We identify as the most efficient SHG sequences governed by equ. 5.1 processes that involve two DE and, very importantly, one DM transition (figure 3 illustrates those processes). This explains

the strong SHG that is observed at the 1s A-exciton resonance: First the DM interaction couples the ground state $|\varnothing\rangle$ to a virtual 2p state. Second, the 2p state can be coupled to the 1s state via the DE interaction. Finally, the DE interaction couples the 1s virtual state back to the ground state $|\varnothing\rangle$, giving rise to the SHG signal. In similar fashion, the ground state can couple to the 2p A-exciton via two DE transitions (energy $\hbar\omega$), and the SHG signal is emitted via the DM interaction, as shown in Fig. 2a. Efficient SHG generation involving relatively weak DM transitions (by typ. 2 orders of magnitude compared to DE) comes from the presence of energetically well defined excitonic resonances in ML WSe_2 with finite damping Γ_{exc}, as can be seen from equation 5.1, explaining the sharp SHG resonances with FWHM very similar to the exciton emission, compare Fig. 2b and 14a.

However the dipolar magnetic effect is known to be much weaker than the dipolar one [116]. An alternative to overcome this issue would be to replace it by a third dipolar electronic interaction, which should give the same results according to the optical selection rules in C_{3h} group. Since $\phi_{2,l}(0) = 0$ a necessary assumption would be that the states are in fact mixed, so that they would correspond to the coherent superposition (K valley):

$$\psi_{2p+} = \alpha\phi_{2,l=1}(r)\,u^{c}_{\mathrm{K}}(r)\,u^{v*}_{\mathrm{K}}(r) + \beta\phi_{2,l=0}(r)\,u^{c}_{\mathrm{K}'}(r)\,u^{v*}_{\mathrm{K}'}(r)$$

which transform according to the Γ_3 representation.

From the C_{3h} table (see annexe A), the 2_{p+} state, obtained by 2 photon generation from the dipolar interaction with a probability proportional to $|\alpha|^2$, would then emit a single photon with $\hat{V}_i^{\mathrm{DE}}$, which would be possible through the 1s component, with a probability proportional to $|\beta|^2$.

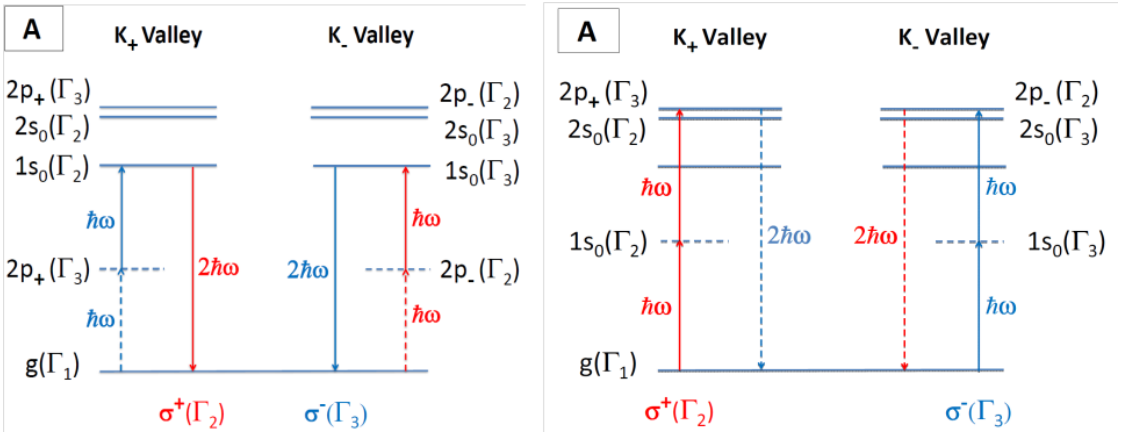

Figure 3: Second harmonic generation process with the $2\hbar\omega$ emitted photon in resonance with the A-$1s_0$exciton states (left), or with the A-$2p_{\pm}$ exciton (right). The solid arrows represent electric dipolar interactions, while the dashed one the magnetic dipolar transitions. Note that the selection rules deduced from the macroscopic description are indeed obtained again. The dashed horizontal lines represent virtual states. color code: red = σ+ polarized; blue = σ− polarized; line code: solid line = DE; dashed line = DM

We tentatively assign to exciton excited states s= 2 and s= 3 associated to the A exciton. We observe clearly in the SHG curve X_A^{1s} and X_B^{1s} strong resonances at E= 1.75 eV and E= 2.17 eV, respectively. From this measurement we get the difference between the SO energy splitting in the conduction and the valence band of 420 meV in agreement with the one photon-PLE results (figure 2f), the reflectivity spectra [110] (see figure 6 in section 4.1.2) and the calculated value of the SO splitting, see figure 8a, in good agreement

with a previous study [71]. The SHG signal at the X_A^{1s} resonance is three orders of magnitude stronger than away from an exciton resonance [117]. In addition to the 1s A- and B-excitons, we observe clear resonances at 1.9eV and 2.03eV. Interestingly we observe in figure 2b a spectral component 140 meV above the X_B^{1s} resonance which could be related to the X_B^{2p} state. This means the energy splitting between the first excited exciton state and its ground state is similar for the X_A and X_B exciton. This result is indeed expected as the A and B valence states have very similar effective masses (see figure 8a). To clarifiy the exact origin of these transitions and to investigate their excitonic nature and their symmetry, we perform in addition to SHG spectroscopy 2-photon and 1-photon PL excitation experiments.

5.2.2 Two-photon absorption experiments.

The dependence of the neutral exciton X_A^{1s} luminescence intensity as a function of twice the laser excitation energy $2\hbar\omega = 2E_{Laser}$ is plotted in figure 2d. In this two-photon Photoluminescence Excitation (2P-PLE) experiment, the laser power is kept constant and the detection energy is set to the emission peak of X_A^{1s}. The intensity variation of the 2P-PLE curve displays two main features: a clear peak at 1.898 eV and a clear monotonous increase in the high energy region 2.35 eV. The first energy peak labeled X_A^{2p}, 140 meV above the X_A^{1s} exciton emission, corresponds to the 2p exciton state absorption allowed for two-photon optical spectroscopy (the X_A^{2s} absorption is forbidden by the two photon selection rules). The vertical arrow labeled $E_{gap} = 2.4 \pm 0.2$ eV corresponds to the calculated energy of the onset of the continuum states (free electron-hole absorption) as evidenced by the single-particle gap in figure 8a, calculated at the GW_0 level including spin-orbit coupling (collaboration with I. Gerber). This value is slightly smaller than a recent theoretical estimate [21] (2.50 eV), the discrepancy can be attributed to differences in computational settings. If we define the exciton binding energy as $E_{gap} - E(X_A^{1s}) = E_b$ we can estimate $E_b = 600 \pm 200$ meV. A high neutral exciton binding energy is consistent with the measured charged exciton binding energy in figure 14d,e : E_b(trion) = 35 meV [72; 118]. The calculated value E_{gap} = 2.4 eV explains very well the 2P-PLE signal increase in the 2.3-2.35 eV region. This increase cannot be assigned to the absorption of an exciton state associated to a Van Hove singularity [81] since the absorption on its ground state is forbidden in a two-photon process. Another possible interpretation lies on "'band nesting effect"', based on single particle transition in region of the Brillouin zone where $\nabla_{\vec{k}} E_c(k) \approx \nabla_{\vec{k}\, E_v(k)}$ [119]
.

Remarkably a detailed analysis of the spectra around the X_A^{2p} absorption region shows two secondary peaks located 30 and 60 meV above the 2p main exciton peak (see figure 4). We interpret these secondary peaks as the result of the enhancement in the ground-state PL signal for excitation energies permitting resonant phonon relaxation down to the X_A^{2p} states. Indeed Raman studies identified two optical phonon modes with energy of about $E_{phonon} = 31meV(250cm^{-1})$ in WSe_2 ML (see figure 5) [120; 121].

The mode labeled E_{2g}^1 is strong in one-photon absorption, whereas the mode labeled A_g^1 is more likely to play a role in two-photon processes for symmetry reasons. Because the resonances are much broader than the spectral width of the exciting laser, the peaks observed are not attributed to simple inelastic scattering of the laser line (i.e., Raman lines), but rather to enhanced PL when the laser energy corresponds to $X_A^{2p} + E_{phonon}$ and $X_A^{2p} + 2E_{phonon}$ for the peaks observed in figure 2a at 1.93 and 1.96 eV respectively. Also, the fast relaxation from 2p to 1s exciton states may contribute to the broadening of the resonances, together with inhomogeneous broadening of the exciton states in the sample.

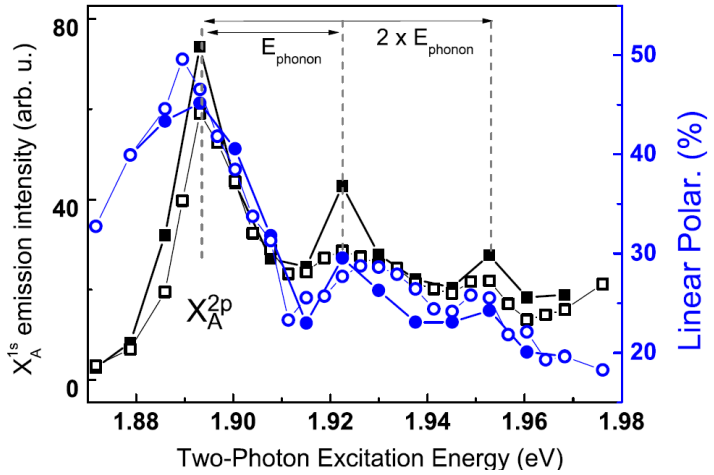

Figure 4: Resonances in two-photon absorption intensity at T=4K corresponding to the X_A^{2p} transition and phonon assisted absorption at energies $X_A^{2p} + E_{phonon}$ $X_A^{2p} + 2E_{phonon}$

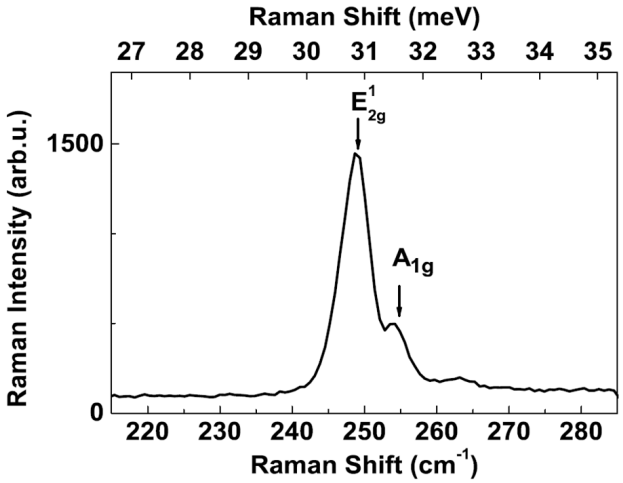

Figure 5: Raman signal on the same sample obtained with HeNe laser excitation. The spectrally narrow emission allows separating the two Raman modes E^1_{2g} and A^1_g.

In contrast to the SHG experiment, the X_A^{1s} and X_B^{1s} absorption are dipolar forbidden and indeed absent in figure 2d, in agreement with electric dipole selection rules. Also, taking the trion emission as a measure for 1s exciton generation, we find that resonant 2-photon excitation of the 2p state results in strong trion emission, whereas resonant 2-photon excitation of the 1s state results in negligible trion emission. This observation is consistent with the assumption that 2-photon excitation of the 1s state is only allowed combining one DE and one DM transition, and not via two DE transitions.

A clear resonant signal is also evidenced at E=2.03 eV, as for SHG spectroscopy. We tentatively assign this peak to the $X_A^{(3p/3s)}$ state though the DFT simulated spectrum does not present a clear feature in this region. The theoretical determination of these high energy exciton excited states, using beyond mean-field approaches is very challenging since it raises serious problem of convergence of computation algorithm [81; 122], due to their highly delocalized character.

In contrast to the SHG results, the 1s exciton transitions are not observed in two-photon *absorption* experiments, as demonstrated in figure 2d, as they are electric-dipole forbidden.

5.2.3 One-photon absorption spectroscopy.

The findings from the two polarization resolved non-linear optical techniques are further complemented by one photon optical spectroscopy. In this case the polarization selection rules give access to the s-exciton states whereas the p-states are dipole forbidden. Figure 2f and in more details figure 7 display the one photon PL Excitation (1P-PLE) results. In this case the luminescence intensity of the 1s neutral exciton is a linear, and not quadratic, function of the laser intensity. A clear peak corresponding to the X_A^{2s} optically allowed absorption is observed at 1.9 eV, 140 meV above the ground state X_A^{1s} . Comparing the results of 1P-PLE and 2P-PLE in figure 2d and f we can infer that the X_A^{2s} and X_A^{2p} exciton states have the same energy within the spectral resolution of our excitation spectra (which is of the order of 5 meV) [123; 124]. An energy splitting $X_A^{2p} - X_A^{2s}$ is possible because of the combined effects of the spin-orbit and exciton exchange interactions. We also observe in figure 2f an additional peak at 1.93 eV, about 30 meV above the X_A^{2s} absorption energy, which could be assigned to the phonon resonances similarly to the one identified in the 2P-PLE (figure 2d).

5.2.4 Efficient generation of exciton valley coherence in two-photon absorption.

A key argument for the attribution of the observed maxima in one and two-photon absorption to excitonic states comes from the simultaneous increase of the PL polarization of the 1s exciton states. Following excitation with linearly polarized light, the X_A^{1s} exciton emission is linearly polarized but its amplitude globally decreases when the laser energy increases (figure 2d, f), except when in resonance with an excited exciton state.

We emphasize that this observation of exciton alignment is independent of the direction of the incident laser polarization (as can be seen in figure 6), which confirms that the observed linear polarization is not due to an in-plane asymmetry inducing exciton anisotropic exchange interaction as for many 1D and 0D semiconductor systems [4]. In

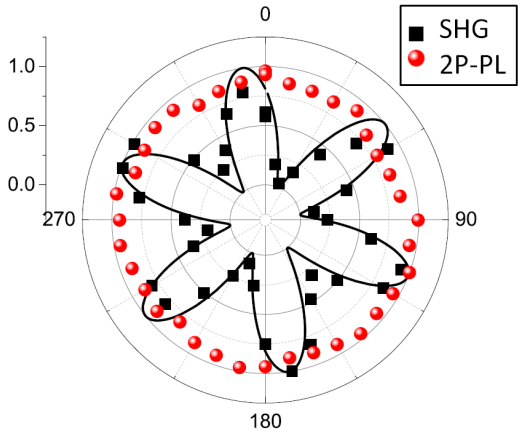

Figure 6: In this experiment excitation and detection are kept lineraly co-polarized, E_{LASER} = 1.893/2 eV. As the laser polarization and the detection polarisation are simultaneously rotated, the maximum of the 2-photon PL signal follows the laser polarization, see red symbols. As a result we observe a circle in the polar plot. In contrast, the polarization axis of the SHG signal is given by the crystal symmetry, shown here as a black line, the black squares show the measured SHG intensity [125].

contrast to the exciton spin coherence evidenced in resonant excitation of GaAs quantum

wells [1; 126], here the linear polarization probes a spin coherence arising from excitons built from electron-hole pairs of two different valleys in k-space [32]. The results presented in figure 2d demonstrate for the first time in a semiconductor, to the best of our knowledge, that significant exciton spin coherence can be created with a two-photon process. It is clear from figures 2d and f that the different resonances in intensity associated to the 2p and 2s exciton absorption are accompanied by a clear enhancement of the exciton PL linear polarization which is multiplied by a factor of more than two. Therefore the photogeneration of a coherent superposition of valley K+ and K- exciton states is enhanced when the absorption occurs on one of its excited exciton states. Valley coherence is strong when the excited state X_A^{2s} (or X_A^{2p}) is directly photogenerated. This probably results from a fast intra-exciton energy relaxation ($2s \rightarrow 1s$ or $2p \rightarrow 1s$) preserving the initially created coherent superposition of states.

In contrast to the coherent exciton alignment with the excitation laser polarization, the second harmonic generation polar plot in figure 2b is simply given by the underlying lattice symmetry. This property can be used to deduce the 2D crystal orientation (see figure 6) [111–113; 125].

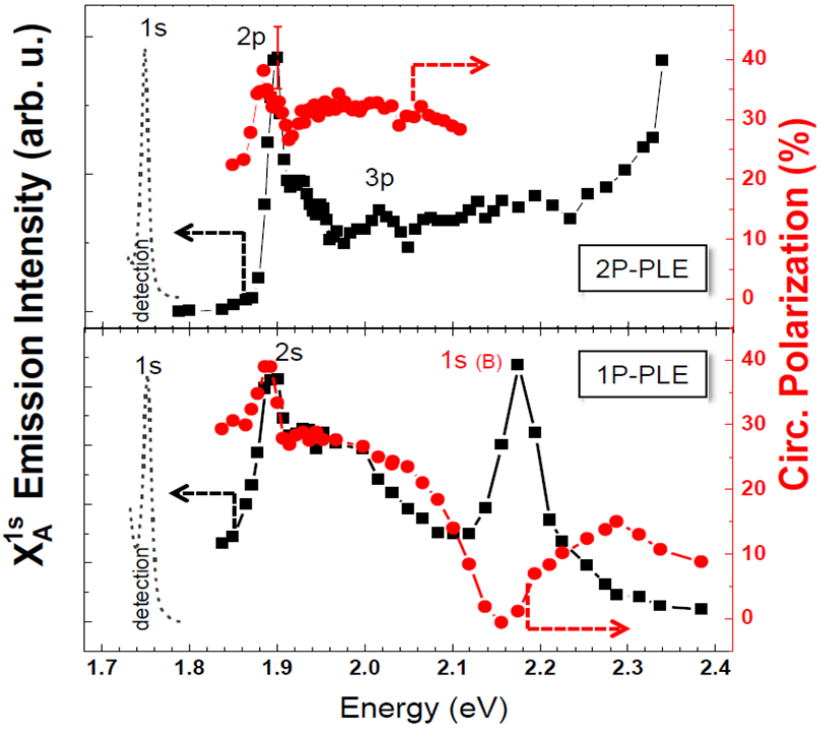

Figure 7: Top. 2-photon PLE intensity (left axis, black squares) and circular polarization degree of the 1s A-exciton PL (right axis, red circles) as a function of $2\hbar\omega = 2E_{Laser}$. Bottom. 1-photon PLE intensity (left axis, black squares) and circular polarization degree of the 1s A-exciton PL (right axis, red circles) as a function of $\hbar\omega$. The polarization decays with time T_1, the coherence with time T_2, where the maximum $T_2 = 2T_1$, see the seminal work of M. Z. Maialle et al, [75]. As the PL emission time is finite and T_2 can be longer than T_1, it is therefore possible to observe higher coherence than polarization for a system in PL experiments. Please note that the K+ and K- valley excitons in the 1s and 2s exciton states are coupled via the Coulomb exchange interaction, which is not the case for the 2p exciton [76].

Remarkably, in addition to the valley coherence, also the valley polarization is strongly enhanced when the circularly polarized excitation energy is resonant with the excited exciton state X_A^{2s} or X_A^{2p}, as probed by the PL circular polarization in the 1P-PLE and 2P-PLE experiments shown in figure 7. A clear polarization peak is observed for an energy

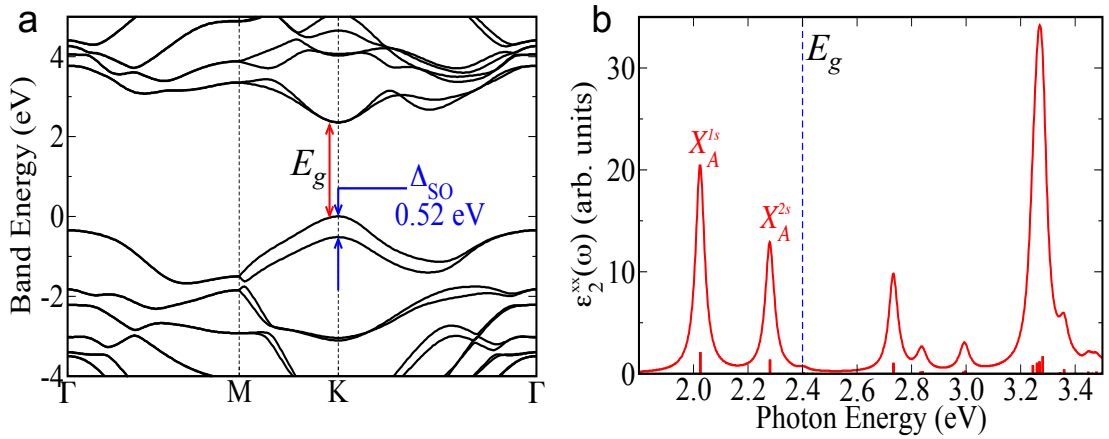

Figure 8: (a) Quasiparticle band structure of WSe_2 monolayer at the GW_0 level, including spin-orbit coupling perturbatively. (b) Frequency dependent imaginary part of the transverse dielectric function including excitonic effects and oscillator strengths of the optical transitions (bars), calculated at the BSE-GW_0 level without spin-orbit coupling. The corresponding GW_0 gap (E_g = 2.4 ± 0.1eV) is also indicated. Collaboration with I. Gerber (LPCNO).

5.3 Exciton levels in ML WSe_2

The A-exciton binding energy is defined as the difference between onset of the free carrier absorption and the X_A^{1s} emission energy. The three complementary experimental techniques presented in Fig. 2b,d and f have uncovered the excited exciton states 2s, 2p and 3p. The onset of free carrier absorption is less clear, so input from theory is needed. The measured energy difference between X_A^{1s} (1.75 eV) and X_A^{2s} (1.90 eV) is in order of magnitude agreement with the calculated one of 250 meV , as shown in figure 8b, based on GW-Bethe-Salpeter equation. Note that the calculation of the absorption spectrum was performed on a fine (21x21x1) k-point grid, an essential requirement to highlight the excited exciton states X_A^{2s} which were missed in most of the previous calculations [81; 105; 122]. To give an idea of the spatial extension of the exciton wavefunctions in the real space for ML WSe_2, we display in figure 9 (b-f) the work of X. Zhang group in Berkeley for the related material WS_2.

For the two-dimensional Wannier-Mott exciton the binding energy of the ground state 1s exciton writes simply[123; 128] $E_b = \frac{2\mu e^4}{(\epsilon\hbar)^2}$, where μ is the exciton reduced mass, ϵ the effective dielectric constant and e the electron charge. Using $1/\mu = 1/m_e + 1/m_h$, with $m_e = 0.32m_0$ and $m_h = 0.35m_0$ (m_0 is the free electron mass) as deduced from the calculated dispersion curves in the K valley [71] figure 8a), we get an order magnitude estimation for the binding energy of $E_b = 600meV$ with an effective dielectric constant $\epsilon \approx 4$. If we assume a simple hydrogenic Rydberg model the energy separation between n=2 and n=1 exciton s-state would be equal to $\frac{8E_b}{9} \approx 440meV$. It is in strong contradiction with the experimental data presented above which shows that this energy splitting (140 meV) is about 3 times smaller, and also in contradiction with GW0-BSE estimate of this energy difference.

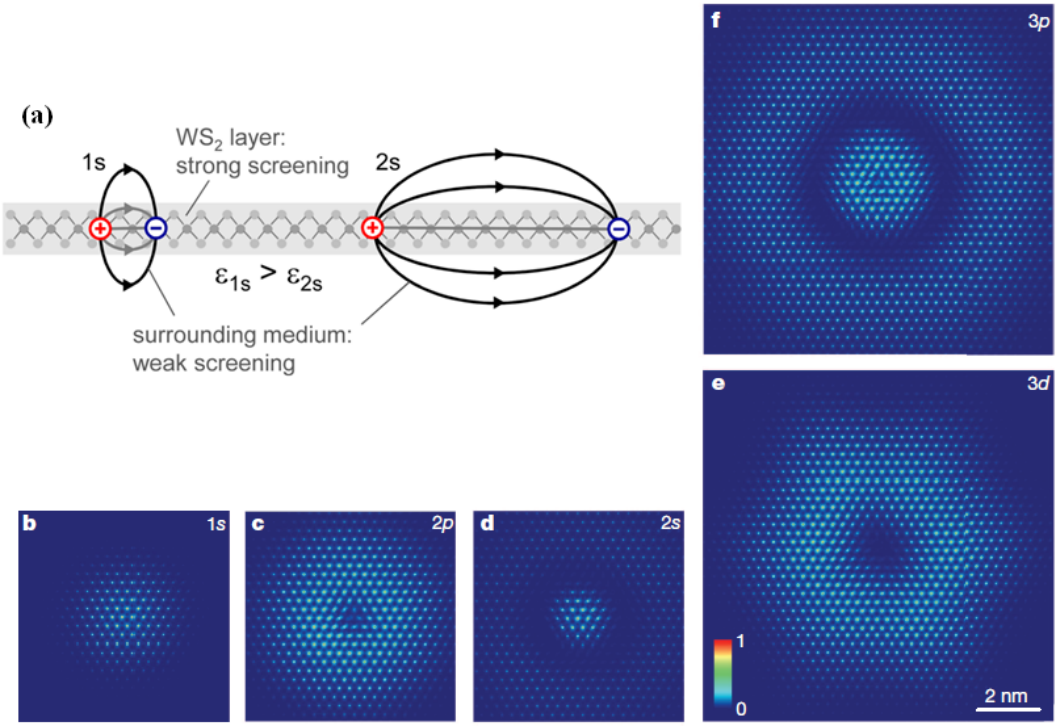

Figure 9: (a) Schematic representation of electron-hole pairs forming 1s and 2s excitonic states in a nonuniform dielectric environment. Figure extracted from ref. [87] (T. Heinz group, Columbia university) (b-f) Real-space exciton wavefunctions in monolayer WS_2 from ab initio GW-BSE calculations. Figure extracted from ref. [127] (X. Zhang group, Berkeley)

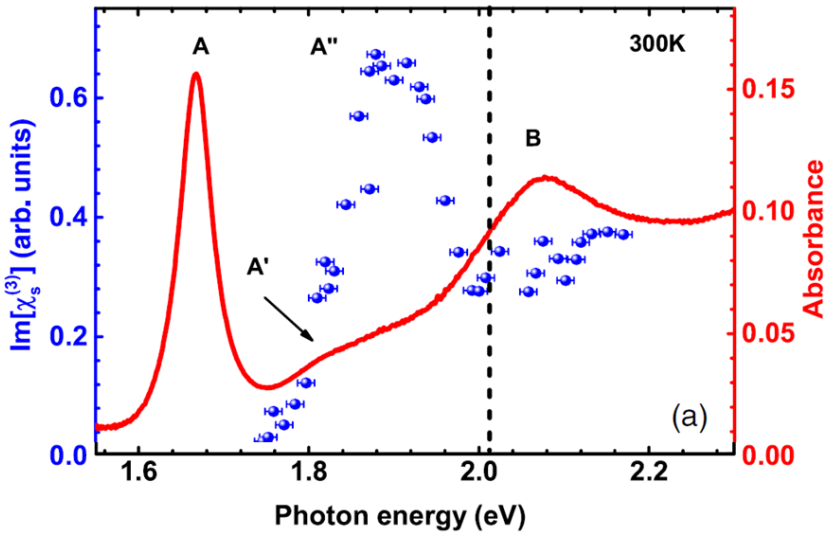

Figure 10: Linear absorption (red line, right axis) and 2PPL excitation spectrum (blue symbols, left axis) measured on monolayer WSe_2 at room temperature (A' corresponds to the 2p state). Figure extracted from ref. [104] (He et al., Cleveland)

Both our experiments and theory demonstrate clearly that the simple hydrogenic model fails to predict the energy of the different exciton states in the TMDC MLs as also predicted by the group of Steven G. Louie [81] and very recently observed in experiments, performed simultaneously to ours, in WS_2 [87; 127; 129], MoS_2 [91], $MoSe_2$ [20] and WSe_2 [104] (see a summary of the main results on figures 10 and 11). In the well known quasi 2D GaAs quantum wells the exciton state series can be well reproduced by the hydrogenic Rydberg

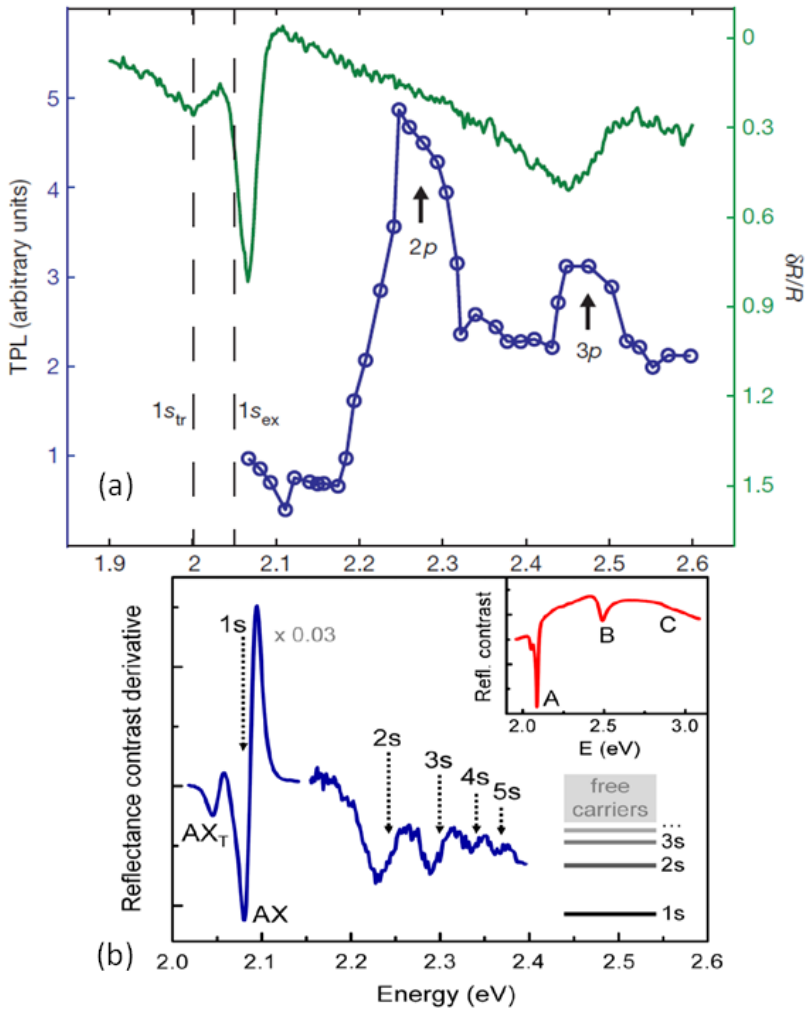

Figure 11: (a) 2photon absorption (blue) and one-photon absorption (green) spectra are measured in single-layer WS2 at 10 K. Figure extracted from ref. [127] (X. Zhang group, Berkeley) (b) The derivative of the reflectance contrast spectrum $\left(\frac{\partial}{\partial E}\right)\left(\frac{\Delta R}{R}\right)$ of the WS2 monolayer. Figure extracted from ref. [87] (T. Heinz group, Columbia university)

model since the 2D layer is surrounded by a barrier material with very similar dielectric constant [106; 107]. In contrast the investigated 2D crystals based on TMDC have an environment perpendicular to the layer with a much smaller dielectric constant than the 2D material (vacuum on one side and SiO_2/Si on the other side). For the exciton ground state, the average distance between the electron and the hole is so short that the exciton wavefunction is mainly located in the WSe_2 layer and the binding energy can be obtained with a simple formula for E_b with an effective dielectric constant close to the bulk WSe_2 value [130]. The excited exciton states such as X_A^{2s} or X_A^{2p} are characterized by a longer average distance between the electron and the hole (see figure 9a). As a consequence the carrier wavefunctions delocalize beyond the WSe_2 2D layer and experience a weaker dielectric constant i.e. stronger Coulomb interaction. The effects of screening/anti-screening associated to the spatial variation of the dielectric constant [131] are in principle well taken into account in ab initio calculations, assuming a large separation between periodic images. The strong dependence of E_b on (anti-)screening explains the remaining difference between the experimental results and the calculations for X_A^{1s} and X_A^{2s} in our work. Also, the calculation neglects the influence of the SiO_2/Si substrate used in the experiment and can be applied, strictly speaking, only to suspended layers.

Concerning the exact determination of the binding energy, one can notice strong differences from one article to the other in the literature. This comes from both the difficulty to estimate the exact gap energy, as well as the difficulties inherent to states identification (see article from T. Stroucken and S.W. Koch [132] in which an alternative theory of excitonic states identification is developed). If we use bandgap values from STS measurements [133; 134], we find respectively $E_B = E_{GAP-E(X_A^{1s})}$ = 400meV and 800meV depending on the reference.

He et al. [104] determined $E_b \approx 370$ meV at T=300 K in ML WSe_2, much lower than our estimated value of 600 meV. Note that the 2p transition is rather weak and difficult to determine in this work. In general a high E_b is consistent with the measured charged exciton binding energy in Fig. 14a and c where : E_b(trion) = 35 meV [72; 118] in this samples. Our value is also consistent with the values reported for E_b by other groups in ML TMDC [20; 87; 91; 104; 127; 129].

Nevertheless, our collaborator I. Gerber has performed an additional calculation of the exciton spectrum. Whereas he initially used a (21x21x1) grid in k-space without spin-orbit coupling to work on the A-exciton only, the new calculation uses a (11x11x1) grid but includes the spin-orbit coupling. The calculation took 2 months to perform using the most advanced clusters (CALMIP) at our disposal. Using a rougher grid in k-space will in principle results in less precision on the excited exciton energies. The key results of this new calculation are:

(a) spin orbit splitting in the valence band between A and B excitons: 410 meV

(b) difference between 1s-2s A exciton state: 120 meV

(c) exciton binding energy 500 meV

So the calculated binding energy of 500 meV is 100 meV lower than the 600 meV obtained in graph 8 presented in this chapter. At this stage it is not clear which of the 2 calculations is a better representation of the physical reality in our sample, but this difficulty is representative of the state of the art of this kind of theory. Further theoretical advances, well beyond the scope of this thesis, are needed to answer precisely the remaining questions.

For those reasons and to give a realistic idea of our precision, we widen the error bars to ±200 meV, which is consistent with the different values estimated from the different bandgap values. Finally, despite the remaining discrepancies, the calculations confirm the strong deviation from the standard hydrogen Rydberg series observed here in the experiment for ML WSe2. We conclude that $E_b = 600 \pm 200$ meV which demonstrates clearly the importance of excitonic effects in TMDCs monolayers.

5.4 Conclusion

In this chapter, we investigate the exciton properties in WSe_2 monolayers. Second harmonic generation spectroscopy, combined with 1 photon and 2 photon PLE, allow us to identify excitonic states. As theoretically predicted, their order and energy spacing cannot be described by the simple hydrogenic model, but can be well reproduced by taking into account the non-locality of the dielectric constant, i.e. screening and anti-screening effects due to spatial variation of dielectric constant and strong spatial delocalization of excited excitonic states. Thus, combined with DFT calculations, our experimental results allow to extract a huge binding energy of about 600 meV.

Finally, we were able to generate exciton valley coherence using 2 photon absorption

when exciting in resonance with 2s and 2p exciton energy, to the best of our knowledge, this is the first experimental demonstration of these effect in a semiconductor.

Now that we have demonstrated the central role played by excitons in WSe_2 (which is true for all TMDCs materials), we will use magneto-PL facilities to further investigate the TMDCs band structure and electronic state symmetries. As for TRPL measurements, where it appears that WSe_2 was more suitable than MoS_2 because of its better optical quality, we will now study the influence of a magnetic field on two high optical quality TMDC materials, namely WSe_2 and $MoSe_2$, whose relatively narrow transition show a clear signature of magnetic field dependence. We will also study the effect of a magnetic field on the optically generated exciton valley coherence.

Chapter 6

Magneto-optics in transition metal diselenide monolayers

In this chapter we present the result of magneto-optics experiments at T=4K performed on two different transition metal diselenides monolayers, namely $MoSe_2$ and WSe_2.[51] The application of a magnetic field perpendicular to the monolayer (ML) plane allow us to lift the underlying degeneracies and extract the Landé g-factors, a technique successfully used in the past to study the bandstructure and excitonic effects of semiconductors [28].
The aim of this comparative study is to perform photoluminescence (PL) experiments on $MoSe_2$ and WSe_2 monolayers in magnetic fields up to ± 9 Tesla in the same set-up, and to measure the neutral exciton and trion emission energy and polarization. We vary the laser excitation energy and helicity, which allows to distinguish between laser induced and magnetic field induced valley polarization, which show very different dependencies on the applied magnetic field when comparing ML $MoSe_2$ with ML WSe_2. The main results are as follows:

In ML $MoSe_2$ the valley polarization of the neutral and the charged exciton (trion) can be tuned with the magnetic field, independent of the excitation laser polarization. In the investigated ML WSe_2 sample the evolution of the valley polarization depends for the trion both on the applied magnetic field and the excitation laser helicity, for the neutral exciton valley polarization only on the latter. For both systems we observe a clear Zeeman splitting (valley splitting) for the neutral exciton and the trion of about ± 2 meV at $B_z \mp 9$ T. The extracted g-factors for both exciton complexes in both materials are of the order of $g \approx -4$.

6.1 Magneto-optics in monolayer $MoSe_2$

The experiments are carried out under the following experimental conditions: as in the previous chapters, WSe_2 and $MoSe_2$ flakes are obtained by exfoliation [35] of a bulk crystal on 90 nm SiO_2 on a Si substrate. The ML regions are identified by optical contrast and very clearly in PL spectroscopy. Experiments at T=4K and in magnetic fields up to ±9 T have been carried out in an ultra-stable confocal microscope developed for spectroscopy on single semiconductor quantum dots [4; 38] which have a typical diameter of 20 nm. We can infer that the mechanical movement of the detection and excitation spot on the sample due to the strong applied magnetic fields is at most in the tens of nm range in our set-up (see details in section 2.4.2). Additional details can be found in section 2.1 for the samples used and in section 2 for setup performances. The sample is excited either by an He-Ne laser (1.96eV) or by a tunable continuous wave Ti:Sa laser. The average laser power is in the μW range, in the linear absorption regime.

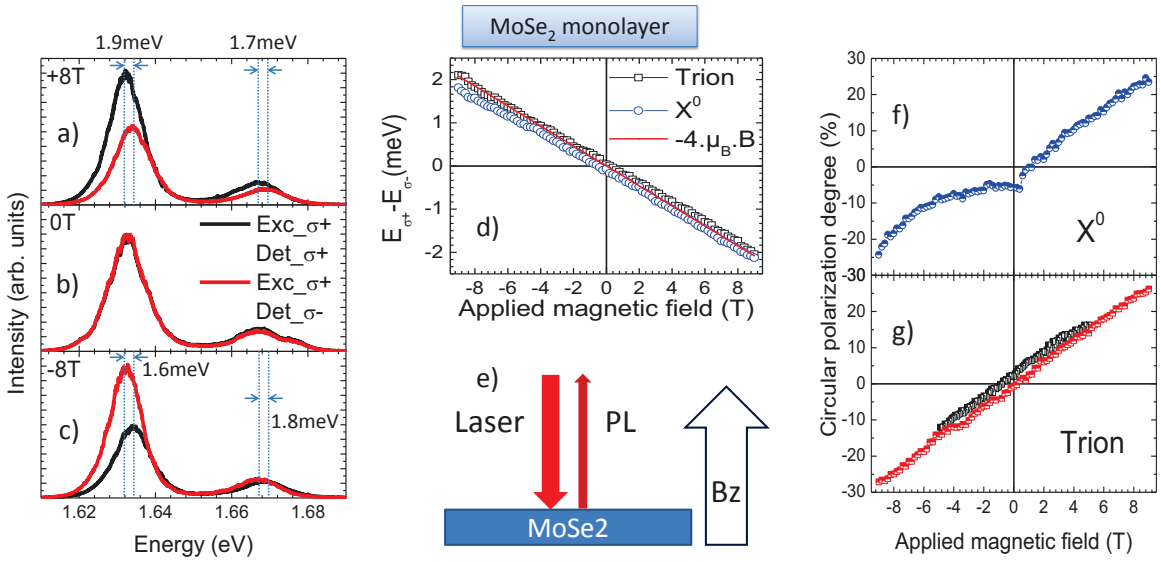

Figure 1: **Data for monolayer $MoSe_2$**; excitation energy E_{Laser} = 1.96 eV (a) PL spectra at B_z = +8 T for σ^+ (black) and σ^- (red) polarized detection using σ^+ polarized laser excitation. (b) same as (a) but at B_z = 0 T. (c) same as (a) but at B_z = −8 T. (d) Splitting between the σ^+ and σ^- polarized PL components for the trion (black squares) and the X^0(blue circles) as a function of magnetic field, the function $-4\mu_B B_z$ is shown for comparison (red line). (e) Schematics of the experimental geometry. (f) Polarization of the PL emission of the X^0 as a function of B_z. (g) Polarization P_c of the PL emission of the trion as a function of B_z using σ^+ (black squares) and σ^- excitation (red squares).

First we discuss the experimental results for $MoSe_2$ MLs. At zero magnetic field, we observe in the PL spectrum two sharp emission features with a full width at half maximum (FWHM) of 10 meV. In accordance with previous reports [135], the low energy emission at 1.63 eV is attributed to the charged exciton (trion) recombination and at 1.67 eV we record the neutral exciton X^0 emission, see Fig. 14b. In our measurements the circular polarization degree P_c of the trion and X^0 emission depends only very little on the excitation laser polarization (σ^+ or σ^-) for the excitation laser energy of 1.96 eV used in Fig. 14b. The maximum P_c generated was of the order of 5% for the excitation energy range investigated [136], much lower than the PL polarization achieved for circular laser excitation

in MoS_2 [18; 50; 55; 56; 67] and WSe_2 MLs [32; 33; 110] as shown in the previous chapters. Below we discuss the magnetic field dependence of the PL emission, whose energy and polarization are essentially independent of the excitation laser polarization, in stark contrast to the results obtained in ML WSe_2 discussed in section. 6.2. The very small PL polarization (even zero) following polarized laser excitation in $MoSe_2$ has been observed by other groups [137; 138] but remains unexplained. In order to gain more insights, some calculations are in progress in the LPCNO to understand the differences in the $MoSe_2$ ML bandstructure compared to MoS_2 or WSe_2 ML [139].

Next we discuss the changes observed in the ML $MoSe_2$ PL emission when applying a magnetic field B_z perpendicular to the layer plane, i.e. along the z-direction, that is also the light propagation axis (Faraday geometry). Comparing Fig. 14a at B_z = +8 T and Fig. 14b at $B_z = 0$ we observe two main differences:

(i) For B_z = +8 T the σ^+ polarized emission is more intense than the σ^- polarized component, for both the trion and X^0.

(ii) The σ^+ polarized emission is shifted to lower energy compared to the σ^- polarized component.

When applying a field of $B_z = -8$ T in Fig. 14c, these results are reversed, i.e. σ^- emission becomes more intense and lower in energy compared to σ^+ in agreement with time-reversal symmetry. In Fig. 14d we plot the full magnetic field dependence of the energy splitting

$$\Delta_Z = E^{PL}_{\sigma^+} - E^{PL}_{\sigma^-} = g\mu_B B_z, \tag{6.1}$$

from $B_z = -9$ T to +9 T with g being the effective g-factor and μ_B being the Bohr magneton.

The Zeeman splitting is extracted by fitting the trion and X^0 emission spectra with Lorentzian curves. We observe a clear linear dependence both for the trion and X^0 splitting on the applied field. This indicates that eventual diamagnetic and higher order contributions are identical for the upper and lower Zeeman branch within our experimental resolution. The slope is $\Delta_Z/B_z = -220 \pm 10$ μeV/T for the X^0 which corresponds to an exciton g-factor of $g_{X^0} = -3.8 \pm 0.2$. For the trion the slope is -226 ± 10 μeV/T which corresponds to a g-factor of $g_T = -3.9 \pm 0.2$. This corresponds to a maximum $\Delta_Z = -2$ meV at 9 Tesla.

The main experimental uncertainty for Δ_Z comes from eventual changes of the overall shape of the PL emission due to imperfections in the optical set-up and sample inhomogeneities, as the recorded shifts are smaller than the linewidth. The Landé-factors for trions and the X^0 in ML $MoSe_2$ extracted from our data are close to the values reported very recently in [137; 138].

It is worth mentioning that trions that form with the excess electron in the same or different valley, with respect to the photo-generated electron hole pair, are separated in energy due to the strong Coulomb effects and the zero-field splitting of conduction band states in each valley, cf. [77]. However, we do not observe any fine structure splitting for the trion emission in the investigated sample. Hence, the measured g_T represents the global magnetic field induced energy shift of the trion emission.

We now discuss the circular polarization of the observed emission summarized in Figs. 14f and 14g. For the trion, P_c increases from zero to 30% when the magnetic field is increased from zero up to 9 T. This strong polarization is reversed when the direction of the applied magnetic field is reversed. Optical valley initialization at higher fields is not at the origin of this effect: For σ^+ polarized laser excitation we observed exactly the same polarization increase with field as for σ^- polarized laser excitation. We conclude

that the PL polarization is the result of magnetic field induced spin/valley polarization build-up during the PL emission time, which has been determined to be in the ps-range [136]. Observing an increase in the emission polarization in applied magnetic fields is a very common observation in semiconductors [63]. For ML $MoSe_2$, where excitons have a strong binding energy [20], this observation is more surprising taking into account the relevant energy scales. At 9T, we have induced a splitting between the valley Zeeman levels of 2 meV, eventually comparable to the spin splitting in the conduction band, predicted to be in the meV range [22; 80]. The polarization of the neutral exciton follows a similar trend as the trion. For the neutral exciton, the applied field B_z can dominate the long-range electron-hole Coulomb exchange interaction, and hence suppress valley depolarization when B_z has a larger amplitude than the effective transverse field associated to exchange effects [75–77; 97].

6.2 Magneto-optics in monolayer WSe_2

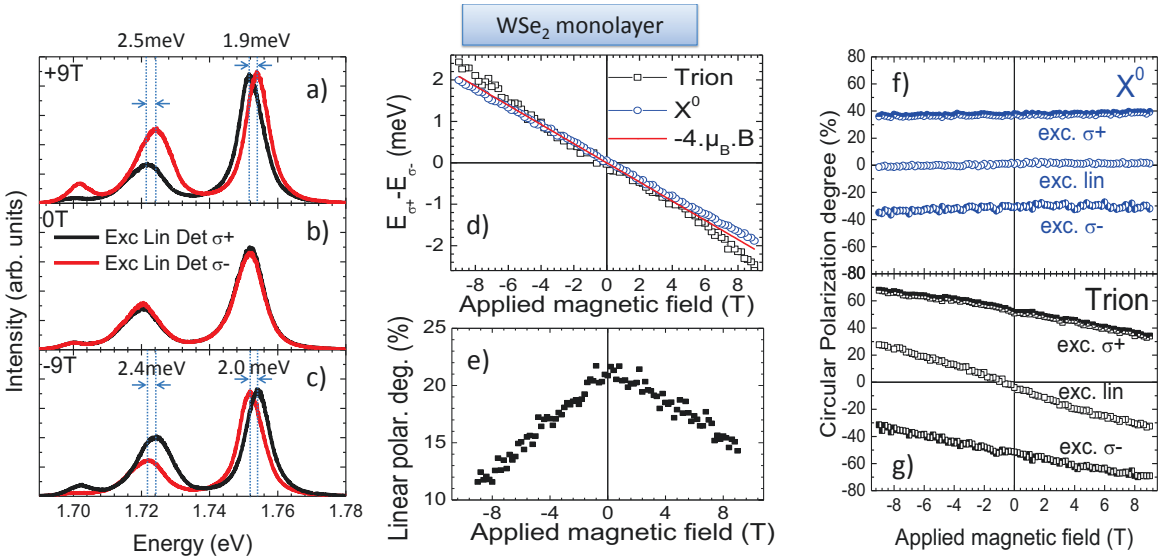

Figure 2: **Data for monolayer WSe_2**; excitation energy E_{Laser} = 1.96 eV (a) PL spectra at B_z = +9 T for σ^+ (black) and σ^- (red) polarized detection using σ^+ polarized laser excitation. (b) same as (a) but at B_z = 0 T. (c) same as (a) but at B_z = −9 T. (d) Splitting between the σ^+ and σ^- polarized PL components for the trion (black squares) and the X^0(blue circles) as a function of magnetic field, the function $-4\mu_B B_z$ is shown for comparison (red line). (e) Linear polarization of the X^0 emission as a function of B_z. (f) Polarization of the PL emission of the X^0 as a function of B_z for three different laser polarizations. (g) Polarization P_c of the PL emission of the trion as a function of B_z for three different laser polarizations.

In order to draw more general conclusions on valley properties in applied magnetic fields, we compare our results in ML $MoSe_2$ with a very well characterized system, namely ML WSe_2 [32; 33; 110] investigated with the same experimental set-up. Therefore all experimental uncertainties are comparable. In Fig. 2b the PL emission of ML WSe_2 is plotted, and just as in the case of ML $MoSe_2$, we observe two well defined emission lines with a typical FWHM of 10 meV. The higher energy transition at 1.75 eV is identified as the neutral exciton X^0 recombination, as valley coherence can be generated [32], see Fig. 2e. The lower energy transition at 1.72 eV stems from the radiative recombination of the charged

	g_{X^0}	X^0 slope [μeV/T]	g_T	Trion slope [μeV/T]
ML $MoSe_2$	-3.8 ± 0.2	-220 ± 10	-3.9 ± 0.2	-226 ± 10
ML WSe_2	-3.7 ± 0.2	-214 ± 10	-4.4 ± 0.2	-254 ± 10

Table 6.1: comparison of Landé factors

exciton (trion). The σ^+ and σ^- polarized PL components correspond to carrier recombination in the K^+ and K^- valley, respectively.

At zero magnetic field the emission spectra in σ^+ and σ^- polarizations are exactly the same due to the time-reversal symmetry and corresponding degeneracy of the valley levels. In a magnetic field of 9 T this valley degeneracy is lifted, and the energy difference $\Delta_Z = E^{PL}_{\sigma^+} - E^{PL}_{\sigma^-}$, Eq. (6.1), is typically -2 meV, see Fig. 2a, very similar to the results on $MoSe_2$ presented in Fig. 14a. In a field of $B_z = -9$ T, the σ^+ polarized component is now at higher energy, corresponding to a positive Zeeman splitting of +2 meV. We plot in Fig. 2d the full magnetic field dependence of the Zeeman splitting for the trion and X^0. The experimental points are very close to a straight line, which allows us to extract for the X^0 a slope of $\Delta_Z/B_z = -214 \pm 10$ μeV/T, corresponding to the neutral exciton g-factor $g_{X^0} = -3.7 \pm 0.2$. For the trion the slope is -254 ± 10 μeV/T, resulting in its g-factor $g_T = -4.4 \pm 0.2$.

The similarities between the measured Landé-factors in $MoSe_2$ and WSe_2 are striking, both with respect to their signs and amplitudes (see table 6.1). Comparing with the very recent literature data on ML WSe_2, the g-factors for the neutral exciton extracted for our sample are slightly smaller than reported in reference [140] and larger than in reference [141]. Note, that as for $MoSe_2$ case we do not resolve any fine-structure of the trion emission in WSe_2.

Although the Zeeman energy evolution of the both ML materials $MoSe_2$ and WSe_2 shows close similarities, we will see below that the evolution of the valley polarization as a function of the applied magnetic field is completely different. The polarization measurements on WSe_2 are all performed with non-resonant HeNe laser excitation. First, we plot the evolution of the X^0 PL polarization under circularly polarized pumping, that corresponds to the valley polarization generation via the chiral optical selection rules [11; 18], as a function of the applied magnetic field. It can be seen in Fig. 2f that the X^0 polarization is essentially independent of the applied field. For a linearly polarized excitation laser, we find $P_c \approx 0$ for all applied field values. Changing to σ^+ circularly polarized excitation, we record at zero Tesla $P_c \approx 40\%$. This value remains practically constant in applied fields from -9 T to +9 T. This indicates that over the entire magnetic field range, the X^0 emission polarization is determined by the initially, optically created valley polarization rather than induced by the magnetic field. During the X^0 PL emission time no valley/spin relaxation occurs, which might simply be a consequence of the extremely short PL emission time in the few ps range measured for this material [110]. Exciting preferentially the K^- valley with a σ^- polarized laser, results in $P_c \approx -40\%$, again independent of the applied magnetic field. This behaviour for the X^0 in ML WSe_2 is in stark contrast to the observations in ML $MoSe_2$. For the former, the optical valley initialization determines the PL polarization, for the latter the applied magnetic field direction and amplitude allow to control the valley polarization. Comparing with the recent literature, the X^0 polarization in the ML WSe_2 sample investigated by Aivazian et al.[141] was slightly more sensitive to the applied magnetic field.

Contrary to the X^0 polarization in ML WSe_2, the trion polarization can be controlled to some extent via the applied magnetic field, shown in Fig. 2g. For linearly polarized laser excitation, the trion PL polarization for $B_z = 0$ is absent, $P_c = 0$, but increases at -9 T to $+30\%$, and at $+9$ T to -30%. This can be directly compared to the trion in ML $MoSe_2$, that also started off at zero field with zero polarization. When comparing the trion polarization evolution in ML $MoSe_2$ (Fig. 14g) and ML WSe_2 (Fig. 2g) we note very contrasting behaviour: application of a positive magnetic field, results in a strong, positive P_c in $MoSe_2$ in contrast to the strong, but negative polarization created in WSe_2. Using σ^+ polarized excitation for the trion, results in high circular polarization $P_c = 50\%$ already at $B_z = 0$. At a magnetic field of $B_z = -9$ T this polarization is increased to $P_c = 68\%$, at $B_z = +9$ T we find $P_c = 34\%$. For the trion using σ^+ excitation, we find a similar trend as under linearly polarized excitation: the PL polarization decreases for positive B_z and increases for negative B_z. The trion polarization depends on both the excitation laser polarization and the applied magnetic field. This latter dependence might be linked to the fact that the PL emission time of the trion in ML WSe_2 is longer than for the X^0 [110], allowing for polarization relaxation to occur before radiative recombination takes place. As can be seen in Fig. 2g, the magnetic field induced change in PL polarization is also observed for σ^- excitation, here we find at $B_z = -9$ T $P_c = -31\%$, while for zero field we record $P_c = -52\%$ (as expected when switching from σ^+ to σ^- excitation) evolving towards $P_c = -69\%$ for $B_z = -9$ T. The three different measurement series presented in Fig. 2g each confirm that the PL polarization of the trion in ML WSe_2 strongly *decreases* with the applied magnetic field, whereas, in stark contrast, the trion PL polarization in ML $MoSe_2$ strongly *increases* as a function of the applied B_z. There is a clear sign reversal.

6.3 Discussion

The emission energies and polarizations are determined by several factors. Most importantly, the Zeeman splittings of exciton and trion in the emission spectra are governed by an interplay of spin splittings of conduction and valence band states, while the polarization is governed by selection rules at optical transitions and occupancies of the spin/valley states and possible spin relaxation processes. Here we briefly discuss theoretical approaches developped in close collaboration with M.M. Glasov and E.L. Ivchenko, to evaluate Zeeman splittings and polarization of emitted radiation in the context of experimental data presented above. Figure 3 summarizes the current approach proposed in the literature [140; 141].

6.3.1 Zeeman effect in two-dimensional crystals

We recall that the electron wavefunction in the two-dimensional crystal can be recast, in accordance with the Bloch theorem, as

$$\Psi_{nq}(r) = \frac{e^{iqr}}{\sqrt{S}} u_{nq}(r), \tag{6.2}$$

where n enumerates bands (including electron spin state) and q is the quasi-wavevector, $u_{nq}(r)$ is the periodic amplitude normalized per volume of the unit cell, Ω_0: $\int_{\Omega_0} |u_{nq}|^2 dr = \Omega_0$, and S is the macroscopic normalization area (see chapter 1).

The bare electron Zeeman effect is described by

$$\mathscr{H}_0 = g_0 \mu_B B \cdot s, \tag{6.3}$$

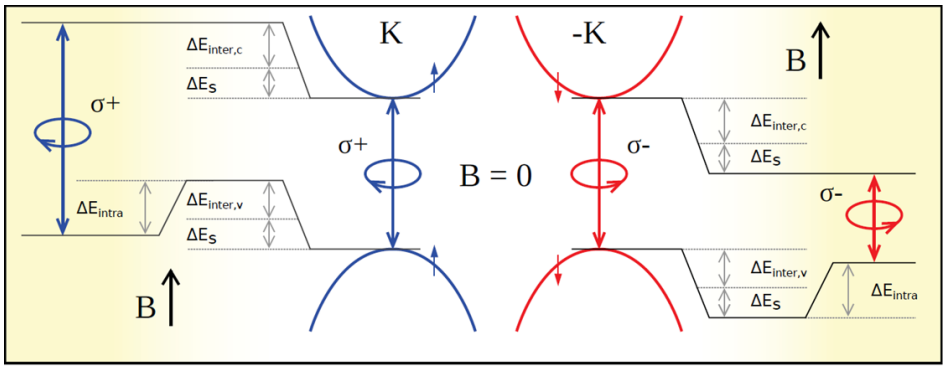

Figure 3: Figure extracted from ref [140]. Valley Zeeman effect - In a finite out-of-plane B, the degeneracy between the ±K valleys is lifted due to contributions from spin Zeeman effect (ΔE_s), the intercellular orbital magnetic moment (ΔE_{inter}), and the intracellular contribution from the $d_{x^2-y^2}$ś2id_{xy} orbitals of the valence band (ΔE_{intra}). The signs of these contributions are opposite in the two valleys. ΔE_s causes equal energy shifts of the conduction and the valence band hence can not be detected in PL.

where $\mu_B = |e|\hbar/(2m_0c)$ is the Bohr magneton, m_0 and $g_0 \approx 2$ are the free electron mass and Landé factor, and s is the spin operator $\sigma/2$ (in $\hbar$ units), σ being the vector composed of the Pauli matrices. In crystals, in addition to (6.3) the orbital contribution to the Zeeman splitting should be taken into account. It is related to the orbital momentum of the electron [142],

$$\mathscr{H}_1 = \mu_B B \cdot L, \tag{6.4}$$

where $L = \hbar^{-1}[r \times p]$ is the angular momentum operator, and $p = -i\hbar\nabla$ is the electron momentum operator. The contribution (6.4) is known to be important for well characterized semiconductors such as GaAs [28; 102].

We recall that in $MoSe_2$ and WSe_2 MLs the direct band gaps are realized at the edges of the Brillouin zone characterized by the wavevectors $K^{\pm}$. The bands at $q = K^{\pm}$ are non-degenerate and can be characterized by a certain spin projection $s_z = \pm 1/2$ onto the sample normal. The time reversal symmetry couples $s_z = \pm 1/2$ states in the K^+ valley with $s_z = \mp 1/2$ states in the K^- valley. In what follows we will be interested in the Zeeman effect in magnetic fields $B \parallel z$. Correspondingly, it is instructive to present the diagonal matrix element of the L_z operator at $q = K^+$ or K^- as

$$\langle \psi_n | \hbar L_z | \psi_n \rangle_{\pm} = \sum_{m \neq n} [\Omega^x_{nm}(K^{\pm}) p^y_{mn}(K^{\pm}) - \Omega^y_{nm}(K^{\pm}) p^x_{mn}(K^{\pm})]. \tag{6.5}$$

Here p^{α}_{nm} ($\alpha = x, y$) are the matrix elements of the electron momentum and

$$\Omega^{\alpha}_{nm} = i\Omega_0^{-1} \int_{\Omega_0} u^*_n \left(\partial u_m / \partial q_{\alpha}\right) dr$$

are the interband matrix elements of the coordinate operator. In derivation of Eq. (6.5) we made use of the completeness relation for the Bloch amplitudes and took into account that $p_{nn}(K^{\pm}) = 0$. Taking into account that $\Omega^{\alpha}_{mn} = i\hbar p^{\alpha}_{mn}/[(E_n - E_m)m_0]$ with E_n, E_m being the energies of corresponding bands, Eq. (6.5) can be rewritten as [102]

$$\langle \psi_n | L_z | \psi_n \rangle_{\pm} = \frac{i}{m_0} \sum_{m \neq n} \frac{p^x_{nm}(K^{\pm}) p^y_{mn}(K^{\pm}) - p^y_{nm}(K^{\pm}) p^x_{mn}(K^{\pm})}{E_m - E_n}. \tag{6.6}$$

Equations (6.3), (6.4) and (6.6) can be used to evaluate Zeeman splittings in $k \cdot p$ theory, as detailed below.

6.3.2 k.p-theory

The multiband $k \cdot p$ model was formulated for TMDCs in Refs. [26; 64; 143]. The effective Hamiltonians describing the states in the vicinity of $K^{\pm}$ edges of the Brillouin zone have the form

$$\mathscr{H}_{+} = \begin{pmatrix} E_{c+2} & \gamma_6 k_- & \gamma_4 k_+ & 0 \\ \gamma_6 k_+ & E_c & \gamma_3 k_- & \gamma_5 k_+ \\ \gamma_4 k_- & \gamma_3 k_+ & E_v & \gamma_2 k_- \\ 0 & \gamma_5 k_- & \gamma_2 k_+ & E_{v-3} \end{pmatrix}, \tag{6.7a}$$

$$\mathscr{H}_{-} = \begin{pmatrix} E_{c+2} & \gamma_6 k_+ & \gamma_4 k_- & 0 \\ \gamma_6 k_- & E_c & \gamma_3 k_+ & \gamma_5 k_- \\ \gamma_4 k_+ & \gamma_3 k_- & E_v & \gamma_2 k_+ \\ 0 & \gamma_5 k_+ & \gamma_2 k_- & E_{v-3} \end{pmatrix}. \tag{6.7b}$$

Here $k_{\pm} = k_x \pm i k_y$ are the cyclic components of the electron wavevector reckoned from the $K^{\pm}$ points, $k_{\pm} = q_{\pm} - K^{\pm}$; the parameters $\gamma_3 \ldots \gamma_6$ are related to the interband momentum matrix elements, and certain convention about the phases of the Bloch functions is assumed. The symbols $c+2$ and $v-3$ denote the closest excited conduction and valence bands coupled through $k.p$ Hamiltonian to the lowest conduction and valence bands (c, v) defining the gap (see [26; 51]. Such a model was shown to allow for adequate description of the spin-orbit coupling and trigonal symmetry effects in TMDCs [26; 64; 143]. In the general theory besides k-linear off-diagonal terms, effective $k \cdot p$ Hamiltonian includes diagonal quadratic in k contributions resulting (i) from the second-order $k \cdot p$ coupling with distant bands and (ii) from bare electron dispersion $\hbar^2 k^2 / 2m_0$ [144]. Usually these contributions are comparable and should be included simultaneously. Diagonalizing Hamiltonians (6.7) in the second order in off-diagonal terms we obtain for the electron effective masses of the conduction and valence bands, respectively,

$$\frac{1}{m_c} = \frac{1}{m^*} + \frac{1}{m_c'} + \frac{1}{m_0} + \frac{1}{m_c''}, \tag{6.8a}$$

$$\frac{1}{m_v} = -\frac{1}{m^*} + \frac{1}{m_v'} + \frac{1}{m_0} + \frac{1}{m_v''}. \tag{6.8b}$$

Here subscripts c, v denote the corresponding bands and we use the electron representation, $m^* = \hbar^2 (E_c - E_v)/(2\gamma_3^2)$ is the two-band effective mass, the terms

$$\frac{1}{m_c'} = \frac{2}{\hbar^2} \left(\frac{\gamma_5^2}{E_c - E_{v-3}} + \frac{\gamma_6^2}{E_c - E_{c+2}} \right), \tag{6.9a}$$

$$\frac{1}{m_v'} = \frac{2}{\hbar^2} \left(\frac{\gamma_2^2}{E_v - E_{v-3}} + \frac{\gamma_4^2}{E_v - E_{c+2}} \right) \tag{6.9b}$$

result from the mixing described by the Hamiltonians (6.7) and $1/m_c''$, $1/m_v''$ contain the above mentioned contributions from remote bands [not included in Eqs. (6.7)].

According to the general theory [144] the magnetic field within the $k \cdot p$ scheme is included (i) by adding the bare electron Zeeman effect in the form of Eq. (6.3) and (ii) by replacing k in Eqs. (6.7) by $k - (e/c\hbar)A$, where $e = -|e|$ is the electron charge, A is the vector potential of the magnetic field. The calculation in the first order in B_z yields the effective g-factors of electrons in $K^{\pm}$ valleys:

$$g_{c,v}^{K^+} \equiv g_{c,v} = 2 + g_{c,v}^{\mathrm{orb}}, \quad g_{c,v}^{K^-} = -g_{c,v}^{K^+}. \tag{6.10}$$

The term 2 in Eq. (6.10) arises from the bare Zeeman effect, Eq. (6.3), while $g^{orb}_{c,v}$ result from the $k\cdot p$-mixing

$$g_c^{\rm orb} = \frac{4m_0}{\hbar^2}\left(\frac{\gamma_3^2}{\mathrm{E}_c-\mathrm{E}_v} - \frac{\gamma_5^2}{\mathrm{E}_c-\mathrm{E}_{v-3}} - \frac{\gamma_6^2}{\mathrm{E}_c-\mathrm{E}_{c+2}}\right), \tag{6.11a}$$

$$g_v^{\rm orb} = \frac{4m_0}{\hbar^2}\left(-\frac{\gamma_3^2}{\mathrm{E}_v-\mathrm{E}_c} + \frac{\gamma_2^2}{\mathrm{E}_v-\mathrm{E}_{v-3}} + \frac{\gamma_4^2}{\mathrm{E}_v-\mathrm{E}_{c+2}}\right). \tag{6.11b}$$

Equations (6.11) can be derived from Eqs. (6.4) and (6.6), taking into account only bands c, $c+2$, v and $v-3$ if we restrict to the four-band Hamiltonian. Additional contribution to $g^{orb}_{c,v}$, namely, $\Delta g^{orb}_{c,v}$ may arise allowing for other distant bands in Eq. (6.6).

6.3.3 Zeeman splittings of direct excitons and trions

The neutral exciton radiative decay involving emission of σ^+ or σ^- photons results from the recombination of a Coulomb-correlated electron-hole pair in the K^+ or K^- valley, respectively. The Zeeman splitting of X^0 is, in accordance with Eq. (6.1), given by

$$\Delta_{\rm Z} = \frac{1}{2}\left[g_c^{\rm K_+} - g_v^{\rm K_+} - \left(g_c^{\rm K_-} - g_v^{\rm K_-}\right)\right]\mu_{\rm B}B_z\,. \tag{6.12}$$

Note that hereafter we neglect the renormalization of g-factor due to the Coulomb effects and band non-parabolicity. Making use of Eqs. (6.10), (6.11) the bright exciton g-factor is given by

$$g_{\rm X} = g_c - g_v = -2\left(\frac{m_0}{m_c'} + \frac{m_0}{m_v'}\right) + \Delta g_c^{\rm orb} - \Delta g_v^{\rm orb}, \tag{6.13}$$

where terms in parenthesis are calculated within the framework of Hamiltonian (6.3) and 4-band Hamitonian (6.7), and the contribution $\Delta g^{orb}_c - \Delta g^{orb}_v$ results form the remote bands not accounted for by Eq. (6.7). At this stage precise measurements of the conduction band effective masses have not been reported yet. First measured values for the valence band effective masses can be obtained from angle-resolved photoemission spectroscopy (ARPES) [17; 145]. Equation (6.13) can also be represented in the form

$$\begin{aligned} g_{\rm X} &= 4 - 2\left(\frac{m_0}{m_c} + \frac{m_0}{m_v} - \frac{m_0}{m_c''} - \frac{m_0}{m_v''}\right) \\ &\quad + \Delta g_c^{\rm orb} - \Delta g_v^{\rm orb}, \end{aligned} \tag{6.14}$$

where the contributions to the Landé factor and effective masses resulting from remote bands are explicitly present. The term 4 arises from inclusion of $1/m_0$ in the inverse effective masses for the conduction and valence band electrons. Note that in the two-band approximation the bright exciton g-factor exactly vanishes because in this approximation the conduction- and valence-band electron effective masses are given by $m_0/m_c^{2b} = 1 + m_0/m^*$, $m_0/m_v^{2b} = 1 - m_0/m^*$ and, therefore,

$$g_x^{2b} = 4 - 2\left(\frac{m_0}{m_c^{2b}} + \frac{m_0}{m_v^{2b}}\right) = 4 - 2\times 2 = 0.$$

It should be emphasized that the inclusion of free electron dispersion $1/m_0$ in Eqs. (6.8) and neglecting the terms $1/m_c''$, $1/m_v''$, Δg^{orb}_c, and Δg^{orb}_v contribution of remote bands cannot formally be justified within the $k\cdot p$ method. Those contributions should be estimated from experimental data or evaluated via more advanced $k\cdot p$ schemes or atomistic approaches.

Since in $MoSe_2$ and WSe_2 the conduction- and valence-band effective masses are close in absolute values but have opposite signs, in accordance with Eqs. (6.13), (6.14), the orbital contribution to the exciton g-factor stems from remote bands. We note that neither Eq. (6.13) with $\Delta g_c^{\rm orb} - \Delta g_v^{\rm orb} = 0$ nor Eq. (6.14) with $m_v'', m_c'' \to \infty$ can satisfactory describe the experiment in respect of both the sign and the magnitude of g-factor. Hence we conclude that the remote band contributions are important. For instance, if we add into consideration one more (distant) band with the same symmetry as the conduction band with band edge energy E_c' and the matrix element of $k \cdot p$ interaction with the valence band γ_3' we obtain an additional contribution to the valence band g-factor $\Delta g_v = 4m_0\gamma_3'^2/[\hbar^2(E_c' - E_v)]$, while $\Delta g_c = 0$ for symmetry reasons. Though our simple calculations disagree with the measured exciton g factors, it shows that previous interpretations based only on momentum of d orbitals (L=2 for valence states, L=0 for conduction states yielding exciton g factor of 4) are probably erroneous. Further experimental studies and theoretical modeling are therefore needed to elucidate the values of Zeeman splitting.

The Zeeman splitting for the bright trion is also given by Eq. (6.12). This is because the optical recombination involves charge carriers of opposite signs in the same valley, while the spin/valley state of the third carrier is not changed. The difference of measured values for excitons and trions could be attributed to renormalization of g-factors induced by band non-parabolicity the Coulomb effects.

6.3.4 Polarization of emission

The polarization of the PL emission is governed by the selection rules and occupancies of spin/valley states of the carriers and Coulomb complexes. In case of $MoSe_2$ ML, neither optical orientation (circular polarization of photoluminescence for circularly polarized excitation at B = 0) nor exciton alignment or valley coherence (linear polarization at linearly polarized excitation) are observed [136]. This allows us to assume that in this material the spin/valley relaxation of both neutral excitons and trions (or individual carriers) is fast compared to the PL emission time. In the presence of a magnetic field the magneto-induced circular polarization seems to result from the preferential occupation of the lowest Zeeman state of the exciton or trion. It is indeed consistent with experiment where, for $B_z > 0$, the state emitting the σ^+-polarized photons has the lower energy and is dominant in the photoluminescence so that $P_c(B_z > 0) > 0$, see Fig. 14. Note, however, that the full thermalization to the lattice temperature does not occur because at $|B_z| \approx 9$ T the Zeeman splitting exceeds by far the temperature expressed in the energy units, while experiment demonstrates only $|P_c| \sim 30$ %. The effective spin temperature deduced from the experiment is about $T_{\rm spin} = 30$ K.

The situation is more complex for WSe_2 where the experiment shows substantial optical orientation, Fig. 2f, and neutral-exciton alignment, Fig. 2e, even at $B_z = 0$. In this case the spin/valley relaxation time is comparable to the lifetime of excitations and, in an applied magnetic field, thermalization may not occur. We checked that the behaviour of alignement with respect to longitudinal magnetic field, which is analogous to a conventional Hanle experiment, is consistent with a sub-picosecond recombination time of the exciton. Additionally, as compared to $MoSe_2$, WSe_2 is characterized by the opposite sign of zero-field spin splitting of the conduction band [22; 80]. Hence, for the exciton and trion ground states the direct intra-valley optical transitions are spin-forbidden. These states could enventually appear in optical spectra due to indirect (e.g. phonon-assisted) transitions similarly to the case of Carbon nanotubes [146]. It follows from symmetry considerations that in this case the polarization is reversed [147]. Further experimental

data using gated devices where positively and negatively charged excitons can be clearly distinguished and theoretical analysis are needed to clarify this issue.

Finally we emphasize that the above analysis is based on the perturbative treatment of the Coulomb interaction while, in TMDC MLs, the exciton binding energy amounts to $\gtrsim$ 500meV or even more and, hence, is comparable to the band gap. Theoretical estimates show that depending on the parameters of the materials and dielectric environment the binding energy is so large that the $1s$ state emission could be in the infra-red range and, moreover, the exciton ground state could even collapse [132; 148]. In the former case the optical transition $2p \rightarrow 1s$ could be relevant as well, its Zeeman splitting and polarization deserve further study. In the latter case the ground state of the system could be strongly renormalized and an excitonic insulator could be formed [149–152]. Its polarization and magnetic field properties should also be studied in future works.

6.4 Conclusion

In this chapter, we presented the results of magneto-photoluminescence experiments performed on both $MoSe_2$ and WSe_2 MLs[51]. For both materials, the transition energy shift dependence with the applied magnetic field allows to extract an effective Landé g-factor of about -4. The trion PL polarization of $MoSe_2$ increases with the applied field whereas it decreases for WSe_2.

Our theoretical k-p four bands approach, developed in collaboration with M.M. Glazov and E. L. Ivchenko, does not suffice to explain the origin of this Landé g factor of about -4 but shows that previous interpretations only based on d orbital momentum are incomplete and further theoretical work is required.

Concerning the polarization dependence with magnetic field, if the hypothesis of a partial spin thermalization is in qualitative agreement with our experimental results, further theoretical investigations are also needed to elucidate the spin relaxation mechanism in the case of the trion and to provide a complete understanding of this phenomenon.

Conclusions and perspectives

In the first experiments on TMDCs carried out at the LPCNO in the framework of this thesis, we investigated the robustness of the circular polarization of the PL emitted by a MoS_2 ML under various experimental conditions. This was an important step towards verifying the theoretically predicted, chiral optical selection rules for interband transitions. We measured a very high circular polarization degree of the emitted PL from the A-exciton when exciting the monolayer using a circularly polarized laser source, confirming optical k-valley initialization. We then demonstrated that the degree of circular polarization of the PL decreases when the temperature increases. In these experiments we used a constant laser energy so as the optical gap decreases with temperature the laser excitation is less and less resonant. We demonstrate a strong recovery of the polarization at room temperature when we excite energetically closer to the A-exciton resonance. Similarly, working at constant temperature, we also observed a strong decrease of the PL circular polarization in PLE experiments as the energy difference between the laser excitation energy and the emission energy is systematically increased. In addition, a decrease of the PL polarization as a function of temperature might be influenced by the activation of phonon assisted intervalley scattering.

In order to further understand the carrier and valley index dynamics in TMDC ML materials, we then performed time-resolved PL experiments. We investigated the PL emission dynamics of two different TMDCs MLs; MoS_2 and WSe_2. For MoS_2 it was not possible to distinguish spectrally the neutral exciton from the charged exciton (trion) emission due to the broad PL linewidth. The overall PL emission time is very short, a few ps, close to the time resolution of our set-up. Such a short emission time in MoS_2 prevents us to investigate the polarization decay dynamics in detail, which is also expected to be in the ps range due to coupling of K^+ and K^- states by the long range exciton Coulomb exchange. For WSe_2, the excellent optical quality of the sample allows to clearly distinguish between the neutral exciton, the trion and the localized states. Although the X^0 PL emission decays very quickly (4ps, same situation as for MoS_2), the trion emission is much longer (tens of ps) and allows to monitor the polarization decay time. A partial, initially rapid polarization decay (τ_1 = 12ps) is followed by a polarization plateau as the polarization remains almost constant (τ_2 = 1ns $\gg$ emission time). This makes the trion a possible candidate for future valley index manipulation experiments.

The very short PL emission times implies that also in the large number of time-integrated experiments reported in the literature on valley polarization and coherence, we can only detect effects occurring during a few ps. In addition, a short PL emission time might indicate that excitonic effects play a central role in the physics of those new materials, as a strong exciton oscillator strength results in principle in a short radiative lifetime. To confirm this idea, we directly demonstrate strong excitonic effects for WSe_2 MLs using several optical spectroscopy techniques. Using second harmonic generation spectroscopy, combined with 1-photon and 2 photon-PLE, allows us to identify discrete excitonic states. Their energy spacing and order cannot be described by a simple hydrogenic model, but

can be well reproduced by taking into account screening and anti-screening effects due to spatial variation of dielectric constant and strong spatial delocalization of excited excitonic states. Thus, combined with DFT calculations, our experimental results allow extracting a considerable binding energy of about 0.6 eV, compared to a free carrier bandgap of around 2.4 eV. Despite this extremely large binding energy, the community is so far working in the Wannier exciton picture (not Frenkel), as the 1s exciton wavefunction extends over a sufficient number of lattice sites.

In addition to valley polarization, probed via the circular polarization degree of the emission, we were also able to generate exciton valley coherence. This coherent superposition of K^+ and K^- states can be generated using a linearly polarized laser source and manifests itself through strongly linearly polarized emission. Creating valley coherence using 2 photon absorption when exciting in resonance with the 2s and 2p exciton energies, is to the best of our knowledge, the first experimental demonstration of these effects in a semiconductor.

We used our magneto-spectroscopy facilities to further probe the TMDC ML electronic band structure. A first set of experiments in magnetic fields perpendicular to the ML on MoS_2 did not show any measurable effects on the PL transitions, probably because of its very large PL spectral linewidth (≈80 meV). In addition, applying a magnetic field up to 9T in the ML plane (perpendicularly to the spin quantization axis) shows no measurable effects on transition energies and PL polarization.

We then performed magneto-photoluminescence experiments on both $MoSe_2$ and WSe_2 MLs which have much narrower PL linewidth. For both materials, the transition energy shift with the applied magnetic field allows extracting a Landé g-factor of about -4. The trion PL polarization of $MoSe_2$ increases with the applied field whereas it decreases for WSe_2. Our theoretical k-p four band approach, developed in collaboration with M.M. Glazov and E. L. Ivchenko, does not suffice to explain the origin of this Landé g factor of about -4 but shows that previous interpretations only based on d orbital momentum are probably incomplete and require further theoretical work. Also the exact reason for the generation of valley polarization in magnetic fields applied perpendicular to the ML in ML $MoSe_2$ is not fully understood and requires further experimental and theoretical efforts. In addition, further theoretical work is needed to understand the origin of this Landé g factor of about -4 for which no satisfying explanation has been presented up to now.

The work presented in this thesis marks the beginning of the optical spectroscopy efforts carried out in order to understand the electronic band-structure, excitonic effects and valley dynamics in ML TMDCs. Many questions remain open and many key material parameters such as effective electron and hole masse still need to be determined.

We are able to optically generate valley polarization in ML MoS_2 and WSe_2, but not in ML $MoSe_2$. Although the latter material shows the sharpest emission lines and no defect states, the PL emission remains unpolarized in the absence of strong, perpendicular magnetic fields. If this is due to sub-ps valley depolarization or an anomaly in the band-structure, leading to different selection rules, still needs to be understood.

A promising way of tuning the valley properties and of better understanding the physics in binary ML materials $MoSe_2$ and WSe_2 is to work with ternary alloys $Mo_{1-x}W_xSe_2$. Here the first results obtained by our group on the high quality material grown at Arizona State University are encouraging [153].

All the optical properties discussed in this work are relevant for optoelectronics appli-

cations and for also the optical manipulation of the valley and spin degrees of freedom. An important example is the still open question of the energetic order of optically bright and dark excitonic transitions. Globally the quantum yield in PL experiments on ML TMDCs is considerably lower as in GaAs quantum wells, for example, despite the much stronger light-matter interaction (absorption 10% / ML). In ML $MoSe_2$ the optically active states are predicted to be the ground states, whereas in ML WSe_2 the bright exciton states are in energy above the dark states, which might lead to losses. The order of the bright and dark exciton states depends on the sign of the conduction band spin splitting, which still needs to be measured experimentally. Information on the bright versus dark state competition can be extracted from temperature dependent measurements [153].

Another promising perspective is the investigation of Van der Waals hetero-structures. Here in addition to the fascinating physics in single layers the interaction between layers needs to be understood. The first demonstration of LEDs with an active WSe_2 layer in a Van der Waals hetero-structure [154] shows that this is a promising route towards engineering device performances and physical properties.

Appendix A

Group theory tables for D_{3h} and C_{3h} groups

For convenience, group theory tables from ref[27] are reproduced here for the groups to which TMDCs symmetry belong to, D_{3h} being the group corresponding to TMDC symmetry at the Γ point and C_{3h} being the group corresponding to TMDC symmetry at the $\mathrm{K}^{+}(\mathrm{K}^{-})$ point which correspond to the optical gap location.

Γ_1	Γ_2	Γ_3	Γ_4	Γ_5	Γ_6	Γ_7	Γ_8	Γ_9	
Γ_1	Γ_2	Γ_3	Γ_4	Γ_5	Γ_6	Γ_7	Γ_8	Γ_9	Γ_1
	Γ_1	Γ_4	Γ_3	Γ_5	Γ_6	Γ_7	Γ_8	Γ_9	Γ_2
		Γ_1	Γ_2	Γ_6	Γ_5	Γ_8	Γ_7	Γ_9	Γ_3
			Γ_1	Γ_6	Γ_5	Γ_8	Γ_7	Γ_9	Γ_4
				$\Gamma_1 + \Gamma_2 + \Gamma_6$	$\Gamma_3 + \Gamma_4 + \Gamma_5$	$\Gamma_7 + \Gamma_9$	$\Gamma_8 + \Gamma_9$	$\Gamma_7 + \Gamma_8$	Γ_5
					$\Gamma_1 + \Gamma_2 + \Gamma_6$	$\Gamma_8 + \Gamma_9$	$\Gamma_7 + \Gamma_9$	$\Gamma_7 + \Gamma_8$	Γ_6
						$\Gamma_1 + \Gamma_2 + \Gamma_5$	$\Gamma_3 + \Gamma_4 + \Gamma_6$	$\Gamma_5 + \Gamma_6$	Γ_7
							$\Gamma_1 + \Gamma_2 + \Gamma_5$	$\Gamma_5 + \Gamma_6$	Γ_8
								$\Gamma_1 + \Gamma_2 + \Gamma_3 + \Gamma_4$	Γ_9

Figure 1: Multiplication Table for the Group D_{3h}.

Γ_1	Γ_2	Γ_3	Γ_4	Γ_5	Γ_6	Γ_7	Γ_8	Γ_9	Γ_{10}	Γ_{11}	Γ_{12}	
Γ_1	Γ_2	Γ_3	Γ_4	Γ_5	Γ_6	Γ_7	Γ_8	Γ_9	Γ_{10}	Γ_{11}	Γ_{12}	Γ_1
	Γ_3	Γ_1	Γ_5	Γ_6	Γ_4	Γ_{11}	Γ_9	Γ_{12}	Γ_7	Γ_{10}	Γ_8	Γ_2
		Γ_2	Γ_6	Γ_4	Γ_5	Γ_{10}	Γ_{12}	Γ_8	Γ_{11}	Γ_7	Γ_9	Γ_3
			Γ_1	Γ_2	Γ_3	Γ_9	Γ_{10}	Γ_7	Γ_8	Γ_{12}	Γ_{11}	Γ_4
				Γ_3	Γ_1	Γ_{12}	Γ_7	Γ_{11}	Γ_9	Γ_8	Γ_{10}	Γ_5
					Γ_2	Γ_8	Γ_{11}	Γ_{10}	Γ_{12}	Γ_9	Γ_7	Γ_6
						Γ_5	Γ_1	Γ_2	Γ_4	Γ_6	Γ_3	Γ_7
							Γ_6	Γ_4	Γ_3	Γ_2	Γ_5	Γ_8
								Γ_5	Γ_1	Γ_3	Γ_6	Γ_9
									Γ_6	Γ_5	Γ_2	Γ_{10}
										Γ_4	Γ_1	Γ_{11}
											Γ_4	Γ_{12}

Figure 2: Multiplication Table for the Group C_{3h}.

D_{3h}	E	$\bar{E}$	σ_h / $\bar{\sigma}_h$	$2C_3$	$2\bar{C}_3$	$2S_3$	$2\bar{S}_3$	$3C_2'$ / $3\bar{C}_2'$	$3\sigma_v$ / $3\bar{\sigma}_v$	Time Inv.	Bases for D_6	Bases for C_{6v}	Bases for D_{3h}
Γ_1	1	1	1	1	1	1	1	1	1	a	R	R or z	R
Γ_2	1	1	1	1	1	1	1	−1	−1	a	S_z or z	S_z	S_z
Γ_3	1	1	−1	1	1	−1	−1	1	−1	a	y^3-3yx^2	x^3-3xy^2	zS_z
Γ_4	1	1	−1	1	1	−1	−1	−1	1	a	x^3-3xy^2	y^3-3yx^2	z
Γ_5	2	2	−2	−1	−1	1	1	0	0	a	(S_x-iS_y), $-(S_x+iS_y)$	(S_x-iS_y), $-(S_x+iS_y)$	(S_x-iS_y), $-(S_x+iS_y)$
Γ_6	2	2	2	−1	−1	−1	−1	0	0	a	$\Gamma_3\times\Gamma_5$	$\Gamma_3\times\Gamma_5$	$\Gamma_3\times\Gamma_5$
Γ_7	2	−2	0	1	−1	$\sqrt{3}$	$-\sqrt{3}$	0	0	c	$\phi(1/2,-1/2)$, $\phi(1/2,1/2)$	$\phi(1/2,-1/2)$, $\phi(1/2,1/2)$	$\phi(1/2,-1/2)$, $\phi(1/2,1/2)$
Γ_8	2	−2	0	1	−1	$-\sqrt{3}$	$\sqrt{3}$	0	0	c	$\Gamma_7\times\Gamma_3$	$\Gamma_7\times\Gamma_3$	$\Gamma_7\times\Gamma_3$
Γ_9	2	−2	0	−2	2	0	0	0	0	c	$\phi(3/2,-3/2)$, $\phi(3/2,3/2)$	$\phi(3/2,-3/2)$, $\phi(3/2,3/2)$	$\phi(3/2,-3/2)$, $\phi(3/2,3/2)$

Figure 3: Character Table and Basis Functions for the Group D_{3h}.

C_{3h}	E	$\bar{E}$	S_3^{-1}	$\bar{S}_3^{-1}$	C_3	$\bar{C}_3$	σ_h	$\bar{\sigma}_h$	C_3^{-1}	$\bar{C}_3^{-1}$	S_3	$\bar{S}_3$	Time Inv.	Bases for C_{3h}
Γ_1	1	1	1	1	1	1	1	1	1	1	1	1	a	R
Γ_2	1	1	$-\omega^2$	$-\omega^2$	ω^4	ω^4	1	1	$-\omega^2$	$-\omega^2$	ω^4	ω^4	b	$(x-iy)^2$
Γ_3	1	1	ω^4	ω^4	$-\omega^2$	$-\omega^2$	1	1	ω^4	ω^4	$-\omega^2$	$-\omega^2$	b	$(x+iy)^2$
Γ_4	1	1	−1	−1	1	1	−1	−1	1	1	−1	−1	a	z
Γ_5	1	1	ω^2	ω^2	ω^4	ω^4	−1	−1	$-\omega^2$	$-\omega^2$	$-\omega^4$	$-\omega^4$	b	$-(S_x+iS_y)$
Γ_6	1	1	$-\omega^4$	$-\omega^4$	$-\omega^2$	$-\omega^2$	−1	−1	ω^4	ω^4	ω^2	ω^2	b	(S_x-iS_y)
Γ_7	1	−1	ω	$-\omega$	ω^2	$-\omega^2$	i	−i	$-\omega^4$	ω^4	$-\omega^5$	ω^5	b	$\phi(1/2,1/2)$
Γ_8	1	−1	$-\omega^5$	ω^5	$-\omega^4$	ω^4	−i	i	ω^2	$-\omega^2$	ω	$-\omega$	b	$\phi(1/2,-1/2)$
Γ_9	1	−1	$-\omega$	ω	ω^2	$-\omega^2$	−i	i	$-\omega^4$	ω^4	ω^5	$-\omega^5$	b	$\phi(5/2,-5/2)$
Γ_{10}	1	−1	ω^5	$-\omega^5$	$-\omega^4$	ω^4	i	−i	ω^2	$-\omega^2$	$-\omega$	ω	b	$\phi(5/2,5/2)$
Γ_{11}	1	−1	−i	i	−1	1	i	−i	−1	1	i	−i	b	$\phi(3/2,-3/2)$
Γ_{12}	1	−1	i	−i	−1	1	−i	i	−1	1	−i	i	b	$\phi(3/2,3/2)$

$\omega = \exp(\pi i/6)$

Figure 4: Character Table and Basis Functions for the Group C_{3h}.

Appendix B

Conduction and valence band states symmetry investigation

Conduction states:

Letting $\hat{C}_{\pm 3}$ being the operator acting in Hilbert space $\mathscr{E}$ corresponding to $C_{\pm 3}$ ($C_3^{-1} = C_{-3}$), we proceed first to the crystal rotation by $R_{e_z}\left(\frac{2\pi}{3}\right) = C_{-3}$ which correspond to $\hat{C}_{-3}$ in $\mathscr{E}_r$. Then the conduction Bloch wave in K transforms as follow:

$$\hat{C}_{-3}\psi_{c,\vec{K}^+}(\vec{r}) = \frac{1}{\sqrt{N}}\sum_{\vec{R}_I} e^{i\vec{K}^+.\vec{R}_I}\phi_c(C_{-3}^{-1}\vec{r} - \vec{R}_I);\ \vec{R}_I \in \text{crystal}$$

$$\hat{C}_{-3}\psi_{c,\vec{K}^+}(\vec{r}) = \frac{1}{\sqrt{N}}\sum_{\vec{R}_I'} e^{i\vec{K}^+.\vec{R}_I}\phi_c(C_3\vec{r} - \vec{R}_I)$$

where $\vec{R}_I' = C_3^{-1}\vec{R}_{I'}$

$$\hat{C}_{-3}\psi_{c,\vec{K}^+}(\vec{r}) = \frac{1}{\sqrt{N}}\sum_{\vec{R}_I'} e^{i\vec{K}^+.C_3\vec{R}_I'}\phi_c\left[C_3(\vec{r} - \vec{R}_I')\right]$$

Since $\phi_c(r) \in \Gamma_1$, $\phi_c\left[C_3(\vec{r} - \vec{R}_I')\right] = \phi_c\left(\vec{r} - \vec{R}_I'\right)$ so that $\hat{C}_{-3}\psi_{c,\vec{K}^+}(\vec{r}) = \frac{1}{\sqrt{N}}\sum_{\vec{R}_I'} e^{i\vec{K}^+C_3\vec{R}_I'}\phi_c\left(\vec{r} - \vec{R}_I'\right)$.
As the scalar product in real space is invariant by any isometric transformation, hence:

$$\vec{K}^+.\hat{C}_3\vec{R}_I' = (\hat{C}_{-3}\vec{K}^+)\cdot(\hat{C}_{-3}\hat{C}_3\vec{R}_I') = \hat{C}_{-3}\vec{K}^+.\vec{R}_I'$$

$$\hat{C}_{-3}\psi_{c,\vec{K}^+(\vec{r})} = \frac{1}{\sqrt{N}}\sum_{\vec{R}_I'} e^{i\hat{C}_{-3}\vec{K}^+.\vec{R}_I'}\phi_c\left(\vec{r} - \vec{R}_I'\right) = \frac{1}{\sqrt{N}}\sum_{\vec{R}_I} e^{i\hat{C}_{-3}\vec{K}^+.\vec{R}_I}\phi_c\left(\vec{r} - \vec{R}_I\right)$$

where we have applied the initial lemma (eq. 1.3) which allows us to make the proper index I substitutions. We get thus: $\hat{C}_{-3}\psi_{c,\vec{K}^+}(\vec{r}) = \psi_{c,\hat{C}_{-3}\vec{K}^+}(\vec{r})$. The same demonstration holds when rotating the crystal with C_3 and finally :

$$\hat{C}_{\pm 3}\psi_{c,\vec{K}^+}(\vec{r}) = \psi_{c,\hat{C}_{\pm 3}\vec{K}^+}(\vec{r})$$

The phase relationship between the two Bloch-wave functions $\psi_{c,\vec{K}^+}(\vec{r})$ and $\hat{C}_{\pm 3}\psi_{c,\vec{K}^+}(\vec{r})$ can be deduced by noticing that ($\hat{C}_{-3}\vec{K}^+ = \vec{K}_3^+$):

$$\vec{K}_3^+.\vec{R}_1 = \frac{4\pi}{3a_0}\left(-\frac{1}{2}, \frac{\sqrt{3}}{2}\right).\frac{a_0}{\sqrt{3}}(0,-1) = -\frac{2\pi}{3}$$

$$\vec{\mathrm{K}}_3^+.\vec{\mathrm{R}}_2 = \frac{4\pi}{3a_0}\left(-\frac{1}{2},\frac{\sqrt{3}}{2}\right).\frac{a_0}{\sqrt{3}}\left(\frac{\sqrt{3}}{2},\frac{1}{2}\right) = 0$$

$$\vec{\mathrm{K}}_3^+.\vec{\mathrm{R}}_3 = \frac{4\pi}{3a_0}\left(-\frac{1}{2},\frac{\sqrt{3}}{2}\right).\frac{a_0}{\sqrt{3}}\left(-\frac{\sqrt{3}}{2},\frac{1}{2}\right) = \frac{2\pi}{3}$$

where the scalar products are calculated in the $\left(0,\vec{e}_{\mathrm{X}},\vec{e}_{\mathrm{Y}}\right)$ frame.

Since we had previously:

$$\vec{\mathrm{K}}^+.\vec{\mathrm{R}}_1 = \frac{4\pi}{3a_0}(1,0).\frac{a_0}{\sqrt{3}}(0,-1) = 0$$

$$\vec{\mathrm{K}}^+.\vec{\mathrm{R}}_2 = \frac{4\pi}{3a_0}(1,0).\frac{a_0}{\sqrt{3}}\left(\frac{\sqrt{3}}{2},\frac{1}{2}\right) = \frac{2\pi}{3}$$

$$\vec{\mathrm{K}}^+.\vec{\mathrm{R}}_3 = \frac{4\pi}{3a_0}(1,0).\frac{a_0}{\sqrt{3}}\left(-\frac{\sqrt{3}}{2},\frac{1}{2}\right) = -\frac{2\pi}{3}$$

it results that $e^{i\vec{\mathrm{K}}_3^+.\vec{\mathrm{R}}_j} = e^{-i\frac{2\pi}{3}}e^{i\vec{\mathrm{K}}^+.\vec{\mathrm{R}}_j},(j=1,2,3)$. For the other points of the Bloch wave, we note that:

$$\vec{\mathrm{K}}_3^+.\vec{a}_1 = \frac{4\pi}{3a_0}\left(-\frac{1}{2},\frac{\sqrt{3}}{2}\right).\frac{a_0}{\sqrt{3}}\left(\frac{1}{2},-\frac{\sqrt{3}}{2}\right) = \frac{2\pi}{3}[2\pi]$$

$$\vec{\mathrm{K}}_3^+.\vec{a}_2 = \frac{4\pi}{3a_0}\left(-\frac{1}{2},\frac{\sqrt{3}}{2}\right).a_0(1,0) = -\frac{2\pi}{3}$$

$$\vec{\mathrm{K}}^+.\vec{a}_1 = \frac{4\pi}{3a_0}(1,0).\frac{a_0}{\sqrt{3}}\left(\frac{1}{2},-\frac{\sqrt{3}}{2}\right) = \frac{2\pi}{3}$$

$$\vec{\mathrm{K}}^+.\vec{a}_2 = \frac{4\pi}{3a_0}(1,0).a_0(1,0) = -\frac{2\pi}{3}[2\pi]$$

so that:

$$e^{i\vec{\mathrm{K}}_3^+.\vec{a}_j} = e^{i\vec{\mathrm{K}}^+.\vec{a}_j};(j=1,2)$$
$$e^{i\vec{\mathrm{K}}_3^+.n_j\vec{a}_j} = e^{i\vec{\mathrm{K}}^+.n_j\vec{a}_j}$$
$$e^{i\vec{\mathrm{K}}_3^+.\vec{\mathrm{T}}_{n_1,n_2}} = e^{i\vec{\mathrm{K}}^+.\vec{\mathrm{T}}_{n_1,n_2}}$$

hence:

$$\forall n_1,n_2\in\mathbb{Z}, e^{i\vec{\mathrm{K}}_3^+.\left(\vec{\mathrm{R}}_j+\vec{\mathrm{T}}_{n_1,n_2}\right)} = e^{-i\frac{2\pi}{3}}e^{i\vec{\mathrm{K}}^+.\left(\vec{\mathrm{R}}_j+\vec{\mathrm{T}}_{n_1,n_2}\right)};(j=1,2,3)$$

Finally:

$$\hat{\mathrm{C}}_{-3}\psi_{c,\vec{\mathrm{K}}^+}(\vec{r}) = e^{-i\frac{2\pi}{3}}\psi_{c,\vec{\mathrm{K}}^+}(\vec{r})$$

A similar demonstration holds when rotating the crystal by C_3, so that:

$$\hat{\mathrm{C}}_{\pm 3}\psi_{c,\vec{\mathrm{K}}^+}(\vec{r}) = e^{\pm i\frac{2\pi}{3}}\psi_{c,\vec{\mathrm{K}}^+}(\vec{r})$$

Valence states:

According to the the character table, starting again with the transformation $C_3^{-1} = C_{-3}$ ($\hat{C}_{-3}$ in $\mathscr{E}_r$), and since $\phi_{v,\vec{K}^+} \in \Gamma_3$,

$$\forall \vec{R}_I \in \text{crystal}, \hat{C}_{-3}\phi_{v,\vec{K}^+}(\vec{r} - \vec{R}_I) = \phi_{v,\vec{K}^+}(\hat{C}_3\vec{r} - \vec{R}_I) = \phi_{v,\vec{K}^+}(\vec{r}) \left[C_3(\vec{r} - \vec{R}'_I)\right]$$

with $\vec{R}_I = C_3\vec{R}'_I$ and $\hat{C}_{-3}\phi_{v,\vec{K}^+}(\vec{r} - \vec{R}_I) = e^{+i\frac{2\pi}{3}}\phi_{v,\vec{K}^+}(\vec{r} - \vec{R}'_I)$

$$\begin{aligned}
\hat{C}_{-3}\left(\frac{1}{\sqrt{N}}\sum_{\vec{R}_I} e^{i\vec{K}^+.\vec{R}_I}\phi_{v,\vec{K}^+}(\vec{r} - \vec{R}_I)\right) &= \frac{1}{\sqrt{N}}\sum_{\vec{R}_I} e^{i\vec{K}^+.\vec{R}_I}\phi_{v,\vec{K}^+}(C_3\vec{r} - \vec{R}_I) \\
&= \frac{1}{\sqrt{N}}\sum_{\vec{R}'_I} e^{i\vec{K}^+.C_3\vec{R}'_I}\phi_{v,\vec{K}^+}\left(C_3\left(\vec{r} - \vec{R}'_I\right)\right) \\
&= \frac{1}{\sqrt{N}}e^{i\frac{2\pi}{3}}\sum_{\vec{R}'_I} e^{iC_{-3}\vec{K}^+.\vec{R}'_I}\phi_{v,\vec{K}^+}\left(\vec{r} - \vec{R}'_I\right) \\
&= \frac{1}{\sqrt{N}}e^{i\frac{2\pi}{3}}\sum_{\vec{R}_I} e^{i\vec{K}_3^+.\vec{R}_I}\phi_{v,\vec{K}^+}\left(\vec{r} - \vec{R}_I\right) \\
&= \frac{1}{\sqrt{N}}e^{i\frac{2\pi}{3}}e^{-i\frac{2\pi}{3}}\sum_{\vec{R}_I} e^{i\vec{K}^+.\vec{R}_I}\phi_{v,\vec{K}^+}\left(\vec{r} - \vec{R}_I\right)
\end{aligned}$$

and finally: $\hat{C}_{-3}\psi_{v,\vec{K}^+}(\vec{r}) = \psi_{v,\vec{K}^+}(\vec{r})$

When rotating the crystal with C_3 we get similarly $\phi_{v,\vec{K}^+}(\vec{r})\left[C_3(\vec{r} - \vec{R}'_I)\right] \equiv e^{-i\frac{2\pi}{3}}\phi_{v,\vec{K}^+}(\vec{r} - \vec{R}'_I)$, but now:

$$\hat{C}_3\psi_{v,\vec{K}^+}(\vec{r}) = \frac{1}{\sqrt{N}}e^{-i\frac{2\pi}{3}}\sum_{\vec{R}'_I} e^{iC_3\vec{K}^+\vec{R}'_I}\phi_v(\vec{r} - \vec{R}'_I) = \frac{1}{\sqrt{N}}e^{-i\frac{2\pi}{3}}e^{+i\frac{2\pi}{3}}\sum_{\vec{R}'_I} e^{iC_{-3}\vec{K}^+\vec{R}'_I}\phi_v(\vec{r} - \vec{R}'_I)$$

Finally:

$$\hat{C}_{\pm 3}\psi_{v,\vec{K}^+}(\vec{r}) = \psi_{v,\vec{K}^+}(\vec{r})$$

Appendix C

Evaluation of $(\tilde{\vec{p}})_{m,m'}(\vec{q})$

In k.p theory or evaluating optical transitions, we need the matrix elements:

$$\tilde{\vec{p}}_{m,m'}(\vec{q}) = \frac{1}{\Omega}\int_{\Omega} u_{\vec{q},m}(\vec{r})\,\hat{p}\,u_{\vec{q},m'}(\vec{r})\,d^3r = \left\langle u_{\vec{q},m}\middle|\hat{p}\middle|u_{\vec{q},m'}\right\rangle_{\Omega}$$

where $\hat{p} = -i\hbar\nabla_{\vec{r}}$ or using the component forms:

$$(\tilde{\vec{p}}_{\pm})_{m,m'}(\vec{q}) = \frac{1}{\Omega}\int_{\Omega} u_{\vec{q},m}(\vec{r})\,\hat{p}_{\pm}\,u_{\vec{q},m'}(\vec{r})\,d^3r$$

$$(\tilde{\vec{p}}_{z})_{m,m'}(\vec{q}) = \frac{1}{\Omega}\int_{\Omega} u_{\vec{q},m}(\vec{r})\,\hat{p}_{z}\,u_{\vec{q},m'}(\vec{r})\,d^3r$$

These matrix elements can be simply related to $(\vec{p}_{\pm})_{m,m'}(\vec{q}) = \left\langle \Psi_{\vec{q},m}\middle|\hat{p}\middle|\Psi_{\vec{q},m'}\right\rangle$ as shown below:

$$\Psi_{\vec{q},m}(\vec{r}) = \frac{1}{\sqrt{\mathrm{N}}}\sum_{\vec{\mathrm{R}}_{\mathrm{I}}} e^{i\vec{q}\,\vec{\mathrm{R}}_{\mathrm{I}}}\phi_m(\vec{r}-\vec{\mathrm{R}}_{\mathrm{I}})$$

$$\begin{aligned}
\vec{p}_{m,m'}(\vec{q}) &= \frac{1}{\mathrm{N}}\int d^3r \sum_{\vec{\mathrm{R}}_{\mathrm{I}},\vec{\mathrm{R}}_{\mathrm{I}'}} e^{-i\vec{q}\,\vec{\mathrm{R}}_{\mathrm{I}}}\phi^*_m(\vec{r}-\vec{\mathrm{R}}_{\mathrm{I}})\,\hat{p}\,e^{i\vec{q}\,\vec{\mathrm{R}}_{\mathrm{I}'}}\phi_{m'}(\vec{r}-\vec{\mathrm{R}}_{\mathrm{I}'}) \\
&= \frac{1}{\mathrm{N}}\int d^3r \sum_{\vec{\mathrm{R}}_{\mathrm{I}},\vec{\mathrm{R}}_{\mathrm{I}'}} e^{i\vec{q}(\vec{\mathrm{R}}_{\mathrm{I}'}-\vec{\mathrm{R}}_{\mathrm{I}})}\phi^*_m(\vec{r}-\vec{\mathrm{R}}_{\mathrm{I}})\,\hat{p}\,\phi_{m'}(\vec{r}-\vec{\mathrm{R}}_{\mathrm{I}'}) \\
&= \frac{1}{\mathrm{N}}\int d^3r \sum_{\vec{\mathrm{T}},\vec{\mathrm{R}}_{\mathrm{I}'}} e^{i\vec{q}\,\vec{\mathrm{T}}}\phi^*_m(\vec{r}-\vec{\mathrm{R}}_{\mathrm{I}'}-\vec{\mathrm{T}})\,\hat{p}\,\phi_{m'}(\vec{r}-\vec{\mathrm{R}}_{\mathrm{I}'}) \\
&\approx \frac{1}{\mathrm{N}}\int d^3r \sum_{\vec{\mathrm{R}}_{\mathrm{I}'}} \phi^*_m(\vec{r}-\vec{\mathrm{R}}_{\mathrm{I}'})\,\hat{p}\,\phi_{m'}(\vec{r}-\vec{\mathrm{R}}_{\mathrm{I}'})
\end{aligned}$$

where the last formulation assumes that there is no overlapping of the orbital Eigen wave functions which belong to adjacent sites. Hence:

$$(\vec{p})_{m,m'}(\vec{q}) \approx \int d^3r\,\phi^*_m(\vec{r})\,\hat{p}\,\phi_{m'}(\vec{r})$$

We go back to the evaluation of $(\tilde{\vec{p}})_{m,m'}(\vec{q})$:

$$\begin{aligned}
\tilde{\vec{p}}_{m,m'}(\vec{q}) &= \frac{1}{\Omega}\int d^3r \frac{\Omega}{N}\sum_{\vec{R}_I,\vec{R}_{I'}} e^{-i\vec{q}(\vec{R}_I-\vec{r})}\phi^*_m(\vec{r}-\vec{R}_I)\hat{p}e^{i\vec{q}(\vec{R}_{I'}-\vec{r})}\phi_{m'}(\vec{r}-\vec{R}_{I'}) \\
&= \frac{1}{N}\int d^3r \sum_{\vec{R}_I,\vec{R}_{I'}} e^{i\vec{q}(\vec{R}_{I'}-\vec{R}_I)}\phi^*_m(\vec{r}-\vec{R}_I)\hat{p}\phi_{m'}(\vec{r}-\vec{R}_{I'}) \\
&- \hbar\vec{q}\sum_{\vec{R}_I,\vec{R}_{I'}} e^{i\vec{q}(\vec{R}_{I'}-\vec{R}_I)}\int d^3r\phi^*_m(\vec{r}-\vec{R}_I)\phi_{m'}(\vec{r}-\vec{R}_{I'}) \\
&= \left(\vec{p}_{\pm}\right)_{m,m'}(\vec{q}) - \hbar\vec{q}\sum_{\vec{R}_I}\delta_{R_I,R_{I'}}\int d^3r\phi^*_m(\vec{r}-\vec{R}_I)\phi_{m'}(\vec{r}-\vec{R}_{I'}) \\
&= \left(\vec{p}_{\pm}\right)_{m,m'}(\vec{q}) - \hbar\vec{q}\int d^3r\left|\phi_{m'}(\vec{r})\right|^2 = \left[\left(\vec{p}_{\pm}\right)_{m,m'}(\vec{q}) - \hbar\vec{q}\right]
\end{aligned}$$

Finally:

$$\left(\vec{p}_{\pm}\right)_{m,m'}(\vec{q}) = \left(\tilde{\vec{p}}_{\pm}\right)_{m,m'}(\vec{q}) + \hbar\vec{q}\,\delta_{m,m'}$$

Appendix D

Résumé en langue française du présent manuscrit

Le présent manuscrit de thèse est consacré à l'étude des propriétés physiques de monocouches atomiques de dichalcogénures à métaux de transition et plus particulièrement à l'étude de leurs propriétés excitoniques ainsi qu'à la dynamique d'indice de vallée des porteurs dans l'espace réciproque.

D.1 Chapitre 1 : Introduction aux monocouches de dichalcogénures à métaux de transition.

L'année 2005 a été marquée par la découverte de nouveaux matériaux 2D. Dans un article désormais célèbre, Novoselov et ses collègues rapportent en effet avoir réussi à fabriquer des monocouches atomiques de différents matériaux, en utilisant une technique d'une simplicité déconcertante : à l'aide d'une bande de scotch, ils sont parvenu à arracher des copeaux de matière à un morceau de matériau massif et à les déposer ensuite sur un substrat. Certains de ces copeaux se révèlent être des monocouches atomiques, toute la difficulté est de parvenir à les repérer. Cette technique, qui fonctionne bien sur les matériaux constitués de couches atomiques fortement liées dans le plan mais tenues entre elles par de simples liaisons de Van der Walls, a bien sûr révélé le graphène, mais également les monocouches de dichalcogénures à métaux de transition qui vont nous intéresser particulièrement ici.

Il faut attendre 2010 pour qu'un nouvel élément braque à nouveau l'attention du monde scientifique sur ces matériaux. De façon quasi-simultanée et indépendante, Splendiani et co. ainsi que Mak et co. démontrent que lorsqu'il est affiné jusqu'à la monocouche, le MoS_2 devient un semi-conducteur à gap direct. Peu de temps après, Xiao et co. ainsi que Cao et co. prédisent des règles de sélections optiques originales, reliant la polarisation de la lumière et l'indice de vallée des porteurs dans l'espace réciproque, pour ce matériaux et pour les autres monocouche de dichalcogénures à métaux de transition. Ces deux éléments combinés laissent présager des possibles applications de ces matériaux, notamment en électronique et suscitent immédiatement un très important engouement de la part de la communauté scientifique. Finalement les graphes 2 présentés ci-après résument cet engouement suscité par les monocouches de dichalcogénures à métaux de transition (MDMT) depuis 2012, date à laquelle commencent les travaux résumés dans ce manuscrit.

Le manuscrit détaille ensuite l'utilisation d'un modèle k.p à deux bandes pour redé-

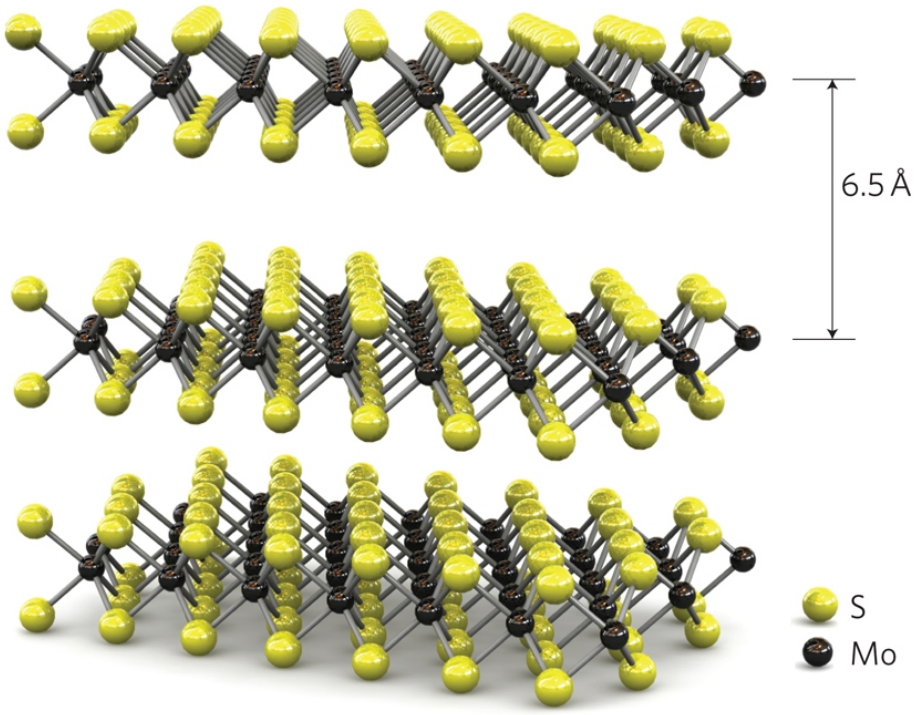

Figure 1: Représentation en 3 dimensions de la structure cristaline des MDMTs. Figure extraite de la référence [7]

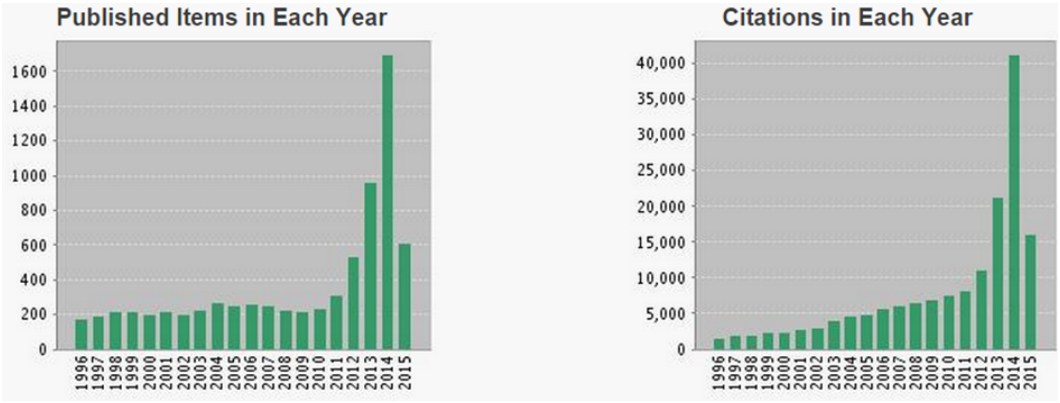

Figure 2: Statistiques issues du site Web of Knowledge (Mai 2015). Plus de 9000 articles ont été publiés sur les dichalcogénures à métaux de transition depuis 20 ans, dont environ 4000 depuis 2012.

montrer les propriétés optiques particulières des MDMT. Le résultat final principal est présenté sur la dernière figure de ce chapitre, à savoir que l'absorption de photons polarisés σ^+ génère des porteurs dans la vallée K^+ de l'espace réciproque et similairement, l'absorption de photons polarisés σ^- génère des porteurs dans la vallée K^-. Les valeurs des écarts entre les niveaux d'énergie généré par l'interaction spin-orbite ainsi que la démonstration détaillée sont présentés dans le manuscrit principal. La bande interdite (gap) des matériaux étudiés dans ce manuscrit se situe dans le spectre visible.

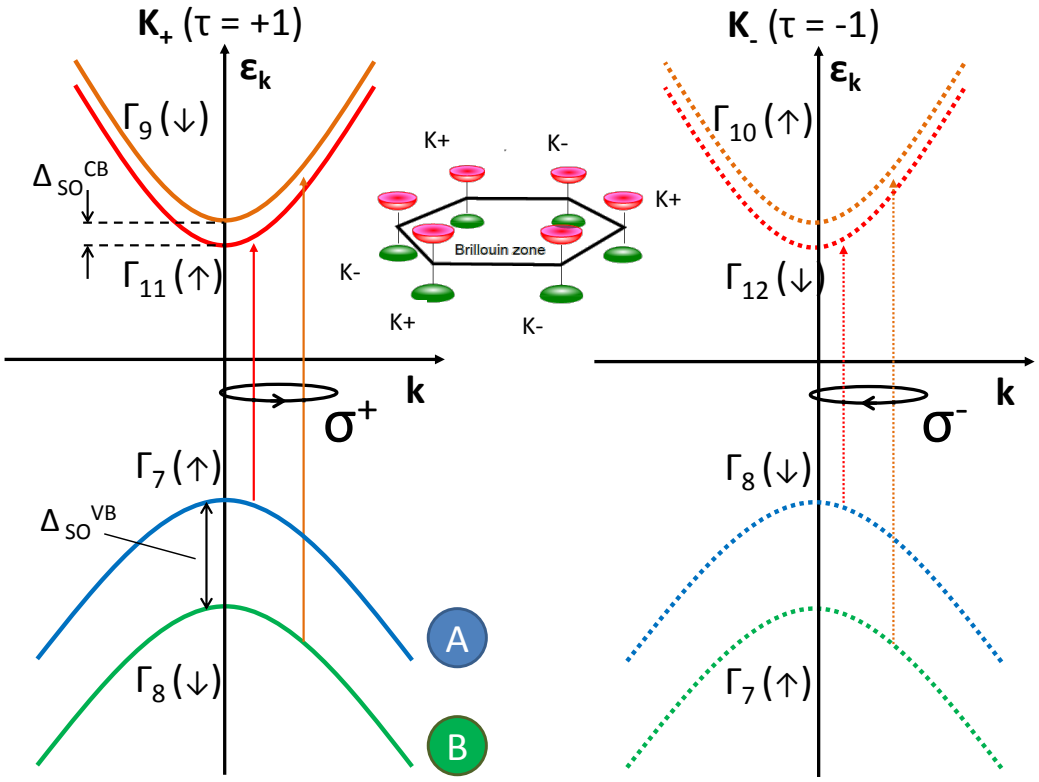

Figure 3: **Représentation schématique de la structure de bande dans MoS_2** Les bandes sont dénommées suivant la représentation irréductible correspondante, la flèche entre parenthèses donne l'orientation du spin. Les flèches continues et en pointillées représentent respectivement les transitions actives en polarisation σ^+ et σ^- (pour une incidence normale). L'ordre des bandes de conduction est cohérent avec la référence [22]

.

D.2 Chapitre 2 : Présentation des échantillons étudiés et des dispositifs expérimentaux utilisés

Dans le second chapitre de ce manuscrit sont présentés en détails les échantillons étudiés. Les figures 4, 5 et 6 qui suivent rassemblent ici les informations importantes. Les figures a) montrent les mesures du décalage en énergie généré par l'interaction spin-orbite que nous avons effectué pour chaque échantillon ($X_B^0 - X_A^0$). Pour chaque matériau, les valeurs mesurées sont proches de celles que l'on peut trouver dans la littérature. Les figures b) montrent la dépendance du spectre de photoluminescence de chaque matériau avec la température. Parmi les différentes informations que l'on peut en retirer, on remarquera particulièrement la disparition rapide des pics correspondants aux excitons localisés (notamment sur WSe_2). Les figures c) montrent les mesures de polarisation à basse température (4K). La présence de polarisation circulaire démontre la possibilité de générer des porteurs dans une vallée souhaitée, de manière contrôlée. La présence de polarisation linéaire témoigne de la possibilité de créer, sous certaines conditions, une superposition cohérente d'états dans les vallées K+ et K- de l'espace réciproque. Le lecteur voudra bien remarquer que si l'on observe une forte polarisation circulaire pour les échantillons de MoS_2 et WSe_2, $MoSe_2$ quant à lui ne présente aucun signe de polarisabilité. De même, la polarisation linéaire n'est observée que pour le seul WSe_2. Nous reviendrons plus en détails sur ce point au chapitre 5. La seconde partie du chapitre 2 est consacrée à la présentation détaillée du dispositif expérimental. Le lecteur pourra se référer aux figures présentées dans le manuscrit, qui sont assez explicites. Par ailleurs ce dispositif expérimental s'inspire des dispositifs de mesures présentés en langue française dans les références [45] et [53], auquelles le lecteur pourra se référer en cas de besoin.

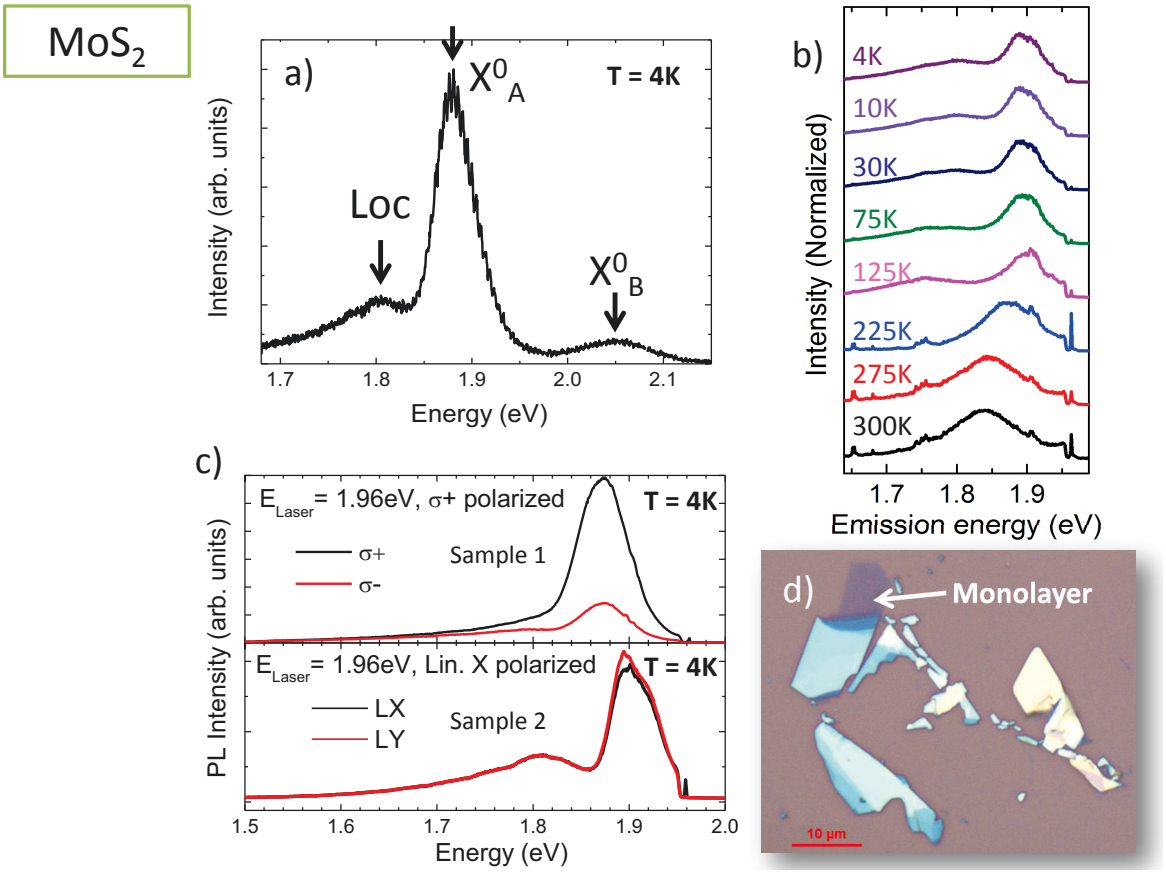

Figure 4: **Vue d'ensemble de l'échantillon : monocouche de MoS_2** (a) Spectre de photoluminescence sous excitation non-résonante. On voit ici simultanément les transition X^0_A et X^0_B ce qui nous permet d'estimer un écart en énergie d'environ ≈ 170 meV, très proche des valeurs couramment admises dans la littérature [26]. En effet $E_{X^0_B} - E_{X^0_A} = \Delta^{VB}_{SO} - \Delta^{CB}_{SO} - \left(E^{X^0_A}_B - E^{X^0_B}_B\right) \approx \Delta^{VB}_{SO}$ si on considère que $\Delta^{VB}_{SO} \gg \Delta^{CB}_{SO}$ et $E^{X^0_A}_B \approx E^{X^0_B}_B$. (b) Dépendance en température de l'émission de photoluminescence (c) Polarisation circulaire et linéaire de la photoluminescence sous excitation respectivement circulairement et linéairement polarisée (d) Image du cristal monocouche observé au microscope optique

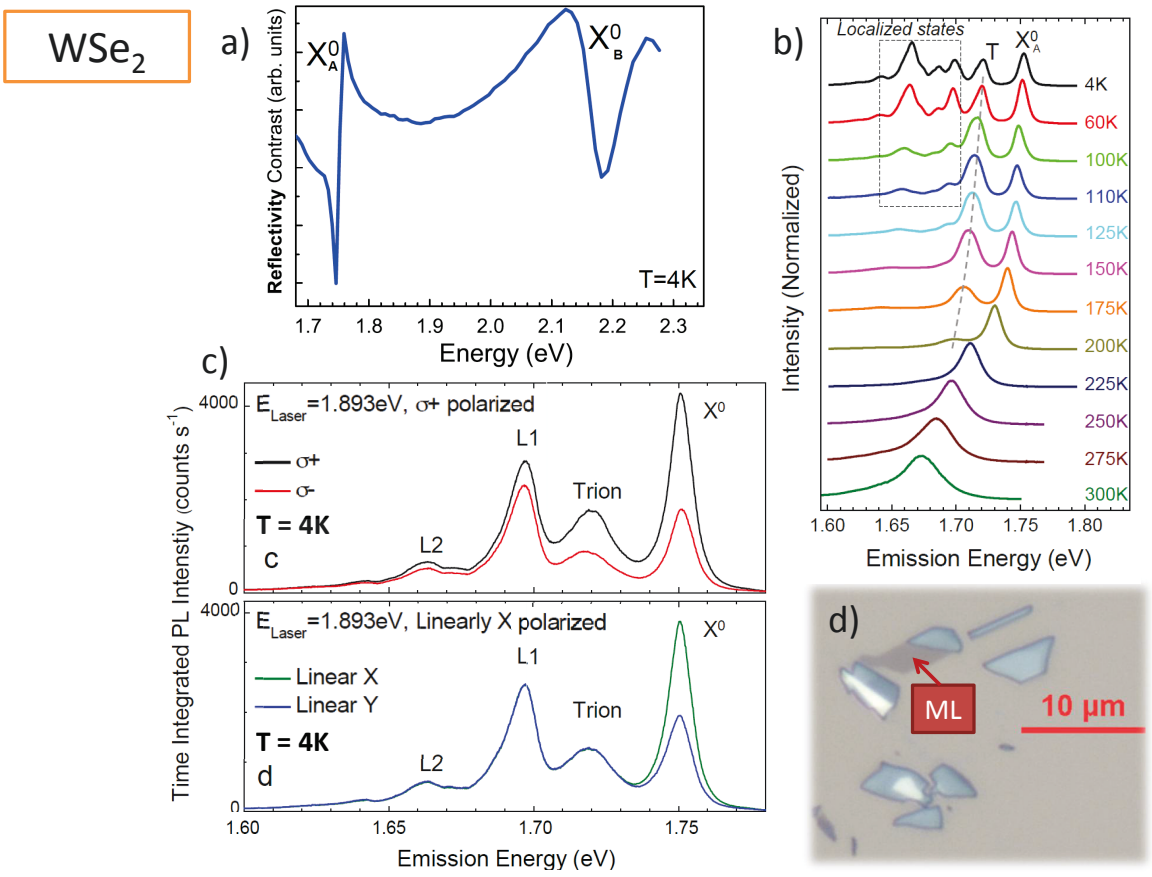

Figure 5: **Vue d'ensemble de l'échantillon : monocouche de WSe_2** (a) Mesure de réfléctivité permettant d'extraire un écart en énergie entre les transitions X^0_A et X^0_B d'approximativement ≈ 450 meV, in good agreement with both experimental and theoretical values of the literature [26] (b) Dépendance en température de l'émission de photoluminescence (c) Polarisation circulaire et linéaire de la photoluminescence sous excitation respectivement circulairement et linéairement polarisée (d) Image du cristal monocouche observé au microscope optique

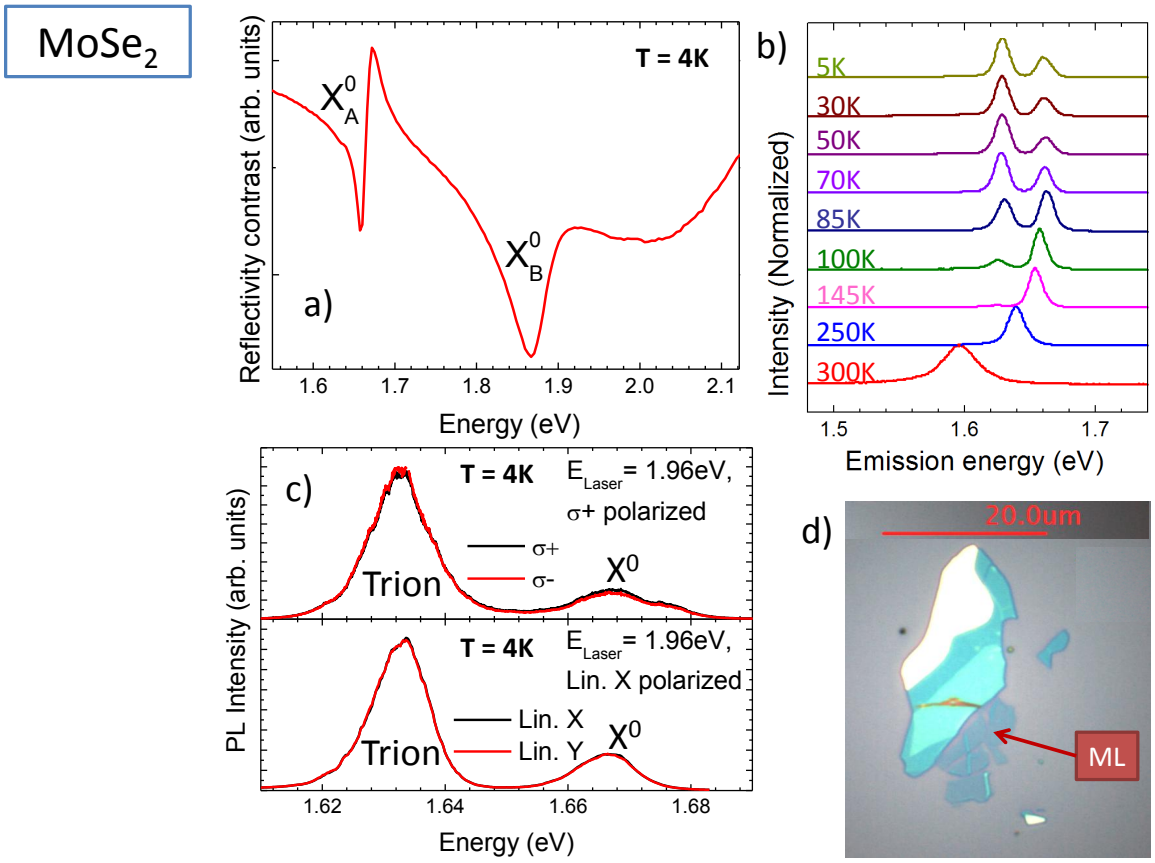

Figure 6: **Vue d'ensemble de l'échantillon : monocouche de $MoSe_2$** (a) Mesure de réfléctivité permettant d'extraire un écart en énergie entre les transitions X^0_A et X^0_B d'approximativement ≈ 220 meV, slightly above experimental and theoretical values of the literature [26] (b) Dépendance en température de l'émission de photoluminescence (c) Polarisation circulaire et linéaire de la photoluminescence sous excitation respectivement circulairement et linéairement polarisée (d) Image du cristal monocouche observé au microscope optique

D.3 Chapitre 3 : Adressage sélectif de porteurs dans les vallées K^+ et K^- de l'espace réciproque par voie optique.

Les premières mesures que nous avons réalisées avaient pour objectif de démontrer expérimentalement les règles de sélection optique des monocouches de MoS_2. Nous avons également étudié la dépendance du degré de polarisation généré en fonction d'une variété de grandeurs, ce qui nous ont permis de mieux comprendre la physique de ces matériaux. Comme exposé au chapitre 1, il y a une correspondance directe entre l'indice de vallée des porteurs, K^+ ou K^- et la polarisation circulaire, respectivement σ^+ ou σ^- des photons qu'ils émettent lorsqu'ils recombinent. Le fait que nous mesurions une forte polarisation de la luminescence, circulairement co-polarisée avec la polarisation du laser utilisé pour l'excitation, est une confirmation expérimentale des règles de sélection optique précédemment évoquées.

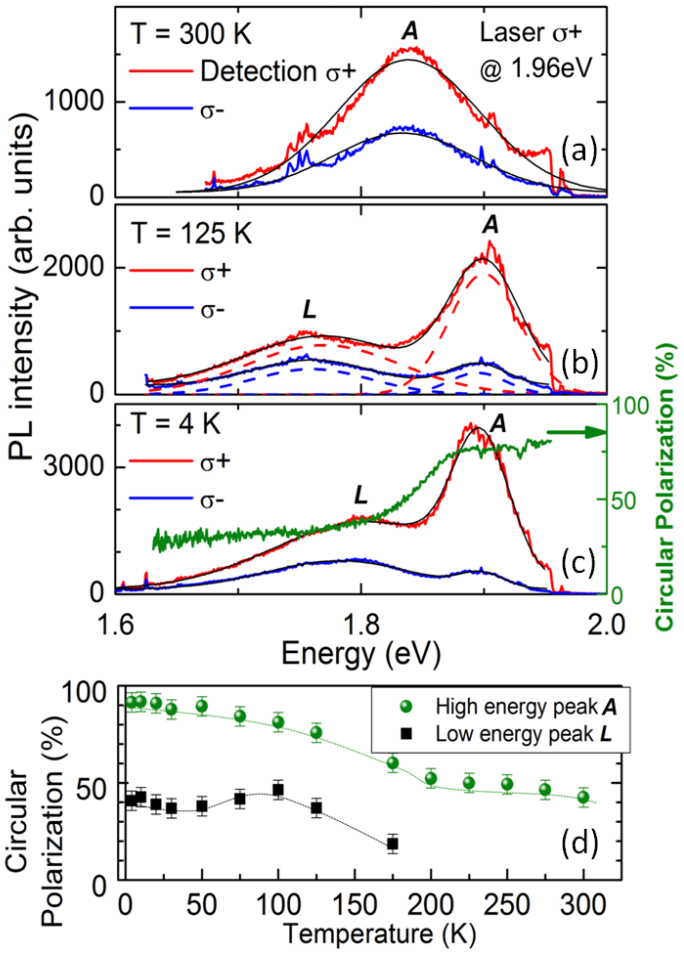

Figure 7: (a) Spectre de photoluminescence co-polarisé (rouge) et contra-polarisé (bleu) par rapport à la polarisation du laser d'excitation σ^+ (HeNe at 1.96eV). A environ 300 K, seul le pic de luminescence à haute énergie est détectable (exciton ***A***). Les courbes en noir indiquent les ajustements de courbe des données par des fonctions Gaussiennes (b) comme la courbe (a) mais pour T = 125 K. Les pics ***L*** et ***A*** sont tous deux détectables et les valeurs de polarisation sont calculés en effectuant des ajustements de courbes séparément (lignes pointillées). (c) comme (b) mais pour T = 4 K, l'axe de droite (vert) montre le degré de polarisation. L'intensité de la photoluminescence descend avec la température.(d) Degré de polarisation circulaire de la photoluminescence d'une monocouche atomique.

Les graphes présentés figure 7 montrent l'évolution du degré de polarisation circulaire

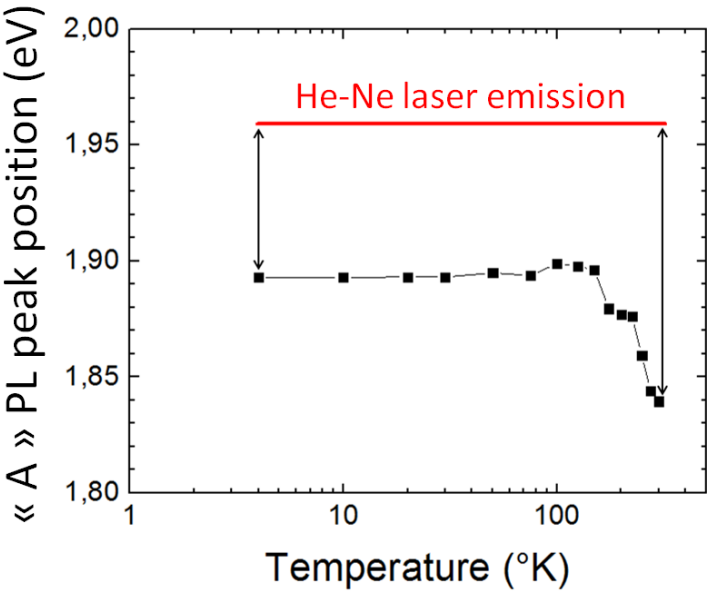

Figure 8: Evolution en fonction de la température de la position en énergie du pic correspondant à l'exciton A. La ligne rouge représente la position en énergie du laser HeNe utilisé pour l'excitation.

ainsi que du spectre de luminescence avec la température. On voit que le pic de luminescence à basse énergie disparaît après 150K, ce qui peut être la signature d'états localisés. La forme de ce pic change également selon les échantillons, ce qui va est cohérent avec notre hypothèse. La décroissance du degré de polarisation peut évidemment être due à l'activation de phonons permettant la diffusion de porteurs d'une vallée à l'autre, mais un autre élément est à prendre en compte. En effet l'énergie de notre laser d'excitation est fixe, alors que l'énergie du pic de luminescence décroît, par conséquent l'écart entre les deux augmente et cela peut affecter la pureté des règles de sélection (notamment en impliquant des phonons dans le processus d'absorption). Ci dessous, le graphe présenté montre l'évolution de l'écart entre énergie du laser et énergie de la photoluminescence, on voit que la polarisation décroît davantage lorsque l'écart augmente.

Cette hypothèse est également cohérente avec le résultat présenté à la figure 9. On voit en effet que le degré de polarisation de la photoluminescence augmente lorsqu'on se rapproche de la résonnance, donc lorsque l'énergie du laser d'émission est plus proche de l'énergie d'émission de la photoluminescence. Cela est vrai à 4K, mais également à température ambiante où l'on voit que changer l'énergie du laser d'excitation permet de recouvrir un fort degré de polarisation circulaire de la photoluminescence.

Finalement, comme montré sur la figure 10 nous avons appliqué un champ magnétique perpendiculaire à l'axe d'orientation du spin des porteurs afin de voir si une précession du spin des porteurs, voire de l'indice de vallée, pouvait être observée. Il apparaît que la polarisation des porteurs reste stable, cela est cohérent avec les règles de sélection optique du matériau, bien que cela puisse également être attribué aux importantes énergies de liaison créés par les effets excitoniques dans les MDMTs.

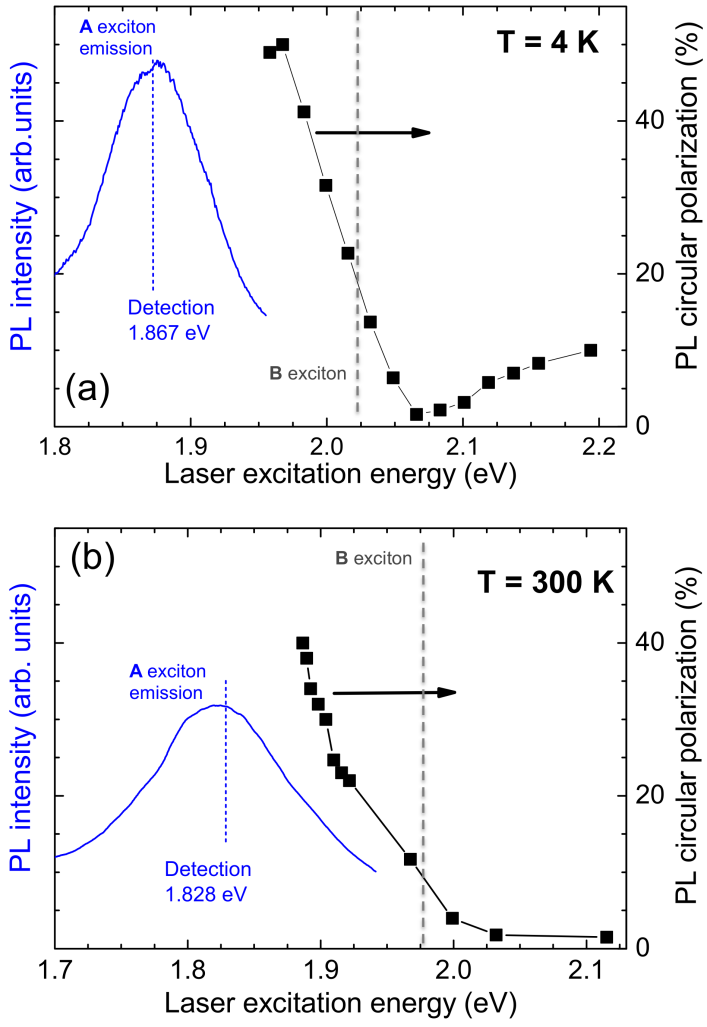

Figure 9: **Polarisation de la photoluminescence en fonction de l'énergie du laser d'excitation** (a) T = 4K, $P_{Laser} \simeq 550\ \mu W/\mu m^2$ détecté au maximum du spectre de photoluminescence de l'exciton A E_{Det} = 1.867 eV. L'émission de l'exciton A est présenté en bleu (b) comme (a) mais pour T = 300 K, $P_{Laser} \simeq 950\ \mu W/\mu m^2$, E_{Det} = 1.828 eV

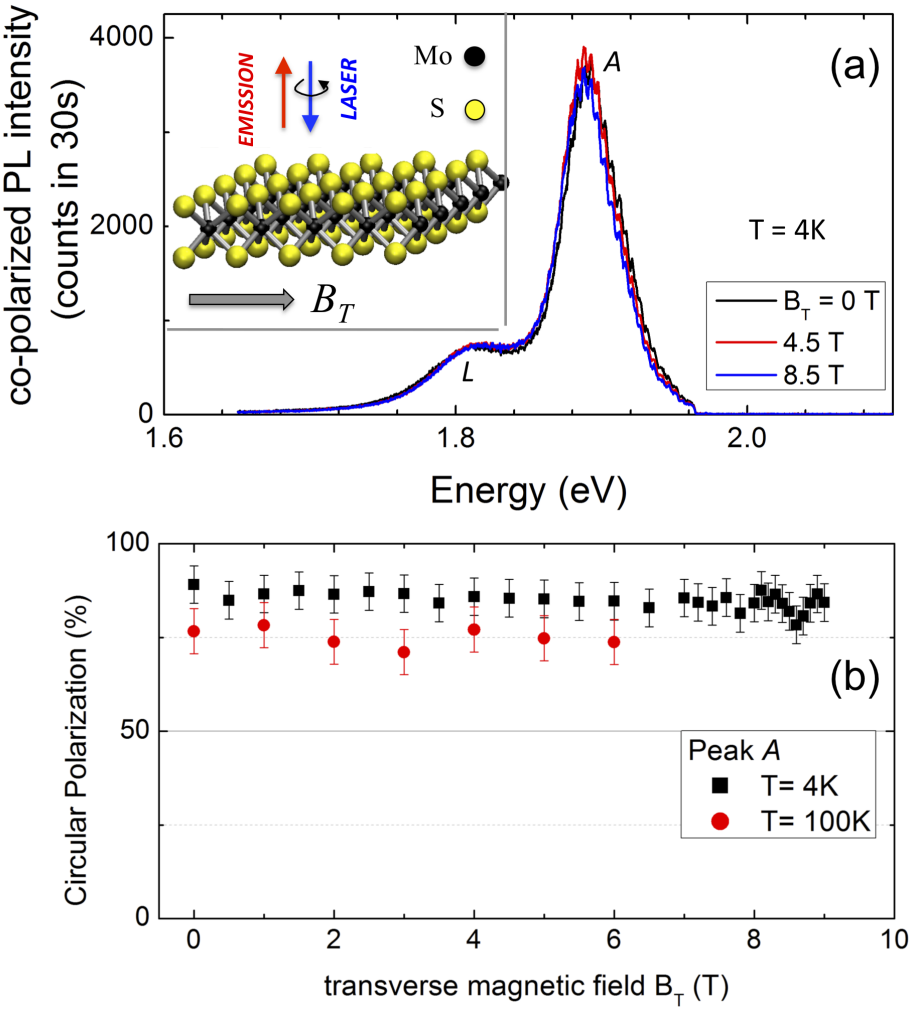

Figure 10: (a) Spectres de photoluminescence d'une monocouche de MoS_2 sous l'influence d'un champ magnétique transverse de valeur $B_T = 0, 4.5$ et 8.5 T respectivement. Les autres paramètres sont gardé constants et le laser d'excitation utilisé est un laser HeNe (1.96eV). Inset: experimental géometrie. (b) Evolution du degré de polarisation circulaire de la photoluminescence mesuré en fonction du champ magnétique transverse appliqué B_T pour l'exciton ***A*** à T = 4 K (carrés) et à T = 100 K (cercles).

D.4 Chapitre 4 : Dynamique d'indice de vallée dans les monocouches de MoS_2 et WSe_2.

Avant d'imaginer réaliser des applications basée sur la manipulation du nouveau degré de liberté qu'est l'indice de vallée, il était nécessaire d'estimer le temps de vie des porteurs dans les MDMTs. En effet, si l'important degré de polarisation qu'il est possible de générer démontre la véracité des règles de sélection, cela peut également signifier que le temps de vie des porteurs avant recombinaison est très court et il est difficile d'imaginer manipuler ce nouveau degré de liberté dans le cas.

Sur le graphe 11 sont résumées les mesures réalisées sur les monocouches de MoS_2, on voit que le temps d'émission des porteurs photo-générés est très court, à peine plus long que le temps d'émission du laser convolué par la réponse du système de détection (Streak camera Hamamatsu S20). Nous avons mesuré un temps aussi court que 4ps. Etant si proche de notre limite de résolution, il ne nous est pas possible de mesurer l'évolution de la polarisation au cours du temps (entre autres parce que les mesures étant prises séquentiellement, il est difficile de les synchroniser avec une précision suffisante). Les même mesures ont été répétées à température ambiante et montrent que les durée de temps d'émission ne changent pas de manière notable et on observe un fort degré de polarisation même à 300K tant que l'on excite le matériau avec un laser d'énergie proche de l'énergie d'émission du matériau.

Les même mesures ont été répétées sur les monocouches de WSe_2. La qualité optique des échantillons de WSe_2 étant meilleure, il est possible d'observer indépendamment les contributions des différents complexes excitoniques : excitons neutres (composés d'un électron et d'un trou), trions (un électron et un trou, plus une charge supplémentaire, généralement un électron dans ces matériaux) qui sont séparé des pics de luminescence générés par la recombinaison des porteurs sur des défauts, qui émet des photons à plus basse énergie.

Il apparaît que l'exciton neutre recombine très rapidement, comme c'est le cas pour MoS_2. Le trion est sensiblement plus long et recombine en 20ps. Nous ne nous intéressons pas à l'émission des localisés dont il ne nous est pas possible de déterminer l'origine dans l'état actuel des connaissances. En revanche le temps de recombinaison plus long du trion permet de mesurer l'évolution temporelle de l'indice de vallée en fonction du temps. Ces mesures sont présentées sur le graphe ci-dessous. On observe dans un premier temps une décroissance rapide de la polarisation en fonction du temps (et donc les porteurs perdent l'indice de vallée qu'ils avaient lors de leur photogénération), mais après 40ps, la polarisation cesse de décroître (temps de dépolarisation >1ns et donc très supérieur à la durée d'émission). Le trion est donc un porteur relativement stable de l'indice de vallée et au vu des informations que nous venons d'exposer, on peut penser qu'il est un candidat potentiel comme support de l'information de l'indice de vallée.

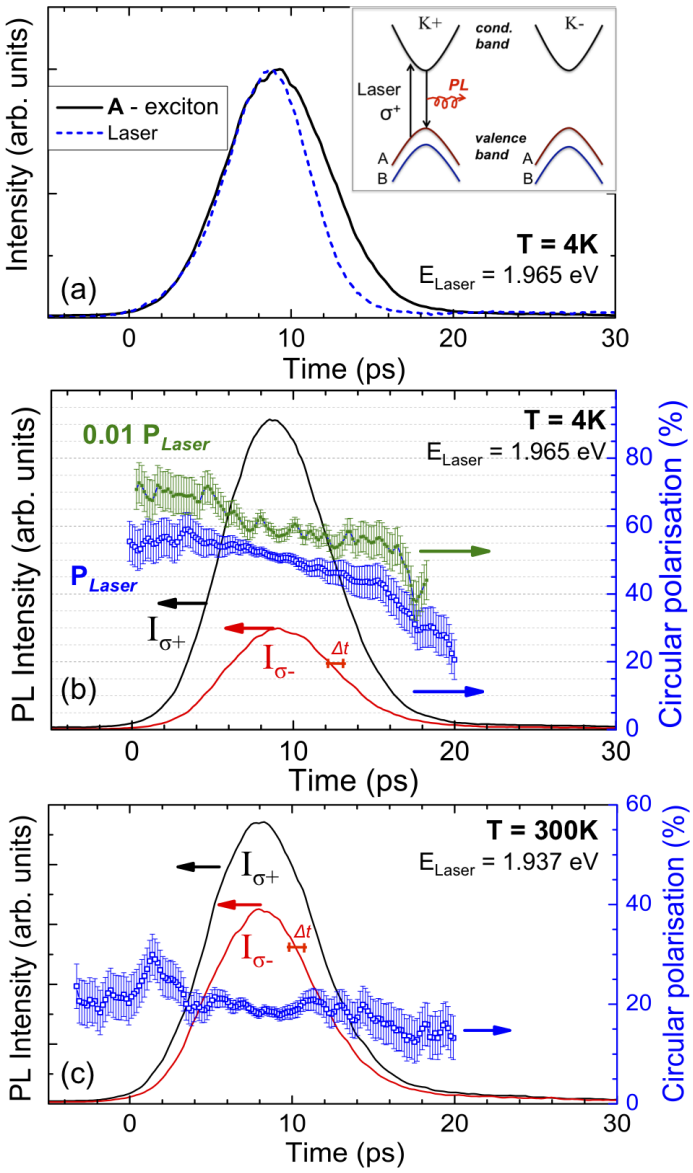

Figure 11: **Mesure de photoluminescence résolue en temps pour d'exciton A.** (a) Laser pulse (bleu) et intensité de la photoluminescence émise (ligne noire) à T = 4 K détecté à l'intensité maximale de l'exciton A E_{Det} = 1.867 eV en fonction du temps. (b) T=4K, E_{laser} = 1.965 eV, E_{Det} = 1.867 eV. Laser polarisé σ^+. Axe de gauche : Intensité de la photoluminescence émise polarisée σ^+ (σ^-) présentée en noir (rouge) en fonction du temps. Axe de droite : degré de polarisation circulaire durant l'émission de l'exciton (carré bleus : puissance d'excitation $P_{laser} \simeq 550$ $\mu W/\mu m^2$, Carrés verts :0.01 P_{laser}), les barres d'erreurs prennent en compte les incertitudes sur l'origine des temps lors de deux mesures successives $\Delta t \sim 0.7 ps$. (c) comme (b), mais pour T=300K, E_{laser} = 1.937 eV, E_{Det} = 1.828 eV.

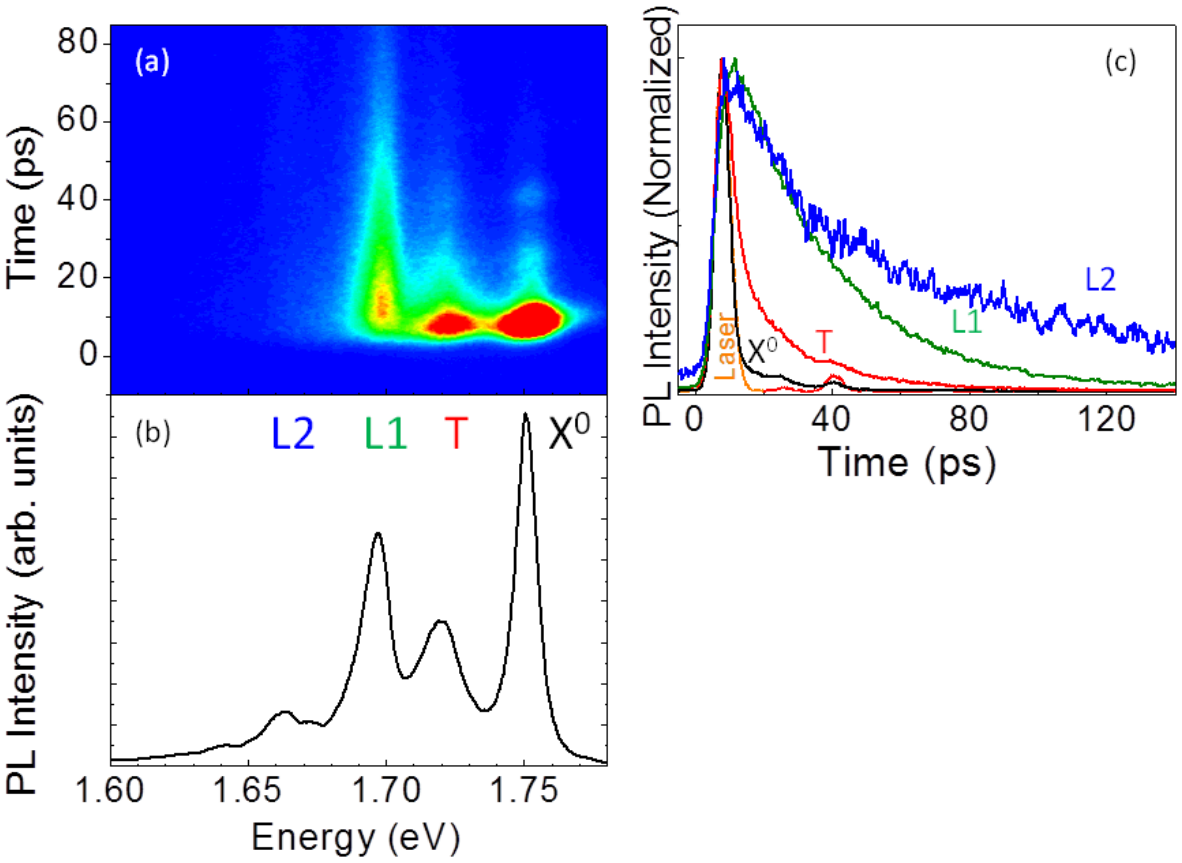

Figure 12: (a) Mesure par une caméra Streak de l'évolution de la photoluminescence en fonction du temps pour les différents complexes excitoniques X^0, trion and les états localisés. La couleur bleu (rouge) corresponds à une intensité de zero (5000).(b) Spectre de photoluminescence par une mesure "'temps intégré"' caractéristique des monocouches de WSe_2. (c) Dynamique de la photoluminescence normalisée (intensité totale du pic) pour chaque pic à T=4K.

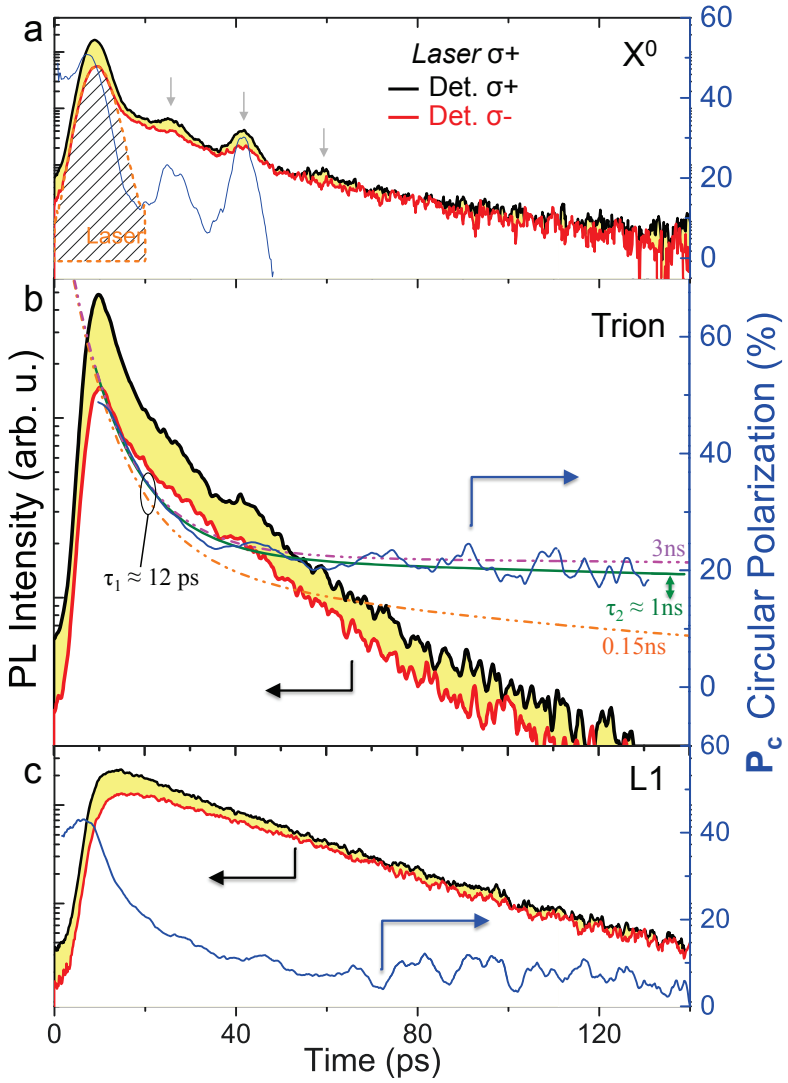

Figure 13: **Mesure de photoluminescence résolue en temps** T=4K. Polarisation du laser : σ^+. (a) axe de gauche : émission de photoluminescence du X^0 (échelle log) co-polarisée (noir) et contra polarisée (rouge) par rapport au laser d'excitation, en fonction du temps. Axe de droite : degré de polarisation circulaire de la photoluminescence émise. L'intensité de luminescence décroissant très rapidement, nous observons clairement une ré-excitation périodique due à des réflexions du laser à l'intérieur du dispositif expérimental, indiquées par des flèches. (b) comme (a), mais pour l'émission du trion. L'évolution de la polarisation suit une décroissance bi-exponentielle avec une première décroissance rapide τ_1 =12 ps et une seconde décroissance très longue τ_2 =1 ns (ligne verte continue). La limite basse (ligne orange pointillée pour τ_2 =150 ps) ainsi que haute (ligne violette en pointillée pour τ_2 =3 ns) de la décroissance lente sont également présentés. (c) comme (a), mais pour les excitons localisés L1.

D.5 Chapitre 5 : Effets excitoniques dans les monocouches de WSe_2.

Dans ce chapitre nous avons cherché à mettre en évidence la nature excitonique des porteurs photogénérés. En effet, il est naturel de penser que le confinement 2D très fort inhérent à ce matériau va favoriser les interactions entre les porteurs généré lors de l'absorption d'un photon. Cette interaction se traduit par l'apparition d'une énergie de liaison entre l'électron et le trou qui ne peuvent alors plus être décrits indépendamment l'un de l'autre et forment une quasi-particule appelée exciton.

Cette énergie de liaison correspond à la différence d'énergie entre le gap du matériau, qui est formé de l'ensemble des niveaux d'énergie électroniques du matériau, et le niveau d'énergie le plus bas de cette quasiparticule. Estimer la valeur de cette énergie de liaison est une information précieuse pour aller plus avant dans la compréhension de la physique de ces matériaux. En effet, si l'énergie de liaison est faible, la nature excitonique des porteurs n'aura que peu d'impact sur les phénomènes observés. En revanche de fortes énergies de liaisons excitoniques implique de les effets excitoniques dominent totalement la physique de ce matériau et doivent donc impérativement être pris en compte pour expliquer les phénomènes observés.

Les figures a, b et c présentés ci-dessus rappellent respectivement la structure cristalline, les règles de sélection optiques de la particule unique et de l'exciton dans WSe_2. Sur la figure d) peut être observé la présence de polarisation linéaire sur l'exciton neutre pour une énergie d'excitation bien précise, sur laquelle nous reviendrons. Enfin, la figure e montre simultanément le pic de luminescence dû à la génération de seconde harmonique (SHG) un effet d'optique non linéaire permit par la symétrie particulière du matériau, et le pic provoqué par l'absorption à deux photons et la recombinaison des porteurs après relaxation sur le niveau d'énergie 1s de l'exciton.

La figure 15 démontre à elle seule et très clairement la dominance des effets excitoniques dans WSe_2. Sont présentés ici trois techniques de spectroscopie complémentaires qui permettent sans aucune ambigüité de trouver la position des niveaux d'énergie de l'exciton. La première courbe montre l'évolution de l'intensité du signal de seconde harmonique en fonction de l'énergie d'excitation. Différents pics, correspondants à des résonnances entre niveaux d'énergies et énergie d'excitation sont observés qui démontrent très clairement la présence de niveaux d'énergie marqués, caractéristiques d'un exciton. On démontre ainsi la nature excitonique des porteurs photogénérés dans WSe_2. La figure 16 permet d'identifier ces pics. En effet, l'adaptation à la physique de la théorie des groupes, basée sur des considérations de correspondances de symétrie entre effets et causes que nous devons à Pierre Curie, nous permet d'affirmer que dans ce matériau l'absorption à 1 photon nous révèle les états de symétrie semblable aux niveaux de nombre quantique s alors que l'absorption à deux photons va nous révèler les niveaux d'énergie de nombre quantique p. Etant bien entendu que les niveaux d'énergie vont croissant, il nous est alors possible d'étiqueter nos pics, en partant toutefois de l'hypothèse que le premier pic est le niveau 1s, hypothèse parfois remise en cause dans la littérature. Notons également au passage que c'est lorsque l'excitation (à 1 ou 2 photons) est résonnante avec un niveau d'énergie que l'on peut générer une importante polarisation linéaire et donc une superposition cohérente d'états K+ et K-. La mesure expérimentale de la position de ces niveaux d'énergie, associé à des calculs de DFT permettant d'estimer la position du gap, permettent d'estimer une énergie de liaison d'environ 600meV, ce qui est absolument énorme! L'ordre de grandeur de cette mesure a depuis été confirmé par différents articles dans la littérature, à la fois sur WSe_2 mais également sur MoS_2, $MoSe_2$, WS2, ... Il

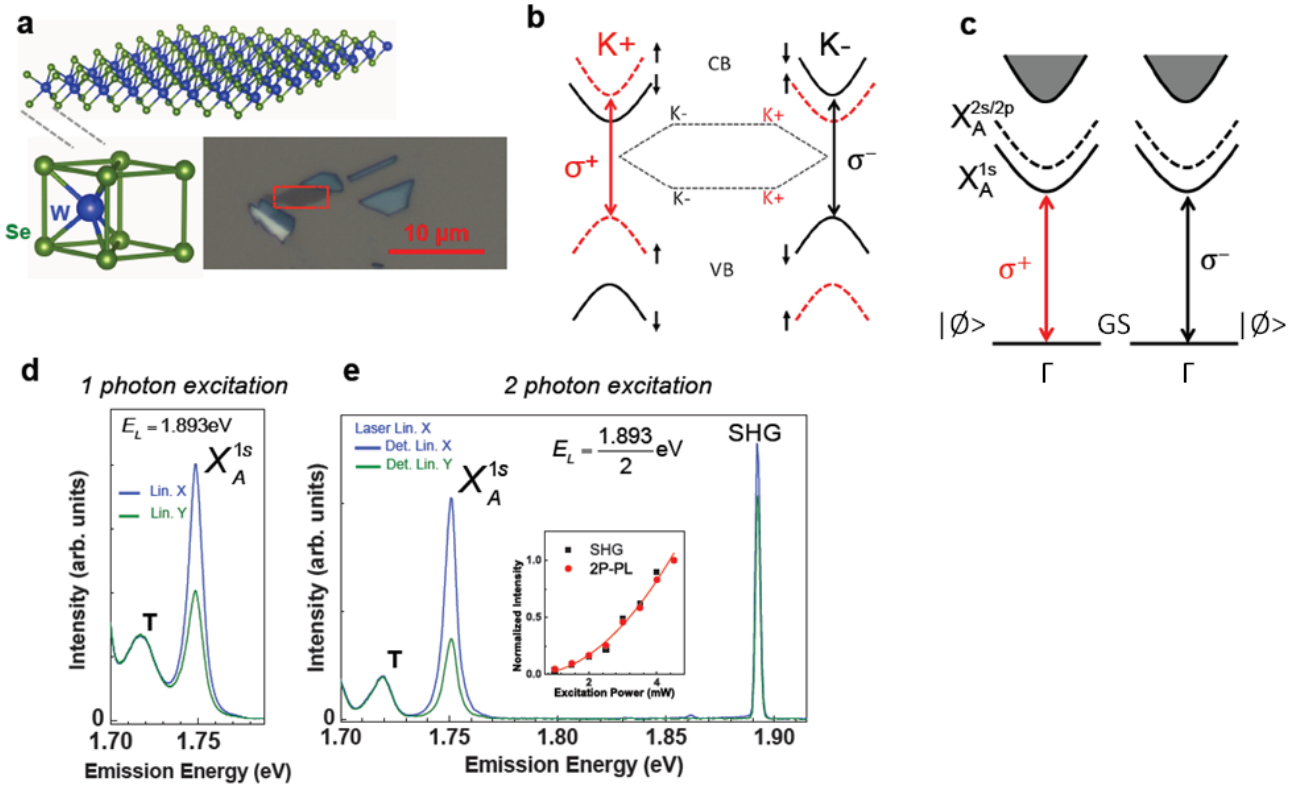

Figure 14: (a) Structure d'une monocouche de WSe_2 avec la brisure de symétrie d'inversion. (b) Règles de sélection optiques des monocouches de WSe_2 pour une excitation circulairement polarisée. (c) Règle de sélection optique de vallée dans la représentation de l'exciton. (d) Génération de superposition cohérence d'états dans les vallées non-équivalentes suite à l'absorption d'un photon unique et linéairement polarisé. Les transitions correspondantes à l'exciton neutre X_A^{1s} et au trion (T) sont indiquées. Les spectres de luminescence co polarisé (contra polarisé) part rapport au laser sont indiqués en bleu (vert). T=4K. (e) Génération de superposition cohérence d'états dans les vallées non-équivalentes suite à l'absorption de deux photons et linéairement polarisés. Les transitions correspondantes à l'exciton neutre X_A^{1s} et au trion (T) sont indiquées. Les spectres de luminescence co-polarisé (contra-polarisé) part rapport au laser sont indiqués en bleu (vert). T=4K.

est bien clair que les effets excitoniques dominent totalement la physique de WSe_2, mais également des autres MDMTs et permettent également d'expliquer certains phénomènes observés, comme les temps d'émission ultracourts de ces matériaux.

Pour finir, la figure 16 montre que les règles de sélection en polarisation sont totalement différentes entre le signal de SHG et la PLE à deux photons. Alors que la polarisation du signal de la génération de seconde harmonique ne dépend que de l'orientation de la polarisation linéaire incidente par rapport à l'orientation des axes cristallins, l'orientation du signal généré par l'excitation à deux photon suit exactement l'orientation de la polarisation d'excitation. Ceci est par ailleurs la première démonstration de la possibilité de générer une superposition cohérente d'états dans un semi-conducteur via une absorption à deux photons.

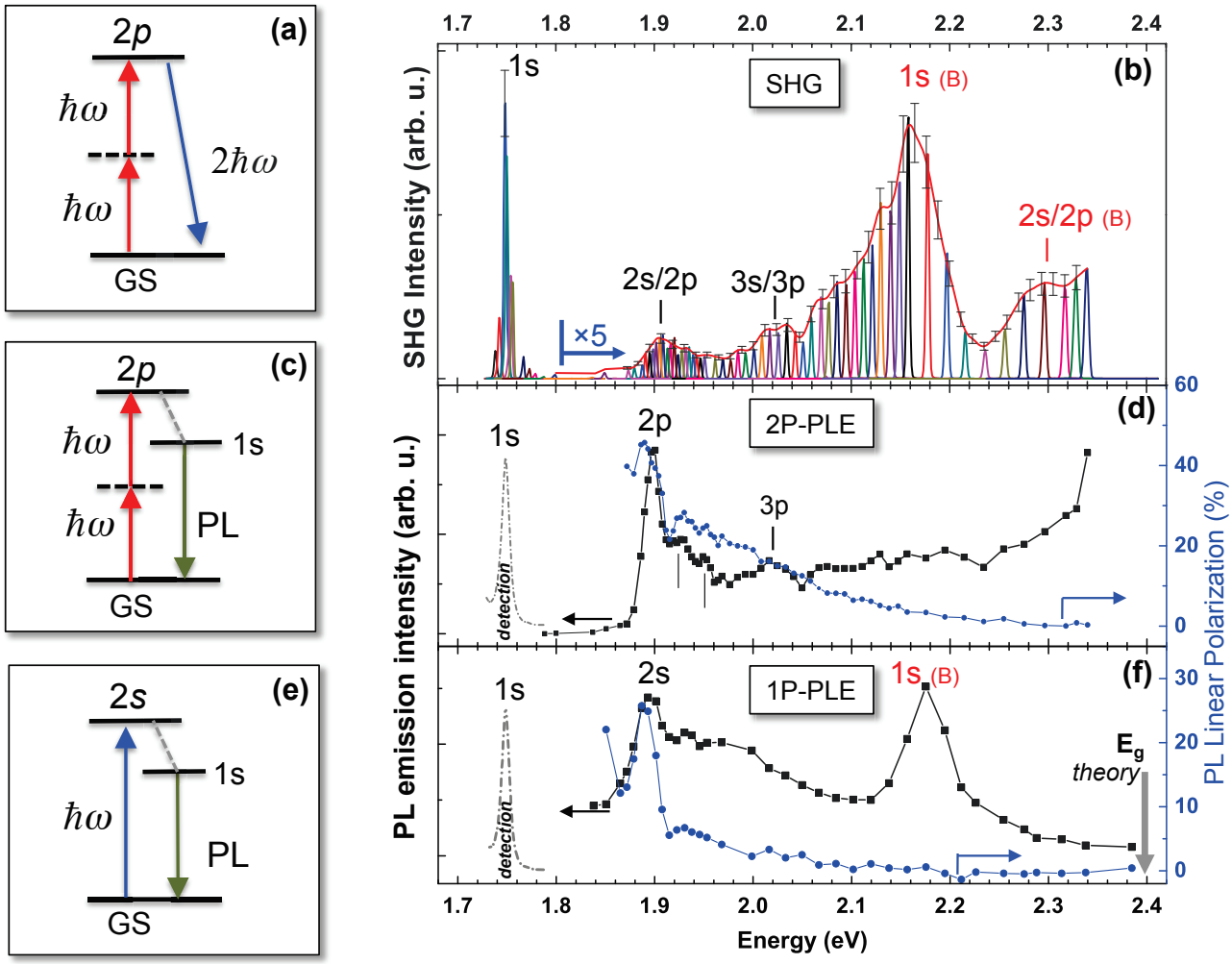

Figure 15: (a) schematic for SHG when 2 incident photons energy is resonant with the 2p state of the A-exciton (b) results of SHG spectroscopy at T=4K as a function of $2\hbar\omega$. (c) schematic for 2 photon PLE (d) 2 photon PLE intensity (left axis, black squares) and linear polarization (right axis, blue circles) as a function of $2\hbar\omega = 2E_{Laser}$). (e) schematic for 1 photon PLE (f) 1 photon PLE intensity (left axis, black squares) and linear polarization (right axis, blue circles)as a function of $\hbar\omega$. The dashed green line in (c) and (e) represent the energy relaxation path, e.g. by phonon emission.

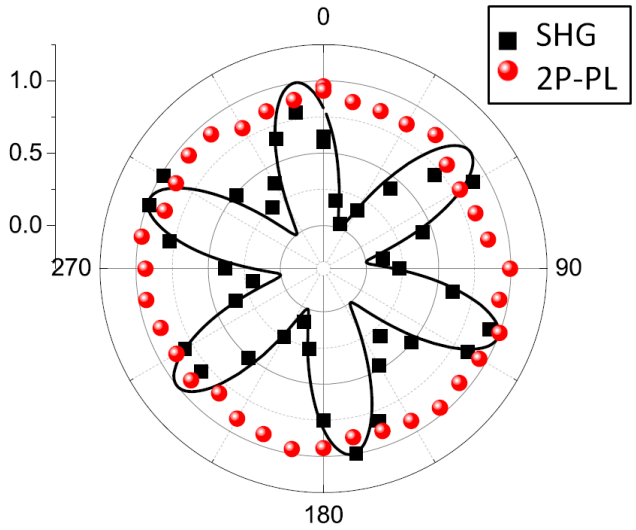

Figure 16: Dans cette expérience, excitation et détection sont tournées de manière synchronisée de façon à rester linéairement co-polarisées, E_{LASER} = 1.893/2 eV. On observe logiquement que l'intensité du signal généré par l'absorption à 2-photons reste maximal et constant quel que soit l'orientation de la polarisation, formant donc un cercle (symboles rouges). En revanche, comme la polarisation du signal issu de la génération de seconde harmonique est donné par l'orientation du cristal, sa dépendance avec l'orientation de la polarisation est très différente et on observe une dépendance de l'intensité du signal correspondant aux carrés noirs.

D.6 Chapitre 6 : Magnéto-spectroscopie dans les monocouches de disélénures à métaux de transition.

Dans ce dernier chapitre, nous avons utilisé des techniques de magnéto-spectroscopie pour aller plus loin dans l'analyse des propriétés physiques des MDMTs. En particulier l'application d'un champ magnétique nous permet de sonder la structure de bandes de ces matériaux. Nous avons réalisé ces expériences sur deux types de MDMTs, $MoSe_2$ et WSe_2. Les résultats de ces mesures sont résumés sur les figures 17 et 18.

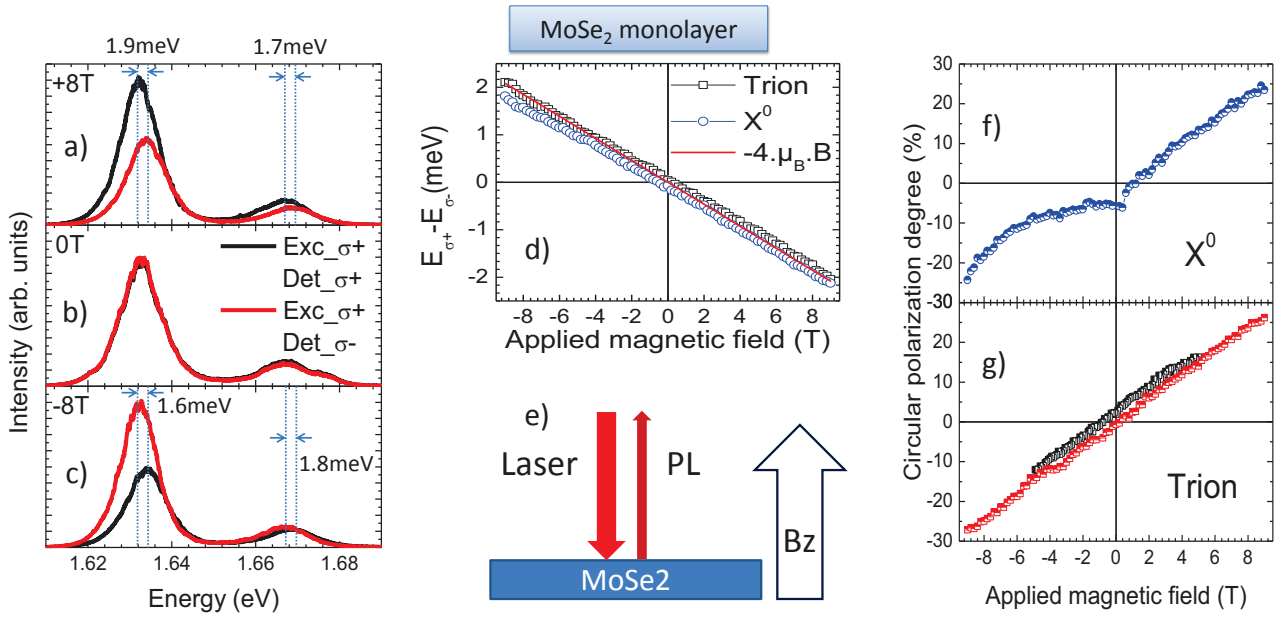

Figure 17: **Magnéto-spectroscopie sur monocouche de $MoSe_2$**; énergie d'excitation E_{Laser} = 1.96 eV (a) spectre de photo-luminescence à B_z = +8 T pour une détection polarisée respectivement σ^+ (noir) et σ^- (rouge) pour une excitation polarisée σ^+. (b) comme (a) mais pour B_z = 0 T. (c) comme (a) mais pour $B_z = -8$ T. (d) Ecart en énergie entre les composantes de la photoluminescence polarisées σ^+ et σ^- pour le trion (carrés noirs) et le X^0(cercles bleus) en fonction du champ magnétique appliqué, la fonction $-4\mu_B B_z$ est tracée pour comparaison (ligne rouge). (e) Schéma présentant la géométrie de l'expérience. (f) Polarisation de la luminescence émise par X^0 tracée en fonction de B_z. (g) Polarisation P_c de le photoluminescence émise par B_z sous excitation σ^+ (carrés noirs) et σ^- (carrés rouges).

Les résultats les plus marquants sont la dépendance très propre de l'écart énergétique entre les deux vallées qui est linéaire, et semble ainsi uniquement affectée par l'effet Zeeman. Le facteur g extrait est de 4, pour les deux matériaux. Une étude théorique basée sur la théorie k.p a été menée pour tenter d'expliquer la valeur de ce facteur mais sans succès. Il est simplement aujourd'hui certain que l'explication n'est pas triviale et requerra d'autres études poussées, à la fois théoriques et expérimentales. En revanche, la dépendance de la polarisation avec le champ magnétique est très différente pour les deux matériaux. Dans le cas de $MoSe_2$, il semble qu'elle soit uniquement dictée par le sens et l'intensité du champ magnétique et donc qu'elle soit, au moins en partie, due à la thermalisation des porteurs. Dans le cas de WSe_2, si le champ magnétique a un effet, il module simplement la polarisation initiale généré lors de la création des porteurs. Par ailleurs les dépendances de $MoSe_2$ et WSe_2 sont opposées. Sans avoir d'explication claire sur ce

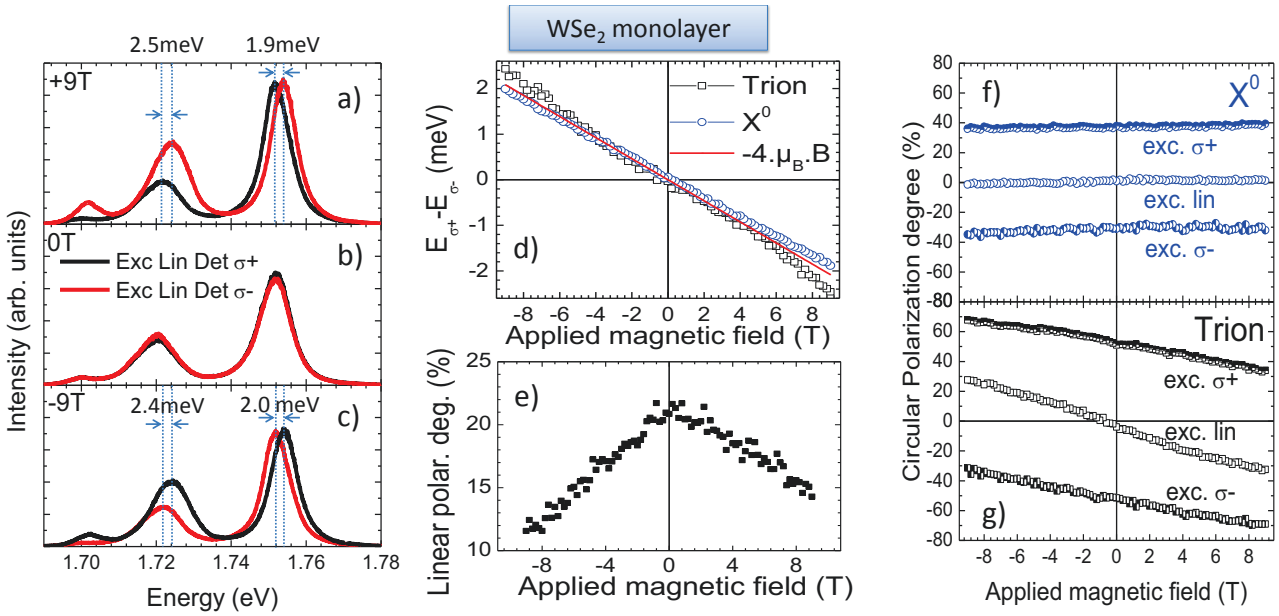

Figure 18: **Magnéto-spectroscopie sur monocouche de WSe_2**; énergie d'excitation E_{Laser} = 1.96 eV (a) spectre de photo-luminescence à B_z = +9 T pour une détection polarisée respectivement σ^+ (noir) et σ^- (rouge) pour une excitation polarisée σ^+. (b) comme (a) mais pour B_z = 0 T. (c) comme (a) mais pour B_z = −9 T. (d) Ecart en énergie entre les composantes de la photoluminescence polarisées σ^+ et σ^- pour le trion (carrés noirs) et le X^0 (cercles bleus) en fonction du champ magnétique appliqué, la fonction $-4\mu_B B_z$ est tracée pour comparaison (ligne rouge). (e) Polarisation linéaire de l'émission du X^0 en fonction de B_z. (f) Polarisation de la luminescence émise par X^0 tracée en fonction de B_z pour trois différentes polarisation du laser d'excitation. (g) Polarisation P_c de la photoluminescence émise par le trion tracée en fonction de B_z pour trois différentes polarisation du laser d'excitation.

point, il est possible que le fait que le signe de l'interaction spin-orbite soit inversé entre ces deux matériaux puisse être à l'origine de ce phénomène. Finalement, ces expériences de magnéto-spectroscopie amènent de nouvelles questions et seules de nouvelles investigations pourront permettre d'aller plus loin dans la compréhension de la physique de ces matériaux.

D.7 Conclusion

Les expériences présentées dans ce manuscrit ont contribuées à l'avancée de l'état de l'art des connaissances des monocouches de métaux de transition à dichalcogénures, matériaux 2D semi-conducteurs qui suscitent actuellement l'engouement de la communauté scientifique. Les perspectives sont riches, on a déjà commencé à réaliser des alliages entre ces différents matériaux, à construire des composants au moyen d'empilements des différentes monocouches de ces matériaux, ouvrant la voie à une véritable ingénierie des propriétés physiques tels que le gap ou l'indice de vallée. Notre compréhension des phénomènes survenant au sein de ces monocouches est encore très imparfaite et ce domaine n'a pas fini de surprendre et d'intéresser la communauté scientifique.

After each reference, the page numbers that contain the reference are listed.

Bibliography

[1] X. Marie, P. Le Jeune, T. Amand, M. Brousseau, J. Barrau, M. Paillard, and R. Planel. Coherent control of the optical orientation of excitons in quantum wells. *Phys. Rev. Lett.*, 79:3222–3225, Oct 1997. 2, 95

[2] M. Paillard, X. Marie, P. Renucci, T. Amand, A. Jbeli, and J. M. Gérard. Spin relaxation quenching in semiconductor quantum dots. *Phys. Rev. Lett.*, 86:1634–1637, Feb 2001.

[3] P.-F. Braun, X. Marie, L. Lombez, B. Urbaszek, T. Amand, P. Renucci, V. K. Kalevich, K. V. Kavokin, O. Krebs, P. Voisin, and Y. Masumoto. Direct observation of the electron spin relaxation induced by nuclei in quantum dots. *Phys. Rev. Lett.*, 94:116601, Mar 2005.

[4] Bernhard Urbaszek, Xavier Marie, Thierry Amand, Olivier Krebs, Paul Voisin, Patrick Maletinsky, Alexander Högele, and Atac Imamoglu. Nuclear spin physics in quantum dots: An optical investigation. *Rev. Mod. Phys.*, 85:79–133, 2013. 2, 94, 103

[5] David D. Awschalom and Michael E. Flatté. Challenges for semiconductor spintronics. *Nature Physics*, 3:153 – 159, 2007. 2

[6] Deep Jariwala, Vinod K. Sangwan, Lincoln J. Lauhon, Tobin J. Marks, and Mark C. Hersam. Emerging device applications for semiconducting two-dimensional transition metal dichalcogenides. *ACS Nano*, 8:1102–1120, 2014. 2, 7

[7] B. Radisavljevic, A. Radenovic, J. Brivio, V. Giacometti, and A. Kis. *Nature. Nanotech.*, 6:147, 2011. 2, 6, 7, 28, X

[8] Andrea Splendiani, Liang Sun, Yuanbo Zhang, Tianshu Li, Jonghwan Kim, Chi-Yung Chim, Giulia Galli, and Feng Wang. Emerging photoluminescence in monolayer mos2. *Nano Letters*, 10:1271, 2010. 2, 7, 12, 68

[9] J. S. Ross, P. Klement, A. M. Jones, N. J. Ghimire, J. Yan, D. G. Mandrus, T. Taniguchi, K. Watanabe, K. Kitamura, W. Yao, D. H Cobden, and X. Xu. *Nature Nanotechnology*, 9:268, 2014. 2, 7

[10] Oriol Lopez-Sanchez, Dominik Lembke, Metin Kayci, Aleksandra Radenovic, and Andras Kis. Ultrasensitive photodetectors based on monolayer mos2. *Nature Nanotechnology*, 8:497–501, Aug 2013. 2, 7

[11] Di Xiao, Gui-Bin Liu, Wanxiang Feng, Xiaodong Xu, and Wang Yao. Coupled spin and valley physics in monolayers of mos_2 and other group-vi dichalcogenides. *Phys. Rev. Lett.*, 108:196802, May 2012. 2, 7, 13, 14, 58, 65, 72, 73, 106

[12] K. F. Mak, K. L. McGill, J. Park, and P. L. McEuen. The valley hall effect in mos2 transistors. *Science*, 344(6191):1489–1492, 2014. 2, 72

[13] J.A. Wilson and A.D. Yoffea. The transition metal dichalcogenides discussion and interpretation of the observed optical, electrical and structural properties. *Advances in Physics*, 18:193–335, 1969. 6

[14] K. S. Novoselov, D. Jiang, F. Schedin, T. J. Booth, V. V. Khotkevich, S. V. Morozov, and A. K. Geim. *Proc. Natl Acad. Sci. USA*, 102:10451, 2005. 6, 28

[15] Kin Fai Mak, Changgu Lee, James Hone, Jie Shan, and Tony F. Heinz. Atomically thin mos_2: A new direct-gap semiconductor. *Phys. Rev. Lett.*, 105:136805, Sep 2010. 7, 68, 89

[16] Weijie Zhao, Zohreh Ghorannevis, Leiqiang Chu, Minglin Toh, Christian Kloc, Ping-Heng Tan, and Goki Eda. Evolution of electronic structure in atomically thin sheets of ws2 and wse2. *ACS Nano*, 7(1):791–797, 2013. 7

[17] Yi Zhang, Tay-Rong Chang, Bo Zhou, Yong-Tao Cui, Hao Yan, Zhongkai Liu, Felix Schmitt, James Lee, Rob Moore, Yulin Chen, Hsin Lin, Horng-Tay Jeng, Sung-Kwan Mo, Zahid Hussain, Arun Bansil, and Zhi-Xun Shen. Direct observation of the transition from indirect to direct bandgap in atomically thin epitaxial mose2. *Nature Nanotechnology*, 9:111, 2014. 7, 21, 110

[18] Ting Cao, Gang Wang, Wenpeng Han, Huiqui Ye, Chuanrui Zhu, Junren Shi, Qian Niu, Pingheng Tan, Enge Wang, Baoli Liu, and Ji Feng. Valley-selective circular dichroism in mos_2. *Nature Communications*, 3:887, 2012. 7, 58, 63, 65, 96, 104, 106

[19] Lei Tang Yibo Jin Tongtong Zhao Faxian Xiu Weiyi Wang, Yanwen Liu. Controllable schottky barriers between mos2 and permalloy. *Scientific Reports*, 4:6928, 2014. 7

[20] M. M. Ugeda, A. J. Bradley, S.-F. Shi, F. H. da Jornada, Y. Zhang, D. Y. Qiu, S.-K. Mo, Z. Hussain, Z.-X. Shen, F. Wang, S. G. Louie, and M. F. Crommie. Observation of giant bandgap renormalization and excitonic effects in a monolayer transition metal dichalcogenide semiconductor. *Nature Materials*, doi: 10.1038/nmat4061, 2014. 7, 21, 86, 97, 99, 105

[21] Hongliang Shi, Hui Pan, Yong-Wei Zhang, and Boris I. Yakobson. Quasiparticle band structures and optical properties of strained monolayer mos_2 and ws_2. *Phys. Rev. B*, 87:155304, Apr 2013. 7, 13, 14, 92

[22] Gui-Bin Liu, Wen-Yu Shan, Yugui Yao, Wang Yao, and Di Xiao. Three-band tight-binding model for monolayers of group-vib transition metal dichalcogenides. *Phys. Rev. B*, 88:085433, Aug 2013. 7, 21, 27, 60, 77, 78, 105, 111, XI

[23] Habib Rostami, Ali G. Moghaddam, and Reza Asgari. Effective lattice hamiltonian for monolayer mos_2: Tailoring electronic structure with perpendicular electric and magnetic fields. *Phys. Rev. B*, 88:085440, Aug 2013.

[24] E. Cappelluti, R. Roldán, J. A. Silva-Guillén, P. Ordejón, and F. Guinea. Tight-binding model and direct-gap/indirect-gap transition in single-layer and multilayer mos_2. *Phys. Rev. B*, 88:075409, Aug 2013. 7

[25] E. O. Kane. *J. Phys. Chem. Solids*, 1:82, 249, 1957. 8, 14

[26] Andor Kormányos, Guido Burkard, Martin Gmitra, Jaroslav Fabian, Viktor Zólyomi, Neil D Drummond, and Vladimir Fal'ko. $k \cdot p$ theory for two-dimensional transition metal dichalcogenide semiconductors. *2D Materials*, 2(2):022001, 2015. 8, 20, 22, 29, 30, 32, 82, 109, XIII, XIV, XV

[27] G. F. Koster, J. O. Dimmock, G. Wheeler, and R. G. Satz. Properties of thirty-two point groups. *M.I.T. Press, Cambridge, Massachusetts USA*, 1963. 11, 13, 14, 19, 25, 68, I

[28] E. L. Ivchenko and G. Pikus, Superlattices and other Heterostructures, Symmetry and Optical Phenomena, Springer Series in Solid State Science 110, Springer Verlag Berlin Heildelberg (1995). 13, 19, 49, 102, 108

[29] Aaron J. Bradley, Miguel M. Ugeda, Felipe H. da Jornada, Diana Y. Qiu, Wei Ruan, Yi Zhang, Sebastian Wickenburg, Alexander Riss, Jiong Lu, Sung-Kwan Mo, Zahid Hussain, Zhi-Xun Shen, Steven G. Louie, , and Michael F. Crommie. Probing the role of interlayer coupling and coulomb interactions on electronic structure in few-layer mose2 nanostructures. *Nano Lett.*, 15:2594–2599, 2015. 21

[30] E. Rosencher and Borge Vinter. *Optoelectronics*. Cambridge University Press, Cambridge (UK), 2002. 23, 53

[31] 2D semiconductor company. "monolayer wse2" http://www.2dsemiconductors.com/monolayer-wse2-p/mlwse2.htm. 2015. 30

[32] Aaron M. Jones, Hongyi Yu, Nirmal J. Ghimire, Sanfeng Wu, Grant Aivazian, Jason S. Ross, Bo Zhao, Jiaqiang Yan, David G. Mandrus, Di Xiao, Wang Yao, and Xiaodong Xu. Optical generation of excitonic valley coherence in monolayer wse2. *Nat. Nanotechnol.*, 8:634, 2013. 31, 72, 77, 78, 87, 88, 95, 104, 105

[33] G. Wang, X. Marie, I. Gerber, T. Amand, D. Lagarde, L. Bouet, M. Vidal, A. Balocchi, and B. Urbaszek. Giant enhancement of the optical second-harmonic emission of wse_2 monolayers by laser excitation at exciton resonances. *Phys. Rev. Lett.*, 114:097403, 2015. 31, 78, 86, 87, 90, 104, 105

[34] G. Wang, M. M. Glazov, C. Robert, T. Amand, X. Marie, and B. Urbaszek. Double resonant raman scattering and valley coherence generation in monolayer wse2. *e-print*, arXiv:1505.06128, 2015. 31

[35] Andres Castellanos-Gomez, Michele Buscema, Rianda Molenaar, Vibhor Singh, Laurens Janssen, Herre S J van der Zant, and Gary A Steele. Deterministic transfer of two-dimensional materials by all-dry viscoelastic stamping. *2D Materials*, 1(1):011002, 2014. 31, 103

[36] Sefaattin Tongay, Jian Zhou, Can Ataca, Kelvin Lo, Tyler S. Matthews, Jingbo Li, Jeffrey C. Grossman, and Junqiao Wu. Thermally driven crossover from indirect toward direct bandgap in 2d semiconductors: Mose2 versus mos2. *Nano Letters*, 12(11):5576–5580, 2012. 31

[37] G.Wang, I. C. Gerber, L. Bouet, D. Lagarde, A. Balocchi, M. Vidal, E. Palleau, T. Amand, X. Marie, and B. Urbaszek. Exciton states in monolayer mose2: impact on interband transitions. *e-print*, arXiv:1504.06333, 2015. 31, 66

[38] L. Bouet, M. Vidal, T. Mano, N. Ha, T. Kuroda, M. V. Durnev, M. M. Glazov, E. L. Ivchenko, X. Marie, T. Amand, K. Sakoda, G. Wang, and B. Urbaszek. Charge tuning in [111] grown gaas droplet quantum dots. *Applied Physics Letters*, 105(8):–, 2014. 32, 37, 103

[39] J. Nilsson, L. Bouet, A. J. Bennett, T. Amand, R. M. Stevenson, I. Farrer, D. A. Ritchie, S. Kunz, X. Marie, A. J. Shields, and B. Urbaszek. Voltage control of electron-nuclear spin correlation time in a single quantum dot. *Phys. Rev. B*, 88:085306, Aug 2013.

[40] M. V. Durnev, M. M. Glazov, E. L. Ivchenko, M. Jo, T. Mano, T. Kuroda, K. Sakoda, S. Kunz, G. Sallen, L. Bouet, X. Marie, D. Lagarde, T. Amand, and B. Urbaszek. Magnetic field induced valence band mixing in [111] grown semiconductor quantum dots. *Phys. Rev. B*, 87:085315, Feb 2013.

[41] G. Sallen, S. Kunz, T. Amand, L. Bouet, T. Kuroda, T. Mano, D. Paget, O. Krebs, X. Marie, K. Sakoda, and B. Urbaszek. Nuclear magnetization in gallium arsenide quantum dots at zero magnetic field. *Nature Communications*, 5, Feb 2014. 32, 37

[42] M. Minsky. *U.S. Patent 3013467*. 34

[43] P. Brackenhoff, G. J. Blom and P. Barends. Confocal scanning light microscopy with high apertureimmersion lenses. *Journal of Microscopy*, 117:219, 1979. 34

[44] T Wilson and C. J. R. Sheppard. *Theory and practice of scanning optical microscopy*. Acad. Press, 1984. 34

[45] P. F. Braun. *Orientation de Spin par Pompage Optique dans les boîtes quantiques InAs/GaAs*. Institut national des Sciences Appliquées, Toulouse, 2007. 38

[46] F. Meier and B. Zakharchenya. Optical orientation. *Modern Problems in Condensed Matter Sciences (North-Holland, Amsterdam).*, 8, 1984. 40, 73

[47] S. Kunz. *Magneto-optical properties of individual GaAs/AlGaAs QDs*. Institut national des Sciences Appliquées, Toulouse, 2013. 42

[48] H. Wang, C. Zhang, C. Weimin, C. Manolatou, S. Tiwari, and F Rana. *e-print*, arXiv:1402.0263, 2013. 44

[49] Roperscientific. "ccd camera specifications sheet". *From roperscientific website: http:/www.roperscientific.de/speccams.html*, 2015. 44

[50] G. Sallen, L. Bouet, X. Marie, G. Wang, C. R. Zhu, W. P. Han, Y. Lu, P. H. Tan, T. Amand, B. L. Liu, and B. Urbaszek. Robust optical emission polarization in mos_2 monolayers through selective valley excitation. *Phys. Rev. B*, 86:081301, 2012. 48, 58, 64, 77, 89, 96, 104

[51] G Wang, L Bouet, M M Glazov, T Amand, E L Ivchenko, E Palleau, X Marie, and B Urbaszek. Magneto-optics in transition metal diselenide monolayers. *2D Materials*, 2(3):034002, 2015. 48, 102, 109, 112

[52] X. Marie A. Balocchi and T. Amand. *Semiconductor research, Experimental techniques*. Springer, 2012. 50, 51

[53] D. Lagarde. *Dynamique de spin dans des structures semiconductrices à base de ZnO et de GaN*. Institut national des Sciences Appliquées, Toulouse, 2008. 52

[54] Z. Y. Zhu, Y. C. Cheng, and U. Schwingenschlögl. Giant spin-orbit-induced spin splitting in two-dimensional transition-metal dichalcogenide semiconductors. *Phys. Rev. B*, 84:153402, Oct 2011. 58, 62, 77, 89

[55] Kin Fai Mak, Keliang He, Jie Shan, and Tony F. Heinz. Control of valley polarization in monolayer mos_2 by optical helicity. *Nat. Nanotechnol.*, 7:494, 2012. 58, 59, 62, 64, 68, 73, 77, 80, 81, 96, 104

[56] Hualing Zeng, Junfeng Dai, Wang Yao, Di Xiao, and Xiaodong Cui. Valley polarization in mos_2 monolayers by optical pumping. *Nat. Nanotechnol.*, 7:490, 2012. 58, 64, 69, 104

[57] O. Gunawan, Y. P. Shkolnikov, K. Vakili, T. Gokmen, E. P. De Poortere, and M. Shayegan. Valley susceptibility of an interacting two-dimensional electron system. *Phys. Rev. Lett.*, 97:186404, Nov 2006. 58

[58] Fan Zhang, Jeil Jung, Gregory A. Fiete, Qian Niu, and Allan H. MacDonald. Spontaneous quantum hall states in chirally stacked few-layer graphene systems. *Phys. Rev. Lett.*, 106:156801, Apr 2011. 58

[59] A. Rycerz, J. Tworzydlo, and C.W. J. Beenakker. *Nature. Phys.*, 3:172, 2007.

[60] S. Y. Zhou, G.-H. Gweon, A. V. Fedorov, P. N. First, W. A. de Heer, D.-H. Lee, F. Guinea, A. H. C. Neto, and A. Lanzara. *Nature Mater.*, 6:770, 2007. 58

[61] T. Korn, S. Heydrich, M. Hirmer, J. Schmutzler, and C. Schüller. Low-temperature photocarrier dynamics in monolayer mos_2. *Applied Physics Letters*, 99(10):102109, 2011. 59, 63, 77, 80

[62] G. Plechinger, F.-X. Schrettenbrunner, J. Eroms, D. Weiss, C. Schüller, and T. Korn. Back cover: Low-temperature photoluminescence of oxide-covered single-layer mos2 (phys. status solidi rrl 3/2012). *phys. stat. sol. (RRL)*, 6:126, 2012. 59

[63] M. Dyakonov. Spin physics in semiconductor nanostructures. *Springer Series in Solid-State Science, Springer-Verlag Berlin*, 157, 2008. 60, 63, 68, 105

[64] Andor Kormányos, Viktor Zólyomi, Neil D. Drummond, Péter Rakyta, Guido Burkard, and Vladimir I. Fal'ko. Monolayer mos: Trigonal warping, the γ valley, and spin-orbit coupling effects. *Phys. Rev. B*, 88:045416, Jul 2013. 62, 65, 76, 89, 109

[65] Hao Qiu, Tao Xu, Zilu Wang, Wei Ren, Haiyan Nan, Zhenhua Ni, Qian Chen, Shijun Yuan, Feng Miao, Fengqi Song, Gen Long, Yi Shi, Litao Sun, Jinlan Wang, and Xinran Wang. Hopping transport through defect-induced localized states in molybdenum disulphide. *Nature Communications*, 4:2642, Oct 2013. 62

[66] Tawinan Cheiwchanchamnangij and Walter R. L. Lambrecht. Quasiparticle band structure calculation of monolayer, bilayer, and bulk mos_2. *Phys. Rev. B*, 85:205302, 2012. 64, 65

[67] G. Kioseoglou, A. T. Hanbicki, M. Currie, A. L. Friedman, D. Gunlycke, and B. T. Jonker. Valley polarization and intervalley scattering in monolayer mos[sub 2]. *Applied Physics Letters*, 101(22):221907, 2012. 64, 104

[68] C. R. Zhu, G. Wang, B. L. Liu, X. Marie, X. F. Qiao, X. Zhang, X. X. Wu, H. Fan, P. H. Tan, T. Amand, and B. Urbaszek. Strain tuning of optical emission energy and polarization in monolayer and bilayer mos_2. *Phys. Rev. B*, 88:121301, 2013. 65

[69] Substantial broadening, and hence overlap of the transitions at 300K can lower the efficiency of valley polarization generation during absorption. 65

[70] Tawinan Cheiwchanchamnangij and Walter R. L. Lambrecht. Quasiparticle band structure calculation of monolayer, bilayer, and bulk mos_2. *Phys. Rev. B*, 85:205302, May 2012. 65, 80, 82, 86, 87, 89

[71] Ashwin Ramasubramaniam. Large excitonic effects in monolayers of molybdenum and tungsten dichalcogenides. *Phys. Rev. B*, 86:115409, Sep 2012. 78, 80, 86, 87, 92, 96

[72] Kin Fai Mak, Keliang He, Changgu, Gwan Hyoung Lee, James Hone, Tony F. Heinz, and Jie Shan. Tightly bound trions in monolayer mos2. *Nature Materials*, 12:207, 2013. 73, 80, 92, 99

[73] Frank J. Crowne, Matin Amani, A. Glen Birdwell, Matthew L. Chin, Terrance P. O'Regan, Sina Najmaei, Zheng Liu, Pulickel M. Ajayan, Jun Lou, and Madan Dubey. Blueshift of the a-exciton peak in folded monolayer $1h$-mos_2. *Phys. Rev. B*, 88:235302, Dec 2013. 65, 80

[74] Goki Eda, Hisato Yamaguchi, Damien Voiry, Takeshi Fujita, Mingwei Chen, and Manish Chhowalla. Photoluminescence from chemically exfoliated mos2. *Nano Letters*, 11(12):5111–5116, 2011. 68

[75] M. Z. Maialle, E. A. de Andrada e Silva, and L. J. Sham. Exciton spin dynamics in quantum wells. *Phys. Rev. B*, 47:15776–15788, Jun 1993. 72, 81, 82, 95, 105

[76] M. M. Glazov, T. Amand, X. Marie, D. Lagarde, L. Bouet, and B. Urbaszek. Exciton fine structure and spin decoherence in monolayers of transition metal dichalcogenides. *Phys. Rev. B*, 89:201302, 2014. 72, 81, 95

[77] H. Yu, G. Liu, P. Gong, X. Xu, and W. Yao. Bright excitons in monolayer transition metal dichalcogenides: from Dirac cones to Dirac saddle points. *Nature Comms.*, 5:3876, 2014. 72, 81, 84, 104, 105

[78] Eric W. Weisstein. "convolution.". *From MathWorld–A Wolfram Web Resource. http://mathworld.wolfram.com/Convolution.html*, 2015. 75

[79] Eric W. Weisstein. "gaussian function.". *From MathWorld–A Wolfram Web Resource. http://mathworld.wolfram.com/GaussianFunction.html*, 2015. 75

[80] K. Kosmider, J. W. González, and J. Fernández-Rossier. Large spin splitting in the conduction band of transition metal dichalcogenide monolayers. *Phys. Rev. B*, 88:245436, Dec 2013. 77, 105, 111

[81] Diana Y. Qiu, Felipe H. da Jornada, and Steven G. Louie. Optical spectrum of mos2: Many-body effects and diversity of exciton states. *Phys. Rev. Lett.*, 111:216805, Nov 2013. 78, 86, 87, 92, 93, 96, 97

[82] B. Deveaud, F. Clérot, N. Roy, K. Satzke, B. Sermage, and D. S. Katzer. Enhanced radiative recombination of free excitons in gaas quantum wells. *Phys. Rev. Lett.*, 67:2355–2358, Oct 1991. 78

[83] T. Amand, J. Barrau, X. Marie, N. Lauret, B. Dareys, M. Brousseau, and F. Laruelle. Optical detection of vertical transport in gaas/algaas superlattices: Stationary and dynamical approaches. *Phys. Rev. B*, 47:7155–7169, Mar 1993. 78

[84] Qiannan Cui, Frank Ceballos, Nardeep Kumar, and Hui Zhao. Transient absorption microscopy of monolayer and bulk wse2. *ACS Nano*, 8(3):2970–2976, 2014. 79

[85] G. Finkelstein, V. Umansky, I. Bar-Joseph, V. Ciulin, S. Haacke, J.-D. Ganière, and B. Deveaud. Charged exciton dynamics in gaas quantum wells. *Phys. Rev. B*, 58:12637–12640, Nov 1998. 79

[86] E. Vanelle, M. Paillard, X. Marie, T. Amand, P. Gilliot, D. Brinkmann, R. Lévy, J. Cibert, and S. Tatarenko. Spin coherence and formation dynamics of charged excitons in cdte/cdmgznte quantum wells. *Phys. Rev. B*, 62:2696–2705, Jul 2000. 79

[87] Alexey Chernikov, Timothy C. Berkelbach, Heather M. Hill, Albert Rigosi, Yilei Li, Ozgur Burak Aslan, David R. Reichman, Mark S. Hybertsen, and Tony F. Heinz. Exciton binding energy and nonhydrogenic rydberg series in monolayer ws_2. *Phys. Rev. Lett.*, 113:076802, Aug 2014. 79, 86, 97, 98, 99

[88] H. Wang, C. Zhang, C. Weimin, C. Manolatou, S. Tiwari, and F Rana. *e-print*, arXiv:1409.3996, 2013. 79, 80

[89] Hongyan Shi, Rusen Yan, Simone Bertolazzi, Jacopo Brivio, Bo Gao, Andras Kis, Debdeep Jena, Huili Grace Xing, and Libai Huang. Exciton dynamics in suspended monolayer and few-layer mos2 2d crystals. *ACS Nano*, 7(2):1072–1080, 2013. 80

[90] Rui Wang, Brian A. Ruzicka, Nardeep Kumar, Matthew Z. Bellus, Hsin-Ying Chiu, and Hui Zhao. Ultrafast and spatially resolved studies of charge carriers in atomically thin molybdenum disulfide. *Phys. Rev. B*, 86:045406, Jul 2012. 80

[91] A. R. Klots, A. K. M. Newaz, B. Wang, D. Prasai, H. Krzyzanowska, D. Caudel, N. J. Ghimire, J. Yan, B. L. Ivanov, K. A. Velizhanin, A. Burger, D. G. Mandrus, N. H. Tolk, S. T. Pantelides, and K. I. Bolotin. Probing excitonic states in ultraclean suspended two-dimensional semiconductors by photocurrent spectroscopy. *Scientific Report*, 4(6608), 2014. 80, 86, 97, 99

[92] E. Varene, L. Bogner, C. Bronner, and P. Tegeder. Ultrafast exciton population, relaxation, and decay dynamics in thin oligothiophene films. *Phys. Rev. Lett.*, 109:207601, Nov 2012. 80

[93] Vasili Perebeinos, J. Tersoff, and Phaedon Avouris. Radiative lifetime of excitons in carbon nanotubes. *Nano Letters*, 5(12):2495–2499, 2005.

[94] Kazuya Watanabe, Tsuyoshi Asahi, Hiroshi Fukumura, Hiroshi Masuhara, Kouji Hamano, and Tetsuyuki Kurata. Ultrafast decay dynamics of excited and charged states in a-sexithienyl film as revealed by femtosecond transient absorption and picosecond fluorescence spectroscopy. *The Journal of Physical Chemistry B*, 101(9):1510–1519, 1997. 80

[95] J. Feldmann, G. Peter, E. O. Göbel, P. Dawson, K. Moore, C. Foxon, and R. J. Elliott. Linewidth dependence of radiative exciton lifetimes in quantum wells. *Phys. Rev. Lett.*, 59:2337–2340, Nov 1987. 80

[96] D. Lagarde, L. Bouet, X. Marie, C. R. Zhu, B. L. Liu, T. Amand, P. H. Tan, and B. Urbaszek. Carrier and polarization dynamics in monolayer mos_2. *Phys. Rev. Lett.*, 112:047401, 2014. 81, 96

[97] T. Yu and M. W. Wu. Valley depolarization due to intervalley and intravalley electron-hole exchange interactions in monolayer mos_2. *Phys. Rev. B*, 89:205303, 2014. 81, 105

[98] Cong Mai, Andrew Barrette, Yifei Yu, Yuriy G. Semenov, Ki Wook Kim, Linyou Cao, and Kenan Gundogdu. Many-body effects in valleytronics: Direct measurement of valley lifetimes in single-layer mos2. *Nano Letters*, 14(1):202–206, 2014. 81, 82

[99] Qinsheng Wang, Shaofeng Ge, Xiao Li, Jun Qiu, Yanxin Ji, Ji Feng, and Dong Sun. Valley carrier dynamics in monolayer molybdenum disulfide from helicity-resolved ultrafast pump–probe spectroscopy. *ACS Nano*, 7(12):11087–11093, 2013. 81, 82

[100] C. R. Zhu, K. Zhang, M. Glazov, B. Urbaszek, T. Amand, Z. W. Ji, B. L. Liu, and X. Marie. Exciton valley dynamics probed by kerr rotation in wse2 monolayers. *Phys. Rev. B*, 90:161302, Oct 2014. 81, 82

[101] M.I. Dyakonov and V.I Perel'. Spin relaxation of conduction electrons in noncentrosymmetric semiconductors. *Sov. Phys. Solid State*, 13:3023, 1972. 81

[102] E. L. Ivchenko. *Optical spectroscopy of semiconductor nanostructures*. Alpha Science, Harrow UK, 2005. 82, 108

[103] Akshay Singh, Galan Moody, Sanfeng Wu, Yanwen Wu, Nirmal J. Ghimire, Jiaqiang Yan, David G. Mandrus, Xiaodong Xu, and Xiaoqin Li. Coherent electronic coupling in atomically thin $mose_2$. *Phys. Rev. Lett.*, 112:216804, May 2014. 84

[104] Keliang He, Nardeep Kumar, Liang Zhao, Zefang Wang, Kin Fai Mak, Hui Zhao, and Jie Shan. Tightly bound excitons in monolayer wse_2. *Phys. Rev. Lett.*, 113:026803, Jul 2014. 86, 97, 99

[105] Hannu-Pekka Komsa and Arkady V. Krasheninnikov. Effects of confinement and environment on the electronic structure and exciton binding energy of mos2 from first principles. *Phys. Rev. B*, 86:241201, 2012. 86, 87, 96

[106] K. Tai, A. Mysyrowicz, R. J. Fischer, R. E. Slusher, and A. Y. Cho. Two-photon absorption spectroscopy in gaas quantum wells. *Phys. Rev. Lett.*, 62:1784–1787, Apr 1989. 87, 88, 98

[107] Ch. Neumann, A. Nöthe, and N. O. Lipari. Two-photon magnetoabsorption of znte, cdte, and gaas. *Phys. Rev. B*, 37:922–932, Jan 1988. 88, 98

[108] F. Wang, G. Dukovic, L.E. Brus, and T.F. Heinz. The optical resonances in carbon nanotubes arise from excitons. *Science*, 308:838, 2005. 87

[109] Giovanni Onida, Lucia Reining, and Angel Rubio. Electronic excitations: density-functional versus many-body green's-function approaches. *Rev. Mod. Phys.*, 74:601–659, Jun 2002. 87

[110] G. Wang, L. Bouet, D. Lagarde, M. Vidal, A. Balocchi, T. Amand, X. Marie, and B. Urbaszek. Valley dynamics probed through charged and neutral exciton emission in monolayer wse_2. *Phys. Rev. B*, 90:075413, Aug 2014. 88, 90, 91, 104, 105, 106, 107

[111] Nardeep Kumar, Sina Najmaei, Qiannan Cui, Frank Ceballos, Pulickel M. Ajayan, Jun Lou, and Hui Zhao. Second harmonic microscopy of monolayer mos_2. *Phys. Rev. B*, 87:161403, Apr 2013. 88, 90, 95

[112] Yilei Li, Yi Rao, Kin Fai Mak, Yumeng You, Shuyuan Wang, Cory R. Dean, and Tony F. Heinz. Probing symmetry properties of few-layer mos2 and h-bn by optical second-harmonic generation. *Nano Letters*, 13(7):3329–3333, 2013.

[113] Hualing Zeng, Gui-Bin Liu, Junfeng Dai, Yajun Yan, Bairen Zhu, Ruicong He, Lu Xie, Shijie Xu, Xianhui Chen, Wang Yao, and Xiaodong Cui. Optical signature of symmetry variations and spin-valley coupling in atomically thin tungsten dichalcogenides. *Scientific Reports*, 3:1608, 2013. 88, 90, 95

[114] D. C. Haueisen and Herbert Mahr. Nonlinear electronic dispersion in cucl. *Phys. Rev. Lett.*, 26:838–840, Apr 1971. 90

[115] M. Lafrentz, D. Brunne, A. V. Rodina, V. V. Pavlov, R. V. Pisarev, D. R. Yakovlev, A. Bakin, and M. Bayer. Second-harmonic generation spectroscopy of excitons in zno. *Phys. Rev. B*, 88:235207, Dec 2013. 90

[116] C. Cohen-Tannoudji, B. Diu, and F. Laloë. *Quantum Mecanics*. Hermann, 1973. 90, 91

[117] M. Grüning and C. Attaccalite. Second harmonic generation in h-bn and mos_2 monolayers: Role of electron-hole interaction. *Phys. Rev. B*, 89:081102, Feb 2014. 92

[118] A. Thilagam. Two-dimensional charged-exciton complexes. *Phys. Rev. B*, 55:7804–7808, Mar 1997. 92, 99

[119] Daichi Kozawa, Rajeev Kumar, Alexandra Carvalho, Kiran Kumar Amara, Weijie Zhao, Shunfeng Wang, Minglin Toh, Ricardo M. Ribeiro, A. H. Castro Neto, Kazunari Matsuda, and Goki Eda. Photocarrier relaxation pathway in two-dimensional semiconducting transition metal dichalcogenides. *Nature Communications*, 5:116601, Feb 2014. 92

[120] H. Sahin, S. Tongay, S. Horzum, W. Fan, J. Zhou, J. Li, J. Wu, and F. M. Peeters. Anomalous raman spectra and thickness-dependent electronic properties of wse2. *Phys. Rev. B*, 87:165409, 2013. 92

[121] Hai Li, Gang Lu, Yanlong Wang, Zongyou Yin, Chunxiao Cong, Qiyuan He, Lu Wang, Feng Ding, Ting Yu, and Hua Zhang. Mechanical exfoliation and characterization of single- and few-layer nanosheets of wse2, tas2, and tase2. *Small*, 9(11):1974–1981, 2013. 92

[122] Falco Hüser, Thomas Olsen, and Kristian S. Thygesen. How dielectric screening in two-dimensional crystals affects the convergence of excited-state calculations: Monolayer mos2. *Phys. Rev. B*, 88:245309, Dec 2013. 93, 96

[123] Ronald L. Greene, Krishan K. Bajaj, and Dwight E. Phelps. Energy levels of wannier excitons in gaas-gaalas quantum-well structures. *Phys. Rev. B*, 29:1807–1812, Feb 1984. 94, 96

[124] L. Vina, R. T. Collins, E. E. Mendez, and W. I. Wang. Excitonic coupling in gaas/gaalas quantum wells in an electric field. *Phys. Rev. Lett.*, 58:832–835, Feb 1987. 94

[125] Amnon Yariv and Pochi Yeh. *Optical waves in crystals: propagation and control of laser radiation*. Wiley, 1984. 94, 95

[126] S. Bar-Ad and I. Bar-Joseph. Absorption quantum beats of magnetoexcitons in gaas heterostructures. *Phys. Rev. Lett.*, 66:2491–2494, May 1991. 95

[127] Z. Ye, T. Cao, K. O'Brien, H. Zhu, X. Yin, Y. Wang, S. G. Louie, and X. Zhang. Probing Excitonic Dark States in Single-layer Tungsten Disulfide. *Nature*, 513:214, 2014. 97, 98, 99

[128] Shinada M. and Sugano S. *J. Phys. Soc. Japan*, page 21, 1966. 96

[129] B. Zhu, X. Chen, and X. Cui. Exciton Binding Energy of Monolayer WS2. *Scientific Reports*, 5, Mar 2015. 97, 99

[130] A R Beal and W Y Liang. Excitons in 2h-wse 2 and 3r-ws 2. *Journal of Physics C: Solid State Physics*, 9(12):2459, 1976. 98

[131] Jack Deslippe, Mario Dipoppa, David Prendergast, Marcus V. O. Moutinho, Rodrigo B. Capaz, and Steven G. Louie. Electronhole interaction in carbon nanotubes: Novel screening and exciton excitation spectra. *Nano Letters*, 9(4):1330–1334, 2009. 98

[132] T. Stroucken and S. W. Koch. Optically bright p-excitons indicating strong Coulomb coupling in transition-metal dichalcogenides. *ArXiv e-prints*, April 2014. 99, 112

[133] Chendong Zhang, Yuxuan Chen, Amber Johnson, Ming-Yang Li, Lain-Jong Li, Patrick C. Mende, Randall M. Feenstra, and Chih-Kang Shih. Probing critical point energies of transition metal dichalcogenides: surprising indirect gap of single layer slwse2. *arXiv*, 2015. 99

[134] H. J. Liu, L. Jiao, L. Xie, F. Yang, J. L. Chen, W. K. Ho, C. L. Gao, J. F. Jia, X. D. Cui, and M. H. Xie. Molecular-beam epitaxy of monolayer and bilayer wse2: A scanning tunneling microscopy/spectroscopy study and deduction of exciton binding energy. *arXiv*, 2015. 99

[135] Jason S. Ross, Sanfeng Wu, Hongyi Yu, Nirmal J. Ghimire, Aaron M. Jones, Grant Aivazian, Jiaqiang Yan, David G. Mandrus, Di Xiao, Wang Yao, and Xiaodong Xu. *Nature Comm.*, 4:1474, 2013. 103

[136] G. Wang, E. Palleau, T. Amand, S. Tongay, X. Marie, and B. Urbaszek. Polarization and time-resolved photoluminescence spectroscopy of excitons in mose2 monolayers. *Applied Physics Letters*, 106(11):–, 2015. 103, 105, 111

[137] Y. Li, J. Ludwig, T. Low, A. Chernikov, X. Cui, G. Arefe, Y. Duck Kim, A. M. van der Zande, A. Rigosi, H. M. Hill, S. H. Kim, J. Hone, Z. Li, D. Smirnov, and T. F. Heinz. Valley Splitting and Polarization by the Zeeman Effect in Monolayer MoSe2. *ArXiv e-prints*, September 2014. 104

[138] David MacNeill, Colin Heikes, Kin Fai Mak, Zachary Anderson, Andor Kormányos, Viktor Zólyomi, Jiwoong Park, and Daniel C. Ralph. Breaking of valley degeneracy by magnetic field in monolayer mose$_2$. *Phys. Rev. Lett.*, 114:037401, Jan 2015. 104

[139] G.Wang, I. C. Gerber, L. Bouet, D. Lagarde, A. Balocchi, M. Vidal, E. Palleau, T. Amand, X. Marie, and B. Urbaszek. Exciton states in monolayer mose2: impact on interband transitions. *e-print*, arXiv:1504.06333, 2015. 104

[140] A. Srivastava, M. Sidler, A. V. Allain, D. S. Lembke, A. Kis, and A. Imamoglu. *Nature Physics*, 11:141, 2015. 106, 107, 108

[141] G. Aivazian, Z. Gong, A. M Jones, R.-L. Chu, J. Yan, D. G Mandrus, C. Zhang, D. Cobden, W. Yao, and X. Xu. *Nature Physics*, 11:148, 2015. 106, 107

[142] L.D. Landau and E.M. Lifshitz. *Quantum Mechanics: Non-Relativistic Theory (vol. 3)*. Butterworth-Heinemann, Oxford, 1977. 108

[143] Andor Kormányos, Viktor Zólyomi, Neil D. Drummond, and Guido Burkard. Spin-orbit coupling, quantum dots, and qubits in monolayer transition metal dichalcogenides. *Phys. Rev. X*, 4:011034, Mar 2014. 109

[144] G. L. Bir and G. E. Pikus. *Symmetry and Strain-induced Effects in Semiconductors*. Wiley/Halsted Press, 1974. 109

[145] J. M. Riley, F. Mazzola, M. Dendzik, M. Michiardi, T. Takayama, L. Bawden, C. Granerod, M. Leandersson, T. Balasubramanian, M. Hoesch, T. K. Kim, H. Takagi, W. Meevasana, Ph. Hofmann, M. S. Bahramy, J. W. Wells, and P. D. C. King. Direct observation of spin-polarized bulk bands in an inversion-symmetric semiconductor. *Nat Phys*, advance online publication:–, 10 2014. 110

[146] Ajit Srivastava, Han Htoon, Victor I. Klimov, and Junichiro Kono. Direct observation of dark excitons in individual carbon nanotubes: Inhomogeneity in the exchange splitting. *Phys. Rev. Lett.*, 101:087402, Aug 2008. 111

[147] M. M. Glazov and E. L. Ivchenko. to be published. 111

[148] A. S. Rodin and A. H. Castro Neto. Excitonic collapse in semiconducting transition-metal dichalcogenides. *Phys. Rev. B*, 88:195437, Nov 2013. 112

[149] LV Keldysh and You V Kopaev. Possible instability of semimetallic state toward coulomb interaction. *SOVIET PHYSICS SOLID STATE, USSR*, 6(9):2219, 1965. 112

[150] A. N. Kozlov and L. A. Maksimov. The metal-dielectric divalent crystal phase transition. *JETP*, 21:790, 1965.

[151] D. Jérome, T. M. Rice, and W. Kohn. Excitonic insulator. *Phys. Rev.*, 158:462–475, Jun 1967.

[152] R. R. Guseinov and L. V. Keldysh. Nature of the phase transition under the conditions of an "excitonic" instability in the electronic spectrum of a crystal. *JETP*, 36:1193, 1973. 112

[153] G. Wang, C. Robert, A. Suslu, B. Chen, S. Yang, S. Alamdari, I. C. Gerber, T. Amand, X. Marie, S. Tongay, and B. Urbaszek. Spin-orbit engineering in transition metal dichalcogenide alloy monolayers. *ArXiv e-prints*, June 2015. 115, 116

[154] F Withers, O Del Pozo-Zamudio, A Mishchenko, AP Rooney, A Gholinia, K Watanabe, T Taniguchi, SJ Haigh, AK Geim, AI Tartakovskii, et al. Light-emitting diodes by band-structure engineering in van der waals heterostructures. *Nature materials*, 2015. 116